

**PONTIFICIA UNIVERSIDAD CATÓLICA DEL PERÚ**

**FACULTAD DE CIENCIAS E INGENIERÍA**



**CHARACTERIZATION OF HEAVY MINERAL CONCENTRATES  
FROM LITHIUM-RICH TUFF AND WHITE TUFFACEOUS  
MUDSTONE IN THE MACUSANI VOLCANIC FIELD, EASTERN  
CORDILLERA, SOUTHERN PERU**

**Tesis para obtener el título profesional de Ingeniera Geóloga**

**AUTORA:**

Lorena Katherine Gomez Gonzales

**ASESOR:**

Lisard Torró i Abat


Lima, 2026

## INFORME DE SIMILITUD

Yo, Lisard Torr  i Abat, docente de la Facultad de Ciencias e Ingenier a de la Pontificia Universidad Cat lica del Per , asesor de la tesis titulada “Characterization of heavy mineral concentrates from Lithium-rich Tuff and white tuffaceous mudstone in the Macusani Volcanic Field, Eastern Cordillera, southern Peru”, de la autora Lorena Katherine Gomez Gonzales, dejo constancia de lo siguiente:

- El mencionado documento tiene un  ndice de puntuaci n de similitud de 15 %. As  lo consigna el reporte de similitud emitido por el software Turnitin el 22/02/2026.
- He revisado con detalle dicho reporte y la Tesis y no se advierten indicios de plagio.
- Las citas a otros autores y sus respectivas referencias cumplen escrupulosamente con las pautas acad micas.

Lugar y fecha: Lima a 22 de febrero de 2026

Apellidos y nombre del asesor: Torr� i Abat, Lisard	
DNI: 49088982	Firma: 
ORCID: 0000-0002-3557-8334	

## **Agradecimientos**

El desarrollo de esta tesis fue posible gracias al apoyo y colaboración de diferentes personas, a quienes deseo expresar mi más sincero agradecimiento por su acompañamiento en este proceso.

En primer lugar, a mis padres Ana y Rodolfo, quienes siempre han apoyado mis ideas y sueños a lo largo de mi vida. De la misma forma, agradezco a mi hermana Camila, por siempre alegrarme los días con sus ocurrencias.

Además, agradezco muchísimo la confianza y la paciencia de mi asesor, Dr. Lisard Torró. Siempre llevaré presente todo el apoyo y las palabras de motivación que me brindó a lo largo de este trabajo, así como su guía académica y valiosa retroalimentación que enriquecieron cada etapa de esta investigación.

Debo agradecer los comentarios y correcciones de Jean Vallance que claramente mejoraron la calidad de este documento. No puedo dejar de agradecer el apoyo del Ing. Pablo Valverde, por su apoyo técnico y amistad, así como por facilitarme el acceso a los recursos necesarios para trabajar con el hidroseparador en el Laboratorio QEMSCAN. A las Ing. Mariana Segovia, Mercy Sanandres y MSc. Johan Ramírez, por su colaboración y apoyo académico en el desarrollo de este proyecto.

Asimismo, agradezco a mis amigos de siempre, Lucía Prati y Miguel Palomino, quienes siempre estuvieron para escucharme y apoyarme desde que empezamos en la universidad. A mis grandes amigos de la carrera, JC Dávila, mi estimada Ivana Cárcamo, Sebastián Castañeda y Kathy Huayllani, por todos los buenos momentos que hemos creado.

## Resumen

El análisis morfológico y geoquímico de minerales pesados en rocas sedimentarias (incluyendo las volcanogénicas) es clave para delimitar procesos de procedencia y petrogénesis. Además, los minerales pesados son fuentes potenciales de algunos de los llamados metales críticos. Esta tesis se centra en la caracterización morfológica y química de minerales pesados encontrados en muestras de *Lithium-rich Tuff*, la unidad principal de mena del Proyecto de Litio Falchani, y otra toba texturalmente similar, caracterizada como lutita tobácea blanca, todas ellas encontradas en el Campo Volcánico Neógeno de Macusani. Los minerales pesados se concentraron usando hidro-separación (HS11) y se analizaron sistemáticamente mediante microscopía electrónica de barrido y espectroscopía Raman. Además, granos de circón de una muestra de lutita tobácea blanca se dataron mediante ICP-MS con ablación láser. Los resultados revelan una diversidad de minerales pesados como rutilo, circón, monacita-Ce, titanita y dumortierita. Asimismo, minerales como corindón, jeremejevita, casiterita, topacio y xenotima-Y fueron encontrados exclusivamente en la unidad *Lithium-rich Tuff*, mientras que anatasa, apatito, turmalina, wickmanita, ilmenita y andradita fueron hallados exclusivamente en la lutita tobácea blanca. Los óxidos de titanio tipo rutilo en la *Lithium-rich Tuff* están enriquecidos en Nb (hasta 8.66 wt. %) y Ta (hasta 5.52 wt.%). La mineralogía y el enriquecimiento en elementos litófilos incompatibles son consistentes con la naturaleza peraluminosa y altamente evolucionada del Campo Volcánico de Macusani y, en particular, de la unidad *Lithium-rich Tuff*. La diversidad morfológica de los granos de zircón sugiere orígenes diversos, lo que es coherente con edades U-Pb de  $222 \pm 3$  y  $7.36 \pm 0.1$  Ma. Algunas de estas fases densas, como los rutilos ricos en Nb y Ta, y los fosfatos de REE, pueden representar potenciales subproductos económicos.

## **Abstract**

Morphological and geochemical analysis of heavy minerals in (volcanogenic-) sedimentary rocks are key to constraining provenance and petrogenesis. In addition, heavy minerals are potential sources for some of the so-called critical metals. This thesis focuses on the morphological and chemical characterization of heavy minerals in samples of Lithium-rich Tuff, the main ore unit from the Falchani Lithium Project, and other texturally similar tuff, here dubbed white tuffaceous mudstone, all of them found in the Neogene Macusani Volcanic Field. Heavy minerals were concentrated using hydroseparation (HS11) and systematically analyzed through scanning electron microscopy and Raman spectroscopy. In addition, zircon grains from one sample of white tuffaceous mudstone were dated by laser-ablation ICP-MS. The results reveal a diverse array of heavy minerals such as rutile, zircon, monazite-Ce, titanite, and dumortierite. In addition, corundum, jeremejevite, cassiterite, topaz, and xenotime-Y were found exclusively in the Lithium-rich Tuff, and anatase, apatite, tourmaline, wickmanite, ilmenite, andradite, and hematite were found exclusively in the white tuffaceous mudstone. Rutile-like minerals from the Lithium-rich Tuff are enriched in Nb (up to 8.66 wt.%) and Ta (up to 5.52 wt.%). The mineralogy and enrichment in incompatible lithophile elements are consistent with the peraluminous, highly evolved nature of the Macusani Volcanic Field and, in particular, the Lithium-rich Tuff. The observed high variety of zircon morphologies may indicate different origins, which is consonant with obtained U-Pb zircon dates of  $222 \pm 3$  and  $7.1 \pm 0.7$  Ma. Some of these heavy minerals, such as Nb- and Ta-rich rutiles, and REE phosphates, may represent potential economic by-products.

## Table of contents

1.	INTRODUCTION.....	1
	1.1. Mineralogy, chemistry, and petrography of heavy minerals.....	1
	1.2. Heavy minerals as a source of critical raw materials for the global economy.....	6
	1.3. Heavy minerals as tracers of orogenic processes.....	11
	1.4. Our study case: Economic importance and previous data of the Lithium-rich Tuff.....	15
	1.5. Conundrum.....	17
	1.6. Objectives.....	18
	1.7. Hypothesis/hypotheses.....	19
	1.8. Justification.....	19
2.	METHODOLOGY.....	20
	2.1. Sampling.....	20
	2.2. Analytical methods.....	21
	2.2.1. Heavy mineral concentration and separation.....	21
	2.2.2. Scanning electron microscopy (SEM-EDS).....	27
	2.2.3. Raman spectroscopy.....	27
	2.2.4. U-Pb dating.....	28
3.	GEOLOGICAL SETTING.....	30
	3.1. The Eastern Cordillera of the Andes in southern Peru: Regional basement and summary of its tectonomagmatic evolution.....	30
	3.2. Regional geology of Macusani Structural Zone.....	35
	3.3. Geology of the Macusani Volcanic Field.....	38
4.	RESULTS.....	41
	4.1. Stereoscopic microscope.....	41
	4.1.1. 2021-MAC-08.....	41
	4.1.2. 2021-MAC-21.....	43
	4.1.3. 2021-MAC-67.....	44
	4.2. SEM-EDS.....	46
	4.2.1. 2021-MAC-08.....	46
	4.2.2. 2021-MAC-21.....	52
	4.2.3. 2021-MAC-67.....	57
	4.3. Raman spectroscopy.....	62
	4.3.1. Silicate minerals.....	62
	4.3.2. Ti-rich oxides.....	70
	4.3.3. Sn-minerals.....	76
	4.3.4. Fe-oxides.....	77
	4.3.5. Borates.....	79
	4.3.6. Phosphates.....	80
	4.3.7. Sulfides.....	84
	4.4. Geochronology.....	84
5.	DISCUSSION.....	87
	5.1. Heavy minerals in tuffaceous rocks of the Macusani Volcanic Field: Inventory and comparative abundances.....	87
	5.2. Petrogenetic constraints from the identified heavy minerals.....	92
	5.3. Zircon as a tracer of basement and magmatism in the Macusani Volcanic Field.....	94
	5.4. Economic potential of heavy minerals in the Macusani tuffs.....	96
6.	CONCLUSIONS.....	97
7.	REFERENCES.....	99

## List of figures

- Figure 1. Zircon typological classification proposed by Pupin (1980) adjusted to a geothermometric scale. Index A correlates the Al/(Na+K) ratio with the development of pyramidal faces, while Index T correlates the temperature of zircon crystallization with the development of prismatic faces. .... 14
- Figure 2. Location of Falchani Lithium Project, composed of the Falchani and Ocacasa 4 concessions, and other exploration concessions in the Macusani Volcanic Field as of 2023. Delimitation of exploration concessions according to GEOCATMIN (2023). .... 16
- Figure 3. Aspect of the rock samples analyzed in this thesis. (A) Lithium-rich Tuff from the Falchani Lithium Project. (B) White tuffaceous mudstone from the Quelcaya zone. (C) White tuffaceous mudstone from the San Vicente White concession. .... 20
- Figure 4. Retsch Jaw Crusher (model BB51) in the QEMSCAN laboratory, PUCP. .... 21
- Figure 5. Dry sieving using a 500  $\mu\text{m}$  sieve screen. .... 21
- Figure 6. Wet sieving using wet sieving through a 355  $\mu\text{m}$  aperture laboratory sieve. ... 22
- Figure 7. A: Sequential wet sieving of <355  $\mu\text{m}$  particulate material through disposable Nylon sieves (200  $\mu\text{m}$ , 100  $\mu\text{m}$ , 75  $\mu\text{m}$ , and 50  $\mu\text{m}$  apertures). B: Cleaning of the retained fraction on disposable sieves. C: Two bowls with coarse and fine (relative to the aperture of the used sieve) particulate material. D: Decantation for the elimination of very fine material (dust). E: Drying of the obtained granulometry fractions in a laboratory dryer at 50  $^{\circ}\text{C}$  overnight. F: Dried sample ready for hydroseparation. .... 23
- Figure 8. Flow sheet showing the procedure followed for the dry and wet sieving of the powdered Lithium-rich Tuff samples before hydroseparation. .... 25
- Figure 9. A: Hydroseparation HS11 equipment in the QEMSCAN laboratory, PUCP. B: Heavy mineral pre-concentrate of sample introduced in the second glass separation tube to be processed to obtain a final concentrate (sample 2021-MAC-21, 50  $\mu\text{m}$  fraction). C: Final concentrate at the base of the glass separation tube; note the concentration of dark colored minerals in the concentrate, which contrasts with the more homogeneous white color of the tailing in the bowl. Abbreviations: WFR = water flow regulator; GST = glass separation tube. .... 26
- Figure 10. A: Sample holder with handpicked mineral grains. B: Handpicking under a binocular loupe in the Laboratory of Geology, PUCP. C: Example of heavy mineral concentrate obtained by hydroseparation under the binocular loupe (100  $\mu\text{m}$  fraction of the sample 2021-MAC-67). .... 27
- Figure 11. Accreted blocks to the western margin of Gondwana and morphotectonic units in the present-day Central Andes. Paleozoic metamorphic and igneous rocks and Late Permian-Triassic granites exposed in the Central Andes are also shown. Morphotectonic zones boundaries based on Oncken et al. (2006) and Carlotto et al. (2009). Outlines of terranes are based on Ramos (2008, 2009, 2018) and Wörner et al. (2018). Triassic

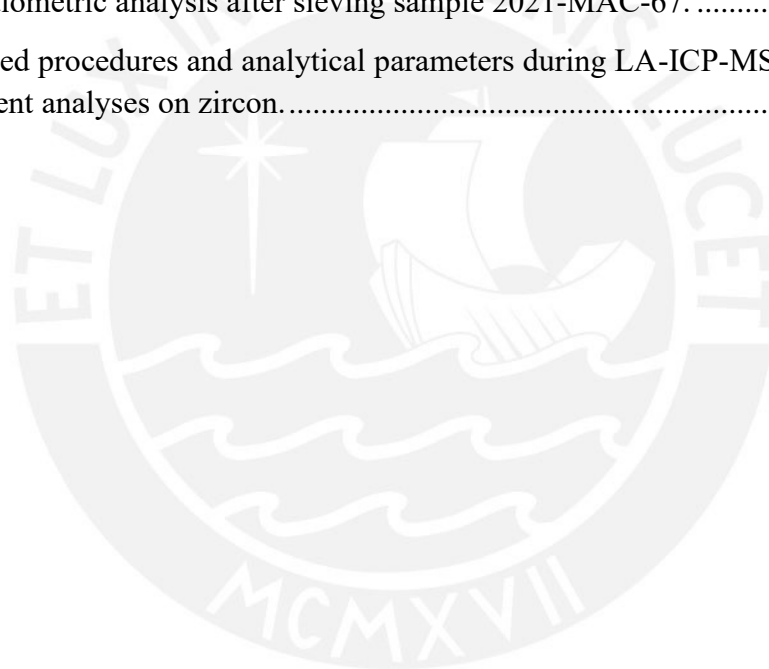
granitoids and plutons after Mišković et al. (2009), Chew et al. (2016), and Spikings et al. (2016).....	33
Figure 12. Simplified geological map of Eastern Cordillera of southern Peru including morpho-structural domains as defined by Perez et al. (2016). Geological map extracted from 1:50,000 sheets in GEOCATMIN (2023). .....	36
Figure 13. Geological map of the Macusani Volcanic Field with. Geological mapping at 1:100,000 scale extracted from GEOCATMIN (2023). .....	39
Figure 14. Grains separated from sample 2021-MAC-08 and classified according to their color and luster under the binocular loupe. A: Dark brown to black opaque crystals with metallic luster and equant to short prismatic habits. B: Green translucent crystals with diverse morphologies. ....	42
Figure 15. Grains separated from sample 2021-MAC-21 and classified according to their color, luster, and morphologies under the binocular loupe. A: Translucent crystals with vitreous luster and equant to prismatic habits. B: Translucent crystals with orange hues and smooth, curved surfaces. C: Dark gray grains with metallic luster and diverse morphologies. D: Pale blue grains with glassy luster and subhedral to anhedral morphologies.....	44
Figure 16. Grains separated from sample 2021-MAC-67 and classified according to their color, luster, and morphologies under the binocular loupe. A: Dark gray and black crystals with a metallic luster and subhedral to anhedral equant to short prismatic habits. B: Brownish white crystals with glassy luster and tabular habits. C: Pale brown to deep green crystals with prismatic habits. D: Reddish-brown grains with adamantine luster. ....	46
Figure 17. SEM-SE images of representative minerals found in heavy concentrates from sample 2021-MAC-08. See the main text for descriptions.....	48
Figure 18. SEM-SE images of heavy minerals from sample 2021-MAC-08 showcasing mineral intergrowths. A: Euhedral, octahedra modified Ti-rich oxide crystal intergrown with smaller, prismatic zircon grains. B: Euhedral Ti-rich oxide crystal intergrown with a small, elongated and prismatic zircon. C: Subhedral monazite-Ce crystal intergrown with smaller, prismatic zircon grains. D: Euhedral, equant pyramidal xenotime-Y crystal intergrown with smaller, prismatic zircon grains. ....	49
Figure 19. Selected EDS analyses (spectra and quantified results) on minerals from sample 2021-MAC-08 including zircon (A), cassiterite (B), Ti-rich oxide (C), monazite-Ce (D), xenotime-Y (E), high-Al unidentified mineral (F), actinolite (G), Fe-oxide (H), epidote (I), and pyrite (J). ....	51
Figure 20. Representative SEM-SE images of crystals in heavy concentrates from sample 2021-MAC-21. See the main text for descriptions. ....	52
Figure 21. Zircon crystal (2021-MAC-67_ML001_005; SEM-SE image) matching the morphology of G1 zircon type in the classification of Pupin (1980). ....	53

Figure 22. SEM-SE images of monazite-Ce grains from sample 2021-MAC-21 intergrown with elongated zircon crystals.....	54
Figure 23. SEM-SE images for a single reticulated Ti-oxide crystal. ....	55
Figure 24. Selected EDS analyses (spectra and quantified results) on minerals from sample 2021-MAC-21 including zircon (A), monazite-Ce (B), apatite (C), pyrite (D), Ti-rich oxide (E), Fe-oxide (F), and dumortierite (G). ....	56
Figure 25. SEM-SE images of crystals in less proportion in heavy concentrates from sample 2021-MAC-21.....	57
Figure 26. Representative SEM-SE images of minerals found in heavy concentrates from sample 2021-MAC-08. See the main text for descriptions.....	58
Figure 27. Zircon crystal (2021-MAC-67_ML001_005; SEM-SE image) morphologically similar to the G2 type in the classification of Pupin (1980). ....	59
Figure 28. Zircon crystal (2021-MAC-67_ML001_048; SEM-SE image) with a morphology similar to the S17 type in the classification of Pupin (1980). ....	59
Figure 29. Selected EDS analyses (spectra and quantified results) on minerals from sample 2021-MAC-67 including zircon (A), monazite-Ce (B), apatite (C), Ti-rich oxide (D), Fe-oxide (E), Sn-hydroxide (F), tourmaline (G), and mica (H).....	61
Figure 30. SEM-SE images of crystals found in minor proportion in heavy concentrates from sample 2021-MAC-67.....	62
Figure 31. Raman results for actinolite-tremolite. ....	63
Figure 32. Raman results for andradite. ....	63
Figure 33. Raman results for dumortierite. ....	64
Figure 34. Raman results for epidote. ....	65
Figure 35. Raman results for muscovite. ....	65
Figure 36. Raman results for titanite.....	66
Figure 37. Raman results for topaz. ....	66
Figure 38. Raman results for tourmaline. ....	67
Figure 39. Raman results for zircon crystals. ....	68
Figure 40. Prismatic zircon (bright) in apatite crystal (dark).....	69
Figure 41. Apatite inclusion (dark) in a zircon crystal (bright). ....	70
Figure 42. Raman results for anatase. ....	71
Figure 43. Raman results for type-1 rutile. ....	72
Figure 44. Raman results for type-2 rutile. ....	73
Figure 45. Raman results for type-3 rutile. ....	74

Figure 46. Raman results for type-1 unidentified Ti-rich oxide. ....	75
Figure 47. Raman results for type-2 unidentified Ti-rich oxide. ....	75
Figure 48. Raman results for type-3 unidentified Ti-rich oxide. ....	76
Figure 49. Raman results for cassiterite. ....	76
Figure 50. Raman results for wickmanite. ....	77
Figure 51. Raman results for goethite. ....	78
Figure 52. Raman results for hematite. ....	78
Figure 53. Raman results for ilmenite. ....	79
Figure 54. Raman results for magnetite. ....	79
Figure 55. Raman results for jeremejevite. ....	80
Figure 56. Raman results for apatite. ....	81
Figure 57. Raman results for monazite-Ce. ....	82
Figure 58. Apatite inclusion (dark) in a monazite-Ce crystal (bright). ....	83
Figure 59. Raman results for xenotime-Y. ....	83
Figure 60. Raman results for pyrite. ....	84
Figure 61. Cathodoluminescence (CL) images of zircon grains from sample 21-MAC-21. A: Subhedral zircon with high-CL intensity core surrounded by a low-CL intensity rim. B: Euhedral zircon with a reabsorbed core, oscillatory-zoning mantle, and low-CL intensity rim. C: Zircon with euhedral habit with a resorbed and zoned core truncated by a high-CL convolute mantle and a low-CL intensity rim. Yellow circles show the location of the point analyses with the corresponding U-Pb dates. ....	85
Figure 62. Results of in situ U-Pb isotope analyses of zircon grains from sample 21-MAC-21 in a Tera-Wasserburg concordia diagram. A weighted mean $^{206}\text{Pb}/^{238}\text{U}$ date is provided for the youngest zircon population. ....	86
Figure 63. Ternary Diagram for Ti-oxides (rutile, unidentified Ti-oxides, and anatase) found in the Lithium-rich Tuff (2021-MAC-08) and white tuffaceous mudstone (2021-MAC-21, 2021-MAC-67) samples. EDS data. In addition, EMPA data on rutile from ash-flow tuff of the Macusani Formation reported by Pichavant et al. (1988) is given for comparison purposes. ....	89

### List of tables

Table 1. Most common heavy minerals, their chemical formula, and their density according to data from MINDAT (2023). .....	1
Table 2. Most common elements in heavy minerals with their respective symbol, atomic weight, density, and first ionization energy, according to data from MINDAT (2023). ....	2
Table 3. Heavy minerals with their respective petrographic characteristics (summarized data from MINDAT 2023; Schouten 1962; Darby and Tsang 1987; Mange and Maurer 1992; Li et al. 2002; Mange and Morton 2007; Elsner 2010; Badanina et al. 2015; Haldar 2020). .....	3
Table 4. Granulometric analysis after sieving sample 2021-MAC-08. ....	24
Table 5. Granulometric analysis after sieving sample 2021-MAC-21. ....	24
Table 6. Granulometric analysis after sieving sample 2021-MAC-67. ....	24
Table 7. Detailed procedures and analytical parameters during LA-ICP-MS U-Pb isotopic and trace element analyses on zircon. ....	28



## 1. INTRODUCTION

### 1.1. Mineralogy, chemistry, and petrography of heavy minerals

Heavy minerals are defined as minerals that are denser than common rock forming minerals such as quartz (density [ $\rho$ ] = 2.65 g/cm<sup>3</sup>) and feldspars ( $\rho$  = 2.55 – 2.76 g/cm<sup>3</sup>) (Morton 1978; Elsner 2010; Subasinghe et al. 2022). The term “heavy” is used to describe minerals with a density of over 2.85 g/cm<sup>3</sup>. In practice, only those minerals with densities greater than the dense media most used in laboratories – i.e., bromoform ( $\rho$  = 2.84 – 2.89 g/cm<sup>3</sup>) or tetrabromomethane ( $\rho$  = 2.94 g/cm<sup>3</sup>) – are considered heavy minerals (Elsner 2010). The most common heavy minerals are presented in Table 1. Elsner (2010) subdivided heavy minerals into:

- Heavy heavy minerals ( $\rho$  = 6.8 – 21 g/cm<sup>3</sup>) such as gold, platinum, and cassiterite;
- Light heavy minerals ( $\rho$  = 4.2 – 6.7 g/cm<sup>3</sup>) such as ilmenite, rutile, zircon, monazite, magnetite, and chromite; and
- Gemstones ( $\rho$  = 2.9 – 4.1 g/cm<sup>3</sup>), mainly diamonds.

Table 1. Most common heavy minerals, their chemical formula, and their density according to data from MINDAT (2023).

Heavy minerals	Formula	Density (g/cm <sup>3</sup> )
Ilmenite	Fe <sup>2+</sup> TiO <sub>3</sub>	4.68 - 4.76
Rutile	TiO <sub>2</sub>	4.23
Zircon	Zr(SiO <sub>4</sub> )	4.6 - 4.7
Baddeleyite	ZrO <sub>2</sub>	5.4 -6
Monazite-group	(Ce,La,Nd,Th)(PO <sub>4</sub> )	4.8 - 5.5
Xenotime-(Y)	Y(PO <sub>4</sub> )	4.4 - 5.1
Kyanite	Al <sub>2</sub> (SiO <sub>4</sub> )O	3.53 - 3.67
Sillimanite	Al <sub>2</sub> (SiO <sub>4</sub> )O	3.23 - 3.27
Andalusite	Al <sub>2</sub> (SiO <sub>4</sub> )O	3.13 - 3.21
Staurolite	Fe <sup>2+</sup> <sub>2</sub> Al <sub>9</sub> Si <sub>4</sub> O <sub>23</sub> (OH)	3.74 - 3.83
Garnet	(Mg,Ca,Fe <sup>2+</sup> ,Mn <sup>2+</sup> ) <sub>3</sub> (Al,Fe <sup>3+</sup> ,Cr <sup>3+</sup> ,V <sup>3+</sup> ) <sub>2</sub> (SiO <sub>4</sub> ) <sub>3</sub>	3.5 - 4.3
Chromite	Fe <sup>2+</sup> Cr <sup>3+</sup> <sub>2</sub> O <sub>4</sub>	4.5 - 4.8
Magnetite	Fe <sup>2+</sup> Fe <sup>3+</sup> <sub>2</sub> O <sub>4</sub>	5.18
Cassiterite	SnO <sub>2</sub>	6.98 - 7.01
Columbite-tantalite	(Mn,Fe)(Ta,Nb) <sub>2</sub> O <sub>6</sub>	-
Wolframite	(Fe,Mn,Mg)WO <sub>4</sub>	7.3
Scheelite	Ca(WO <sub>4</sub> )	6.1

Heavy minerals may contain dozens of chemical elements, both structural (i.e., those that are normally detailed in the structural formulae) and substitution (in minor amounts and not detailed in the structural formulae). In the particular case of heavy minerals, structural elements are typically characterized by having high atomic weights and atomic numbers (Table 2).

**Table 2.** Most common elements in heavy minerals with their respective symbol, atomic weight, density, and first ionization energy, according to data from [MINDAT \(2023\)](#).

<b>Element</b>	<b>Symbol</b>	<b>Atomic weight</b>	<b>Density (g/cm<sup>3</sup>)</b>	<b>Atomic number</b>
Titanium	Ti	47.87	4.51	22
Vanadium	V	50.94	6.11	23
Chromium	Cr	52.00	7.14	24
Manganese	Mn	54.94	7.47	25
Iron	Fe	55.85	7.87	26
Yttrium	Y	88.91	4.47	39
Zirconium	Zr	91.22	6.51	40
Niobium	Nb	92.91	8.57	41
Tin	Sn	118.71	7.31	50
Lanthanum	La	138.91	6.15	57
Cerium	Ce	140.12	6.69	58
Neodymium	Nd	144.24	7.01	60
Hafnium	Hf	178.49	13.31	72
Tantalum	Ta	180.95	16.65	73
Tungsten	W	183.84	19.25	74
Thorium	Th	232.04	11.72	90

Heavy minerals have some distinctive, often shared, petrographic characteristics ([Gheith et al. 2021](#)). The features of some of the main heavy minerals are briefly described in [Table 3](#).

Table 3. Heavy minerals with their respective petrographic characteristics (summarized data from MINDAT 2023; Schouten 1962; Darby and Tsang 1987; Mange and Maurer 1992; Li et al. 2002; Mange and Morton 2007; Elsner 2010; Badanina et al. 2015; Haldar 2020).

Mineral	Crystal system	Morphology	Color	Occurrence	Comments
<b>Ilmenite</b>	Trigonal	<ul style="list-style-type: none"> <li>- Common: thick tabular crystals</li> <li>- Rare: thin laminae, acute rhombohedral, and compact massive</li> </ul>	Iron black or black	Common in intrusive and extrusive rocks, including pegmatites and other vein rocks, and metamorphic rocks (e.g., schists). Particularly important in norites, gabbros, and anorthosites	<ul style="list-style-type: none"> <li>- Can be altered to leucoxene</li> </ul>
<b>Rutile</b>	Tetragonal	<ul style="list-style-type: none"> <li>- Common: prismatic, often slender to acicular. Prism zone vertically striated or furrowed</li> <li>- Rare: pyramidal or granular massive</li> </ul>	Blood red, brownish yellow, brown-red, yellow, greyish-black, black, brown, bluish, or violet	Predominantly in Al-rich metamorphic rocks Typical accessory mineral in high-pressure, high-temperature igneous rocks and detrital sediments	<ul style="list-style-type: none"> <li>- Ultra-stable mineral</li> <li>- Usually found with other Ti-bearing (leucoxene, anatase, and sphene) phases.</li> <li>- Can incorporate other metals such as Nb, Cr, and Zr</li> </ul>
<b>Zircon</b>	Tetragonal	<ul style="list-style-type: none"> <li>- Tabular to square prismatic crystals</li> <li>- Tetragonal-bipyramidal crystals</li> </ul>	Colorless, yellow, grey, reddish-brown, green, brown, black	In a variety of igneous and metamorphic rocks, although it is most abundant in silicic igneous rocks (e.g., granitoids). It reaches high concentrations in detrital sediments	<ul style="list-style-type: none"> <li>- Ultra-stable mineral</li> <li>- Variable contents of rare earth elements (REE) and other elements such as Hf, Nb, U, Th, and Ta</li> </ul>
<b>Baddeleyite</b>	Monoclinic	<ul style="list-style-type: none"> <li>- Common: tabular crystals elongated on [010]</li> <li>- Short to long prismatic crystals along [001]</li> <li>- Rarely equant prism faces and striated parallel to [001]</li> <li>- Botryoidal masses with radially fibrous structure and concentric banding</li> </ul>	Colorless to yellow, green, greenish, reddish brown, brown, iron-black	Occurs as an accessory mineral in carbonatites and kimberlites	<ul style="list-style-type: none"> <li>- Associated with pyrochlore and zircon</li> </ul>

Mineral	Crystal system	Morphology	Color	Occurrence	Comments
<b>Monazite group</b>	Monoclinic	<ul style="list-style-type: none"> <li>- Common: small (sometimes coarse) crystals</li> <li>- Frequently flattened or elongated prismatic crystals</li> <li>- Crystal faces commonly rough, striated, or uneven</li> </ul>	Light yellow, brown, orange brown, reddish brown	In a variety of rocks (e.g., granites, granodiorites, monzonites, granite pegmatites, carbonatites, hydrothermal veins, laterites rich in REE phosphates)	<ul style="list-style-type: none"> <li>- May incorporate U, Th, Sn, Ti, Zr, and Ta</li> </ul>
<b>Xenotime group</b>	Tetragonal	<ul style="list-style-type: none"> <li>- Short to long prismatic crystals</li> <li>- Crude radial aggregates of coarse crystals</li> </ul>	Yellowish brown, reddish brown, light red, flesh-red, light green, gray, grayish-white, yellow	As an accessory mineral in granites, syenites, granite pegmatites, and quartzose micaceous gneisses	<ul style="list-style-type: none"> <li>- Can incorporate REE (chiefly Yb and Y) and variable amounts of U, Th, Si, V, Zr, S, and Ca</li> </ul>
<b>Kyanite</b>	Triclinic	<ul style="list-style-type: none"> <li>- Bladed crystals</li> <li>- Tabular crystals</li> </ul>	Blue, white, light gray, green, rarely yellow, orange, pink	Common metamorphic mineral in Al-bearing rocks	<ul style="list-style-type: none"> <li>- Associated with corundum, rutile, topaz, tourmaline, and Al phosphates</li> <li>- Can incorporate chromium (up to 1.8 %)</li> </ul>
<b>Sillimanite</b>	Ortho-rhombic	<ul style="list-style-type: none"> <li>- Common: fibrous crystals in wavy bundles</li> <li>- Rare: in well-defined rectangular to square cross-sectioned prisms</li> </ul>	Colorless, white, yellow, brown, green, blue, gray	Common metamorphic mineral in Al-bearing rocks	<ul style="list-style-type: none"> <li>- Inclusions of corundum, rutile, Fe oxides, topaz, mica, clay minerals, and silica</li> <li>- Trace elements such as Fe, Mn, Ti, and Cr</li> </ul>
<b>Andalusite</b>	Ortho-rhombic	<ul style="list-style-type: none"> <li>- Columnar aggregates having nearly square cross sections, commonly elongated</li> <li>- Fibrous, compact, massive</li> </ul>	Pink to red, brown, occasionally yellow, green, white, gray, and rarely violet	Common metamorphic mineral in Al-bearing rocks	<ul style="list-style-type: none"> <li>- Associated with staurolite and almandine</li> <li>- Inclusions of graphite, ilmenite, muscovite, biotite, or chlorite</li> </ul>
<b>Staurolite</b>	Monoclinic	<ul style="list-style-type: none"> <li>- Prismatic crystals</li> <li>- Common: typical cruciform twins</li> </ul>	Dark brown, brownish-black, red-brown	Occurs in mesozonal contact zones in regional metamorphism	<ul style="list-style-type: none"> <li>- Associated with sillimanite, kyanite, andalusite, garnet, muscovite, or biotite</li> </ul>

Mineral	Crystal system	Morphology	Color	Occurrence	Comments
<b>Garnet group</b>	Isometric	<ul style="list-style-type: none"> <li>- Common: well-crystallized dodecahedron or trapezohedron</li> <li>- In rounded grains and massive</li> </ul>	All colors	Typical in metamorphic facies as porphyroblasts in schists and gneisses. It can also occur in some peraluminous granites and pegmatites	<ul style="list-style-type: none"> <li>- Commonly mixed compositions between grossular, andradite, almandine, pyrope, and spessartine</li> <li>- May show inclusions of rutile and zircon</li> <li>- Can incorporate trace elements such as Fe, Mn, Cr, V, Na, Ni, and Sn</li> </ul>
<b>Chromite</b>	Isometric	<ul style="list-style-type: none"> <li>- Common: massive, fine granular to compact</li> <li>- Uncommon: octahedral crystals</li> </ul>	Black	It typically occurs as disseminated grains or as vein fillings in ultramafic rocks	<ul style="list-style-type: none"> <li>- Commonly associated with magnetite, hematite, and ilmenite</li> <li>- Can incorporate trace elements such as Ti, V, and Mn</li> </ul>
<b>Magnetite</b>	Isometric	<ul style="list-style-type: none"> <li>- Common octahedral crystals</li> <li>- Sometimes dodecahedral, striated on {011}</li> <li>- Massive, granular, coarse to fine</li> </ul>	Greyish black or iron black	It usually occurs in magmatic and metamorphic rocks	<ul style="list-style-type: none"> <li>- Associated with hematite, ilmenite, pyrite, rutile, and Mn oxides</li> <li>- Can incorporate trace elements such as Mg, Mn, Zn, Ni, Cr, Ti, Al, and V</li> </ul>
<b>Cassiterite</b>	Tetragonal	<ul style="list-style-type: none"> <li>- Common: short prismatic untwinned crystals</li> <li>- Less commonly: long prismatic with acute terminations, pyramidal, fibrous, botryoidal crusts, or concretionary masses</li> </ul>	Black, yellow, brown, red, or white	It commonly occurs in granites, pegmatites, and other felsic intrusive rocks, as well as in hydrothermal veins	<ul style="list-style-type: none"> <li>- Frequently associated with rutile, lepidolite, columbite, and tantalite</li> <li>- Can incorporate trace amounts of Ti, Li, Sc, Zn, Fe, W, Nb, Ta, and Mn</li> </ul>

Mineral	Crystal system	Morphology	Color	Occurrence	Comments
<b>Columbite-tantalite</b>	Ortho-rhombic	<ul style="list-style-type: none"> <li>- Short prismatic crystals</li> <li>- Often rectangular prisms with prominent pinacoids</li> <li>- Thin or thick tabular crystals</li> <li>- Less often pyramidal</li> <li>- Massive</li> </ul>	Black, dark brown, reddish brown	Pegmatites, granites, carbonatites, syenites, and nepheline syenites	<ul style="list-style-type: none"> <li>- Associated with beryl, cassiterite, pyrochlore, and phosphates</li> <li>- Inclusions of zircon, cassiterite, and tapiolite</li> </ul>
<b>Wolframite</b>	Monoclinic	<ul style="list-style-type: none"> <li>- Common: prismatic and striated crystals on [001]</li> <li>- Radiating groups or in parallel configuration</li> <li>- Crystals wedge-shaped, commonly flattened</li> <li>- Massive</li> </ul>	Dark grey, brown black	Occurs in granites, high-temperature hydrothermal veins, granitic pegmatites, and placer deposits	<ul style="list-style-type: none"> <li>- Usually associated with cassiterite, scheelite, and molybdenite</li> <li>- Incorporations of a columbite-tantalite (up to ~ 25%) component</li> <li>- Can incorporate trace elements such as In, Mo, Bi, Zr, Sc, and Y</li> </ul>
<b>Scheelite</b>	Tetragonal	<ul style="list-style-type: none"> <li>- Common: pseudo-octahedral crystals</li> <li>- Usually granular, massive, and columnar</li> </ul>	Tan, golden-yellow, colorless, white, greenish, dark brown	Commonly occurs in, pegmatites, skarns, and high-temperature veins. It is also present in contact metamorphic rocks around granitic intrusions	<ul style="list-style-type: none"> <li>- One of the most fluorescent minerals</li> <li>- Associated with apatite, cassiterite, fluorite, and tourmaline</li> </ul>

## 1.2. Heavy minerals as a source of critical raw materials for the global economy

In addition to traditional commodities such as gold, heavy minerals may host significant contents of the so-called *high-tech* elements with a remarkable global economic importance, largely due to their extensive use in industrial production. The [European Commission \(2020\)](#) has identified 30 Critical Raw Materials (CRMs) including titanium (Ti), tantalum (Ta), tungsten (W), niobium (Nb), hafnium (Hf), and rare earth elements (REE), which are essential components in different heavy minerals ([Table 1](#)). In addition, other elements of high economic importance found in heavy minerals include zirconium (Zr) and tin (Sn).

*Titanium* is the ninth most abundant element in the Earth's crust (0.6 % of the total crustal mass). It is lithophile and occurs mostly as a tetravalent cation in a wide range of oxides and silicates (e.g., ilmenite, leucosene, and rutile; [Farges 1998](#)). It is typically extracted

from ilmenite and rutile in magmatic and sedimentary deposits (Elsner 2010). The most significant deposits of titanium include massif-type anorthosite (e.g., Lac Tio, Canada; Tellnes, Norway), titanium-vanadium (e.g., Gusevogorsk, Russia), and fluvial placer deposits of heavy mineral sands (rutile, leucoxene, e.g., Sierra Leone) (Elsner 2010; Subasinghe et al. 2022). Titanium is a highly versatile metal with a variety of industrial and consumer applications (Hanson 1986). Its high strength-to-weight ratio and corrosion resistance make it valuable material in the aerospace and defense industries, where it is used in the fabrication of aircraft components, missile casing, and armor plating (Henriques 2009). Moreover, titanium is biocompatible, which means it does not react with the human body, making it useful for medical implants (Hanawa 2019). Additionally, titanium is used in the automotive industry to make lightweight components that improve fuel efficiency and performance (Kiernan 2020). In addition, titanium is used in compounds such as titanium dioxide ( $\text{TiO}_2$ ), which is employed as a pigment in paints, plastics, and paper, titanium tetrachloride ( $\text{TiCl}_4$ ), which is used in the production of titanium metal, and titanium carbide ( $\text{TiC}$ ), which is utilized in the fabrication of cutting tools (Elsner 2010). The demand for titanium is expected to increase in the coming years driven by the growing demand from the aerospace, automotive, and medical industries (Woodruff et al. 2017). This is projected to result in a rise from USD 24.7 billion in 2021 to USD 33.5 billion by 2026 (MarketsandMarkets 2021).

*Tungsten* is a siderophile and metallic transition element with an average estimated abundance of 1.25 – 1.50 ppm in the Earth's crust (BGS 2011). Tungsten is exclusively mined from scheelite and wolframites in skarns (e.g., Cantung, Canada) and Sn-W vein stockwork deposits (e.g., Panasqueira, Portugal; Xihuashan, China) (Han et al. 2021). It is characterized by its high thermal resistance, high tensile strength, very high hardness, and good conductivity, rendering it an ideal material in industrial alloys for steelmaking, aerospace, and defense (Elsner 2010). Additionally, its high density and ability to absorb gamma rays makes it a valuable component in radiation shielding (BGS 2011). Tungsten is commonly utilized in the compound form of tungsten carbide ( $\text{WC}$  or  $\text{W}_2\text{C}$ ) for cutting tools, abrasives, and wear-resistant parts. Other compounds, such as tungsten oxide ( $\text{WO}_3$ ), are used in the production of pigments and ceramics (BGS 2011). The current demand for tungsten is primarily driven by the industrial alloy and tungsten carbide markets (Shedd 2022). According to Global Market Insights (2018), the global tungsten market size was

estimated to be worth over USD 3.5 billion in 2017 and is projected to reach USD 8.5 billion by 2025.

*Tin* is a metal siderophile and lithophile element with an average abundance of 2.3 ppm in the Earth's crust (Kamilli et al. 2017). The principal ore of tin is cassiterite, which is found in placer deposits (residual-alluvial; e.g., Pitinga, Brazil; Bangka Island, Indonesia), in primary hydrothermal tin ± silver ± polymetallic deposits (e.g., San Rafael, Peru; Huanuni, Llallagua, and Cerro Rico de Potosí, Bolivia), in pegmatites and greisens (e.g., Bikita, Zimbabwe; Phuket, Thailand), in skarn and carbonate-sulfide replacement deposits (e.g., Cuomolong, China), and in massive sulfide deposits (e.g., Nerves Corvo, Portugal) (Elsner 2010; Kamilli et al. 2017; Bowles 2021; Lehmann 2021). Tin is utilized in soldering materials in the electronics manufacturing industry, as a coating for electronic components to prevent corrosion, as a packaging material for cans and containers, and for transportation and construction materials (Kamilli et al. 2017). Additionally, tin is used in technological alloys such as indium-tin oxide (ITO), which is present in all flat-touch screens and photovoltaic cells (Shanks et al. 2017). With regards to tin demand, it has been relatively stable in recent years (Kamilli et al. 2017), at around 305,000 metric tons in 2021 and 310,000 metric tons in 2022 (USGS 2023). Mordor Intelligence (2022) predicts that the future demand for tin will increase with the tin market size projected to register a compound annual growth rate of over 2.5% during the 2023-2028 period with the electronic sector as the primary driver of the market growth.

*Niobium* and *tantalum* are transition metals with average crustal abundances of 20 ppm and 2.0 ppm, respectively (Elsner 2010; Haynes 2014). These elements are found in nature almost systematically together (Schulz et al. 2017). Niobium is usually mined from pyrochlore and columbite, while tantalum is exclusively extracted from tantalite (Elsner 2010). Niobium and tantalum deposits include carbonatites and associated rocks (e.g., Catalao, Brazil; Niobec, Canada), alkaline to peralkaline granites and syenites (e.g., Ilímaussaq Complex and Motzfeldt, Greenland), and 'rare-metal' granites and granitic pegmatites of the LCT (lithium, cesium, tantalum) (e.g., Greenbushes and Wodgina, Australia) and NYF (niobium, yttrium, fluorine) families (Schulz et al. 2017; Howell et al. 2020). The principal application of niobium is in the production of high-strength alloy steels for a variety of applications, including construction, automotive, and aerospace (Elsner 2010; Gasik 2013). Furthermore, niobium alloys are used in the manufacture of

superconducting materials (Schulz et al. 2017). Tantalum has the capacity to store and release energy, which is harnessed in the production of capacitors for cellphones, hearing aids, and hard drives (Schulz et al. 2017). According to Mordor Intelligence (2022), the future demand for both elements is expected to increase, particularly in the electronics, automotive, and aerospace industries. The niobium market size is projected to register a compound annual growth rate of over 5.5% during the 2023-2028 period, while the tantalum market size is projected to register a compound annual growth rate of over 5% during the same period.

*Zirconium* is a lithophile element that is classified as incompatible with an average crustal abundance of 165 ppm (Haynes 2014; Jones et al. 2017). Its most common form in nature is in zircon (Elsner 2010). Zircon crystallizes mostly from magmas, but it can also form from hydrothermal fluids or during metamorphism (Schaltegger 2007). Given its extreme resistance to weathering and abrasion, this mineral is also common in sedimentary rocks and in beach and alluvial placer deposits (Subasinghe et al. 2022). The recovery of zirconium from primary deposits is not economically viable, with the exception of the Kovdor deposit in Russia, which produces zirconium from baddeleyite as a byproduct of apatite and magnetite (Jones et al. 2017). Zirconium deposits in modern coastal placer systems include the Douglas and Jacinth-Ambrosia mines in Australia (Jones et al. 2017). Zirconium is mostly used in the ceramic industry as zirconia ( $ZrO_2$ ), which is particularly employed due to its high chemical purity, high melting point, high fracture resistance, and good dielectric-piezoelectric properties for the fabrication of specialized electro ceramics utilized in solar cells, biomedical implants, and casting alloys for turbine blades (Elsner 2010; Subasinghe et al. 2022). Between 2002 and 2022, global production of zirconium mineral concentrates increased by 50 % (from 830 to 1,400 thousand Mt). This growth is expected to continue, driven by the ceramics, chemicals, and metals industries (Jones et al. 2017).

*Hafnium* is an incompatible lithophile element (Jones et al. 2017) with an estimated average crustal abundance of 3.0 ppm (Taylor and McLennan 1995). Hafnium and zirconium are chemically similar, sharing nearly identical charge, ionic radius, and ionic potential, which makes hafnium always incorporated into the crystal lattice of zircon, which is its main ore followed by baddeleyite (Elsner 2010; Jones et al. 2017). The main ore deposits worldwide are heavy mineral sands (e.g., coastal placer and paleo placer systems) in which hafnium

is mined as a byproduct (e.g., Trail Ridge, USA; Old Hickory, USA) (Elsner 2010). Due to its high melting point, thermal stability, and resistance to corrosion, hafnium is used in a range of applications (Jones et al. 2017). Its principal application is in zirconium alloys, which are widely used in the nuclear industry due to their excellent corrosion resistance (Sangine and Gambogi 2018). Hafnium is also employed in the manufacture of electrodes for plasma cutting and as a component of high-temperature alloys used in jet engines (Jones et al. 2017). In terms of hafnium compounds, hafnium oxide is employed as a dielectric material in the fabrication of semiconductor devices within the microelectronics industry (Rupich and Chabal 2018). Hafnium carbide is used as a refractory material in high-temperature applications, including rocket nozzles and cutting tools (Sangine and Gambogi 2018). According to Strategic Metals Invest (2023), the demand for hafnium in super alloys used in aerospace and gas turbine blades and vanes will double over the next 20 years and their price is expected to keep rising over the next 10 to 20 years. It is important to underscore the increasing demand of hafnium from the aerospace industry, which has been the largest contributor to the massive price spike of 179% from \$1,632.40/kg in 2022 to \$4,560.00/kg in 2023.

The *Rare Earth Elements* (REE) are a group of 17 elements, including the lanthanide series elements (La to Lu), yttrium (Y), and scandium (Sc), which share a similar geochemical behavior with a total abundance ( $\Sigma$ REE) of 169.1 ppm on Earth's crust (Chakhmouradian and Wall 2012; Dushyantha et al. 2020). REE are most commonly found in nature in the form of phosphates, silicates, carbonates, oxides, and halides (e.g., monazite, bastnasite, and xenotime; Table 1) (Dushyantha et al. 2020; Subasinghe et al. 2022). The economic contents of REE are typically associated with carbonatites and alkaline-peralkaline igneous rocks (e.g., Bayan Obo, China, which is the world's largest REE deposit; Mountain Pass, USA) and lateritic ion adsorption clay and placers deposits (e.g., South China clays; Buena Norte in Brazil) (Kynicky et al. 2012; Mariano and Mariano 2012). Karst bauxites are also receiving attention as non-conventional REE sources (Reinhardt et al. 2018; Villanova-de-Benavent et al. 2023). REE have a multitude of applications, predominantly in the form compounds such as rare earth oxides (REO; Hatch 2012). The most common uses are as catalysts in a variety of processes (e.g., petroleum refining, and automotive catalytic converters), as colorants and polishing agents, in the production of glass and ceramics, in the production of battery cells for energy storage, in energy-efficient lighting (e.g., compact

fluorescent bulbs and LED lights), and in the fabrication of permanent magnets which are used in electric motors, wind turbines, hard disk drives, and medical devices (Elsner 2010; Hatch 2012; Dushyantha et al. 2020). The demand of REEs has been consistently rising over the past few decades driven by their expanding utilization. This trend is expected to persist, as the demand for electric vehicles, renewable energy technologies, and other high-tech applications continues to grow (Golroudbary et al. 2022). According to Global Markets Insights (2020), the REE market size was valued on USD 13.2 billion in 2019 and is expected to reach around USD 19.8 billion in 2026. The demand for REE is expected to keep increasing by several orders of magnitudes over the next decade, potentially leading to a shortage if new sources are not developed (Haque et al. 2014).

### 1.3. Heavy minerals as tracers of orogenic processes

Heavy minerals serve as powerful tools for unraveling Earth's history. Morphological and geochemical analysis of diverse heavy mineral assemblages provides valuable constraints on petrogenetic processes and plays a crucial role in provenance studies (Morton and Hallsworth 1999; Mange and Morton 2007; Garzanti et al. 2008; Shimizu et al. 2019). Noteworthy, heavy minerals are commonly employed in geochronology and thermochronology, thereby serving as a fundamental tool for dating geologic processes (Stow 1946; Yim et al. 1985; Malusà and Garzanti 2019). Of particular interest as tracers of igneous and orogenic processes are monazite, xenotime, titanite, rutile, cassiterite, garnet, zircon, and baddeleyite.

*Monazite* and *xenotime* are widely used for dating magmatic and metamorphic processes due to the incorporation of U and Th in their structure. These minerals can retain their primary geochemical compositions even through high-temperature and deformation events (Montel et al. 1996; Parrish 2015; Barnes et al. 2018, 2021). Both monazite and xenotime are common accessory minerals in a variety of rocks such as metapelites, peraluminous granites, and siliciclastic sedimentary rocks (e.g., Braun et al. 2006; Liu et al. 2011; Zhang et al. 2015). Furthermore, monazite and xenotime in hydrothermal assemblages are ideal chronometers for hydrothermal processes (e.g., Zi et al. 2015).

*Rutile* is also a robust and common accessory mineral. It may provide information about sedimentary provenance thanks to its ability to host considerable amounts of trace elements in its crystalline structure. Element content ratios in rutile such as Nb/TiO<sub>2</sub> and Cr/TiO<sub>2</sub> are

key to trace source rocks (Mange and Morton 2007; Bracciali et al. 2013). In addition, the content of Zr in rutile is extremely temperature-dependent and thus serves as a thermometer (Rubatto 2015). Rutile often has low U content, which may preclude accurate U-Pb dating (Rubatto 2015). In contrast, the great amounts of U and Pb in *titanite*—a highly stable and common accessory mineral in a variety of rocks—makes it ideal for U-Pb dating. Titanite is particularly suitable for the dating of metasediments and complex magmatic, metamorphic, and hydrothermal processes (Sun et al. 2012; Rubatto 2015; Liu et al. 2022). In addition, the content of trace elements in titanite can be employed as a petrogenetic indicator and a provenance tracer (Stearns et al. 2015; Scibiorski et al. 2019).

*Cassiterite* is also an important tracer mineral due to its incorporation in minor and trace amounts of a variety of elements in its crystal lattice structure, its chemical and physical robustness, and its deposition in a wide range of geological conditions (Plimer et al. 1991; Serranti et al. 2002; Cheng et al. 2019). Besides, the moderate  $U^{4+}$  and low  $Pb^{2+}$  contents in cassiterite render this mineral suitable for U-Pb dating (Romer 2015; Neymark et al. 2018; Carr et al. 2021). The application of cassiterite dating provides the most straightforward information about the timing of tin mineralization events (e.g., Mao et al. 2020; Gemrich et al. 2021; Benites et al. 2022; Harlaux et al. 2023). The morphology of cassiterite grains, their mineral inclusions, chemical compositions, and radiometric dates are employed in sediment provenance studies (e.g., Nwamba et al. 2023).

*Garnet* group minerals are other heavy phases that are commonly used in geochronology and geochemical analysis due to their notable compositional diversity, including major and trace element, and their widespread occurrence in a variety of rock types (Wood et al. 2013). Several isotope systems can be employed in garnet geochronology, including Lu-Hf and Sm-Nd (Baxter et al. 2013). Garnet crystals usually exhibit concentric growth patterns with element, isotope, textural, and inclusion records that are frequently used to trace pressure-temperature-time trajectories in metamorphic and metasomatic rocks (Pollington and Baxter 2010; Baxter et al. 2013; Caddick and Kohn 2013; Godet et al. 2021). Furthermore, garnet minerals are also important for the determination of sediment provenance, as they are stable under weathering and burial diagenetic conditions (Mange and Morton. 2007; Baxter et al. 2013).

Zirconium minerals of interest for the reconstruction of tectonic events are *zircon* and *baddeleyite*. Although zircon is the cornerstone of geochronology (Parrish 2015), baddeleyite is also of significance in U-Pb geochronology. Baddeleyite is particularly useful in ultramafic and mafic rocks in which it may crystallize as a minor or trace mineral. Compared to zircon, baddeleyite is rarely inherited from country rocks and is more resistant to Pb loss (Wall and Scoates 2016; Pohlner et al. 2020; Li et al. 2021). In contrast, the crystallization of zircon is documented in a vast range of igneous, metamorphic, and hydrothermal processes (Schaltegger 2007; Scherer et al. 2007). It excludes effectively Pb during crystallization and its closure temperature is around 1,000 °C (i.e., higher than typical magmatic and metamorphic temperatures). This makes zircon an accurate U-Pb chronometer to determine the timing of magmatic, metamorphic, hydrothermal, and sedimentary events (Harley et al. 2007; Schaltegger 2007; Romer 2015). In addition, U-Th-He thermochronometry is utilized to determinate exhumation rates (Reiners 2005; Harley et al. 2007; Maino et al. 2012). Titanium-in-zircon thermometry is applied to determine temperatures of crystallization (Watson et al. 2006; Cherniak et al. 2007). Moreover, the analysis of O and Hf isotopes in zircon is essential for elucidating crustal residency, continental growth, crustal recycling, and fingerprinting the contribution of sediments to magmas (Hawkesworth et al. 2006; Harley et al. 2007; Zhu et al. 2017). The morphology of zircon grains itself can provide significant insights into the source and evolution of the parental magma, its chemical composition, and the geological setting (Belousova et al. 2006; Brites Martins et al. 2014). In the seminal work of Pupin (1980), variations in the chemical composition of the crystallization medium (i.e., origin) were correlated with the relative growth of zircon pyramids, while temperature of the source magmas was identified as the leading factor related to the development of zircon prisms (Fig. 1).

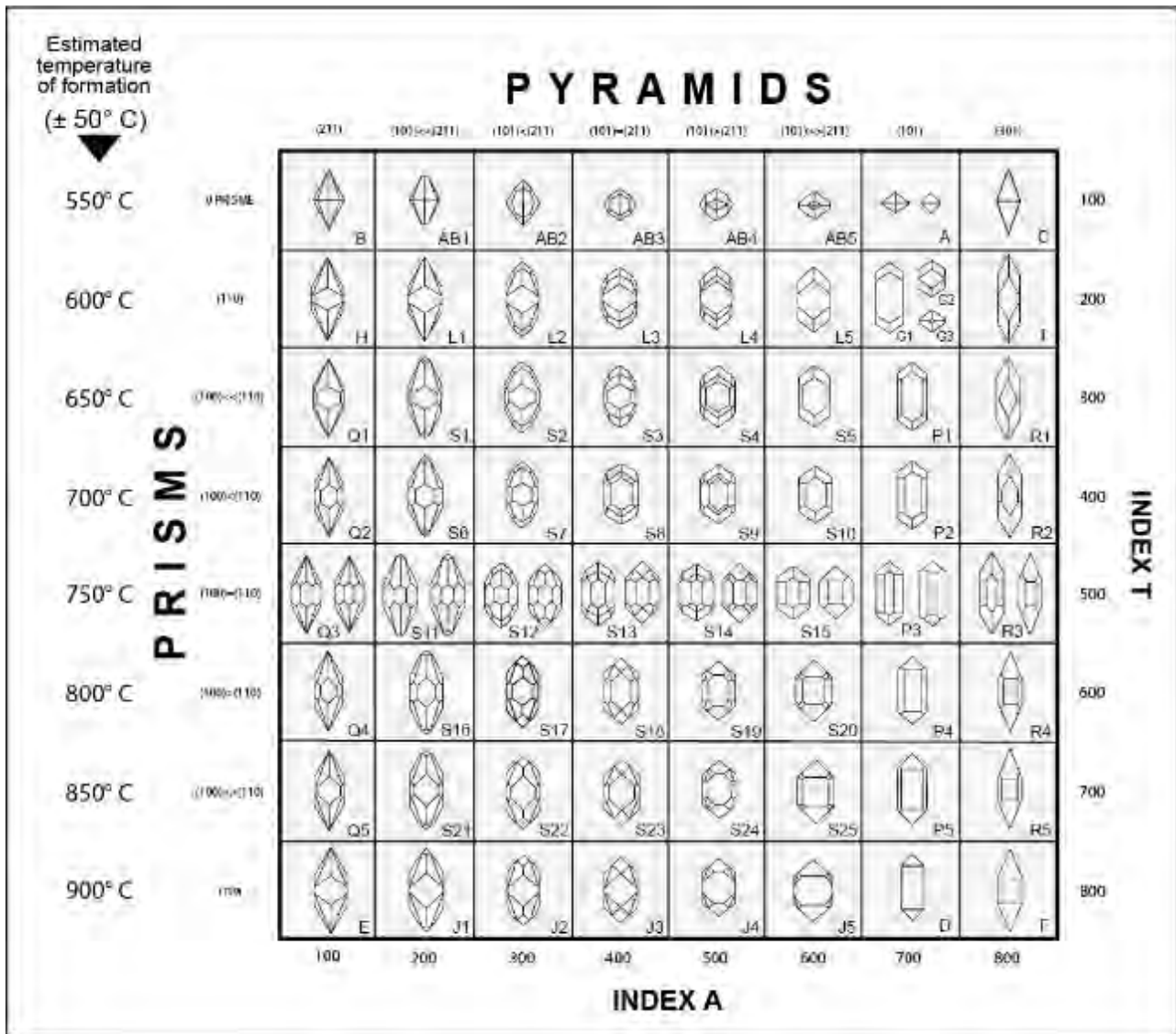


Figure 1. Zircon typological classification proposed by Pupin (1980) adjusted to a geothermometric scale. Index A correlates the Al/(Na+K) ratio with the development of pyramidal faces, while Index T correlates the temperature of zircon crystallization with the development of prismatic faces.

The importance of zircon in Earth science also lies in its extreme resistance to physical and chemical changes. This quality enables zircon to survive to most igneous, metamorphic, and sedimentary processes often serving as the sole remaining witness to ancient geologic events (Hanchar et al. 2007). The evidence of the resistance and strength of zircon can be observed in its ubiquitous inheritance. Inherited zircons are zircon crystals found in a given igneous or metamorphic rock that did not crystallize *in situ* but were incorporated from the source or host rocks (Harley et al. 2007; Olierook et al. 2020). An older-than-host zircon could have originated either in the mantle or crust, meaning that it survived in magma sources and rocks derived from them (Bea et al. 2018; Cambeses et al. 2023) and therefore

is a potential source of information on the petrogenesis and provenance of magmas (Davis 2015). For example, recycled zircons in mantle-derived, island-arc rocks are important to track crustal recycling (Rojas-Agramonte et al. 2016; Torró et al. 2018) and mechanisms of transport of crustal material (Proenza et al. 2018) in subduction zones. Inherited zircons are also valuable for tracing crustal magma sources and pathways. For example, inherited zircons have been used in geodynamic reconstructions in the Central Andes to assess the occurrence of Archean-Paleoproterozoic cratons assembled to the supercontinent Rodinia in the Mesoproterozoic and the growth and reworking in an accretionary orogen (Damm et al. 1994; Loewy et al. 2004; Chew et al. 2007; Ramos 2009; Romero et al. 2013; Jones et al. 2015; Pepper et al. 2016; Sundell et al. 2019). Noteworthy, the absence of inherited zircons is also meaningful. For example, the absence of Proterozoic inherited zircons has been used to infer the lack of old, Amazonian-derived basement beneath segments of the Western Cordillera between Chimbote and Pisco by Polliand et al. (2005) and Miskovic et al. (2009).

1.4. Our study case: Economic importance and previous data of the Lithium-rich Tuff

In November 2017, a significant lithium resource was announced in the Falchani Lithium Project, situated within the Macusani Volcanic Field in the Carabaya Province of the Puno Department (Fig. 2). This project encompasses two exploration concessions that are owned by Macusani Yellowcake S.A.C., the Peruvian subsidiary of American Lithium, formerly Plateau Energy Metals (The Mineral Corporation 2019). At approximately the same time, a different company, Fission Energy 3.0, also disclosed its involvement in lithium exploration in the area (Redacción EC 2018; F3 Uranium Corp 2023). Until 2018, Plateau Energy Metals and Fission Energy 3.0 were the sole entities engaged in the exploration of lithium and uranium in the Macusani Volcanic Field (Redacción EC 2018). However, there has been a growing interest among mining companies and individuals in lithium exploration in the area.

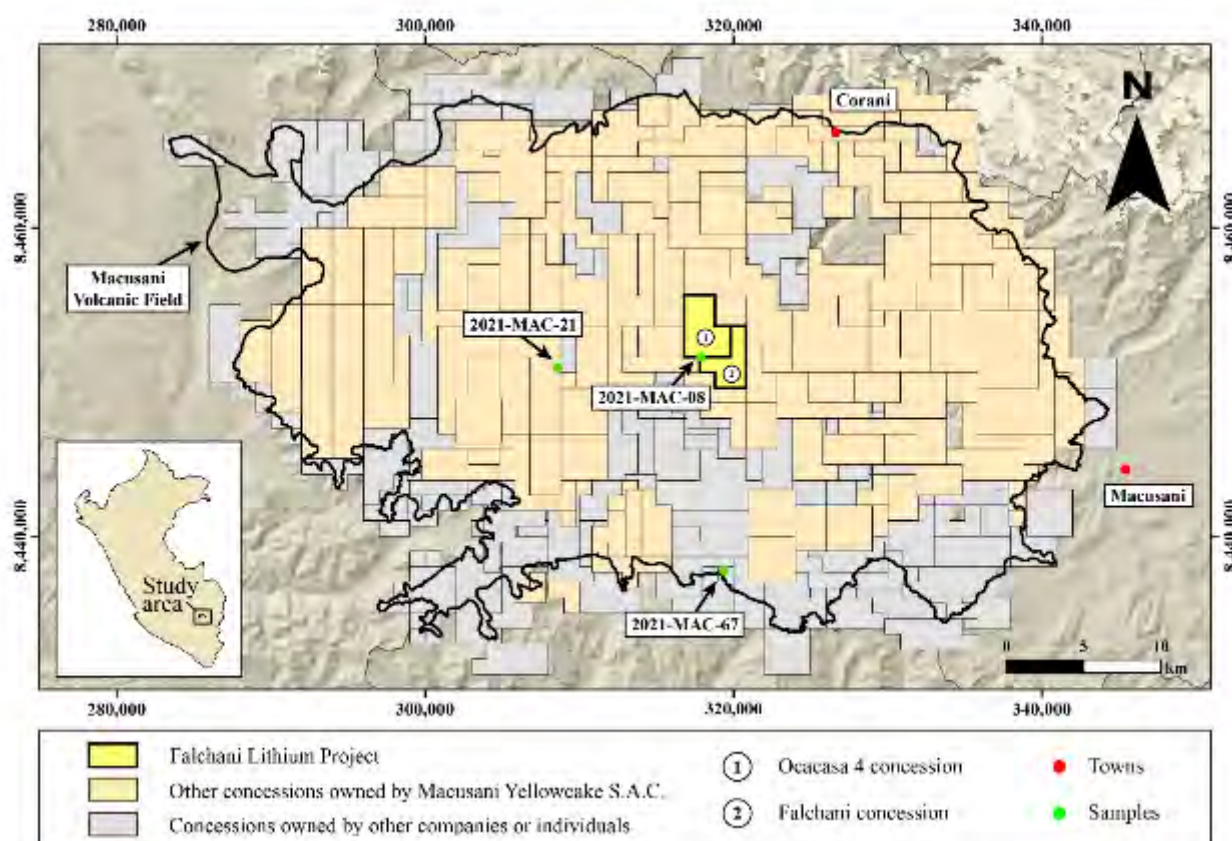


**Figure 2.** Location of Falchani Lithium Project, composed of the Falchani and Ocaca 4 concessions, and other exploration concessions in the Macusani Volcanic Field as of 2023. Delimitation of exploration concessions according to [GEOCATMIN \(2023\)](#).

Exploration activities in the Falchani Lithium Project were initiated upon identification of a radiometric anomaly ([The Mineral Corporation 2019](#)). As of October 31, 2023, indicated resources amounted to 0.19 Mt Li and inferred resources, to 0.75 Mt Li ([Loveday and Kartick 2023](#)). Mining activities are planned to begin as soon as 2026 ([Quinde 2023](#)). Lithium is associated with Tertiary acidic tuffs of the Quenamari Formation ([The Mineral Corporation 2019](#)), also known as the Macusani Formation ([Sandeman et al. 1997](#); see descriptions below). The main lithium host is a newly defined unit known as the “Lithium-rich Tuff”, which has been stratigraphically correlated by [The Mineral Corporation \(2019\)](#) with the Sapanuta Member of the Macusani Formation (see [López 1996](#)). The Lithium-rich Tuff has a thickness of between 50 and 140 m and has been interpreted to have been deposited sub-aerially in a lake environment ([The Mineral Corporation 2019](#)). Lithium contents in this unit are mostly between 3,000 and 4,000 ppm. The Lithium-rich Tuff is sandwiched between the so-called Upper Breccia and Lower Breccia, which are also mineralized with average Li contents of ~1,400 and 1,900 ppm, respectively ([The Mineral Corporation 2019](#)). The exploration efforts now encompass other concessions in the

Macusani Volcanic Field, such as in the Quelcaya area located west of the Falchani Lithium Project ([American Lithium 2024](#)).

The lithogeochemistry of the Lithium-rich Tuff has been examined by [Ramírez-Briones et al. \(2025\)](#). According to these authors, the major and trace element composition of the Lithium-rich Tuff is consistent with derivation from a strongly peraluminous rhyolitic magma. [Ramírez-Briones et al. \(2025\)](#) also found that the composition of the Lithium-rich Tuff is more analogous to the compositional profile of the so-called ‘macusanite’ glass than to other tuffaceous units within the Macusani Volcanic Field. Macusanite is a rhyolitic glass that extruded between ca. 8 and 4 Ma in the Macusani Volcanic Field ([Pichavant et al. 1987](#); [Cheilletz et al. 1992](#); [Poupeau et al. 1993](#)) that is extremely enriched in incompatible lithophile elements and interpreted as a rare case of extreme fractionation of felsic peraluminous magmas ([Pichavant et al. 1987, 2024](#)). [Segovia-More et al. \(2023\)](#) conducted a mineralogical analysis of the Lithium-rich Tuff using X-ray diffraction (XRD) and transmission electron microscopy (TEM), which revealed that it is composed primarily of quartz, plagioclase, K-feldspar, trioctahedral micas, kaolinite ± halloysite, and dioctahedral smectites, in addition to rare cristobalite and mordenite in a few samples. Finally, [Torró et al. \(2025\)](#) classified the trioctahedral micas as zinnwaldite and lepidolite through electron-probe microanalysis (EPMA), laser ablation inductively coupled plasma mass spectrometry (LA-ICP-MS), and Raman spectroscopy. These authors also found that mica crystals in the Lithium-rich Tuff are consistently enriched in incompatible, fluid-mobile lithophile elements compared to micas in other Neogene pyroclastic and intrusive rocks from the Macusani Volcanic Field. The micas yielded plateau  $^{40}\text{Ar}/^{39}\text{Ar}$  dates between  $8,978 \pm 73$  ka and  $8,717 \pm 44$  ka ([Sanandrés-Flores 2024](#); [Torró et al. 2025](#)).

### 1.5. Conundrum

Neogene volcanogenic units from the Macusani Volcanic Field, Eastern Cordillera of SE Peru, have significant economic potential due to their high lithium contents. In the Falchani Lithium Project, the indicated plus inferred resources amount to 1.6 Mt Li ([Loveday and Kartick 2023](#)). Most of these resources are hosted by a previously uncatalogued volcanogenic unit, which has been designated as the Lithium-rich Tuff by the geologists engaged in Li exploration in the area. Detailed studies of the Lithium-rich Tuff are relatively recent and have focused on its lithogeochemistry and major mineralogy ([Segovia-More et al. 2023](#); [Ramírez-Briones et al. 2025](#); [Torró et al. 2025](#)). However, a

comprehensive characterization of heavy minerals in the Lithium-rich Tuff has not yet been undertaken.

The mineralogical and geochemical characterization of heavy minerals may provide significant insights into geological processes. On the one hand, provenance studies based on heavy minerals may unveil details about orogenic cycles, volcanic activity, and sedimentation. Geochronology and thermochronology on heavy minerals represent a crucial tool for the temporal reconstruction of geologic events. Furthermore, morphological and geochemical characteristics of certain heavy minerals allow for the identification of petrogenetic controls that were responsible for their formation. In the specific study case of the Lithium-rich Tuff, the analysis of heavy minerals can provide valuable insights into the petrogenesis of volcanic rocks in the Macusani Volcanic Field in general and of the Lithium-rich Tuff in particular.

#### 1.6. Objectives

General objective:

To elucidate petrological and geodynamic features of the Lithium-rich Tuff in the Falchani Lithium Project through the mineralogical and geochemical characterization of heavy mineral concentrates and assess their potential economic impact.

Specific objectives:

- To obtain heavy mineral concentrates of the fine-fraction ( $< 100 \mu\text{m}$ ) through the novel hydroseparation HS11 technique;
- To characterize the mineralogy of heavy mineral concentrates;
- To describe the morphology and major-element composition of the separated heavy minerals;
- To discuss genetic constraints that controlled the occurrence, distribution, and composition of heavy minerals in the study zone;
- To perform U-Pb zircon geochronology to trace basement rocks and magmatism in the Macusani Volcanic Field; and
- To evaluate the economic potential for high-tech elements hosted in heavy minerals in the Lithium-rich Tuff.

### 1.7. Hypothesis/hypotheses

Ramírez-Briones et al. (2025) concluded that the Lithium-rich Tuff derived from a strongly peraluminous rhyolitic magma probably associated with partial melting of (meta)sedimentary rocks in the lower and middle crust (Barbarin 1999; Fiannacca et al. 2008). This would anticipate the occurrence of inherited zircons in the samples studied, with a higher proportion than magmatic zircons crystallized from the magma associated to the Lithium-rich Tuff. Moreover, the highly specialized magmas from which the magmatic component of the Lithium-rich Tuff crystallized (Ramírez-Briones et al. 2025) would be consistent with the presence of exotic minerals that are typically only found in highly differentiated igneous rocks. For example, Azevedo et al. (2021) identified the presence of heavy minerals in macusanite (i.e., highly differentiated rhyolitic obsidian related to the Macusani Formation, the same unit that hosts the Lithium-rich Tuff) boulders, such as andalusite in addition to zircon. Furthermore, it is hypothesized that heavy mineral phases in the Lithium-rich Tuff will exhibit enrichment in incompatible elements such as Nb, Ta, U, Th, and REE.

### 1.8. Justification

The Falchani Lithium Project is estimated to contain total inferred resources of at least 1.6 Mt Li (Loveday and Kartick 2023). Lithium is considered a strategic raw material, primarily due to its use in rechargeable batteries that are essential for the energy transition (Bibienne et al. 2020; Jowitt and McNulty 2021; European Commission 2023). Most of the lithium resources in the Falchani Lithium Project are hosted by the so-called Lithium-rich Tuff. Despite recent studies have advanced our understanding of the Lithium-rich Tuff through bulk mineralogy and geochemical analyses (Ramírez-Briones et al. 2025; Segovia-More et al. 2023; Torró et al. 2025), the heavy mineral assemblages within this unit remain uncharacterized. This represents a significant knowledge gap, as heavy minerals can provide crucial insights into petrogenesis, provenance determination, and geochronological constraints. In addition, volcanogenic Li deposits commonly host additional critical elements such as REE, which are frequently concentrated in heavy minerals (Crespo et al. 2025). This thesis addresses this gap by characterizing heavy mineral concentrates from the Lithium-rich Tuff to enhance our understanding of its genesis and explore the economic potential of heavy minerals as a source of critical elements in this unit.

## 2. METHODOLOGY

### 2.1. Sampling

A field campaign developed in October 2021 in the Macusani Volcanic Field resulted in a total of 67 samples of Lithium-rich Tuff and cospatial units. One sample of Lithium-rich Tuff and two samples of white tuffaceous mudstone were selected for analysis in this thesis. Since the term Lithium-rich Tuff is specific to the principal lithium-ore unit within the Falchani Lithium Project, the other tuffaceous mudstones collected outside the Falchani Lithium Project and studied in this thesis will be referred to as “white tuffaceous mudstone” to avoid confusion. The selection was intended to encompass different sampling locations (Fig. 2) and textural varieties (Fig. 3).

The sample 2021-MAC-08 (Lithium-rich Tuff) was collected from the Imagina zone of the Falchani concession (14°00'01'' S – 70°41'10''W, 4,899 m.a.s.l.). It is a finely bedded, folded and slumped, cohesive, tuffaceous mudstone showing cavities and concretions with long axes aligned parallel to bedding (Fig. 3A). The sample 2021-MAC-21 was collected from the Quelcaya zone of the Huarituña 4 concession (14°00'21'' S – 70°46'19'' W, 4,849 m.a.s.l.). It is a massive, cohesive, white, tuffaceous mudstone (Fig. 3B). The sample 2021-MAC-67 was collected from the Atlas prospect zone of the San Vicente White concession (14°07'32'' S – 70°40'24'' W, 5,031 m.a.s.l.). It is a massive, cohesive, pale pink, matrix-supported, crystal-rich, tuffaceous mudstone (Fig. 3C). In this sample, crystals and crystal fragments are unevenly distributed and correspond mostly to medium- to coarse-grained (up to 5 mm), roundish quartz. Lesser amounts of medium-grained fragments of feldspars, dark micas, and tourmaline are also observed in sample 2021-MAC-67.

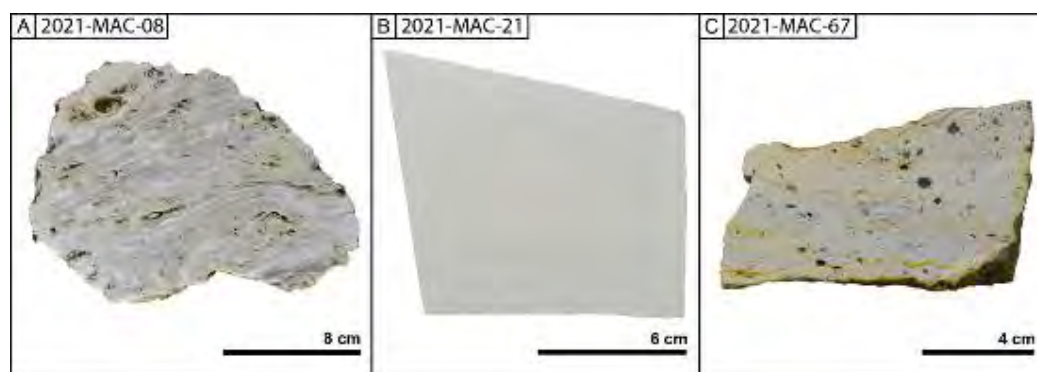


**Figure 3.** Aspect of the rock samples analyzed in this thesis. (A) Lithium-rich Tuff from the Falchani Lithium Project. (B) White tuffaceous mudstone from the Quelcaya zone. (C) White tuffaceous mudstone from the San Vicente White concession.

## 2.2. Analytical methods

### 2.2.1. Heavy mineral concentration and separation

In order to reduce the size of the rock pieces, large samples were initially cut using a GEOFORM 102 – Metkon diamond saw available in the QEMSCAN laboratory at PUCP. After the rock slabs were dried at 50°C overnight, they were crushed using a jaw crusher BB51 (stainless steel – Retsch) in the same laboratory (Fig. 4). The crushing process was repeated until all the material passed a 500- $\mu$ m sieve (Fig. 5).



Figure 4. Retsch Jaw Crusher (model BB51) in the QEMSCAN laboratory, PUCP.



Figure 5. Dry sieving using a 500  $\mu$ m sieve screen.

Subsequently, the < 500  $\mu$ m particulate material was manually wet-sieved on a 355  $\mu$ m round sieve (Fig. 6). The retained fraction was then dried and stored. The fine fraction was further wet-sieved using Nylon disposable sieves to avoid cross-contamination. Sieves with

apertures of 200  $\mu\text{m}$ , 100  $\mu\text{m}$ , 75  $\mu\text{m}$ , and 50  $\mu\text{m}$  were used (Fig. 7A-B). Very fine waste (dust) was eliminated from each granulometric fraction by decantation (Fig. 7C). After decantation, the respective sample fractions were dried overnight at 50°C (Fig. 7D). The dried particulate material was then weighed and stored (Fig. 7E). The procedure followed is graphically presented in Figure 8. The particle size distributions obtained are provided in Tables 2-4.



Figure 6. Wet sieving using wet sieving through a 355  $\mu\text{m}$  aperture laboratory sieve.



**Figure 7.** A: Sequential wet sieving of  $<355\ \mu\text{m}$  particulate material through disposable Nylon sieves ( $200\ \mu\text{m}$ ,  $100\ \mu\text{m}$ ,  $75\ \mu\text{m}$ , and  $50\ \mu\text{m}$  apertures). B: Cleaning of the retained fraction on disposable sieves. C: Two bowls with coarse and fine (relative to the aperture of the used sieve) particulate material. D: Decantation for the elimination of very fine material (dust). E: Drying of the obtained granulometry fractions in a laboratory dryer at  $50\ ^\circ\text{C}$  overnight. F: Dried sample ready for hydroseparation.

Table 4. Granulometric analysis after sieving sample 2021-MAC-08.

2021-MAC-08			
Sieve ( $\mu\text{m}$ )	Total mass (g)		1,502.70
	Retained mass (g)	% retained	% retained accumulated
355	527.70	35.12	35.12
200	289.30	19.25	54.37
100	204.00	13.58	67.94
75	35.40	2.36	70.30
50	73.90	4.92	75.22
<50	335.90	22.35	97.57
Total retained	1,466.20	97.57	
Loss	36.50	2.43	
Total	1,502.70	100.00	

Table 5. Granulometric analysis after sieving sample 2021-MAC-21.

2021-MAC-21			
Sieve ( $\mu\text{m}$ )	Total mass (g)		1,306.80
	Retained mass (g)	% retained	% retained accumulated
355	504.20	38.58	38.58
200	200.40	15.34	53.92
100	117.40	8.98	62.90
75	20.00	1.53	64.43
50	54.80	4.19	68.63
<50	391.20	29.94	98.56
Total retained	1,288.00	98.56	
Loss	18.80	1.44	
Total	1,306.80	100.00	

Table 6. Granulometric analysis after sieving sample 2021-MAC-67.

2021-MAC-67			
Sieve ( $\mu\text{m}$ )	Total mass (g)		1,439.40
	Retained mass (g)	% retained	% retained accumulated
355	510.20	35.45	35.45
200	270.30	18.78	54.22
100	195.10	13.55	67.78
75	26.40	1.83	69.61
50	66.60	4.63	74.24
<50	331.70	23.04	97.28
Total retained	1400.30	97.28	
Loss	39.10	2.72	
Total	1,439.40	100.00	

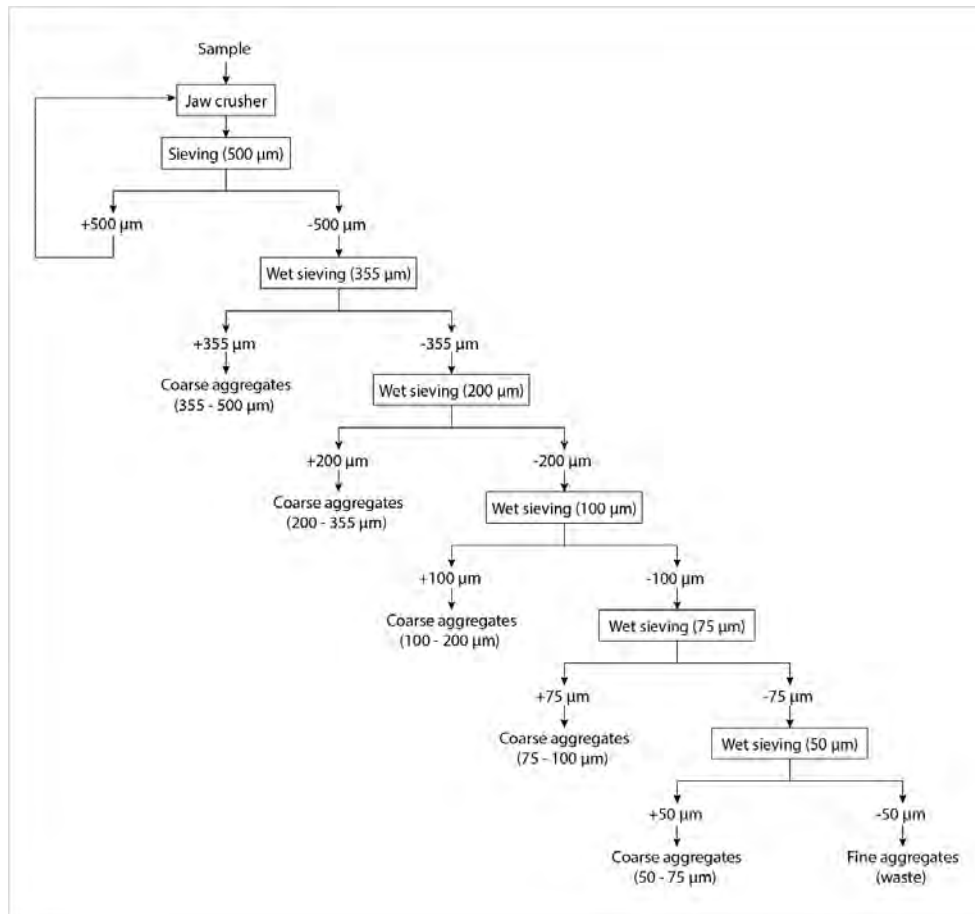
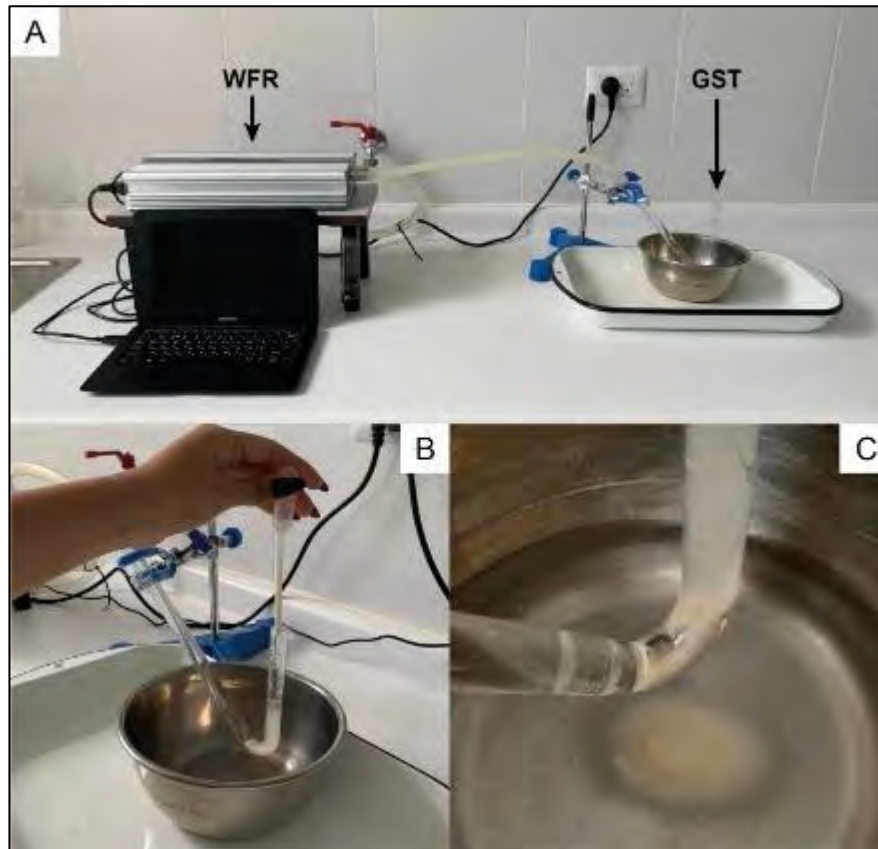


Figure 8. Flow sheet showing the procedure followed for the dry and wet sieving of the powdered Lithium-rich Tuff samples before hydroseparation.

Dense minerals from each granulometric fraction were concentrated using the hydroseparation technique (Rudashevsky et al. 2001) with HS11 equipment available in the Laboratory of Geology at PUCP (Fig. 9). The hydroseparation technique simulates concentration processes during the formation of natural placers (Rudashevsky et al. 2002). It involves the use of two separate components: a water flow regulator (WFR), which helps to create and moderate the flow pattern, and a glass separation tube (GST), which collects the heavy mineral concentrate at the base of the lower end of the vertical part of the tube. Hydroseparation is particularly indicated for heavy mineral processing due to its efficiency for a wide range of concentrations at fine-size fractions ( $< 100 \mu\text{m}$ ) and the environmentally friendly water-based equipment (Cabri et al. 2006).



**Figure 9.** A: Hydroseparation HS11 equipment in the QEMSCAN laboratory, PUCP. B: Heavy mineral pre-concentrate of sample introduced in the second glass separation tube to be processed to obtain a final concentrate (sample 2021-MAC-21, 50  $\mu\text{m}$  fraction). C: Final concentrate at the base of the glass separation tube; note the concentration of dark colored minerals in the concentrate, which contrasts with the more homogeneous white color of the tailing in the bowl. Abbreviations: WFR = water flow regulator; GST = glass separation tube.

Individual grains of interest were handpicked from the dried heavy mineral concentrates with the help of a binocular loupe (Figs. 10A-B). The selected mineral grains were first disposed in a circular container (Fig. 10A) and then transferred into double-faced adhesive carbon tape for scanning electron microscopy imaging and chemical analysis.

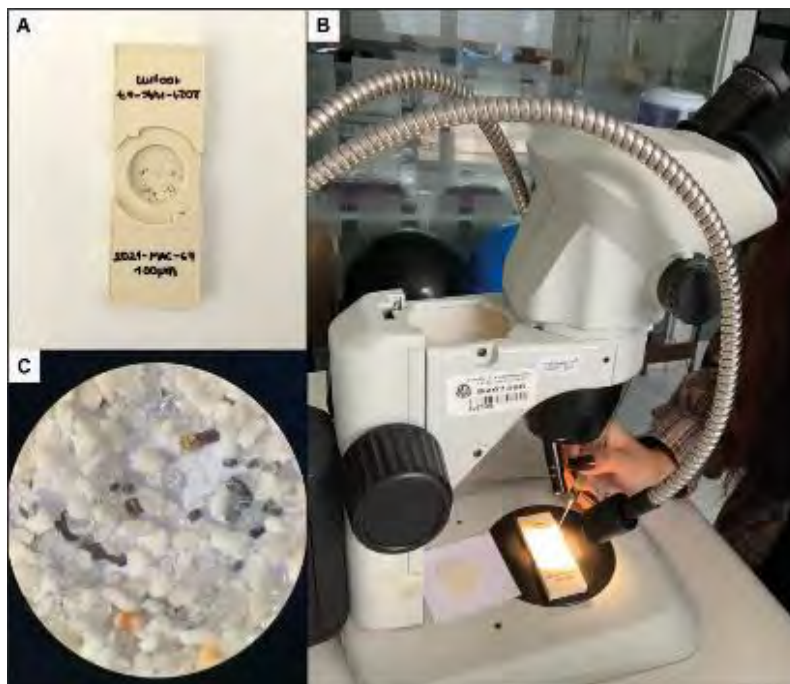


**Figure 10.** A: Sample holder with handpicked mineral grains. B: Handpicking under a binocular loupe in the Laboratory of Geology, PUCP. C: Example of heavy mineral concentrate obtained by hydroseparation under the binocular loupe (100  $\mu\text{m}$  fraction of the sample 2021-MAC-67).

### 2.2.2. Scanning electron microscopy (SEM-EDS)

Heavy mineral separates were examined using a Quanta 650 FEI scanning electron microscope (SEM) equipped with an EDAX-Octane Pro EDS microanalysis system at Centro de Caracterización de Materiales (CAM-PUCP). The images were obtained in secondary electron (SE) mode and the composition of the imaged mineral phases was obtained using the EDS detector. The operating conditions were an accelerating voltage of 25 keV, a current of 5 nA, and a beam diameter of 3  $\mu\text{m}$ . SE images of heavy minerals are presented in [Appendix A](#), and major element contents obtained by SEM-EDS are presented in [Appendix B](#).

### 2.2.3. Raman spectroscopy

Raman spectra on mineral phases were collected at CAM-PUCP using a Renishaw spectrometer with an inVia confocal microscope equipped with 5x, 20x, and 50x objectives. For this investigation, the Raman spectra were excited by an Ar-ion laser producing light at 514 nm and collected with a spectral resolution (FWHM) around 0.3  $\text{cm}^{-1}$ . The spectra were collected within the 100 to 1,200  $\text{cm}^{-1}$  range, as this interval is the one that contains the most relevant spectral information for mineral identification. Raman

spectra were identified using the WiRE (Windows-based Raman Environment) software and the RRUFF database.

#### 2.2.4. U-Pb dating

Zircon grains from sample 2021-MAC-21 were dated. Due to time and budgetary constraints, the analysis of zircon grains from the remaining two samples were not feasible within the scope of this thesis. Zircon grains mounted in polished monolayer sections were imaged using cathodoluminescence (CL) on a Tescan Vega 4 SEM at Géosciences Environnement Toulouse (GET), France. CL images helped to visualize the internal structures of the zircon grains prior to isotopic analysis. U-Pb analyses of zircon were performed by laser ablation–inductively coupled plasma– mass spectrometry (LA-ICP-MS) at GET (Toulouse, France) using a ESI (New Wave Research) NWR Femto, dual-volume, 213-nm laser ablation system attached to an Element XR (Thermo Scientific) sector-field ICP-MS. Concordia and weighted mean plots were produced using Iolite v2.5 (Hellstrom et al. 2008) with VisualAge data reduction scheme (Petrus and Kamber 2012). Age concordance was calculated using the ratio of  $^{206}\text{Pb}/^{238}\text{U}$  and  $^{207}\text{Pb}/^{235}\text{U}$  ages. Details about the instrumentation and analytical conditions can be found in Table 7, and data from unknowns and reference materials are presented in Appendix C.

Table 7. Detailed procedures and analytical parameters during LA-ICP-MS U-Pb isotopic and trace element analyses on zircon.

Laser ablation system	
Make, Model and type	ESI (New Wave Research) NWR Femto
Ablation cell and volume	Dual-volume, effective cup volume <1 cm <sup>3</sup>
Laser wavelength (nm)	213 nm
Pulse width (ns)	ca. 235 fs
Fluence (J cm <sup>-2</sup> )	ca. 2.5 J cm <sup>-2</sup>
Repetition rate (Hz)	8 Hz
Spot diameter (mm)	30 μm
Ablation duration	25 s
Ablation pit depth / ablation rate	ca. 6 μm pit depth, equivalent to average 0.03 μm/pulse
Sampling mode / pattern	Static spot ablation
Carrier gas	100% He in the cell, Ar make-up gas admixed downstream
Cell carrier gas flow (l min <sup>-1</sup> )	ca. 0.65 l min <sup>-1</sup>

Table 7. Continued.

ICP-MS Instrument	
Make, Model and type	Thermo Element XR, Sector-field single collector ICP-MS
Sample introduction	Direct
Interface parameters	Normal interface equipped with Ni sampler and H-skimmer cones
RF power (W)	1,200 W (tuned daily)
Make-up gas flow (l min <sup>-1</sup> )	ca. 0.85 l min <sup>-1</sup> Ar (tuned daily)
Detection system	Triple (pulse counting, analog, Faraday), except at amu 29, 91, 238 (analog only)
Integration time per peak/dwell times (ms)	10 ms except at amu 49 (20 ms), 238 (50 ms); 206 and 207 (150 ms)
Total integration time per output data point (s)	0.834 s
Dead time (ns)	20
Typical oxide rate ( <sup>254</sup> UO <sup>+</sup> / <sup>238</sup> U <sup>+</sup> )	0.04%
Typical doubly charged rate (Ba <sup>++</sup> /Ba <sup>+</sup> )	3.50%
Data Processing	
Gas blank	20 s
Calibration strategy	GJ-1 used as primary reference material for U-Pb dating; 91500, AUSZ5 and AUSZ7 as secondary (validation) reference materials.
Reference Material info	GJ-1 <sup>206</sup> Pb/ <sup>238</sup> U = 0.097877 ± 0.000068 ; <sup>207</sup> Pb/ <sup>206</sup> Pb = 0.060171 ± 0.00005 (Horstwood et al. 2016)
	91500 (Wiedenbeck et al. 1995)
	AUSZ5 (Kennedy et al. 2014)
	AUSZ7 (Kennedy et al. 2014)
Data processing package used / Correction for LIEF	Iolite v2.5 (Hellstrom et al. 2008) with VisualAge data reduction scheme (Petrus and Kamber 2012); laser induced elemental fractionation (LIEF) corrected based on primary reference material and extrapolated to all unknowns (Paton et al. 2010)
Mass discrimination / drift correction	Normalization to primary reference material by conventional standard-sample bracketing
Common-Pb correction, composition and uncertainty	No common Pb correction applied
Uncertainty level and propagation	Uncertainty on ratios and ages are at 2σ absolute, including propagated uncertainty based on the scatter of the primary reference material (Paton et al. 2010).
Quality control / validation (uncertainties quoted without systematic uncertainty propagation)	AUSZ5 - weighted mean <sup>206</sup> Pb/ <sup>238</sup> U date = 2.85 ± 0.09 Ma (2σ, n = 8/8; MSWD = 1.5)
	AUSZ7 - weighted mean <sup>206</sup> Pb/ <sup>238</sup> U date = 38.3 ± 0.5 Ma (2σ, n = 8/8; MSWD = 0.91)
	91500 - weighted mean <sup>206</sup> Pb/ <sup>238</sup> U date = 1069 ± 17 Ma (2σ, n = 4/4; MSWD = 0.3)

### 3. GEOLOGICAL SETTING

#### 3.1. The Eastern Cordillera of the Andes in southern Peru: Regional basement and summary of its tectonomagmatic evolution

The Andes have a complex history ruled by the subduction of oceanic plates under a continental margin, producing domains with diverse tectonic architecture and geodynamic history (Gansser 1973; Ramos 1999; Kay and Mpodozis 2021). The Andes are typically subdivided into the Northern, Central, and Southern segments (Kay and Mpodozis 2021). The study area is located in the Central Andes, which extend from the Guayaquil Gulf in Ecuador (3°S) to the Pissis Mountain in Argentina (28°S) across part of Chile and the entire Peruvian territory (Kay and Mpodozis 2021). This segment represents the archetypical Andean-type orogen and formed by the subduction of the Nazca oceanic crust beneath the South American margin (Ramos 2009).

At the latitudes of southern Peru, the Central Andes comprise, west to east, 1) the Western Cordillera, 2) the Altiplano, 3) the Eastern Cordillera, and 4) the Subandean Belt morphotectonic zones (Kay and Mpodozis 2021). The study area is located in the Eastern Cordillera. The Eastern Cordillera has an approximate length of 1,200 km, a width around 100 km, and reaches modern elevations up to 6,000 m. It is defined as an east-directed retroarc fold-thrust belt exposing one of the longest Paleozoic metamorphic and magmatic belts in South America (Dorbath et al. 1991; Chew et al. 2005; Horton 2018; Sundell et al. 2019; Gérard et al. 2021). The Eastern Cordillera has been subjected to significant contractional deformation during the middle Eocene to Late Miocene (Kley et al. 1997; Kay and Mpodozis 2021). It is made up mainly of deformed Paleozoic meta-sedimentary rocks of marine origin unconformably overlain by marine and non-marine Jurassic and younger sedimentary rocks (Sempere et al. 1995, 1997). Igneous rocks exposed in the Eastern Cordillera register 1.1 G.y of intermittent magmatism developed during different orogenic and post-orogenic episodes (Miskovic et al. 2009; Chew et al. 2016).

A regional synthesis about the Proto-Andean evolution of the Eastern Cordillera of Peru by Chew et al. (2016) documents a series of polycyclic orogenies that shaped the initial framework for the subsequent Andean orogeny. In this model, the Eastern Cordillera stretches between the tectonic boundaries of Western Amazonia and allochthonous to parautochthonous terranes (Fig. 11; see also Mišković et al. 2009). The early stages of the proto-Andean evolution are recorded in basement rocks of the Proterozoic-Paleozoic

Arequipa Massif. The Arequipa Massif is interpreted as part of a terrane (i.e., an isolated crustal fragment with a geology history distinct from its surroundings and typically delineated by faults; Ramos 2008, 2018). The Arequipa block is preserved as a Mesoproterozoic granulitic basement exposed in the coastal region of southern Peru and northern Chile for 800 km and with a 100 km extent inland. Just north of the Arequipa terrane is located the Paracas terrane, which is interpreted either as a para-autochthonous or a completely exotic terrane underlying the Western Cordillera and offshore interval (Ramos 2008). However, the presence of the Paracas terrane underneath the present-day Western Cordillera and contiguous domains in Peru has been called into question by different authors due to the extremely primitive isotopic signatures of rocks of the Coastal Batholith and Cordillera Blanca in Peru and the lack of inherited zircons thereof. Nevertheless, Ramos (2008) interpreted this as a consequence of crust attenuation during intra-arc extension in the Cretaceous (see discussion in Chew et al. 2016 and Ramos 2018). Further north, other smaller terranes accreted to the Andean continental margin at the latitudes of present-day Peruvian territory. These include the Late Paleozoic Tahuín terrane, which might represent a detached part of Laurentia accreted to Gondwana during the Alleghenide orogeny in the Permian or a once detached autochthonous part of Gondwana re-accreted as a result of subduction dynamics and eventual collision between Laurentia and Western Gondwana in the Late Carboniferous (see discussion in Ramos 2018).

Both, the Arequipa and Paracas terranes are considered to represent part of a dismembered, Grenville-age orogenic belt first accreted to the Amazonian craton during the amalgamation of Rodinia in the Mesoproterozoic. During the extensional phase in the Late Neoproterozoic that followed the first accretion of the Arequipa and Paracas terranes, a passive margin developed along the western proto-Gondwanan margin with little evidence of magmatism restricted to some outcrops in the Eastern Cordillera of A-type granites (Mišković et al. 2009; Chew et al. 2016). Unlike the Arequipa terrane, the Paracas terrane probably detached during the opening of the Iapetus Ocean by westward drift of Laurentia, associated to the breakup of Rodinia, and re-accreted to the Amazonian craton during the Famatinian Orogeny in the Early Paleozoic leading the formation of the Marañón Complex (Fig. 11; Mišković et al. 2009; Romero et al. 2013; Chew et al. 2016; Ramos 2018).

The study area is located very close to the north-eastern suture of the Arequipa-Antofalla terrane as delineated by Ramos (2018; Fig. 11). In contrast, it is located approximately 100 km to the north of the northeastern tip of the Arequipa basement terrane as outlined by other modern authors (e.g., Mišković et al. 2009; Chew et al. 2016; Spikings et al. 2016; Wörner et al. 2018). These later authors base the delimitation of the Arequipa terrane mostly on an unusually nonradiogenic domain in Neogene volcanics noted by Mamani et al. (2005) in southernmost Peru extending to Bolivia and Chile (Fig. 11). Consequently, in the general geologic framework of presently known tectonic domains of Mišković et al. (2009; their Fig. 2), the study area would completely fall within the Western Amazonia tectonic domain. If so, the study area rests on or close to the westernmost Amazonia basement terrane, particularly its San Ignacio (1.57–1.24 Ga) and Sunsás (1.19–0.92 Ga) tectonic provinces (Tassinari and Macambira 1999; Cordani and Sato 2000).



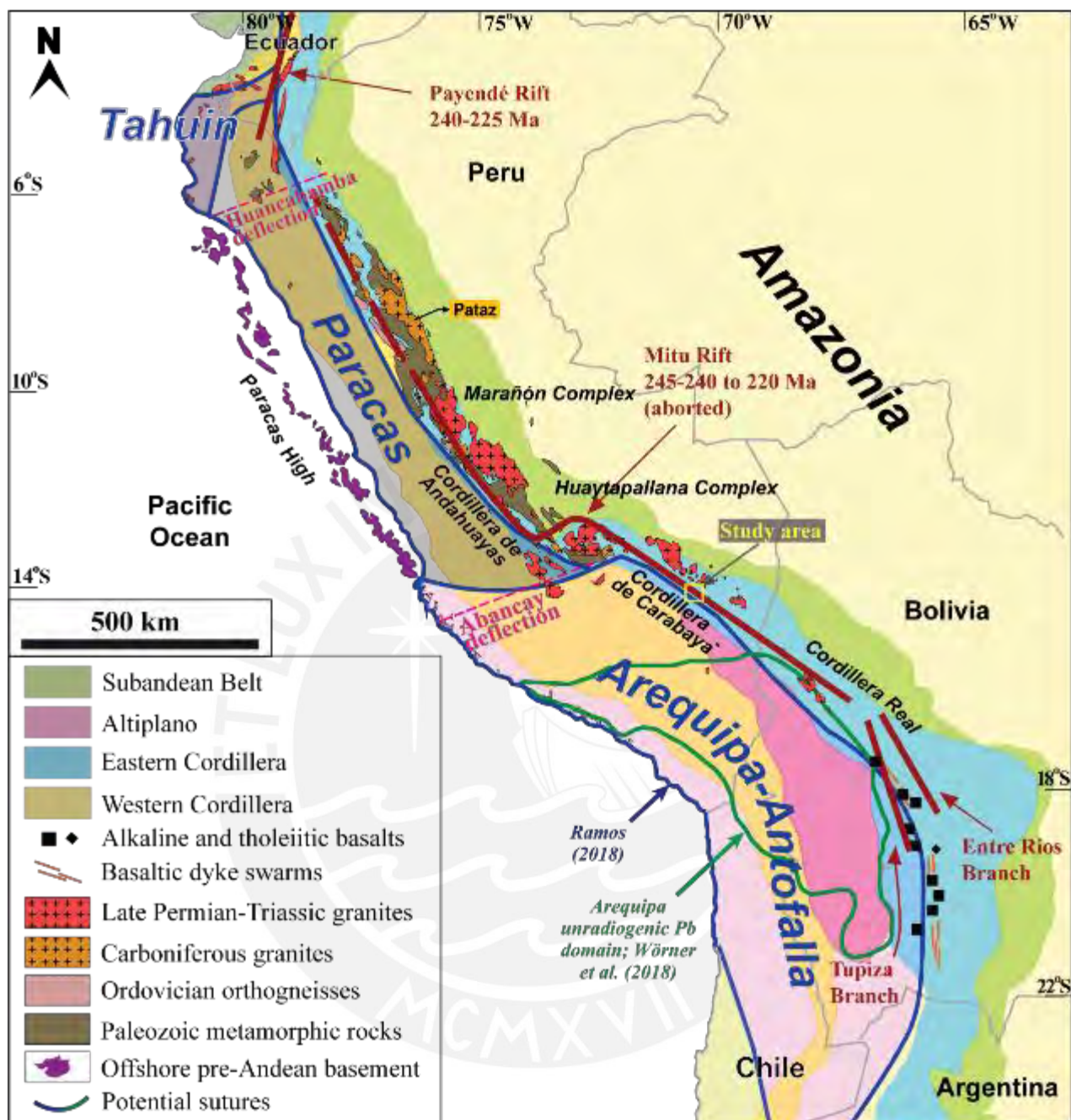


Figure 11. Accreted blocks to the western margin of Gondwana and morphotectonic units in the present-day Central Andes. Paleozoic metamorphic and igneous rocks and Late Permian-Triassic granites exposed in the Central Andes are also shown. Morphotectonic zones boundaries based on Oncken et al. (2006) and Carlotto et al. (2009). Outlines of terranes are based on Ramos (2008, 2009, 2018) and Wörner et al. (2018). Triassic granitoids and plutons after Mišković et al. (2009), Chew et al. (2016), and Spikings et al. (2016).

Around the Early Cambrian, global plate reorganization and the final amalgamation of Gondwana resulted in the return of the compressional tectonics, as evidenced in the diachronous rift-drift transition in the north of the Arequipa terrane (Mišković et al. 2009). An Ordovician, subduction-related magmatic belt runs along the western coastal margin of

the Arequipa-Antofalla basement and is also identified in the north and central portion of the Eastern Cordillera of Peru (Fig. 11). The formation of this magmatic belt was broadly contemporaneous with the Famatinian Orogeny and the formation of associated metamorphic complexes, including those found along ophiolitic sutures in the western margin of the Marañón Massif (Fig. 11; Mišković et al. 2009; Castroviejo et al. 2010; Romero et al. 2013; Chew et al. 2016).

There is no evidence of magmatic activity associated with subduction in the Central Andes during the Late Silurian and Devonian, which has been correlated with a period of a passive margin development in the western Gondwana region (Mišković et al. 2009). Following this phase, the magmatic arc activity resumed during the Early Carboniferous in the context of the Gondwanide orogeny, a pan-Pacific orogenic event heralding the final assembly of Pangea, and which in Peruvian territory is documented in the Eastern Cordillera in Pataz (Fig. 11; Mišković et al. 2009). During the Late Permian and Triassic, crustal extension and thinning, and the ensued magmatic activity accelerated along the western margin of Gondwana as the initial stages of the dismemberment of Pangea unfolded. This resulted in the development of a back-arc rift system along the paleo-suture of the western Amazonia craton and the Arequipa and Paracas and the deposition of the volcano-sedimentary Mitu Group at the latitudes of present-day Peru and northern Bolivia (Mišković et al. 2009; Sempere et al. 2002). Permo-Triassic intrusive activity in the Eastern Cordillera in southeastern Peru developed slightly inboard of the Carboniferous arc (Fig. 11) and included the emplacement of mostly peraluminous granitic batholiths along the Cordillera de Carabaya in Peru extending into the Cordillera Real of Bolivia. The Triassic rifting was followed by a hiatus in sedimentation in the Late Triassic-Jurassic, which was associated with uplift and erosion before the Early Cretaceous suggesting partial rift inversion (Sempere et al. 2002).

The axis of this rift system coincides with the axis of the Eastern Cordillera in Bolivia and southern Peru (Sempere et al. 2002; Ramos 2018). The Eastern Cordillera is thought to have originated from a transition from stretching-dominated to shortening-dominated conditions that facilitated the thickening of a pre-orogenic, thin crust. The compressional to transpressional reactivation of faults resulted in the inversion and shortening of the rift system during the Oligocene-Miocene, which involved additional tectonic processes, such

as rapid plateau uplift and dynamic interactions among climate, erosion, and fold-thrust activity (Sempere et al. 1995, 2002, 2008; Roperch et al. 2006; Horton 2018; Ramos 2018).

### 3.2. Regional geology of Macusani Structural Zone

The term Macusani Structural Zone was coined by Perez et al. (2016) to refer to the morphostructural domain intervening between two important NW-trending features of the Eastern Cordillera of southern Peru: the Central Andean Backthrust Belt and the Cordillera de Carabaya (Fig. 12). The latter serves as a high-altitude geomorphologic boundary between the Altiplano and the Subandean morphotectonic zones (Kontak et al. 1990; Mišković et al. 2009; Perez et al. 2016). The Central Andean Backthrust Belt is primarily characterized by fold-thrust structures that predominantly tilt southwestward. These structures involve Cretaceous marine sandstone, shale, and limestone (Perez et al. 2016). In contrast, the Cordillera de Carabaya is defined by the presence of Triassic plutonic rocks (e.g., Aricoma, Ayapata, Coasa, Limbani, and San Gabán plutons) that intruded Ordovician-Devonian metasedimentary rocks.

Most faults and folds in the Macusani Structural Zone preserve N-S, NE-SW, and NNW-SSE orientations and hence do not follow the typical NW trends in southern Peru (Perez et al. 2016). These oblique orientations have been interpreted as the reactivation of pre-Andean structures attributed to Late Paleozoic deformation and Triassic extension (Perez et al. 2016). Pre-Andean basement rocks exposed along the Macusani Structural Zone are predominantly of Paleozoic and Triassic ages. The oldest unit in the Macusani Structural Zone is the Lower to Upper Ordovician Sandia Formation, which comprises a strongly folded, 1,500-m-thick sequence of quartzitic sandstone, silt, and shale (Laubacher 1978; Chávez et al. 1997). This formation is overlain by the Ananea Formation, a thick Silurian-Devonian pelitic sequence intercalated with sandstone that is exposed in the homonymous locality and extends to the Cordillera Real in Bolivia (López 1996). The Ananea Formation which is distinguished by its soft morphology with hills and low mountains, is overlain by the Upper Paleozoic Ambo, Tarma, and Copacabana groups and the Triassic Mitu Group. López (1996) indicates that the contact between the Ananea Formation and the Upper Paleozoic units is concordant, while in a more regional study Laubacher (1978) documents a strong angular discordance between the Lower and Upper Paleozoic units.

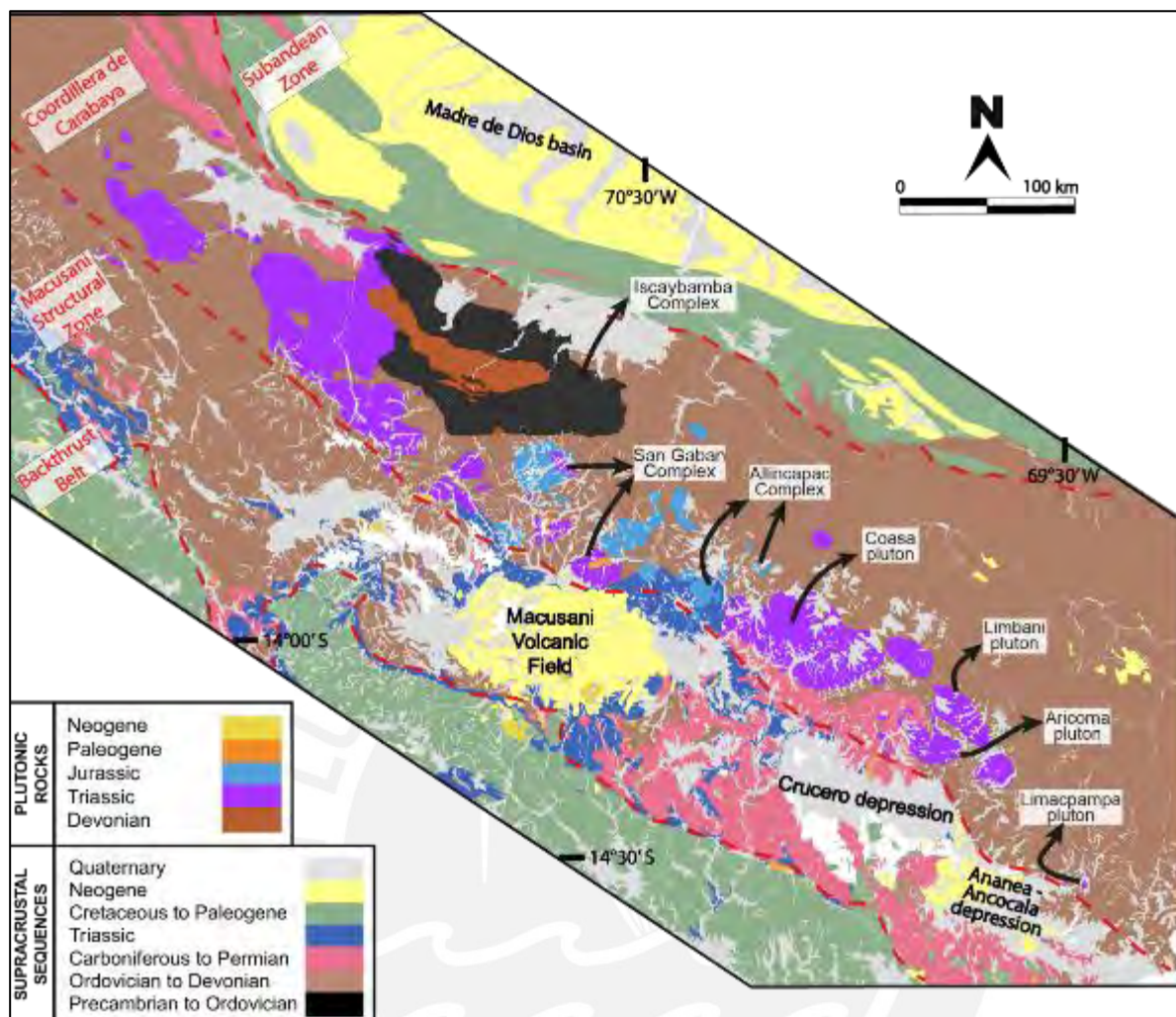


Figure 12. Simplified geological map of Eastern Cordillera of southern Peru including morpho-structural domains as defined by Perez et al. (2016). Geological map extracted from 1:50,000 sheets in GEOCATMIN (2023).

The Ambo Group is a Lower Carboniferous pelitic-psammite continental sequence (López 1996). It forms a variety of landscapes, including high hills with steep slopes and deeply incised valleys with subvertical walls. The Ambo Group is concordantly overlain by the Tarma Group, which is an Upper Carboniferous pelitic-calcareous sandstone sequence (López 1996). The relative hardness of the sedimentary suite results in steep morphologies. The Copacabana Group is a Permian pelitic-calcareous sequence with a morphology that is commonly abrupt, generating vertical scarps that are notably evidenced in the stratification planes (López 1996). The Tarma group underlie conformably the carbonate rocks of the Copacabana Group (Valdivia et al. 2021).

The Paleozoic units are discordantly overlain by the Triassic Mitu Group (López 1996). The Mitu Group is defined as a 2-km-thick sequence of red siliciclastic rocks intercalated

with lava flows that were deposited in subaerial basins along the SW front of the Eastern Cordillera (López 1996; Spikings et al. 2016). The Mitu Group has been divided into a clastic sequence and a dominantly volcanic sequence. The clastic deposits are mainly arkosic, spanning from mudstone to coarse sandstone and conglomerate. The clasts within conglomerate are primarily the result from the reworking of Mitu Group lavas (Spikings et al. 2016). The volcanic rocks of the Mitu Group display a prominent basaltic to andesitic composition and alkaline, intraplate signatures and are dominant in the Macusani Structural Zone (Kontak et al. 1990; Spikings et al. 2016). The group is characterized by a diagnostic violet or reddish violet color and characteristic abrupt geomorphology with peaks and high slopes (López 1996).

Following the Mitu Group, sequences of Upper Jurassic and Cretaceous sedimentary rocks are extensively exposed in southern Peru, particularly along the Mesozoic belt of the Central Andean Backthrust Belt, and less extensively along the Macusani Structural Zone. The Huancané Formation discordantly overlies the Ambo and Mitu groups and comprises a Lower Cretaceous sequence of quartzose sandstone that generates abrupt morphologies of steep flanks (López 1996). Also Cretaceous in age is the Moho Group, a psammite-pelitic-calcareous sequence comprising the Viluyo, Ayavacas, and Hanchipapa formations (López 1996).

Overlying the Paleozoic to Cretaceous basement, a series of Tertiary intermontane depressions—namely Macusani, Crucero, and Ananea—occur in the Macusani Structural Zone (Fig. 12). The volcanic and sedimentary units of Oligocene and Miocene ages exposed in these intermontane depressions were grouped by Sandeman et al. (1997) under the Crucero Supergroup, whereas the cogenetic subvolcanic stocks and plugs were grouped under the Crucero Intrusive Supersuite. The same authors further subdivided the Crucero Supergroup—and cogenetic hypabyssal units—into two major volcanic associations with contrasting compositions. The first of these is the Upper Oligocene-Lower Miocene Picotani Group, which comprises lava flows and pyroclastic rocks of diverse compositions including lamprophyres (minette), calc-alkaline basalts, shoshonites, S-type rhyodacites and rhyolites, as well as commingled and mixed associations of these. Based on the predominant peraluminous compositions of the rhyodacitic rocks, Sandeman et al. (1997) proposed that the silicic magmas of the Picotani Group originated from the melting of pelitic rocks resulting from the incursion of a diversity of mantle-derived melts and heat

(Sandeman et al. 1997). The Picotani Group comprises the following formations: Cerro Sumpiruni, Pucalacaya, Lago Perhuacarca, Cerro Cancahuine, Jama Jama, Pachachaca, Cerro Huancahuancane, and Cerro Queuta (Sandeman et al. 1997). On the other hand, the Picotani Suite comprises elliptical to rounded stocks and concentric arrays of dikes mainly composed of cordierite-biotite monzogranites (Sandeman et al. 1997). The Picotani Suite is comprised of the stocks of Cerro Esquinani, Quebrada Centilla, and Ninahuisa, as well as the Revancha dike. It is worth noting that the San Rafael granite, host of the largest high-grade tin deposit in the world is related to the Picotani Group (Harlaux et al. 2021 and references therein).

The second volcanic association is the Lower to Upper Miocene Quenamari Group, which encompasses an extensive sequence of rhyolitic, strongly peraluminous ash-flow tuff (Sandeman et al. 1997). The Quenamari Group is comprised of the Quebrada Escalera, Huacchane, and Macusani formations. The Quenamari Suite is comprised of the Chacaconiza, Cerro Surini, and Cerro Viscachani stocks, the Cerro Cajo Orjo and Nevado Ollo Quenamari plugs, and the Cerro Lintere Intrusive Complex.

### 3.3. Geology of the Macusani Volcanic Field

The Macusani Volcanic Field represents the northernmost volcanic field and with the youngest eruptive system of the Macusani Structural Zone (Fig. 12; Cheillett et al. 1992). The Macusani Volcanic Field lies over a pre-eruption basement, which is mainly constituted by a Paleozoic-Mesozoic sequence comprising shale, quartzite, and carbonate rocks of the Ananea, Tarma, and Copacabana groups that are discordantly overlain by alkaline basalts and red-beds of the Mitu Group (Fig. 13; Kontak et al. 1985; Pichavant et al. 1988; Cheillett et al. 1992).

As outlined by Sandeman et al. (1997), the Late Oligocene to Early Miocene Cerro Sumpiruni, Pucalacaya, and Lago Perhuacarca formations of the Picotani Group are exposed in the southern margin of the Macusani Volcanic Field. However, the GEOTCATMIN (2023) database does not map these units nor disclose any information about them. Consequently, these units have not been represented in the geological map shown in Figure 13.

Most Tertiary volcanic and sedimentary rocks exposed in the volcanic field belong to the Macusani Formation, the youngest unit of the Quenamari Group of Sandeman et al. (1997). The Macusani Formation has not been described in any other Neogene volcanic field within

the Macusani Structural Zone. The Macusani Formation is a 250- to 500-m-thick, poorly sorted, and almost unstratified sequence of crystal-rich, rhyolitic ash-flow tuff with ash-to-lapilli-size pyroclastic fragments that include occasional lithic debris and pumice shards and rare occurrences of bombs and lithic blocks (Cheilletz et al. 1992). The mineralogical assemblage at the Macusani Formation is characterized by quartz, sanidine, plagioclase, and biotite, with some unusual phases such as sillimanite, andalusite, muscovite, and tourmaline (Pichavant et al. 1988).

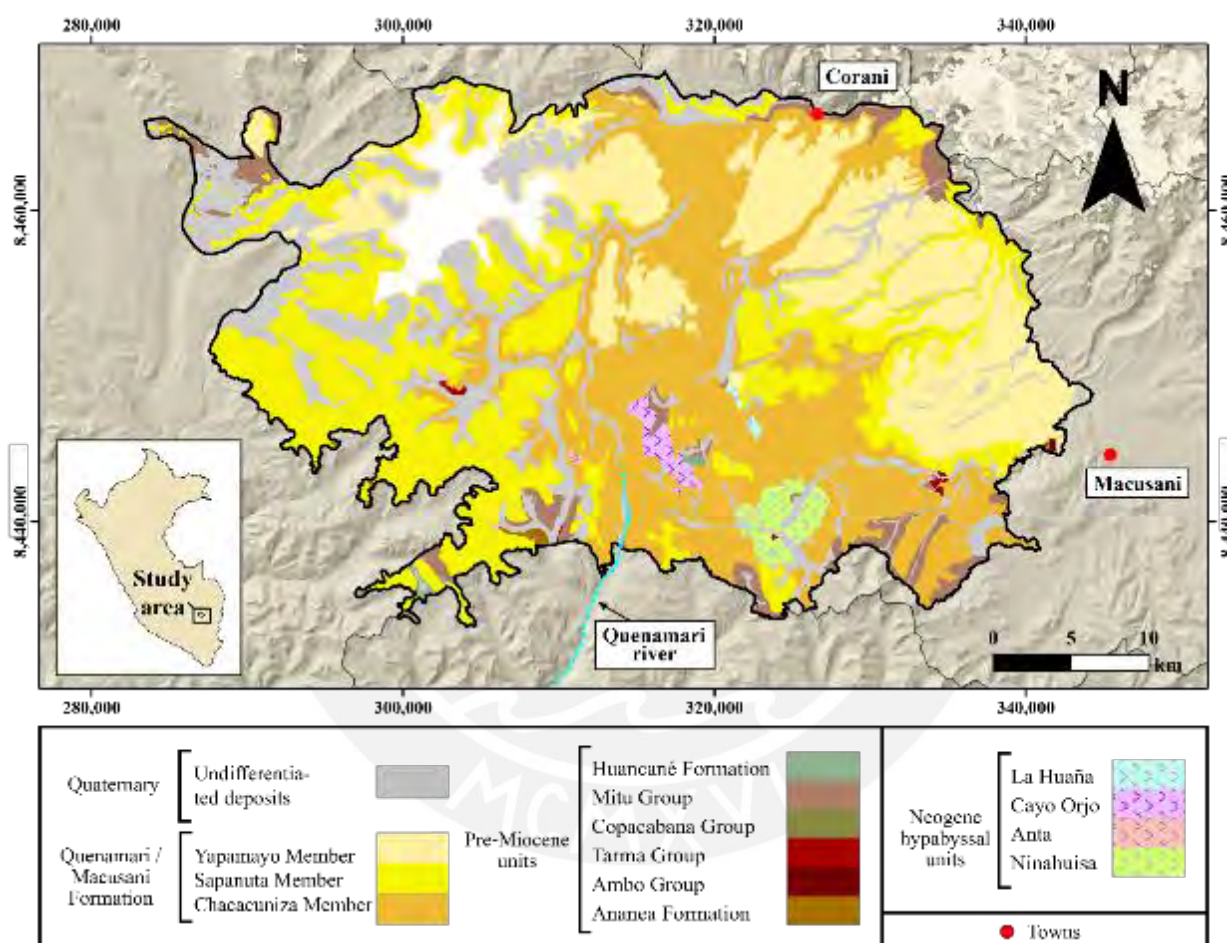


Figure 13. Geological map of the Macusani Volcanic Field with. Geological mapping at 1:100,000 scale extracted from GEOCATMIN (2023).

López (1996) further subdivided the Macusani (a.k.a. Quenamari) Formation into the Chacacuniza, Sapanuta, and Yapamayo members based on lithomorphostructural characteristics of the tuff (Fig. 13). The Chacacuniza Member is a stratified tuff sequence with a thickness between 170 and 350 m. It is considered the first volcanic episode recorded in the Macusani Formation, equivalent to the first eruptive event identified by Cheilletz et al. (1992). In terms of geomorphology, the Chacacuniza Member typically forms hills of

moderate relief that are deeply bisected by rivers and streams. The Sapanuta Member is a 240-m-thick tuffaceous sequence chiefly exposed at the western side of the Quenamari River (Fig. 13). The distinctive columnar jointing structures that gave rise to "rock forests" are unique to this member. Finally, the Yapamayo Member is a poorly stratified tuff sequence that encompasses the flat areas that conform the Quenamari meseta (López 1996).

The Macusani Volcanic Field is the locality of the so-called macusanite, an intriguing, strongly peraluminous obsidian glass largely found as pebbles in stream gravels (Pichavant et al. 1987; Cheilletz et al. 1992). The macusanite exhibits moderate to low SiO<sub>2</sub>, high to very high Al<sub>2</sub>O<sub>3</sub>, high contents of alkalis, F, B, P, and low contents of CaO, FeO<sub>t</sub>, MgO, and TiO<sub>2</sub> (Pichavant et al. 1987). The lithium contents in macusanite are very high, with an average 3,440 ppm (London et al. 1988). The peraluminous character and conspicuous enrichment in incompatible lithophile elements in macusanite have been catalogued by London et al. (1988) as a "good compositional analogue to highly differentiated Li-rich pegmatites". The macusanite rhyolitic glasses host virgilite (a lithium aluminum silicate mineral for which it is the type locality), quartz, sanidine, plagioclase, andalusite, and biotite as mineral inclusions. Other minerals (e.g., sillimanite, ilmenite, zircon, and monazite) are found as inclusions in andalusite (Pichavant et al. 1987). The mineral phases in macusanite are nearly identical to those of the Pliocene Macusani tuff according to Pichavant et al. (1987, 1988). The age of the Macusani glasses has been constrained between 7.9 and 4.3 Ma (Naeser et al. 1980; Pichavant et al. 1987; Poupeau et al. 1993), overlapping with the deposition of the Macusani Formation.

In the Macusani Volcanic Field, four Neogene sub-volcanic units have been documented (López 1996; Sandeman et al. 1997). One of these units, the Ninahuisa Stock, belongs to the Picotani Suite of Sandeman et al. (1997). The remaining three units, namely the La Huaña (or Chaccaconiza) stock, the Cayo Orjo plug, and the Anta (or Nevado Ollo Quenamari) plug, belong to the Quenamari Suite. The Ninahuisa Stock is a large body, exceeding 20 km<sup>2</sup>, of peraluminous monzogranite exposed in the south-central area of the Macusani Volcanic Field (Fig. 13). It is distinguished by its large sanidine crystals (~ 9 cm) and bimodal mica association (Sandeman et al. 1997). The Chaccaconiza Stock is a highly peraluminous syenogranite with tourmaline, muscovite, and biotite exposed in the southern Macusani Volcanic Field (Fig. 13). This subvolcanic intrusion is near the Cerro Cayo Orjo Plug, which is a syenogranite primarily composed of phenocrysts of sanidine,

plagioclase, quartz, and biotite (Sandeman et al. 1997). The Cerro Cayo Orjo plug is coeval with the Yapamayo Member of the Macusani Formation and shares a similar age with the Nevado Ollo Quenamari plug, a sanidine-quartz-biotite flow-banded syenogranite (Clark et al. 1990; Cheilletz et al. 1992).

## 4. RESULTS

### 4.1. Stereoscopic microscope

#### 4.1.1. 2021-MAC-08

The heavy mineral concentrates from this sample were found to comprise seven main groups of minerals, as determined by their morphology, exfoliation, color, and luster under the binocular loupe. The first group comprises grains that are opaque and dark brown to black in color, exhibiting shiny surfaces with metallic luster. Some of the grains are relatively easy to break with a simple needle scratch, while others are much harder. Most grains show well-developed faces, cubic or orthorhombic habits, and complete terminations. In general, these crystals might represent different mineral species that share similar color and luster properties. Together, these minerals account for ~58 % of the heavy mineral grains extracted from this sample and are more abundant in the 50 and 75  $\mu\text{m}$  fractions than in the 100  $\mu\text{m}$  fraction (Fig. 14A).

The second group is composed of transparent and translucent grains with a shining adamantine luster. When euhedral and subhedral, they form medium to long prismatic crystals. Most of the grains present double terminations. Some crystals show rounded edges, while most retain their typical sharp edges. These crystals represent ~20 % of the heavy mineral grains separated from this sample and are equally abundant in the three fractions.

The third group is composed of dark green to brown translucent crystals with a vitreous or resinous luster. Some of these crystals exhibit clear tabular habits, while in some anhedral grains it is impossible to distinguish any particular habit. Terminations in these grains are not discerned. Minerals of this group represent ~17 % of the heavy mineral grains separated in the sample. Dark green crystals were found in the 50  $\mu\text{m}$  fraction while brown crystals were found in the three granulometric fractions (Fig. 14B).

The fourth group consists of yellow to greenish yellow crystals with a resinous luster and a gentle greasy sheen in some crystals. These grains occur as subhedral to anhedral crystals

that exhibit a poorly defined tetragonal morphology with commonly rough faces and rounded edges. Most grains are doubly terminated. These crystals represent ~2 % of the heavy mineral grains separated from this sample and were exclusively picked from the 50  $\mu\text{m}$  fraction.

The fifth group comprises five colorless grains with a vitreous luster, some of which exhibit only a light green tint. The grains have a clear prismatic habit, which is typically capped by bipyramids. Four of the grains are slender and display well-defined faces, while one grain is roundish. The crystals of this group, which are probably of zircon, represent ~1.5 % of the heavy mineral grains separated from this sample and were found in the 50 and 75  $\mu\text{m}$  fractions.

The sixth group comprises minerals that exhibit pale brass yellow color and metallic luster. The few identified grains within this group form crystal clusters with no discernible habits. These crystals represent ~1 % of the heavy mineral grains separated from this sample and were found in the 75  $\mu\text{m}$  fraction.

Finally, a seventh group which includes few individual grains, representing < 1 % of the heavy mineral grains separated from the sample globally, are colorless and host orange to brown inclusions with no distinguishable habit.

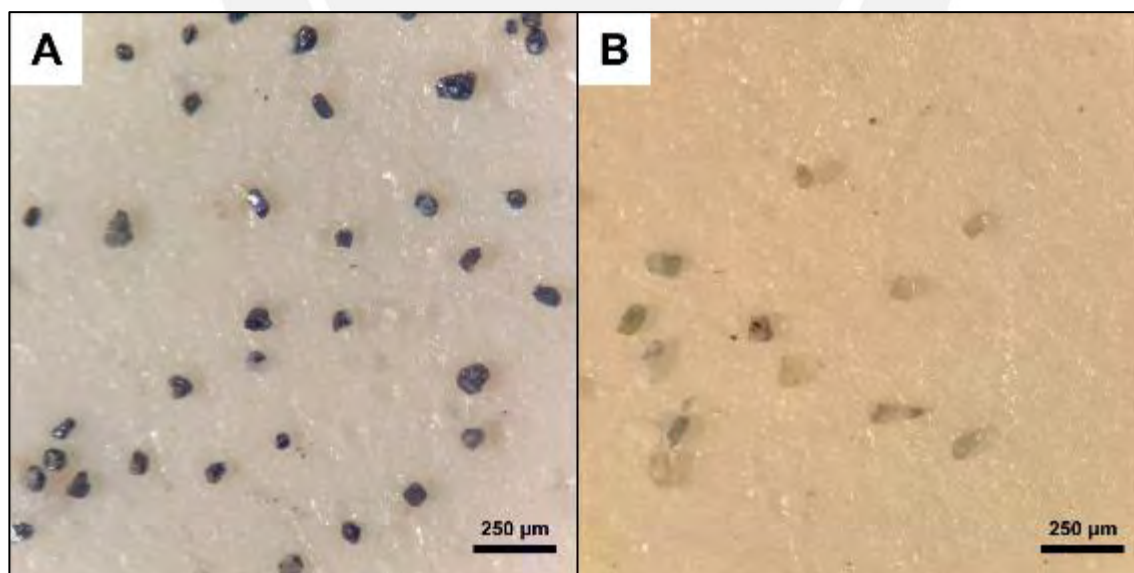


**Figure 14.** Grains separated from sample 2021-MAC-08 and classified according to their color and luster under the binocular loupe. A: Dark brown to black opaque crystals with metallic luster and equant to short prismatic habits. B: Green translucent crystals with diverse morphologies.

#### 4.1.2. 2021-MAC-21

Six main groups of minerals were identified in the heavy mineral concentrates from this sample under the binocular loupe. The first group includes translucent, colorless crystal grains with a vitreous luster. Some of them have a light orange tint, while others have a light green tint. One grain has a distinctive white color and greasy luster. These crystals can be divided into two subgroups according to their habits. The first subgroup comprises euhedral to subhedral, short to long tetragonal prisms capped by bipyramids. The second subgroup comprises grains that exhibit well-defined bipyramids without intervening prisms. Additionally, two crystal grains stand out for presenting twinning. The grains belonging to this group represent ~27 % of the separated mineral grains in the sample, with many of them being found in the 50 and 75  $\mu\text{m}$  fractions (Fig. 15A).

The second group comprises crystals with a light orange tint and a resinous luster. These grains are mostly anhedral and have sub-rounded edges with smooth mamillated crusts. These grains represent ~22 % of the total mineral grains recovered and are distributed between the 50, 75, and 100  $\mu\text{m}$  fractions (Fig. 15B).

The third group is composed of opaque crystals with tones ranging from light to dark gray and dark brown and exhibiting a metallic luster. They present very rough surfaces and most of them lack discernible habits and exhibit rounded to subrounded edges. These crystals represent ~22 % of the mineral grains separated and were found in the 75  $\mu\text{m}$  fraction (Fig. 15C).

The fourth group comprises crystals displaying yellowish green and light orange hues and resinous luster. Most of them are roundish and lack distinguishable habits. However, some of the grains show a wedge shape with loose terminations. These crystals represent 17 % of the heavy mineral grains separated in the sample and most of them were found in the 50 and 75  $\mu\text{m}$  fractions.

The fifth group is composed of grains with a characteristic sky-blue color with a lilac tint and resinous luster. The grains are mostly anhedral and show rounded edges. These grains represent ~8 % of the heavy mineral grains separated in the sample and were equally distributed in the three granulometric fractions (Fig. 15D).

The sixth group embraces minerals of pale brass yellow color and metallic luster, most probably corresponding to pyrite. They form crystal clusters with no discernible habits.

They represent ~4 % of the heavy mineral grains separated in the sample and were found in the 50 and 75  $\mu\text{m}$  fractions.

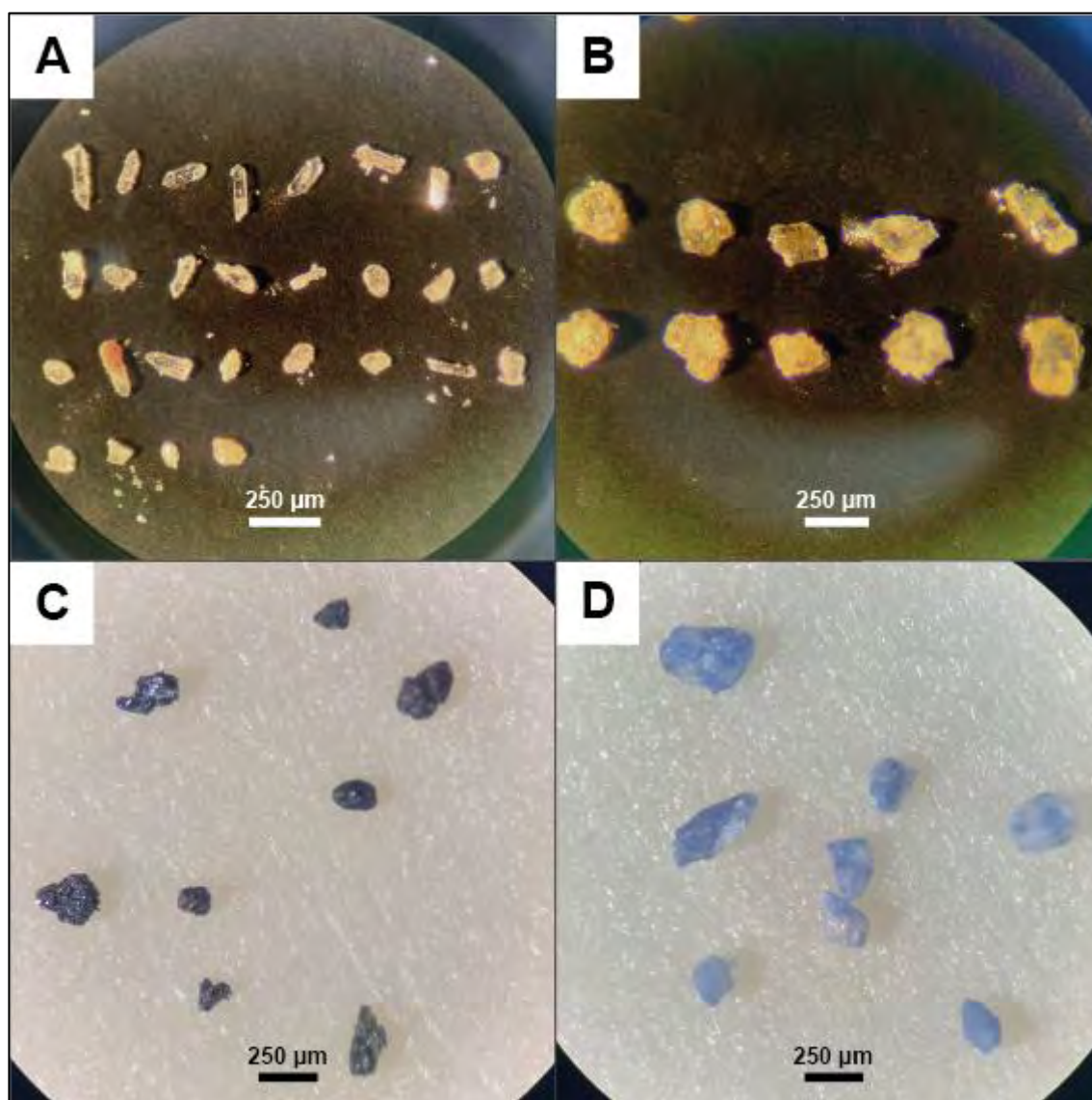


**Figure 15.** Grains separated from sample 2021-MAC-21 and classified according to their color, luster, and morphologies under the binocular loupe. A: Translucent crystals with vitreous luster and equant to prismatic habits. B: Translucent crystals with orange hues and smooth, curved surfaces. C: Dark gray grains with metallic luster and diverse morphologies. D: Pale blue grains with glassy luster and subhedral to anhedral morphologies.

#### 4.1.3. 2021-MAC-67

In heavy mineral concentrates from this sample, six main groups of minerals were identified under the binocular loupe. The first group contains light to dark gray and black crystals with a common metallic luster. Morphologies can be classified into two subgroups. The first subgroup includes well-defined black tabular crystals, while the second subgroup comprises subhedral to anhedral equant to short prismatic crystals with mostly subrounded

edges. These crystals represent ~32 % of the heavy mineral grains picked in this sample and were found in the three granulometric fractions (Fig. 16A).

The second group includes orange-tinged crystals with resinous luster. These grains exhibit a variety of habits, ranging from subhedral to euhedral shapes. Two distinct morphologies can be discerned. The first one comprises prismatic crystals with subrounded edges, and the second one includes equant grains with rounded edges. Collectively, they represent ~26 % of the total mineral grains separated in this sample and were found in the 50  $\mu\text{m}$  fraction.

The third group is constituted of pale brown to deep green crystals with vitreous luster. The majority of grains form slender prisms with parallel striation on the crystal surface and sharp edges. They represent ~20 % of the separated grains from the sample and were found in the three granulometric fractions (Fig. 16B).

The fourth group includes brownish white crystals with a glassy luster. These grains exhibit tabular habits and well-defined sharp edges. Grains from this group represent ~11 % of the separated mineral grains in this sample, with the majority of them found in the 50 and 75  $\mu\text{m}$  fractions (Fig. 16C).

The fifth group consists of reddish-brown grains with an adamantine luster. The selected crystals lack recognizable habits and exhibit sharp edges. They represent ~5 % of the extracted mineral grains and were predominantly found in the 50 and 75  $\mu\text{m}$  fractions (Fig. 16D).

The sixth group is characterized by vitreous luster with predominantly colorless crystals and less abundant orange-tinted crystals. Their morphologies are diverse, ranging from euhedral tetragonal prisms to subhedral complex habits. These grains represent ~5 % of the heavy mineral grains separated from this sample and were found in the 50  $\mu\text{m}$  fraction.

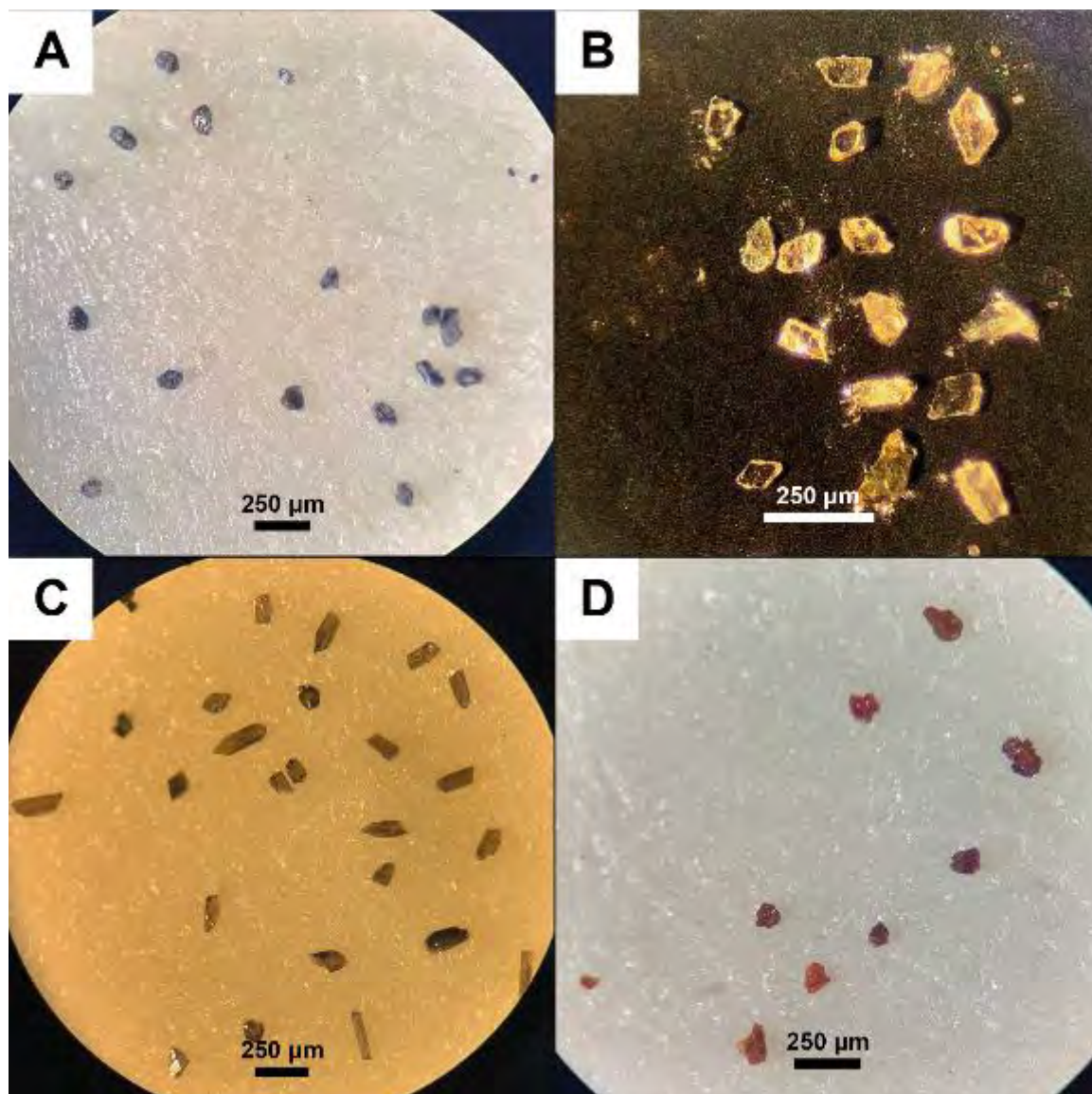


**Figure 16.** Grains separated from sample 2021-MAC-67 and classified according to their color, luster, and morphologies under the binocular loupe. A: Dark gray and black crystals with a metallic luster and subhedral to anhedral equant to short prismatic habits. B: Brownish white crystals with glassy luster and tabular habits. C: Pale brown to deep green crystals with prismatic habits. D: Reddish-brown grains with adamantine luster.

## 4.2. SEM-EDS

### 4.2.1. 2021-MAC-08

In this sample, 323 grains were analyzed by SEM-EDS. Representative SEM-SE images of mineral species and groups identified in this sample are shown in [Figures 17-18](#). Zircon grains ( $n = 5$ ) exhibit lengths of 75-250  $\mu\text{m}$  along the c-axis, thicknesses of 30-75  $\mu\text{m}$ , and aspect ratios (length/width) between 1 and 5. Two distinct morphological types of zircons were observed. The first type consists of crystals with highly elongated prisms capped by dipyrramids with irregular faces. The second type embraces short-prismatic to equant

dipyramid crystals with irregularly developed faces. EDS analyses indicate stoichiometric zircon compositions (Fig. 19A).

Cassiterite crystals ( $n = 5$ ) vary from 50 to 100  $\mu\text{m}$  in size. In some grains, cassiterite crystals measuring  $\sim 50 \mu\text{m}$  form clusters up to 250  $\mu\text{m}$  in size. Individual crystals exhibit a tetragonal trapezohedron habit, though some also form concretionary masses or have uneven faces. EDS analyses indicate stoichiometric cassiterite compositions (Fig. 19B).

The opaque crystals described in the previous section present a distinguishing high Ti content and hence are grouped herein as Ti-rich oxides ( $n = 175$ ). This group includes crystals with sizes between 25 to 75  $\mu\text{m}$  that may form 100  $\mu\text{m}$ -sized crystal clusters. Most crystals are euhedral and subhedral and show sharp edges, though some other crystals exhibit rough and not well-defined faces and roundish edges. This group of minerals comprises a marked variety of habits including cuboctahedrons and rhombohedrons. Some are intergrown with smaller elongated zircon crystals (Figs. 18A-B). The EDS analyses yielded relatively wide compositional ranges with mean and standard deviation ( $\sigma$ ) values of  $42 \pm 7 \text{ wt } \% \text{ Ti}$ ,  $45 \pm 7 \text{ wt } \% \text{ O}$ ,  $4 \pm 2 \text{ wt } \% \text{ Fe}$ ,  $5 \pm 2 \text{ wt } \% \text{ Nb}$ , and  $3 \pm 1 \text{ wt } \% \text{ Ta}$  (Fig. 19C). The mineralogical classification of Ti-rich oxides is addressed in Chapter 4.3.

Monazite-Ce grains ( $n = 2$ ) are 50 to 75  $\mu\text{m}$  in length. The grains exhibit subhedral, rounded, or irregular shapes, and rough and striated faces. Intimate intergrowths between monazite and zircon grains are a common occurrence (Fig. 18C). Compositional ranges include 28 to 39 wt % O, 17 to 20 wt % P, 19 to 25 wt % Ce, 2 to 10 wt % La, and 5 to 10 wt % Nd (Fig. 19D).

Xenotime-Y crystals ( $n = 4$ ) range in size from 50 to 75  $\mu\text{m}$  and show euhedral to subhedral bipyramidal habits, and in some cases, faces cut by small zircon crystals (Fig. 18D). The compositional ranges are  $50 \pm 3 \text{ wt } \% \text{ O}$ ,  $34 \pm 3 \text{ wt } \% \text{ P}$ , and  $16 \pm 1 \text{ wt } \% \text{ Y}$  (Fig. 19E).



Figure 17. SEM-SE images of representative minerals found in heavy concentrates from sample 2021-MAC-08. See the main text for descriptions.

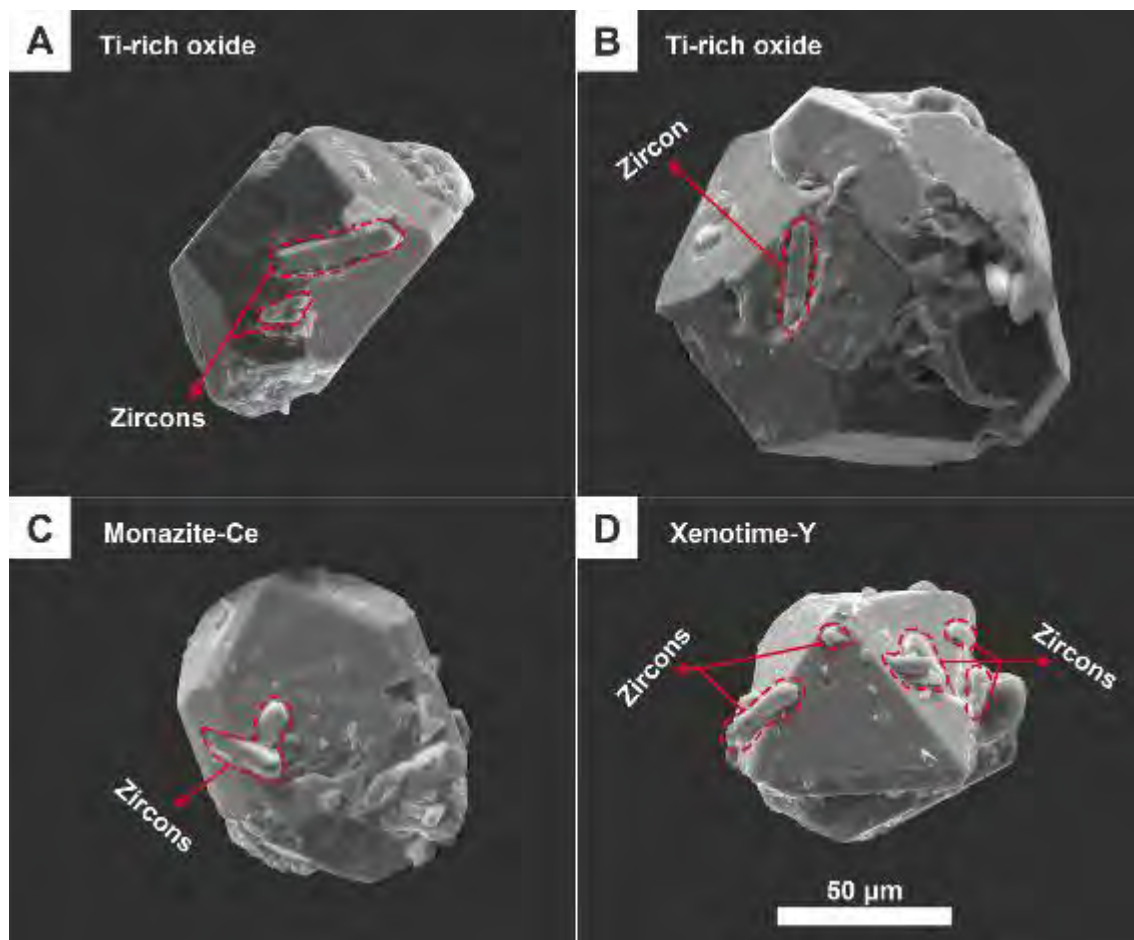


**Figure 18.** SEM-SE images of heavy minerals from sample 2021-MAC-08 showcasing mineral intergrowths. A: Euhedral, octahedra modified Ti-rich oxide crystal intergrown with smaller, prismatic zircon grains. B: Euhedral Ti-rich oxide crystal intergrown with a small, elongated and prismatic zircon. C: Subhedral monazite-Ce crystal intergrown with smaller, prismatic zircon grains. D: Euhedral, equant pyramidal xenotime-Y crystal intergrown with smaller, prismatic zircon grains.

Other minerals present in heavy mineral concentrates in this sample include high-Al unidentified minerals, actinolite, Fe-oxide, epidote, and pyrite. The high-Al unidentified mineral grains ( $n = 55$ ) exhibit a variety of sizes, from 75 to 250  $\mu\text{m}$  along the  $c$ -axis, well-developed faces, and slightly barrel-shaped prismatic and rhombohedral prisms capped by poorly faceted hexagonal dipyrramids. EDS analyses indicate high contents of O ( $45 \pm 5$  wt %), Al ( $39 \pm 6$  wt %), and F ( $13 \pm 5$  wt %; Fig. 19F).

The Fe-oxide crystals ( $n = 2$ ) range in size from 50 to 100  $\mu\text{m}$  and show euhedral to subhedral octahedral morphology. EDS results provide information about the contents of O ( $33 \pm 4$  wt %), and Fe ( $67 \pm 4$  wt %; Fig. 19G).

Actinolite grains ( $n = 6$ ) have lengths that are in the range between 50 and 300  $\mu\text{m}$  and display a typical fibrous habit. Their EDS spectra include O ( $44 \pm 4$  wt %), Si ( $24 \pm 3$  wt %), Al ( $4 \pm 4$  wt %), Fe ( $8 \pm 2$  wt %), Mg ( $10 \pm 5$  wt %), and Ca ( $10 \pm 4$  wt %; Fig. 19H).

Epidote grains ( $n = 8$ ) vary in size between 50 and 75  $\mu\text{m}$  and show massive aggregates and, in a few cases, fibrous habits. The compositional range according to EDS analyses is O ( $44 \pm 5$  wt %), Fe ( $12 \pm 6$  wt %), Al ( $10 \pm 5$  wt %), Si ( $19 \pm 3$  wt %), and Ca ( $13 \pm 6$  wt %; Fig. 19I).

The grains of pyrite ( $n = 3$ ) have a size range between 50 and 100  $\mu\text{m}$  and exhibit the typical cubic habit, with some uneven faces with rounded edges. EDS analyses indicate stoichiometric compositions (Fig. 19J).



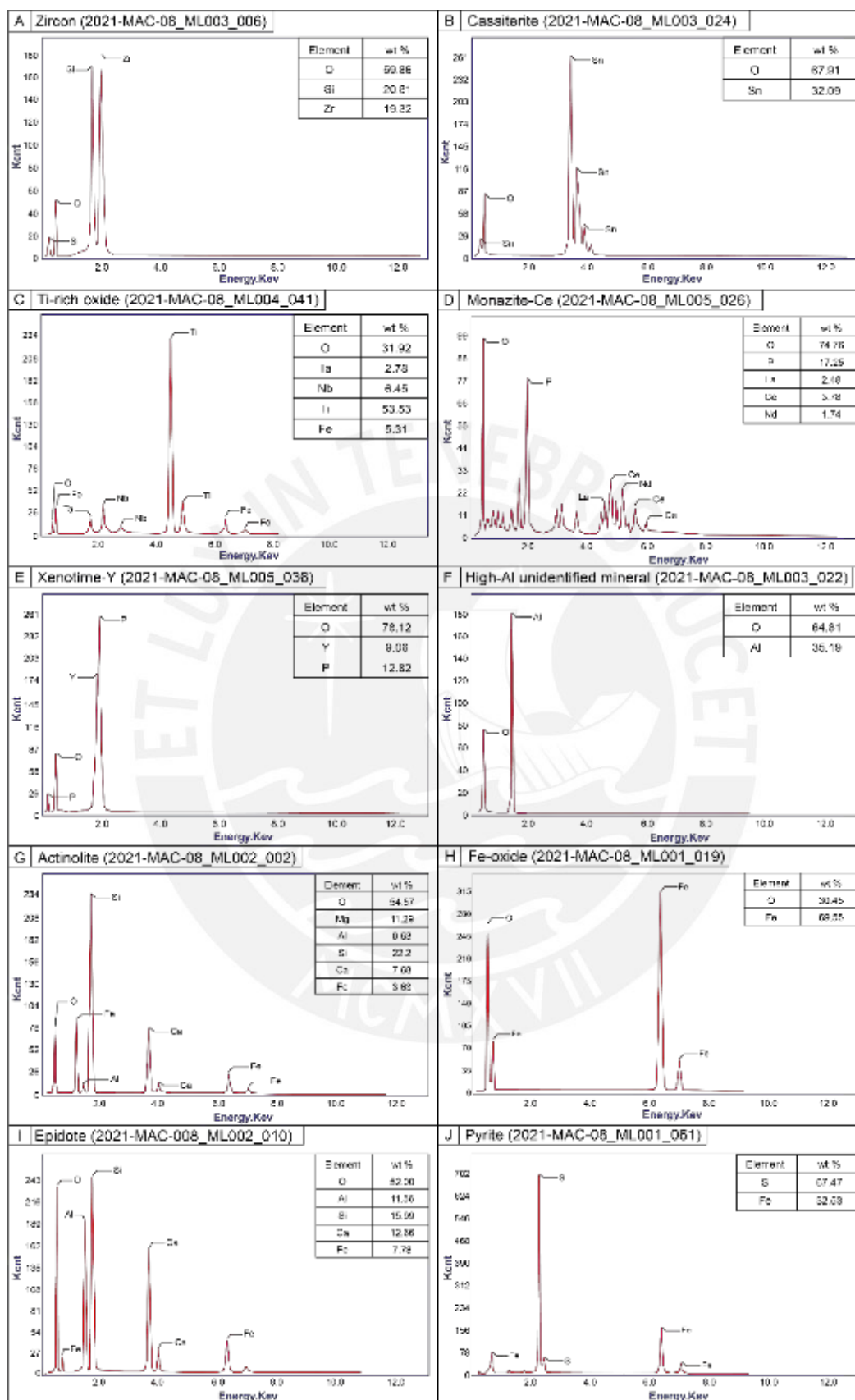
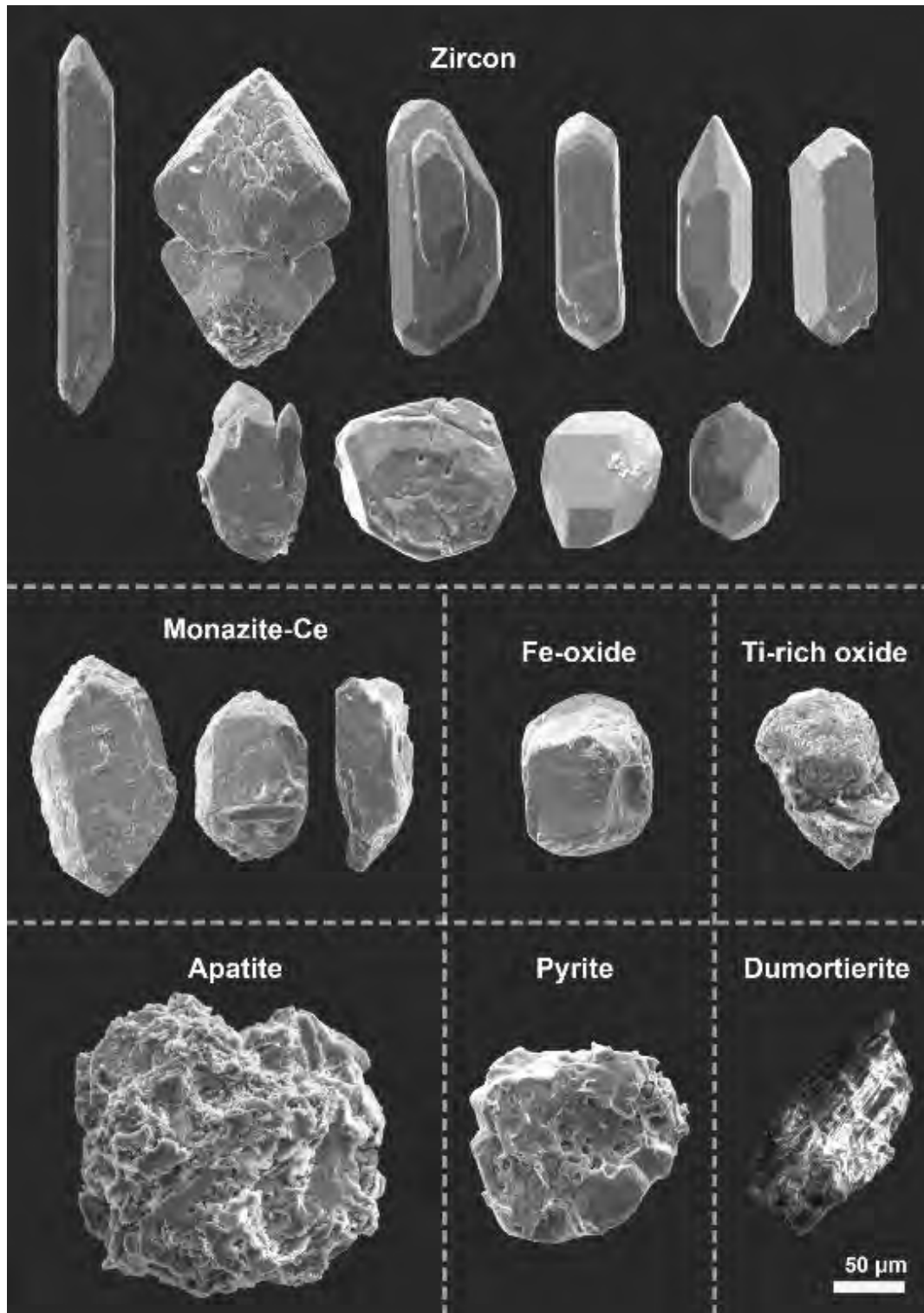


Figure 19. Selected EDS analyses (spectra and quantified results) on minerals from sample 2021-MAC-08 including zircon (A), cassiterite (B), Ti-rich oxide (C), monazite-Ce (D), xenotime-Y (E), high-Al unidentified mineral (F), actinolite (G), Fe-oxide (H), epidote (I), and pyrite (J).

#### 4.2.2. 2021-MAC-21

In this sample, a total of 237 grains have been analyzed. Representative SEM-SE images of the mineral species and groups identified in this sample are shown in [Figures 20-23](#).



**Figure 20.** Representative SEM-SE images of crystals in heavy concentrates from sample 2021-MAC-21. See the main text for descriptions.

Zircon grains ( $n = 54$ ) exhibit a length along the c-axis that ranges from 75 to 300  $\mu\text{m}$ , with thicknesses that vary between 100 to 25  $\mu\text{m}$  and aspect ratios of 1 to 7. Four broad zircon morphologies were identified. The first is composed of crystals with prismatic habits that are capped by dipyrramids with sharp terminations and regular faces. One of the zircon crystals within this first group matches the morphology of G1 type zircons in the classification scheme of Pupin (1980) (Fig. 21). The second comprises twinned crystals with smooth to rough faces. The third exhibits subhedral to anhedral crystals with a set of irregularly developed faces. The fourth comprises zircon crystals with more complex and irregular morphologies. EDS analyses indicate stoichiometric compositions (Fig. 24A).

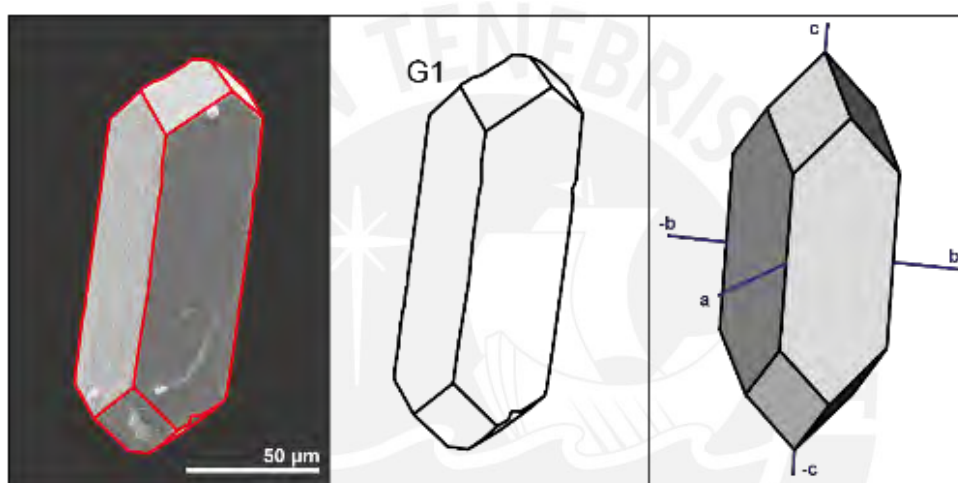


Figure 21. Zircon crystal (2021-MAC-67\_ML001\_005; SEM-SE image) matching the morphology of G1 zircon type in the classification of Pupin (1980).

Monazite-Ce grains ( $n = 35$ ) range in size from 50 to 100  $\mu\text{m}$ . Monazite crystals display a variety of morphologies including subhedral to anhedral, rounded or irregularly shaped grains as well as grains that show prismatic habits. The faces are commonly rough and striated and occasionally cut by elongated zircon grains (Fig. 22). EDS analysis indicates that the monazite composition is typically dominated by Ce ( $23 \pm 3$  wt %) over La ( $12 \pm 2$  wt %) and Nd ( $10 \pm 3$  wt %) and have high O ( $29 \pm 7$  wt %) and P ( $16 \pm 1$  wt %; Fig. 24B).

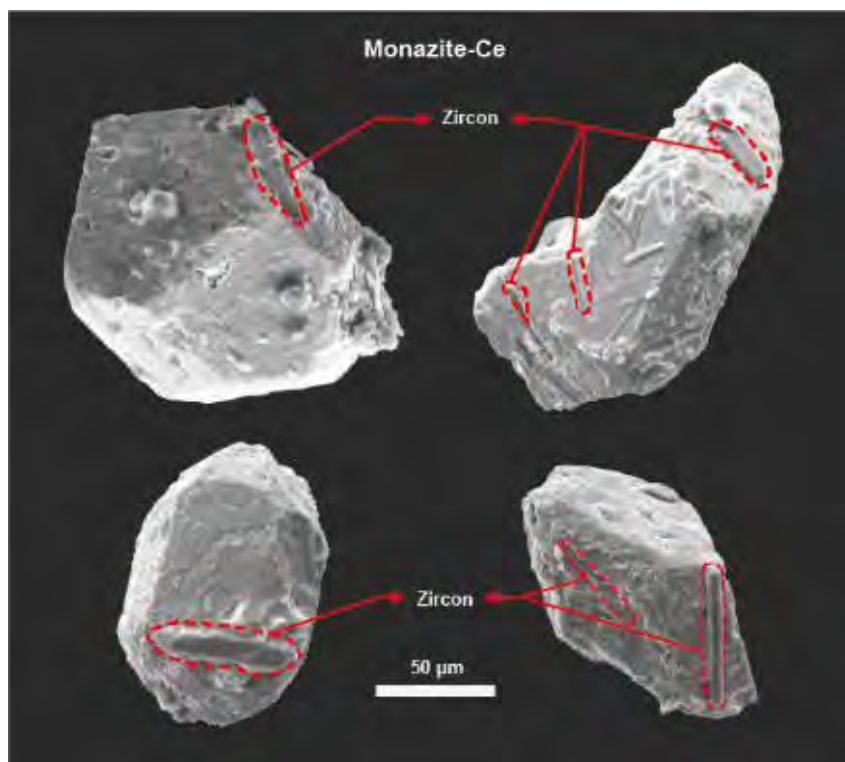


Figure 22. SEM-SE images of monazite-Ce grains from sample 2021-MAC-21 intergrown with elongated zircon crystals.

The crystals of apatite ( $n = 50$ ) are between 75 and 300  $\mu\text{m}$  in size. These grains are completely anhedral, highly porous, and cariated, with rough-developed faces. EDS analysis yielded O ( $40 \pm 5$  wt %), P ( $17 \pm 2$  wt %), Ca ( $38 \pm 6$  wt %), and F ( $5 \pm 2$  wt %; Fig. 24C).

Pyrite grains ( $n = 10$ ) exhibit sizes that range from 100 to 150  $\mu\text{m}$ . Although the grains are anhedral and display cariated textures, some pseudo-cubic habits are found in some of the crystal phases. The EDS analyses indicate stoichiometric compositions (Fig. 24D).

Ti-rich oxide crystals ( $n = 24$ ) range in size from 50 to 200  $\mu\text{m}$  and most have anhedral habits with rounded edges and rough faces. In addition, a few grains exhibit a complex cluster of cross-hatched thin platy crystals with reticulated, snowflake-like textures (Fig. 23). EDS analyses revealed elevated contents of O ( $42 \pm 9$  wt %) and Ti ( $51 \pm 9$  wt %) and lower, though highly variable, contents of Fe ( $3 \pm 2$  wt %), Nb ( $2 \pm 1$  wt %), and Ta ( $5 \pm 4$  wt %; Fig. 24E).

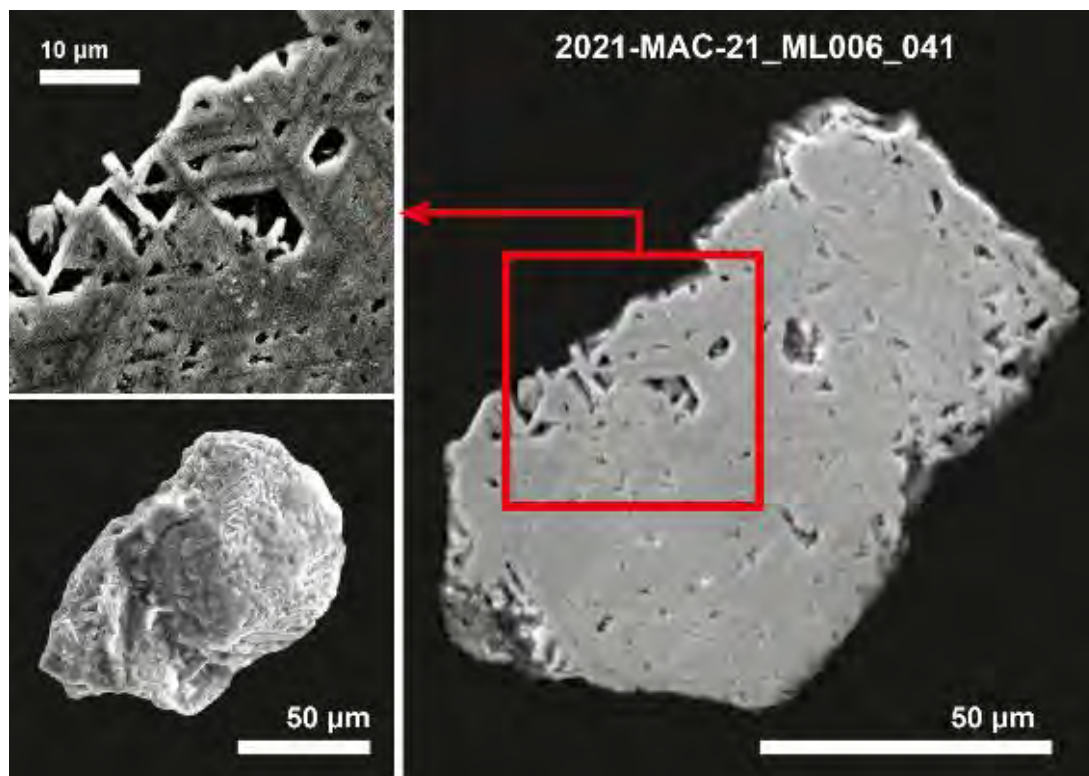


Figure 23. SEM-SE images for a single reticulated Ti-oxide crystal.

The Fe-oxide group ( $n = 26$ ) comprises crystals with a variety of morphologies and sizes in the range from 50 to 300  $\mu\text{m}$ . The grains are predominantly anhedral, yet some have subhedral habits with edges that vary from sharp to rounded. Additionally, a few grains form euhedral crystals with octahedral morphologies. EDS results indicate significant contents of Fe ( $65 \pm 3$  wt %) and O ( $32 \pm 9$  wt %), with lower proportions of other elements such as Si ( $7 \pm 4$  wt %) and Al ( $6 \pm 4$  wt %; Fig. 24F).

Dumortierite ( $n = 19$ ) crystals range in width and length from 50 to 300  $\mu\text{m}$  and exhibit two different habits. The first habit is fibrous and is characterized by slender and elongated crystals that are parallel arranged. The second habit is massive and appears as densely packed aggregates. EDS results indicate the presence of Al ( $13 \pm 12$  wt %), Si ( $34 \pm 13$  wt %), and O ( $53 \pm 4$  wt %; Fig. 24G).

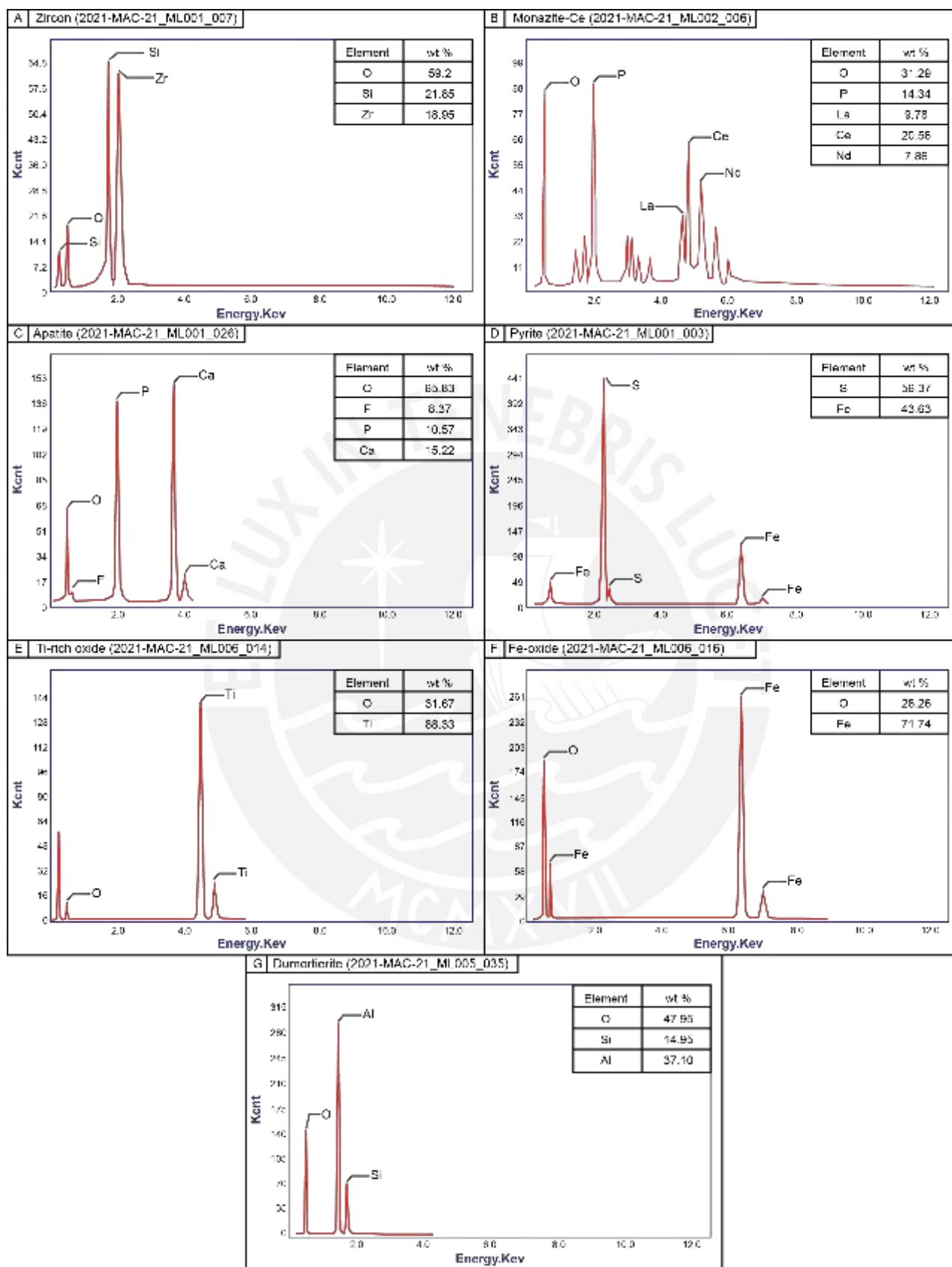


Figure 24. Selected EDS analyses (spectra and quantified results) on minerals from sample 2021-MAC-21 including zircon (A), monazite-Ce (B), apatite (C), pyrite (D), Ti-rich oxide (E), Fe-oxide (F), and dumortierite (G).

In addition to the aforementioned minerals, other heavy minerals present in the sample in much lesser proportions are actinolite ( $n = 4$ ), tourmaline ( $n = 2$ ), hematite ( $n = 1$ ), titanite ( $n = 1$ ), and epidote ( $n = 1$ ; Fig. 25).

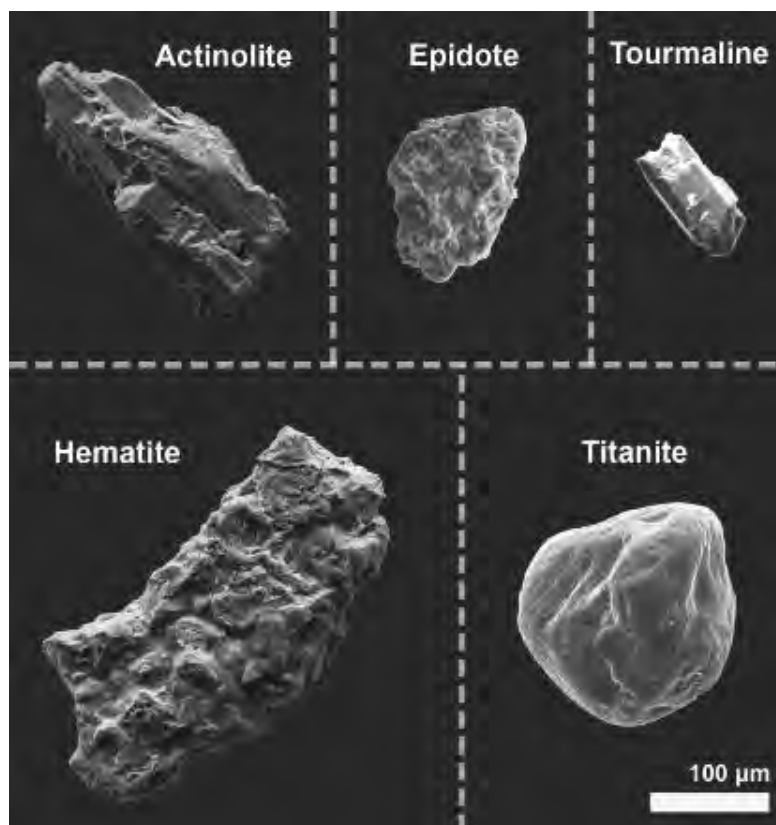


Figure 25. SEM-SE images of crystals in less proportion in heavy concentrates from sample 2021-MAC-21.

#### 4.2.3. 2021-MAC-67

In this sample, 278 grains were selected for SEM-EDS analyses (Figs. 26-29). The first group comprises zircon grains ( $n = 8$ ) ranging from 50 to 200  $\mu\text{m}$  in length, 50 to 125  $\mu\text{m}$  in width, and 1 to 4 in aspect ratio. Two morphological types of zircon grains are distinguished. The first includes elongated prisms capped by dipyrramids with distinguishable faces. The second groups crystals with more complex symmetry as clearly evidenced in Figure 27—crystal made of a prism (110) and a dipyramid (101) with short elongation—and in Figure 28—crystal composed of two prisms capped by two dipyrramids. EDS results indicate stoichiometric zircon compositions (Fig. 29A).

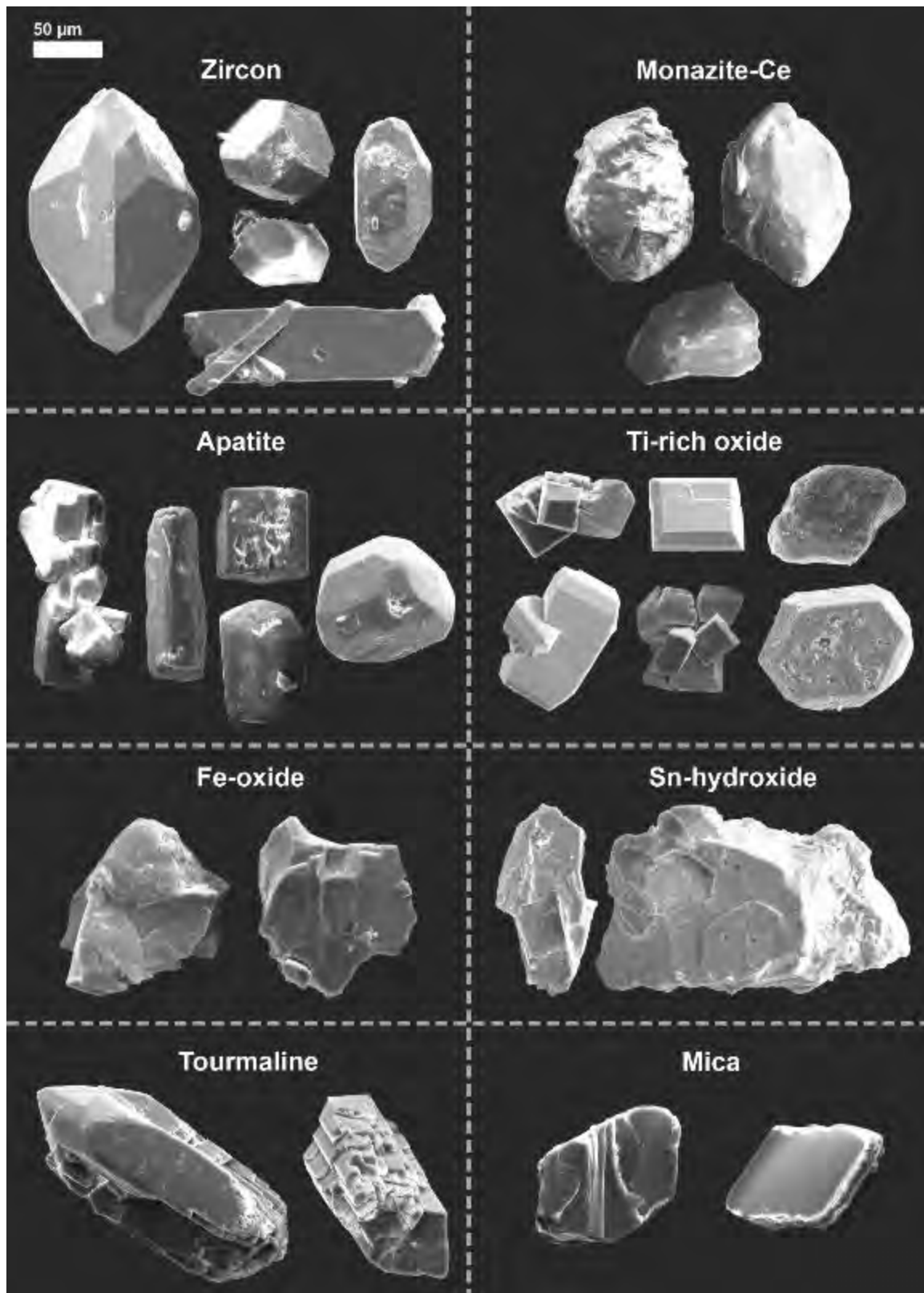


Figure 26. Representative SEM-SE images of minerals found in heavy concentrates from sample 2021-MAC-08. See the main text for descriptions.

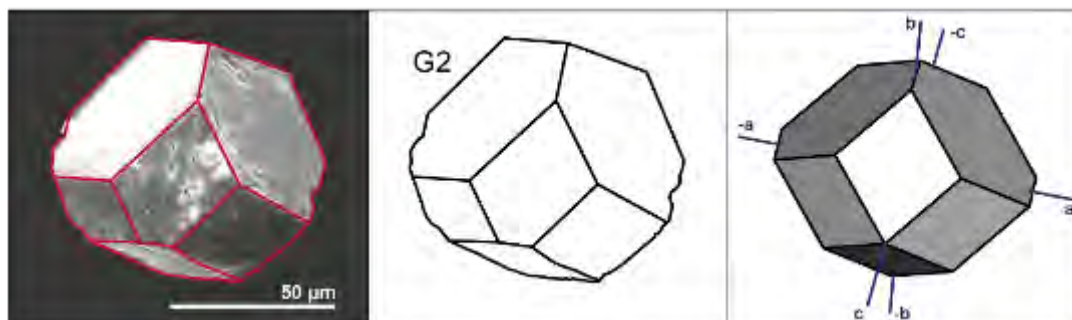


Figure 27. Zircon crystal (2021-MAC-67\_ML001\_005; SEM-SE image) morphologically similar to the G2 type in the classification of Pupin (1980).

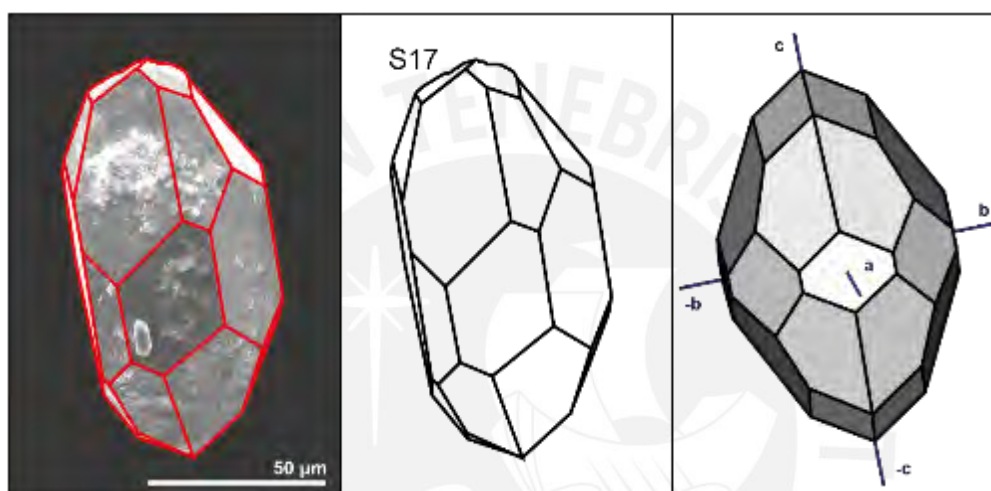


Figure 28. Zircon crystal (2021-MAC-67\_ML001\_048; SEM-SE image) with a morphology similar to the S17 type in the classification of Pupin (1980).

Monazite-Ce crystals ( $n = 5$ ) have sizes comprised between 50 and 150  $\mu\text{m}$ . The grains exhibit equant tabular habits with subrounded edges. Some of them are intergrown with smaller zircon grains. EDS results indicate high contents of O ( $31 \pm 2$  wt %), P ( $17 \pm 1$  wt %), and REE, with systematically higher Ce ( $23 \pm 3$  wt %) than La ( $11 \pm 1$  wt %) and Nd ( $10 \pm 1$  wt %; Fig. 29B).

Apatite grains ( $n = 44$ ) range from 50 to 200  $\mu\text{m}$  in size and can be subdivided into three subtypes according to their morphology. The first subtype groups equant crystals with subrounded edges and smooth faces. The second subtype includes long-prismatic crystals with elongation ratios ranging from 2:1 to 4:1 with rounded to subrounded edges. The third subtype comprises a few minute grains ( $\sim 10$   $\mu\text{m}$ ) forming a crystal aggregate. EDS results indicate the presence of Ca ( $40 \pm 9$  wt %), P ( $17 \pm 3$  wt %), F ( $5 \pm 2$  wt %), and O ( $37 \pm 7$  wt %; Fig. 29C).

Ti-rich oxide crystals ( $n = 87$ ) range from 50 to 250  $\mu\text{m}$  in size and can be subdivided into two morphological subgroups. The first subgroup is composed of small crystals (50-100  $\mu\text{m}$ ) with euhedral, tetragonal shapes (e.g. dipyrramids and prisms) with sharp edges. The second subgroup includes prismatic crystals with subrounded edges and rough faces grading to anhedral shapes with unrecognizable faces that vary from 50 to 250  $\mu\text{m}$  in size. EDS results indicate high contents of Ti ( $50 \pm 11$  wt %) and O ( $44 \pm 9$  wt %) and lesser contents of Fe ( $2 \pm 2$  wt %), Nb ( $1 \pm 1$  wt %), and Sn ( $4 \pm 3$  wt %; Fig. 29D).

Fe-oxide grains ( $n = 9$ ) vary from 50 to 125  $\mu\text{m}$  in width and length. These crystals exhibit anhedral shapes with no recognizable habits and conchoidal fracture. A few grains show an earthy habit with no visible crystalline affinities. EDS results yield high contents of O ( $29 \pm 11$  wt %) and Fe ( $57 \pm 15$  wt %; Fig. 29E).

Sn-oxide crystals ( $n = 7$ ) vary from 50 to 200  $\mu\text{m}$  and are grouped into two morphological subtypes. The first includes grains with elongated habits, rough faces, and sharp edges, while the second comprises anhedral crystals with sharp edges. EDS analyses indicate high contents of O ( $26 \pm 6$  wt %), Sn ( $47 \pm 4$  wt %), and Mn ( $26 \pm 2$  wt %; Fig. 29F).

Tourmaline grains ( $n = 56$ ) present lengths typically between 50 to 100  $\mu\text{m}$  and elongation ratios from 2 to 4. Euhedral and long-prismatic crystals represent the typical morphological type in this sample, with recognizable faces, a rough surface, and common striation. EDS results indicate high contents of O ( $46 \pm 4$  wt %), Si ( $18 \pm 1$  wt %), Al ( $21 \pm 1$  wt %), and Fe ( $11 \pm 4$  wt %) and smaller though highly variable contents of Mg ( $1 \pm 1$  wt %) and Na ( $2 \pm 1$  wt %; Fig. 29G).

Mica crystals ( $n = 31$ ) vary from 50 to 150  $\mu\text{m}$  in size and show the typical two-dimensional platy morphology. EDS analyses provide information about high contents of O ( $45 \pm 3$  wt %), Si ( $23 \pm 2$  wt %), Al ( $19 \pm 2$  wt %), K ( $9 \pm 1$  wt %), and Fe ( $3 \pm 1$  wt %; Fig. 29H).

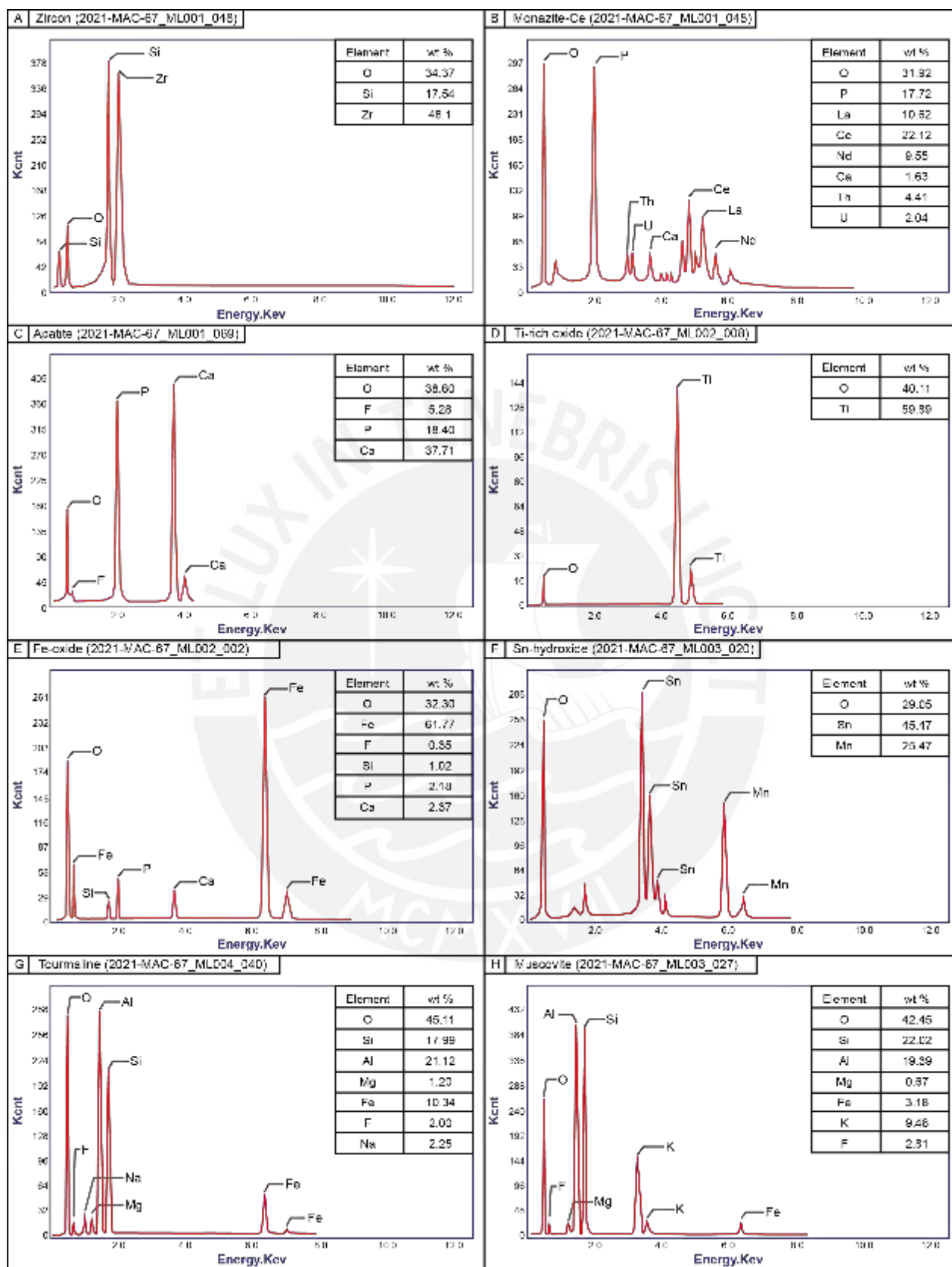


Figure 29. Selected EDS analyses (spectra and quantified results) on minerals from sample 2021-MAC-67 including zircon (A), monazite-Ce (B), apatite (C), Ti-rich oxide (D), Fe-oxide (E), Sn-hydroxide (F), tourmaline (G), and mica (H).

Other heavy minerals found in the sample in much lesser proportions include tremolite-actinolite (n = 5), ilmenite (n = 1), andradite (n = 1), and pyrite (n = 1; Fig. 30).

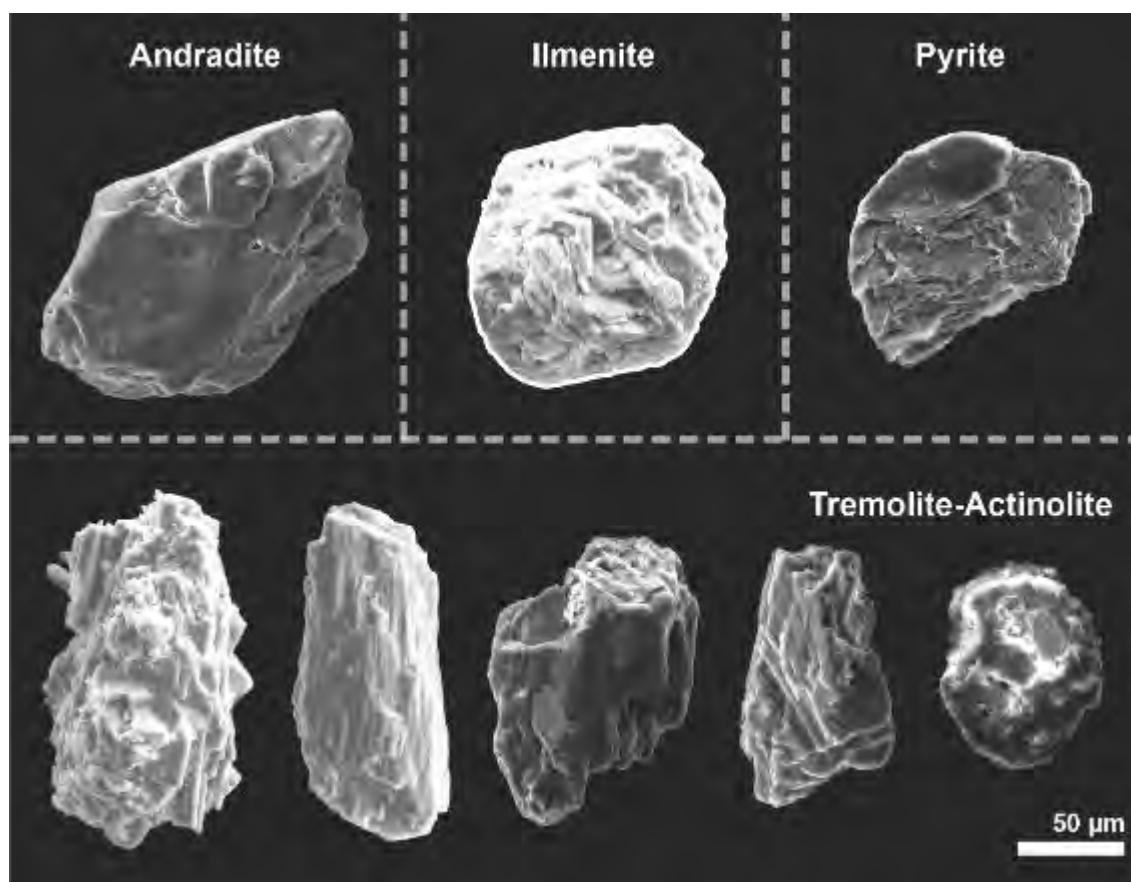


Figure 30. SEM-SE images of crystals found in minor proportion in heavy concentrates from sample 2021-MAC-67.

### 4.3. Raman spectroscopy

#### 4.3.1. Silicate minerals

##### Actinolite-Tremolite series

Raman spectra of tremolite and actinolite are characterized by typical features between 100 to 1,200  $\text{cm}^{-1}$  with characteristic high peaks at 671  $\text{cm}^{-1}$  and smaller peaks at 1,064  $\text{cm}^{-1}$ . Raman spectra are similar to actinolite-tremolite reference data in the WiRE database (Fig. 31).

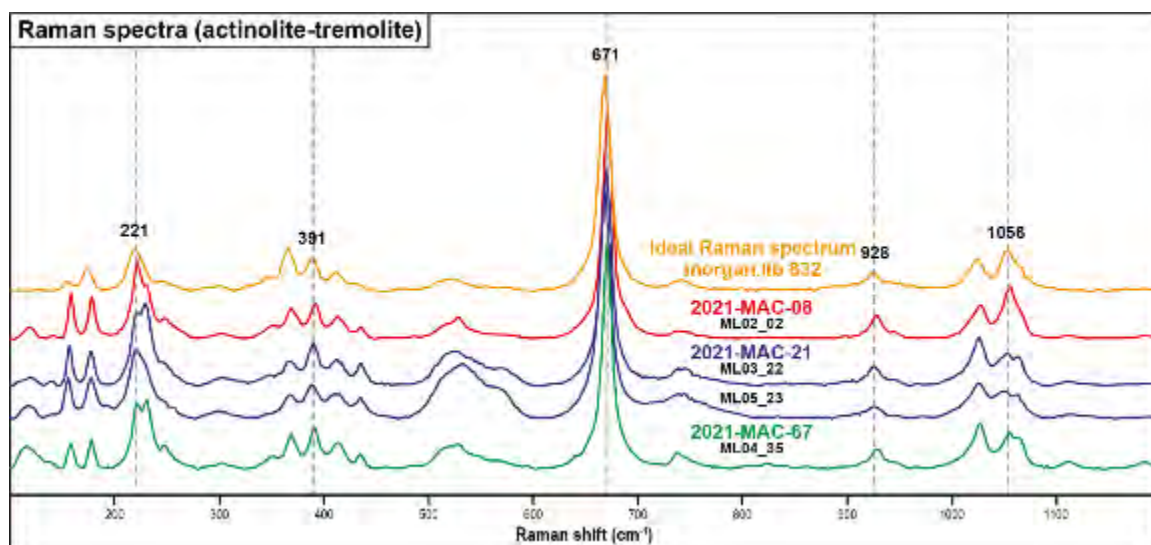


Figure 31. Raman results for actinolite-tremolite.

### Andradite

Raman results indicate the presence of an andradite grain with all the band positions remaining similar to the spectrum from the WiRE database (Fig. 32). Important peaks were registered at 361, 374, 532, 819, and 878  $\text{cm}^{-1}$ .

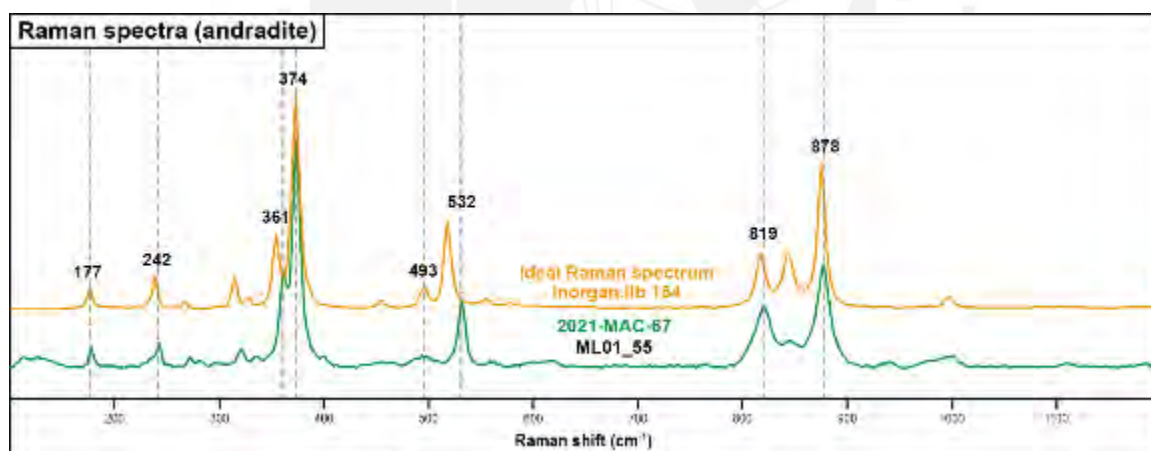


Figure 32. Raman results for andradite.

### Dumortierite

The Raman spectra of dumortierite comprise two reference types in the sample. The first one includes three notable bands (207, 355, and 464  $\text{cm}^{-1}$ ). The second one comprises six prominent bands (207, 287, 509, 563, 946, and 999  $\text{cm}^{-1}$ ). The positions of the bands are in good agreement with those in the dumortierite spectra from the WiRE database (Fig. 33).

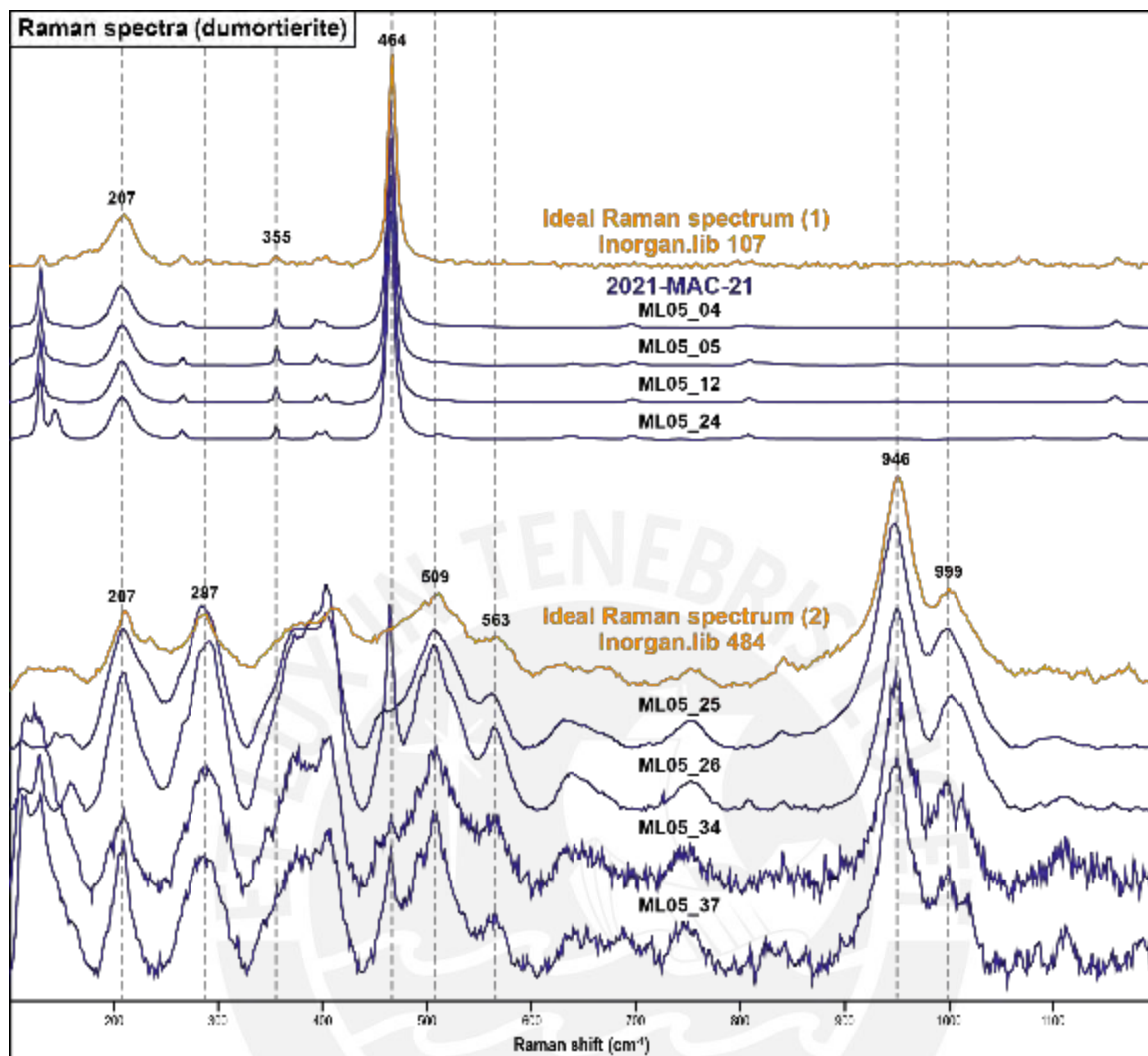


Figure 33. Raman results for dumortierite.

### Epidote

Raman spectra for epidote are characterized by sharp bands at 455, 565, 599, and 915  $\text{cm}^{-1}$ , and other weak bands at 350 and 980  $\text{cm}^{-1}$ . The Raman spectra obtained from these samples are very similar to those of epidote from the WiRE database (Fig. 34).

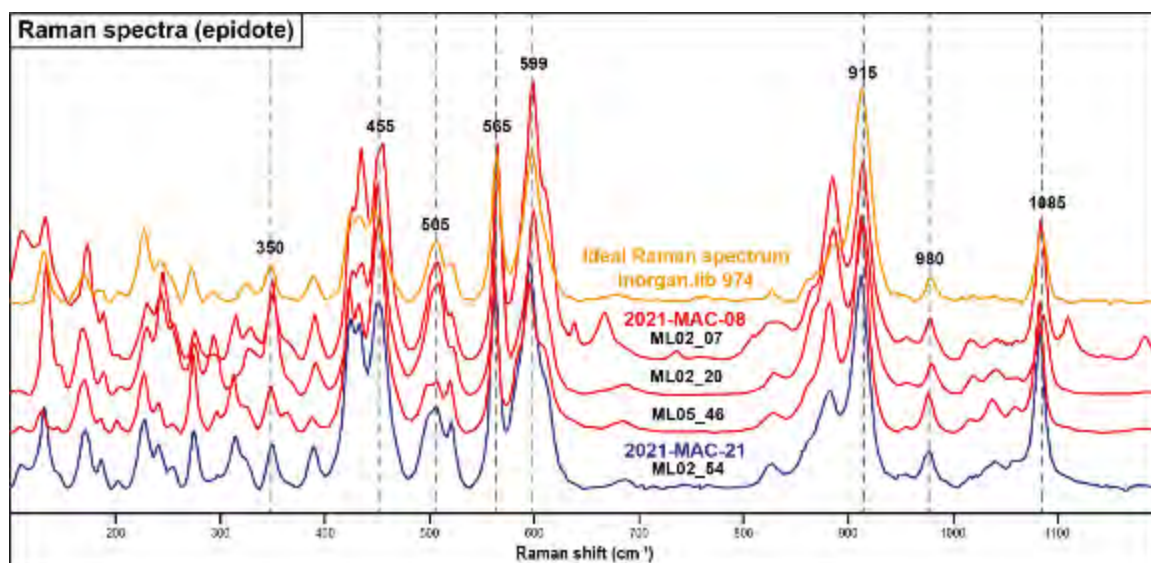


Figure 34. Raman results for epidote.

### Muscovite

The spectra of the studied muscovite grains are characterized by the existence of two main peaks at 701 and 1,111  $\text{cm}^{-1}$ , which are common spectral patterns in phyllosilicates (Wang et al. 2015). Other important peaks are registered at 263 and 414  $\text{cm}^{-1}$  (Fig. 35).

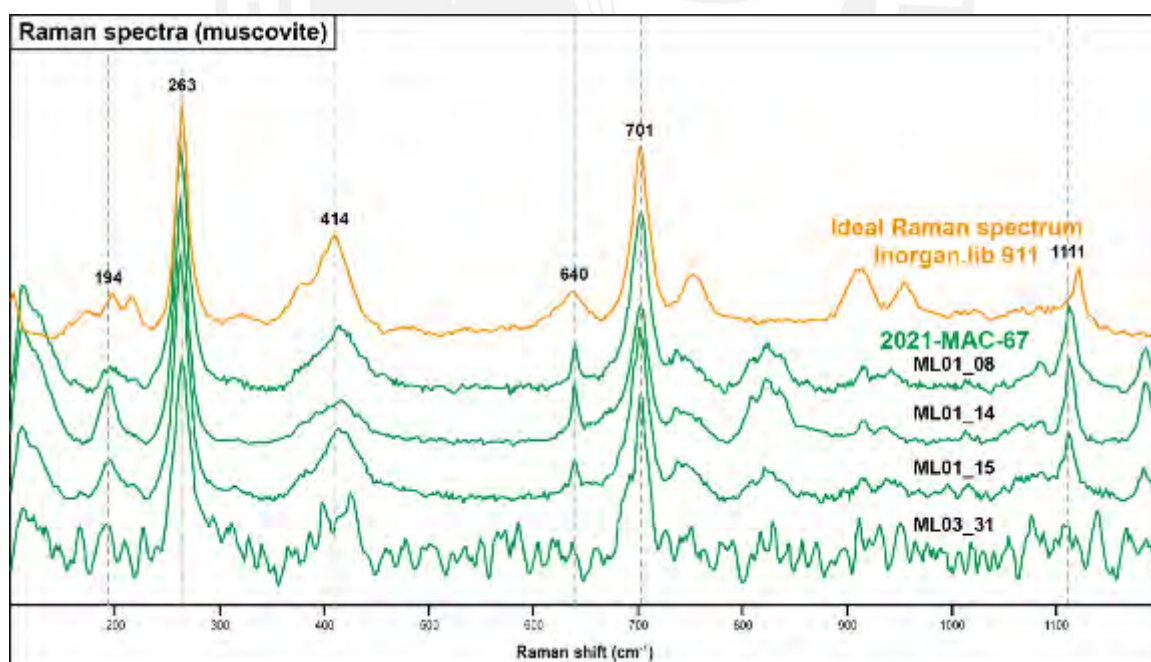


Figure 35. Raman results for muscovite.

### Titanite

Titanite Raman spectra show broad bands at 255, 316, 422, 544, and 611  $\text{cm}^{-1}$ . These bands strongly agree with the titanite spectrum from the WiRE database (Fig. 36).

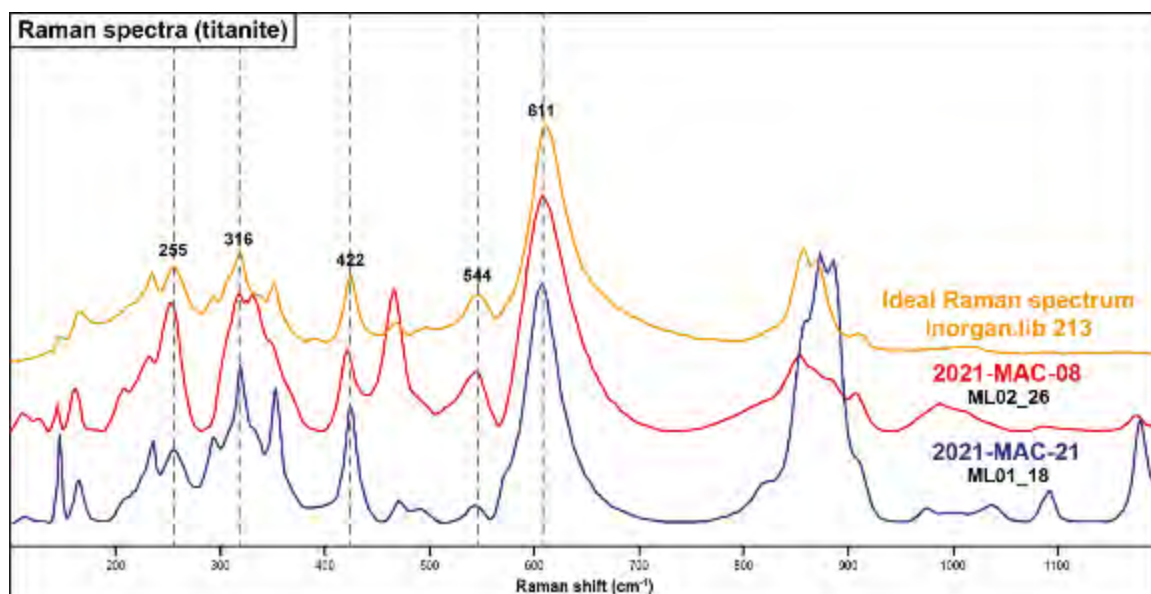


Figure 36. Raman results for titanite.

### Topaz

The spectra obtained for topaz are comparable to those found in the WiRE database (Fig. 37). The main intense bands observed were located at 236, 264, and 284  $\text{cm}^{-1}$ . Other important bands were registered at 453 and 923  $\text{cm}^{-1}$ .

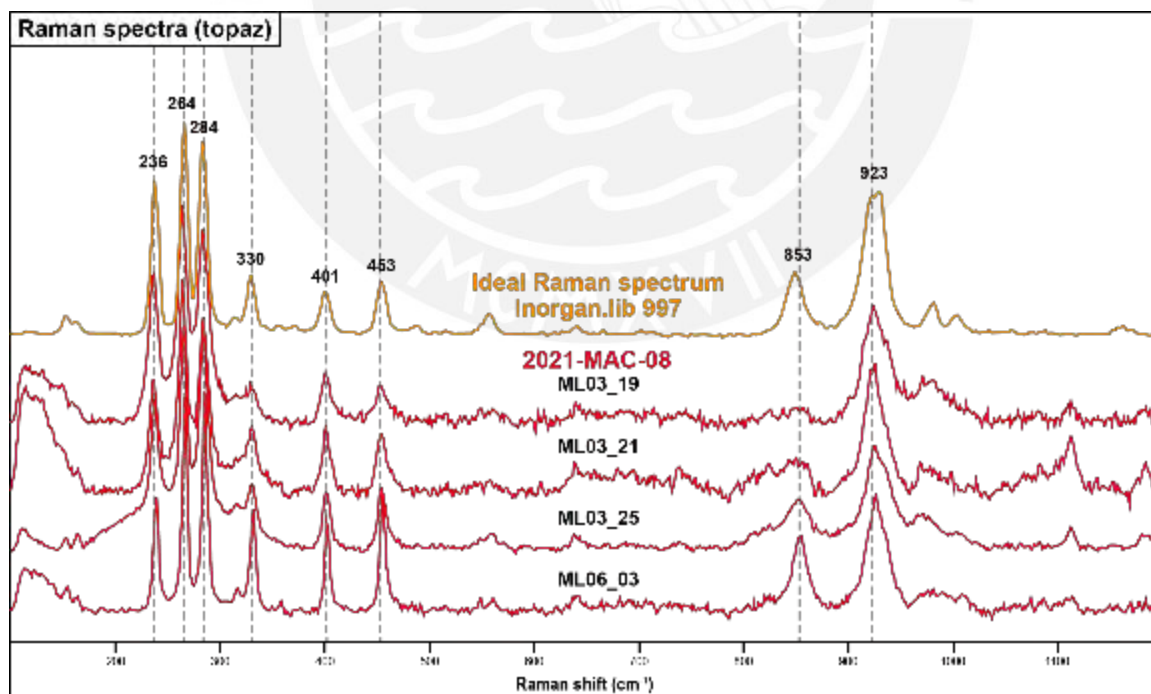


Figure 37. Raman results for topaz.

### Tourmaline

Tourmaline spectra are characterized by one intense peak at  $368\text{ cm}^{-1}$  and two other significant peaks at  $775$  and  $1,054\text{ cm}^{-1}$  (Fig. 38). These Raman spectral features match the tourmaline spectrum from the WiRE database.

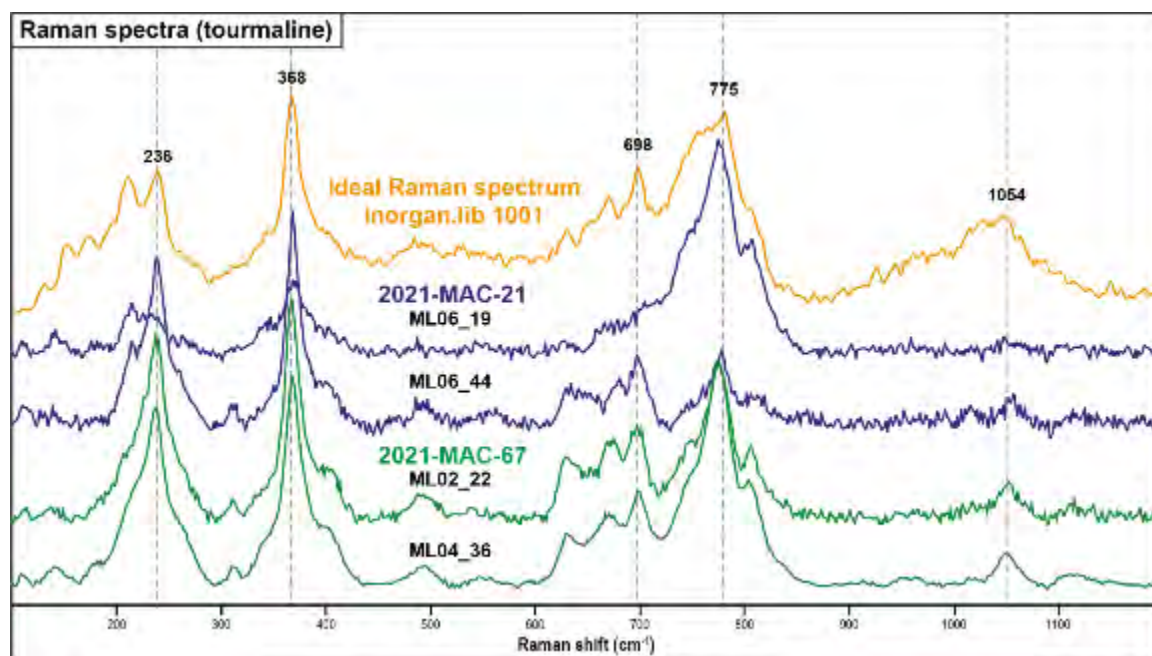


Figure 38. Raman results for tourmaline.

### Zircon

Zircon grains from the 3 samples were analyzed, which agreed with the ideal Raman spectra for zircon and showed similar band values compared to the spectrum from WiRE database. Dominant peaks were located at 202, 225, 356, 439, 972, and  $1,007\text{ cm}^{-1}$  (Fig. 39). The results also confirmed the presence of smaller zircon grains (less than  $20\text{ }\mu\text{m}$ ) in titanium oxides, apatite, and xenotime-Y (Fig. 40). On the other hand, the presence of apatite inclusions in zircons was also confirmed (Fig. 41).

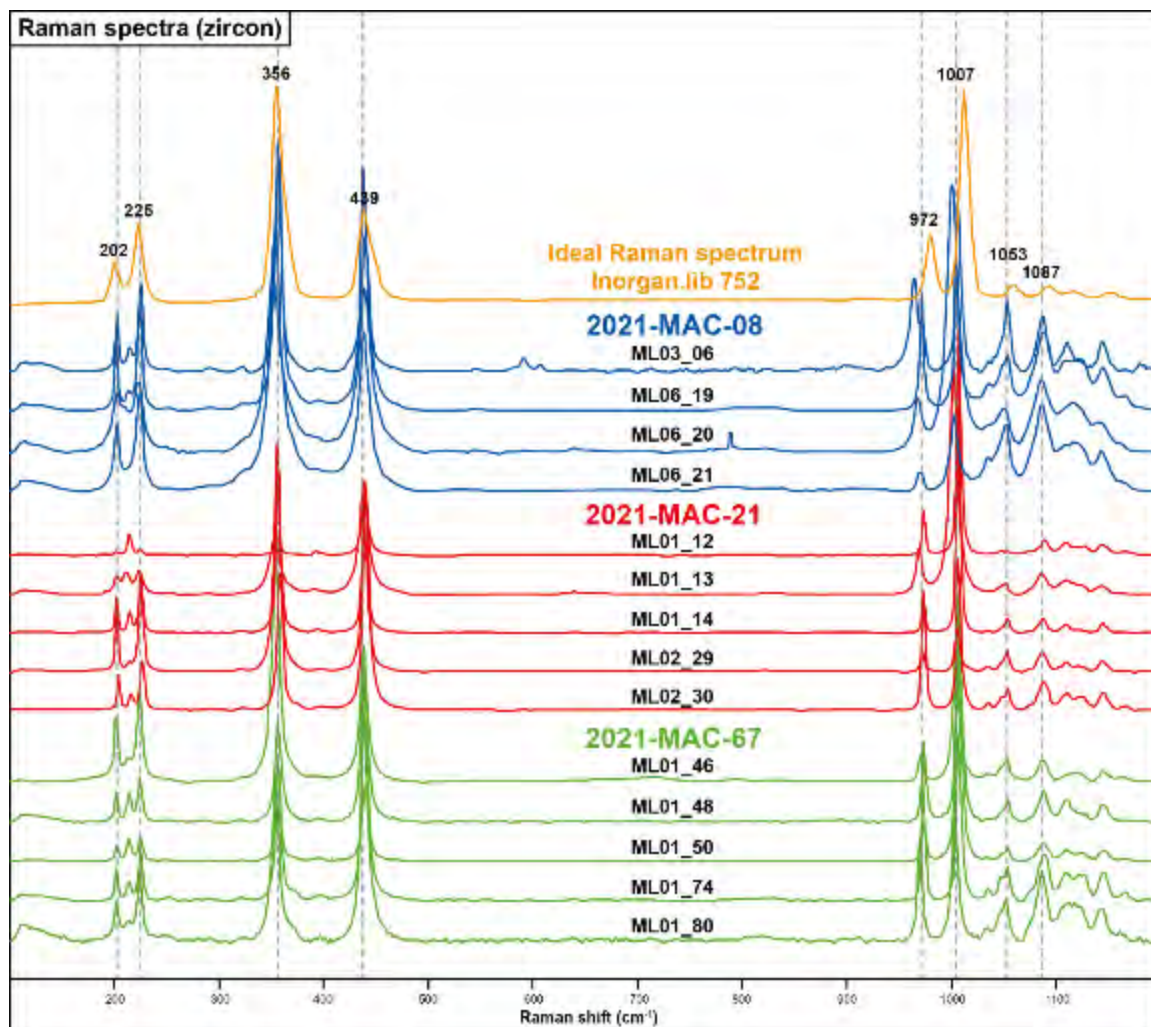


Figure 39. Raman results for zircon crystals.

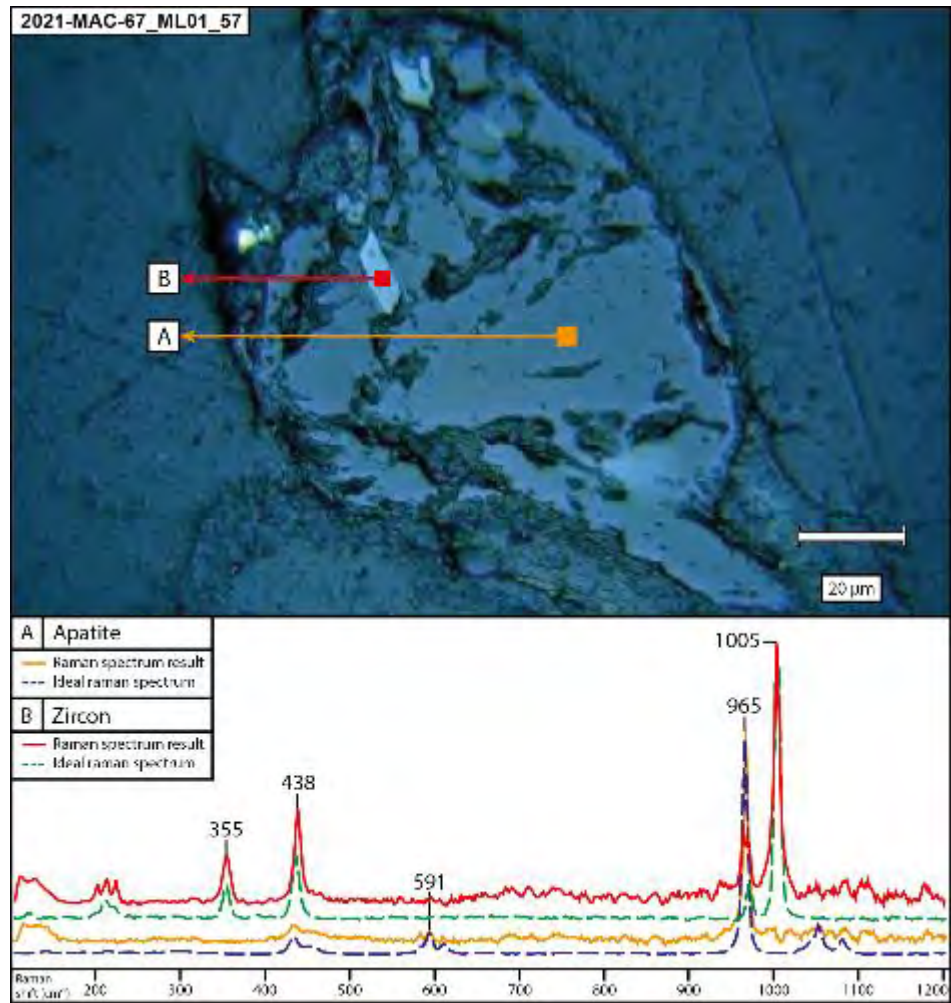


Figure 40. Prismatic zircon (bright) in apatite crystal (dark).

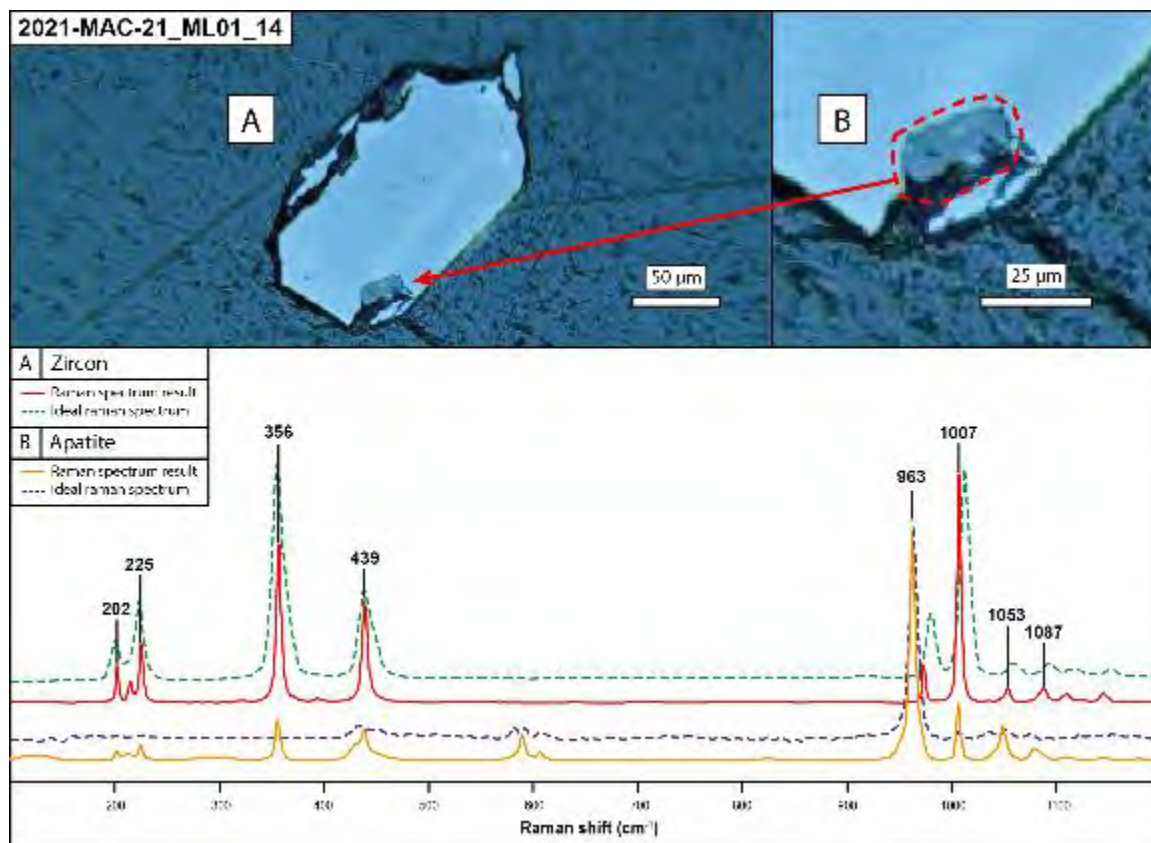


Figure 41. Apatite inclusion (dark) in a zircon crystal (bright).

#### 4.3.2. Ti-rich oxides

##### Anatase

Anatase grains were only found in sample 2021-MAC-67. This mineral species is well characterized by Raman spectroscopy since the four peaks at 149, 392, 516, and 639 cm<sup>-1</sup> are distinctive and match the anatase spectrum on the WiRE database (Fig. 42).

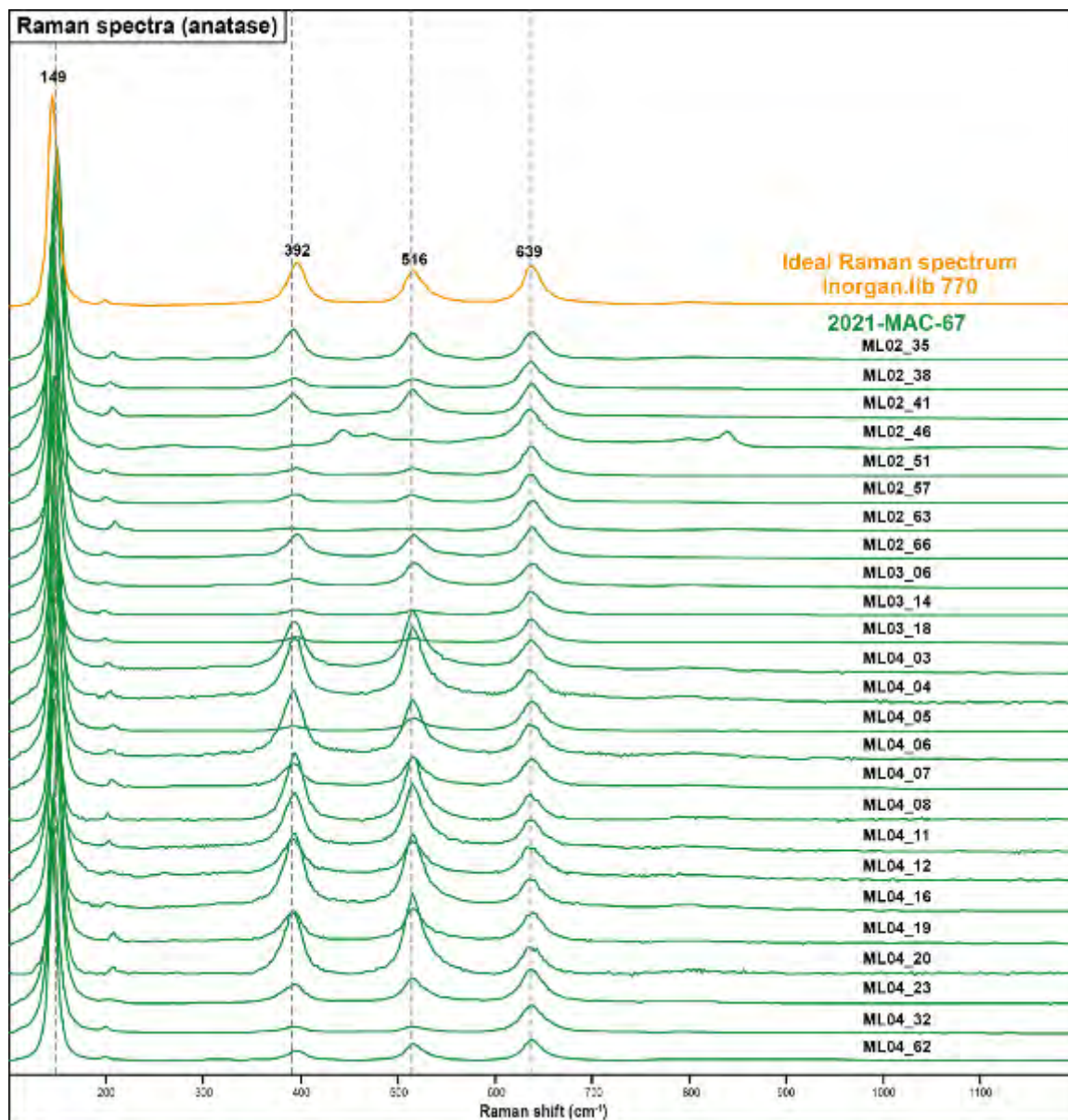


Figure 42. Raman results for anatase.

### Rutile

Raman spectra of Ti-oxide grains likely corresponding to rutile separated from the three samples can be separated into three different spectrum types. The first is characterized by two broad peaks at 446 and 609  $\text{cm}^{-1}$ , which agree with two of the four Raman vibration characteristic peaks of rutile (Fig. 43; Guo et al. 2006). The second type is only observed in grains from sample 2021-MAC-08 and is characterized by three peaks at 426, 627, and 836  $\text{cm}^{-1}$ , which vaguely match Raman vibration characteristic peaks (Fig. 44) and probably evidence an atypical rutile phase. Likewise, the third type exhibits four different

peaks at 304, 485, 625, and 841  $\text{cm}^{-1}$ , which does not accurately match the rutile spectrum from the WiRE database and also probably evidence an atypical rutile phase (Fig. 45).

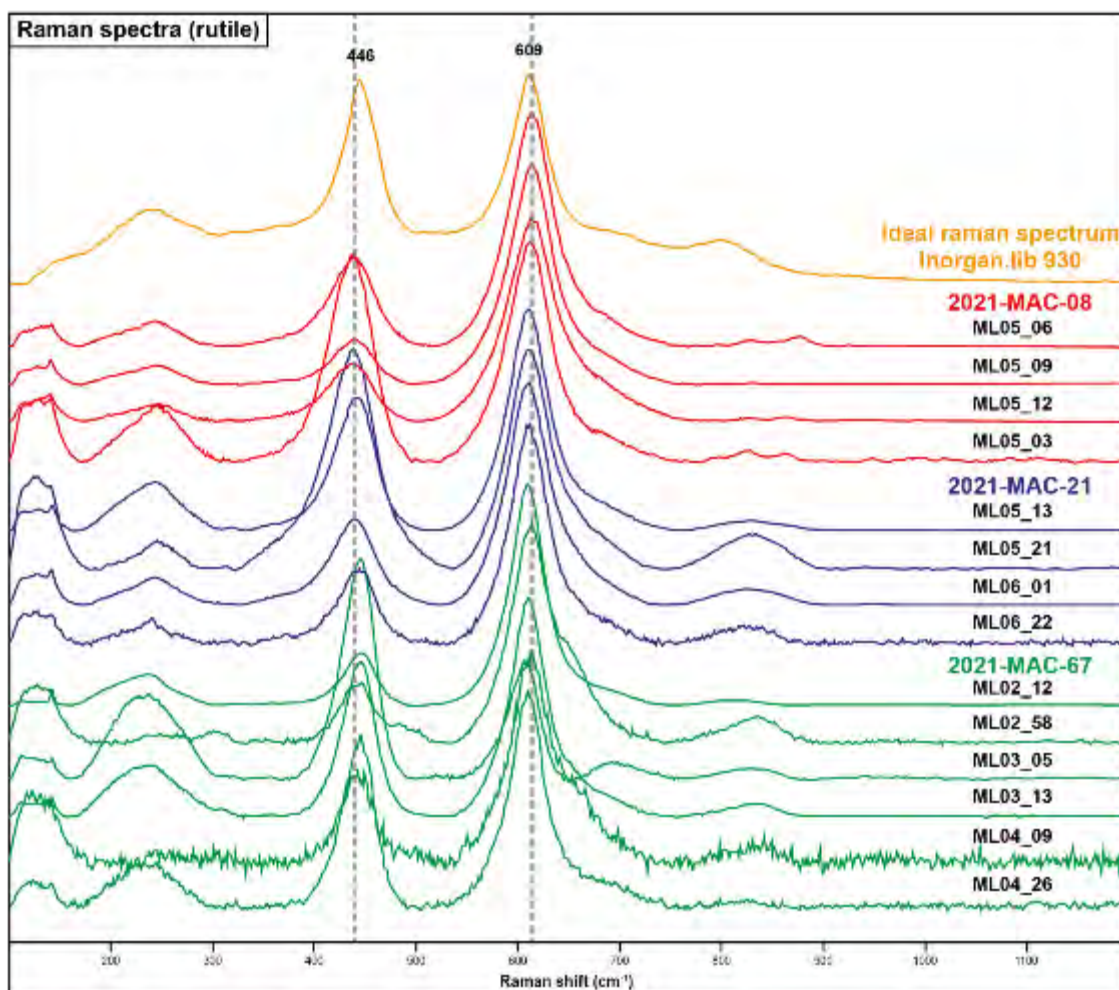


Figure 43. Raman results for type-1 rutile.

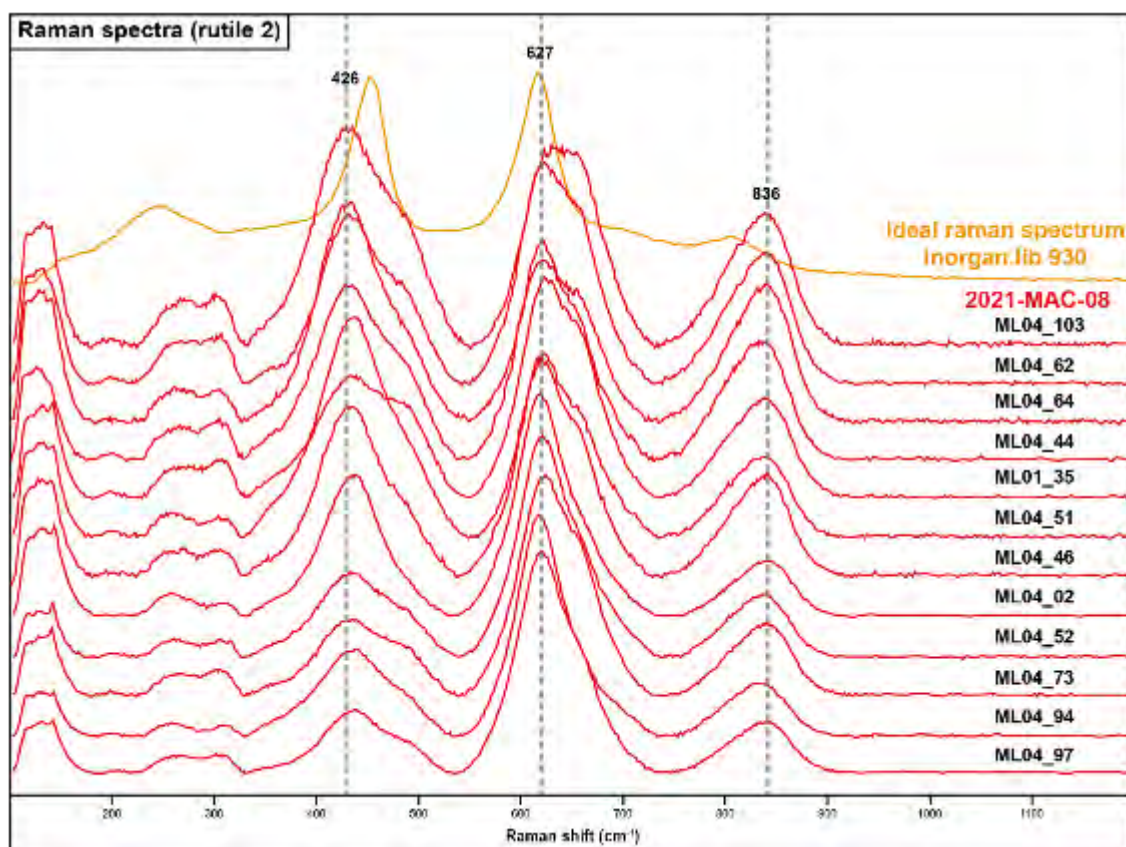


Figure 44. Raman results for type-2 rutile.

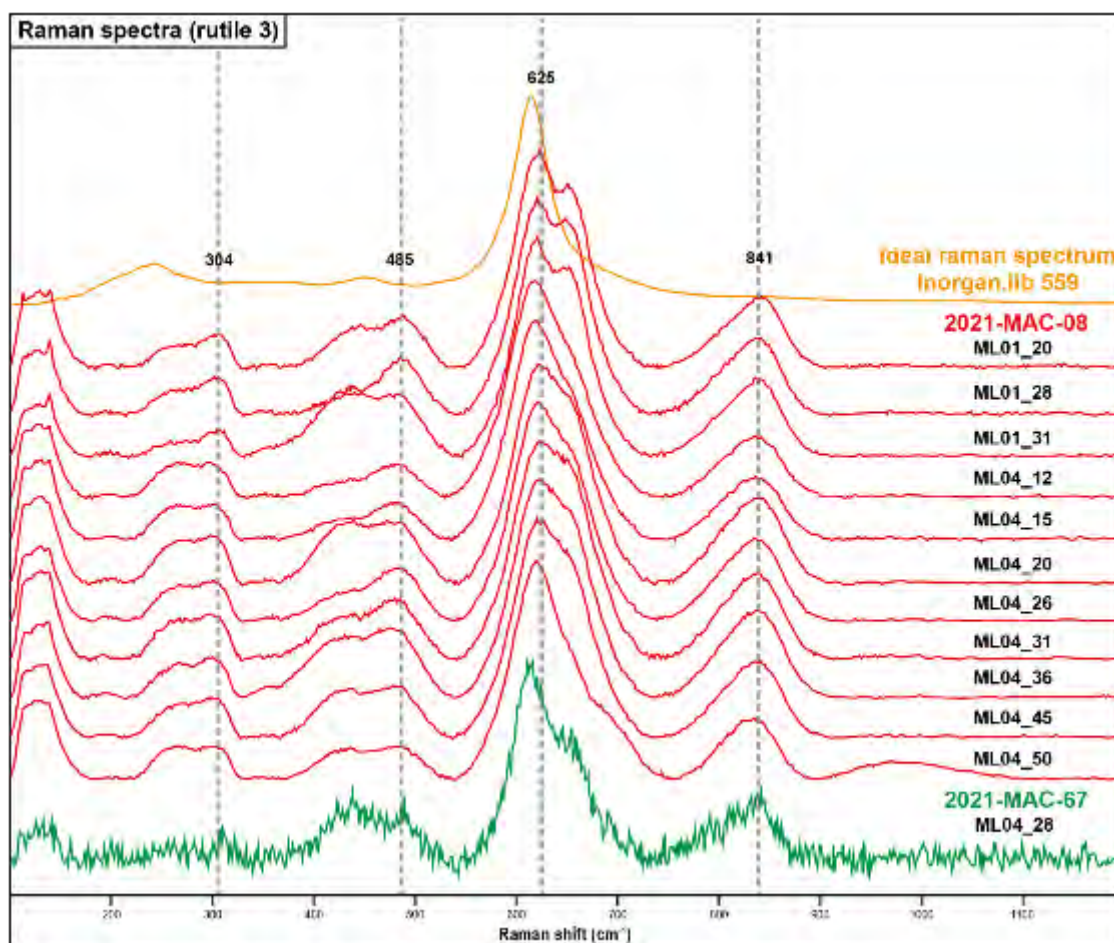


Figure 45. Raman results for type-3 rutile.

### Unidentified Ti-rich oxide

Raman spectra for some Ti-rich oxides exclusively found in sample 2021-MAC-08 have no accurate coincidences with any available Raman spectra in the WiRE database nor the RRUFF database. However, it could tentatively be associated with rutile spectra with slightly displaced (inaccurate) position of peaks or missing peaks. Three different groups sharing some similar peaks around 432, 650, and 836  $\text{cm}^{-1}$  were differentiated. The first type exhibits three distinctive broad and rod-shaped peaks at 427, 651, and 837  $\text{cm}^{-1}$  (Fig. 46). The second type shows four important asymmetric broad peaks at 438, 620, 650, and 837  $\text{cm}^{-1}$  (Fig. 47). The third type consists of five important and broad peaks located at 254, 432, 614, 686, and 836  $\text{cm}^{-1}$  (Fig. 48).

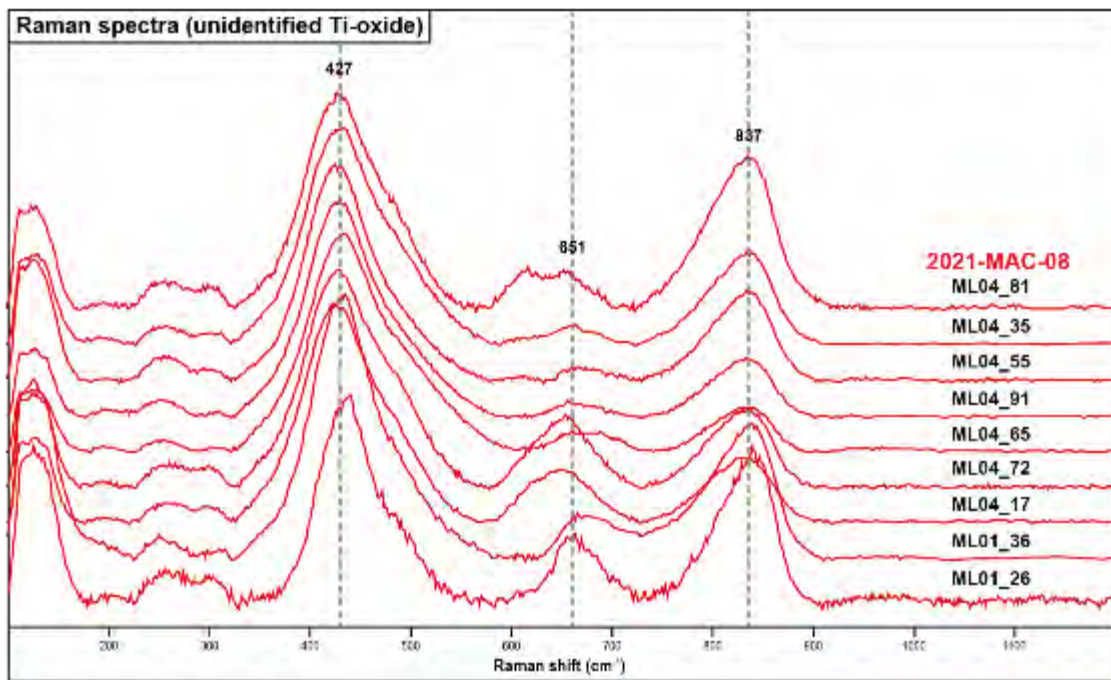


Figure 46. Raman results for type-1 unidentified Ti-rich oxide.

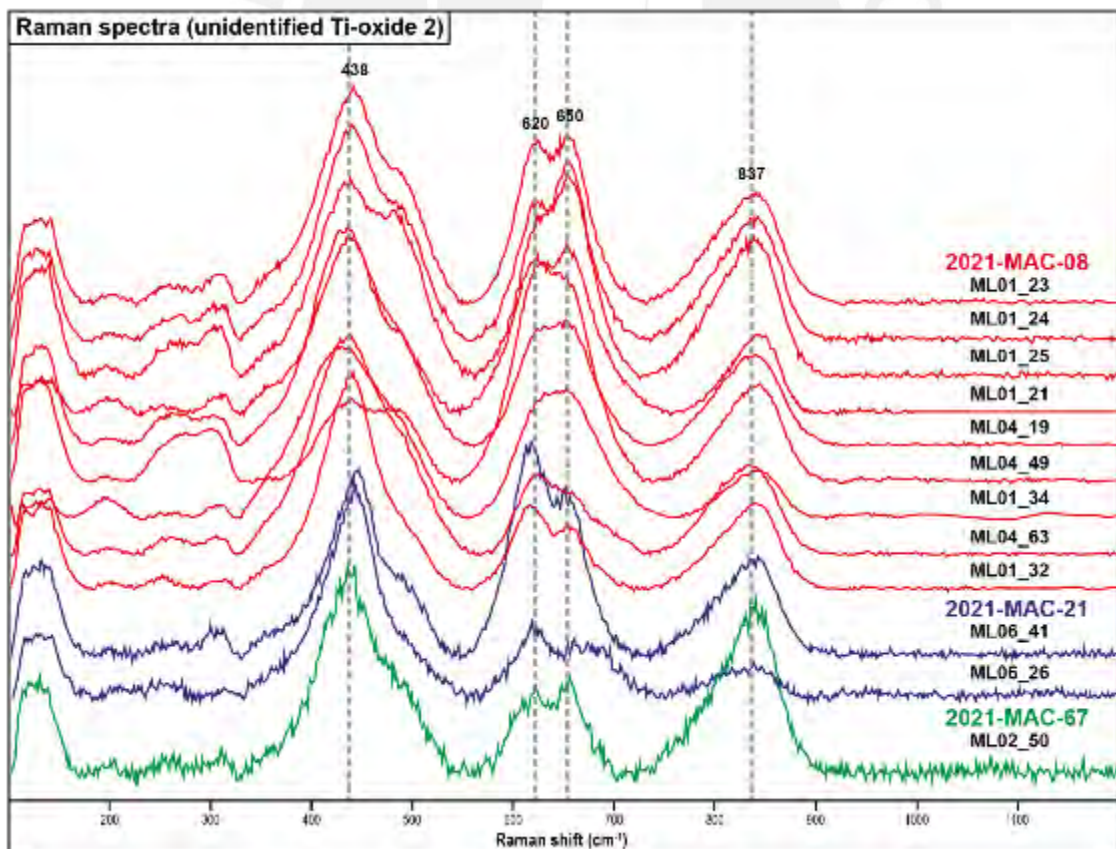


Figure 47. Raman results for type-2 unidentified Ti-rich oxide.

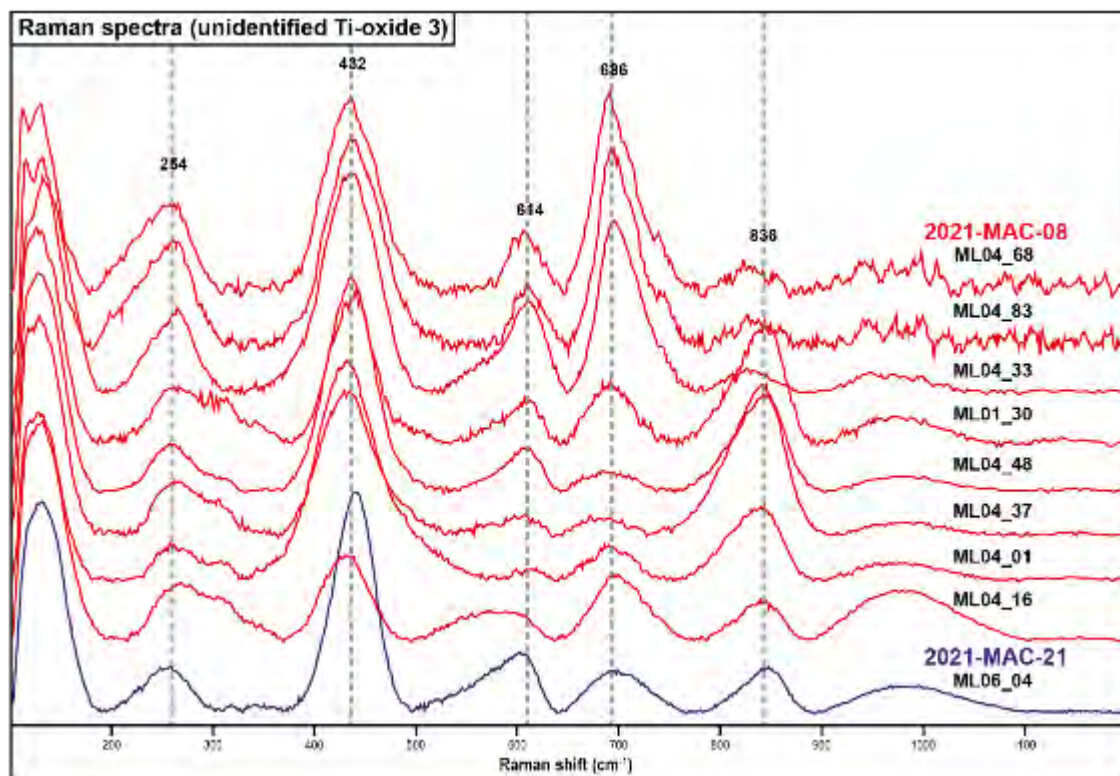


Figure 48. Raman results for type-3 unidentified Ti-rich oxide.

#### 4.3.3. Sn-minerals

##### Cassiterite

The main cassiterite bands are consistent with reference data in the WiRE database. Raman spectra show important peaks at 633, 474, and 775 cm<sup>-1</sup> (Fig. 49).

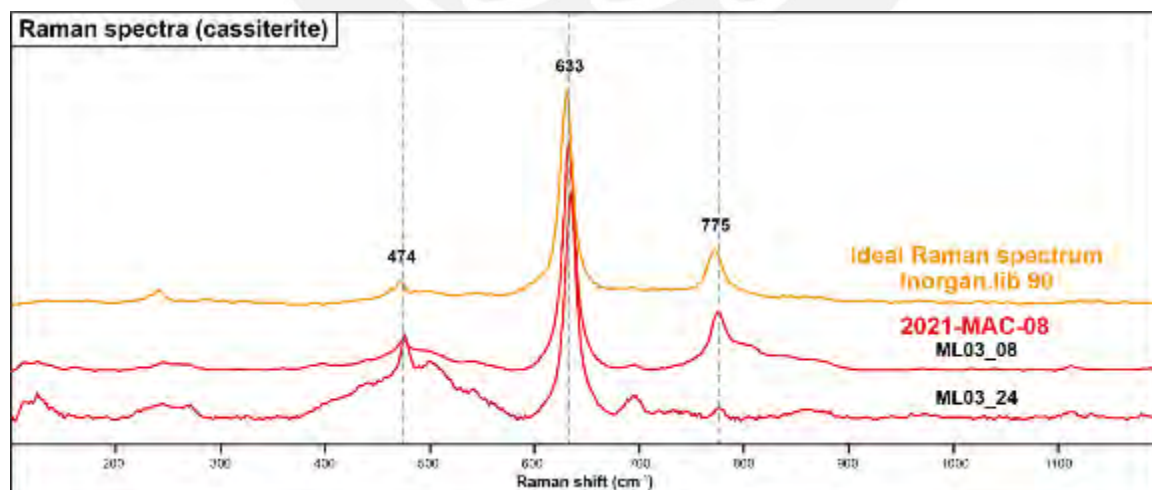


Figure 49. Raman results for cassiterite.

### Wickmanite

Crystals from sample 2021-MAC-67 with high contents of Sn and Mn according to EDS analysis matched the typical Raman spectrum for wickmanite, a rare Sn-Mn hydroxide species  $[\text{Mn}^{+2}\text{Sn}^{+4}(\text{OH})_6]$ , obtained from the RRUFF database (Fig. 50). Three bands were noticed at 293, 375, and 596  $\text{cm}^{-1}$ .

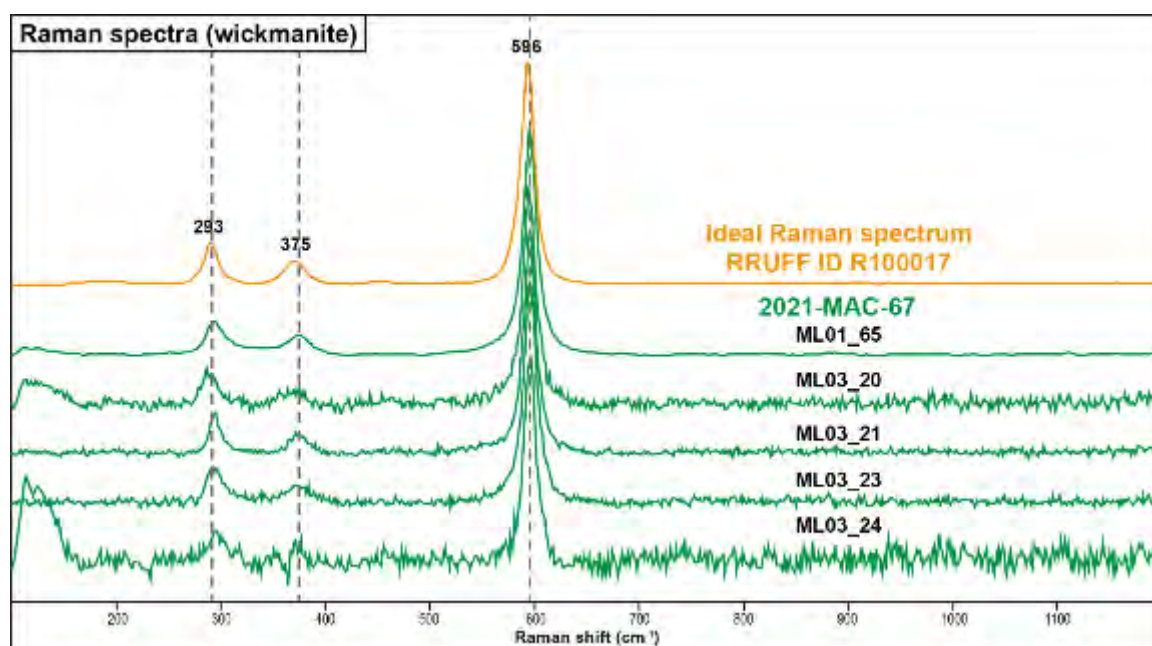


Figure 50. Raman results for wickmanite.

#### 4.3.4. Fe-oxides

### Goethite

Significant features in Raman spectra are three important peaks at 215, 278, and 392  $\text{cm}^{-1}$ . The goethite spectrum matches the information from the WiRE database for this mineral (Fig. 51).

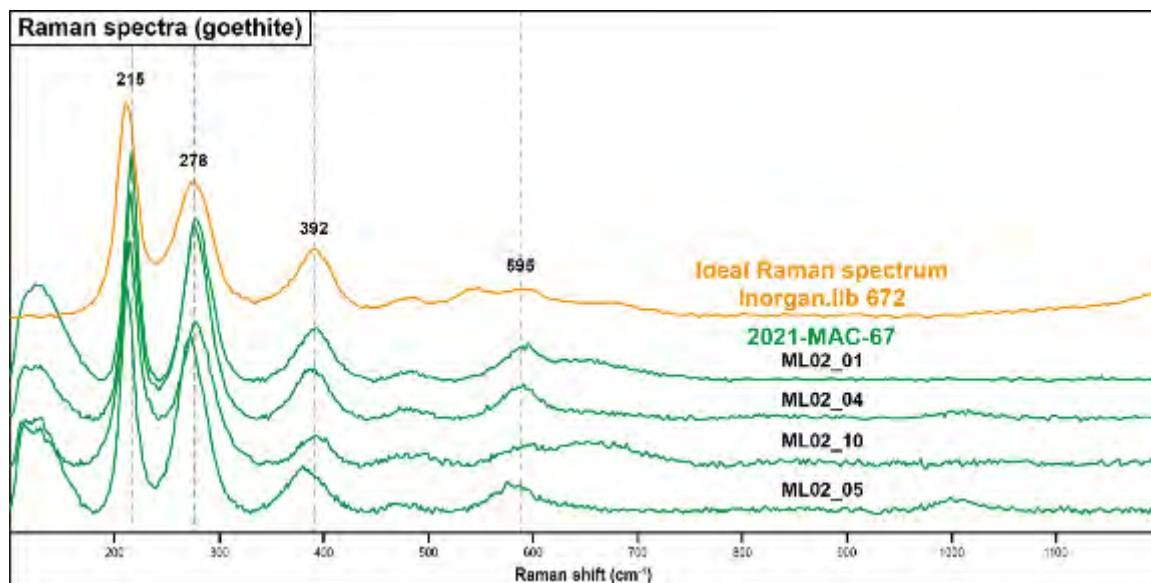


Figure 51. Raman results for goethite.

### Hematite

A single hematite grain was found in sample 2021-MAC-21, with typical rod-shaped peaks located at 228, 294, 415, and 501  $\text{cm}^{-1}$ . The obtained Raman spectrum is consistent with reference data on the WiRE database (Fig. 52).

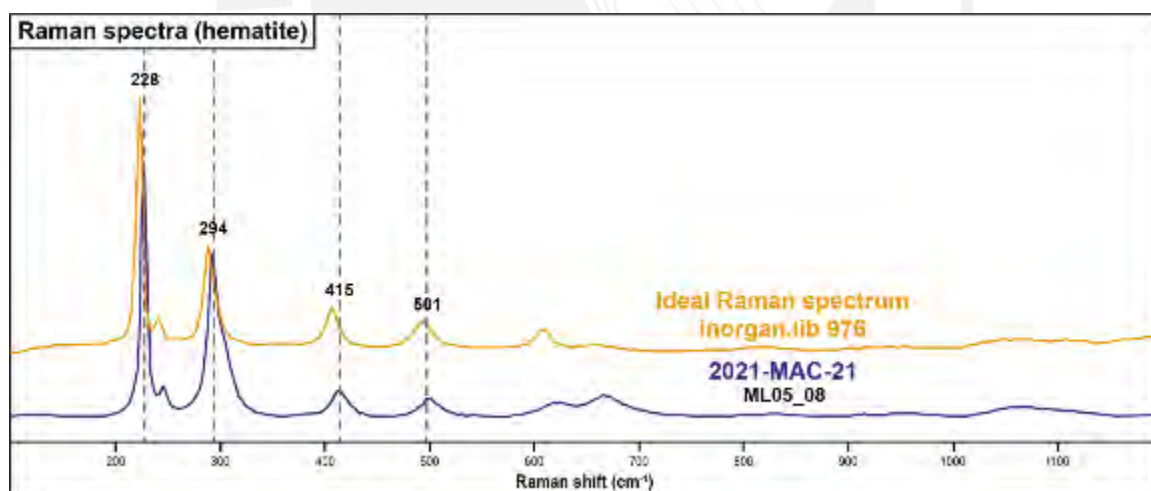


Figure 52. Raman results for hematite.

### Ilmenite

Raman spectrum of ilmenite exhibits three indicative bands at 253, 334, and 681  $\text{cm}^{-1}$ . Some extra weak bands occur at 454 and 592  $\text{cm}^{-1}$ . Raman patterns of these samples agree with the ilmenite spectrum from the WiRE database (Fig. 53).

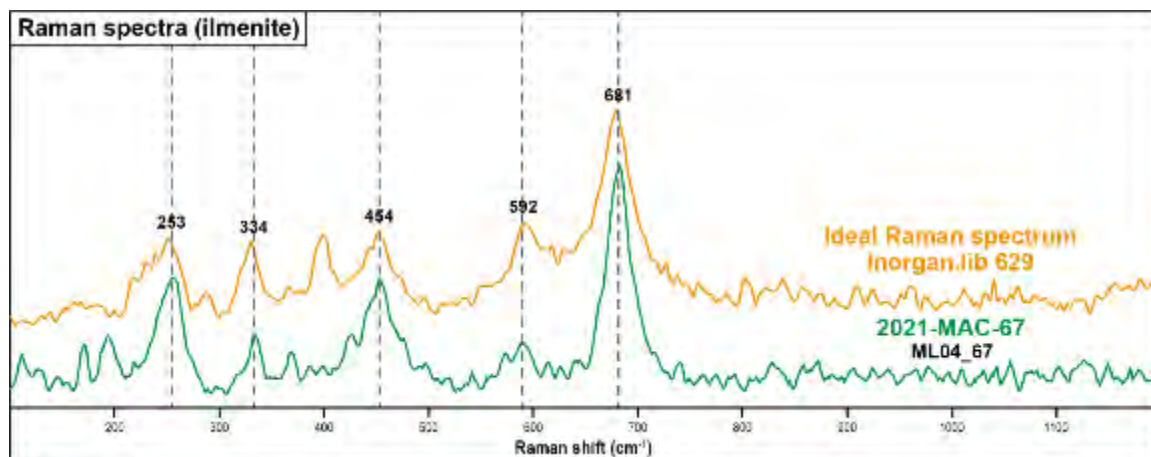


Figure 53. Raman results for ilmenite.

### Magnetite

Presence of magnetite in sample 2021-MAC-21 is confirmed by matching the spectral data reported on the WiRE database (Fig. 54). Important peaks were registered at 545 and 665  $\text{cm}^{-1}$ .

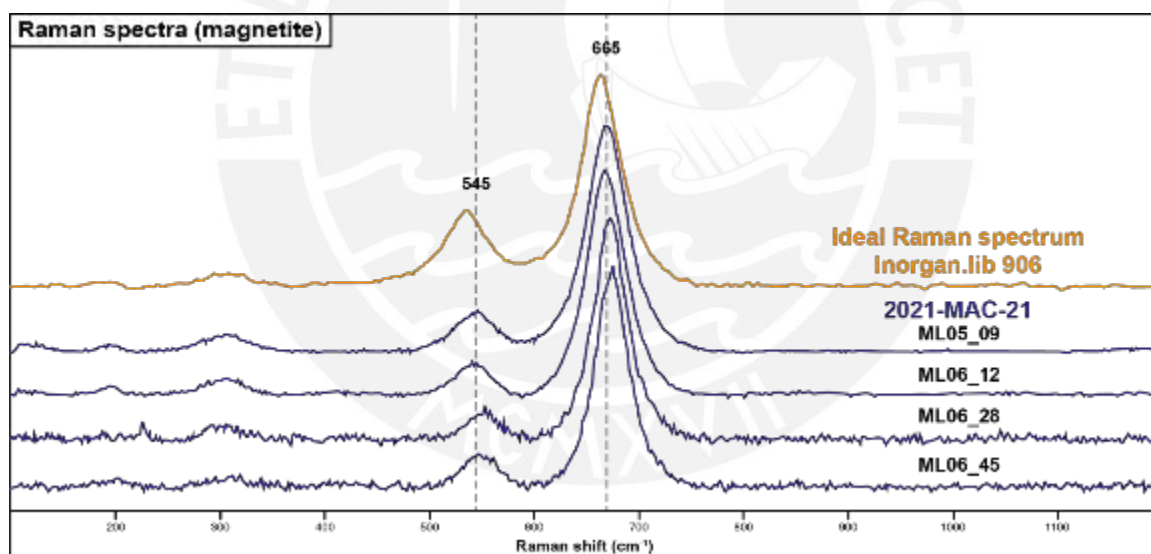


Figure 54. Raman results for magnetite.

### 4.3.5. Borates

#### Jeremejevite

Raman results consistent with jeremejevite  $[\text{Al}_6(\text{BO}_3)_5(\text{F},\text{OH})_3]$  were detected only in grains from the sample 2021-MAC-08 (Fig. 55). Intense high peaks were detected at 176, 231, 326, 371, 960, and 1,066  $\text{cm}^{-1}$ , which coincide with jeremejevite data available in RRUFF.

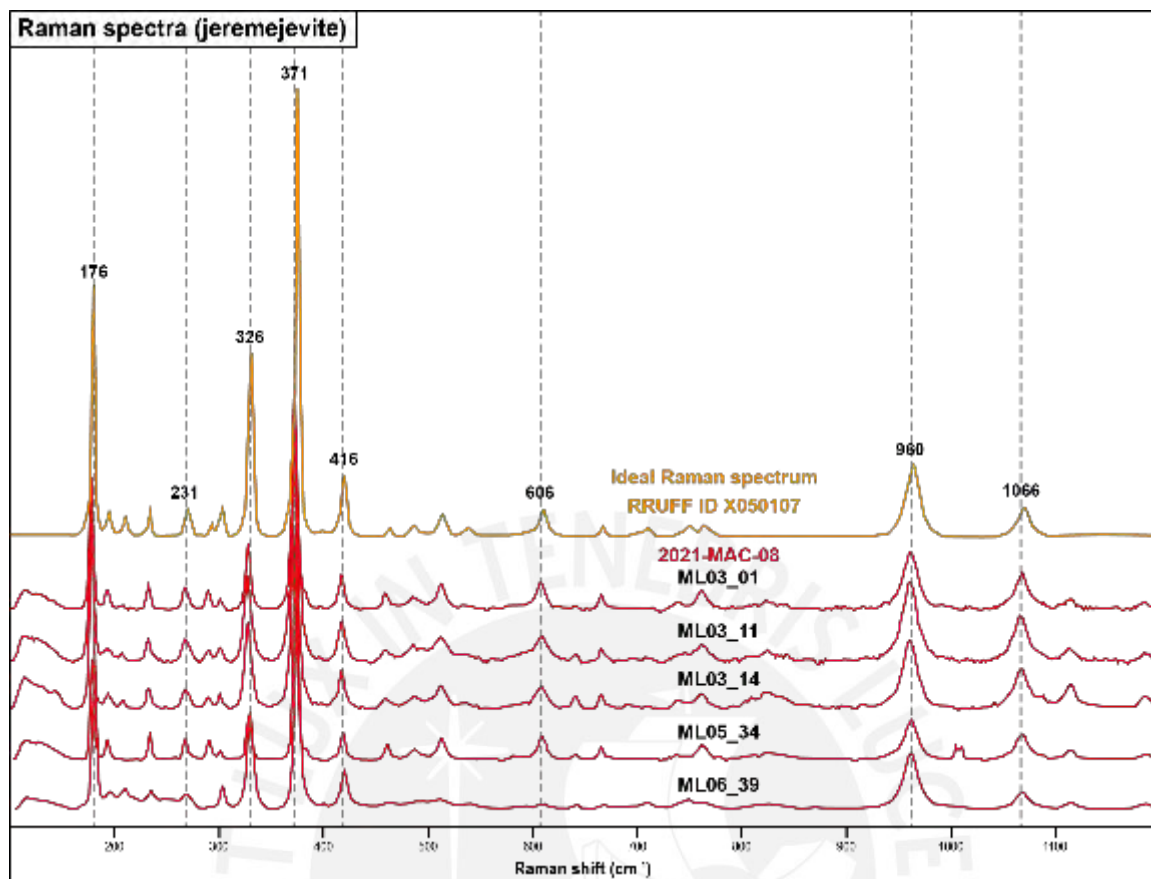


Figure 55. Raman results for jeremejevite.

#### 4.3.6. Phosphates

##### Apatite

Raman spectroscopy results for apatite revealed a well-defined band at 964 cm<sup>-1</sup> which coincides with the one observed in apatite from the WiRE database (Fig. 56).

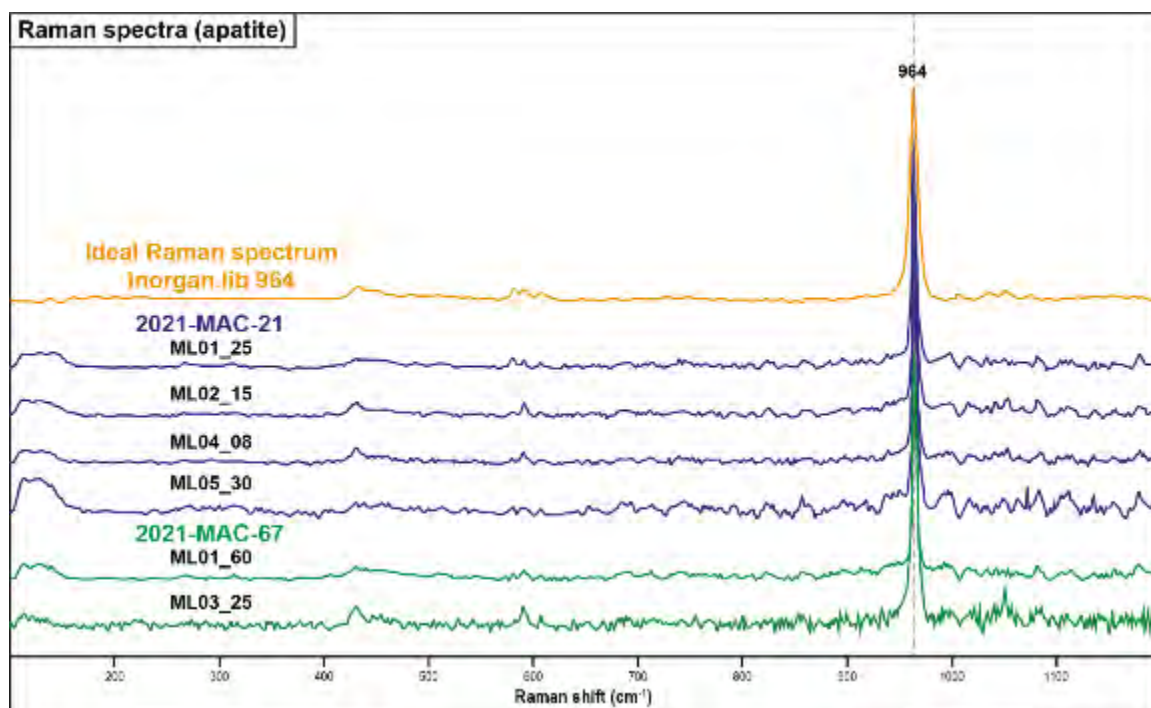


Figure 56. Raman results for apatite.

### Monazite-Ce

Monazite grains were analyzed and agreed with the respective ideal Raman spectra (Fig. 57). Important bands were registered at 225, 465, and 974  $\text{cm}^{-1}$ , which are consistent with monazite-Ce reference data in the WiRE database. Moreover, the existence of mineral apatite inclusions (around 10  $\mu\text{m}$  in length) could be verified (Fig. 58).

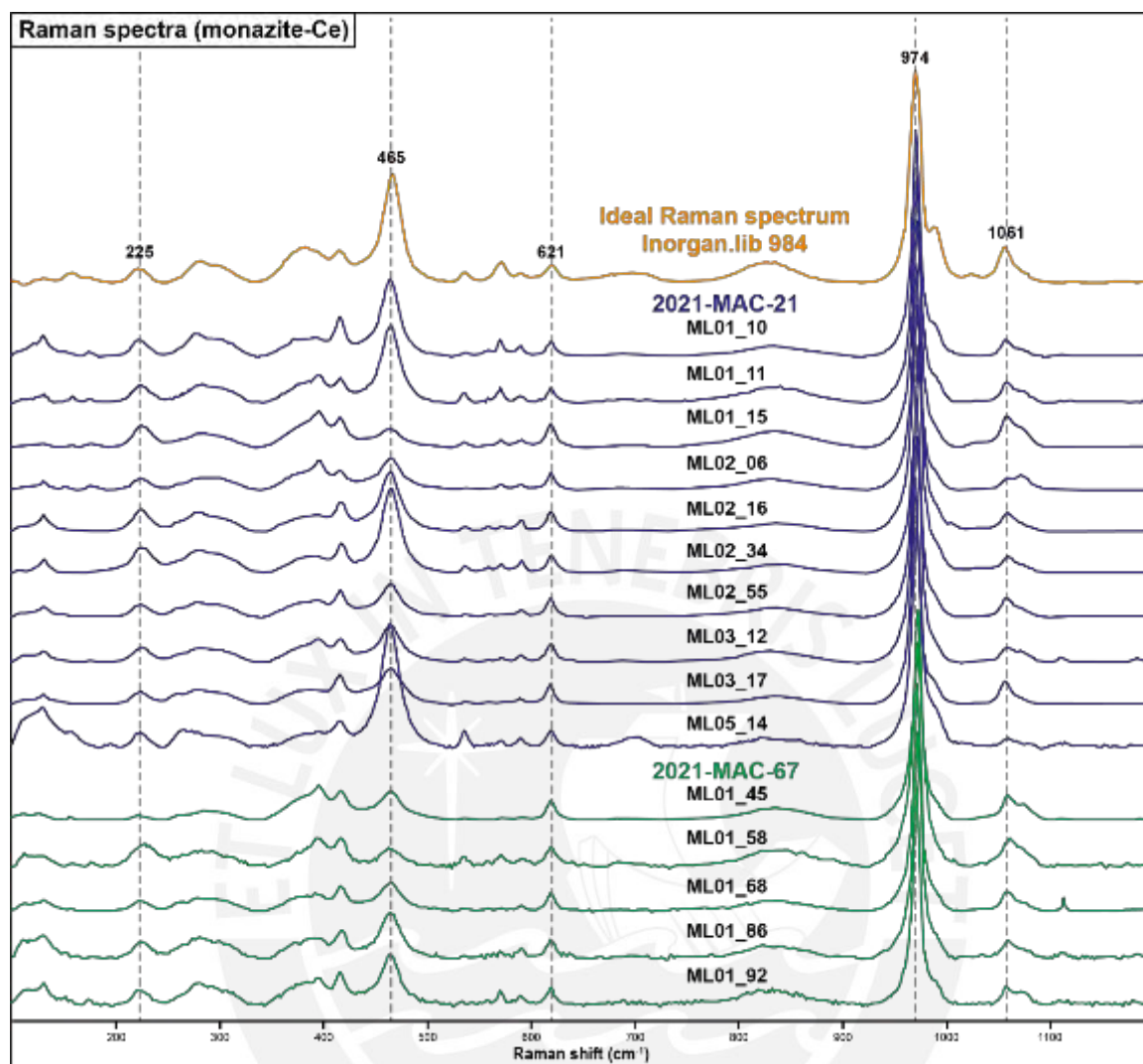


Figure 57. Raman results for monazite-Ce.

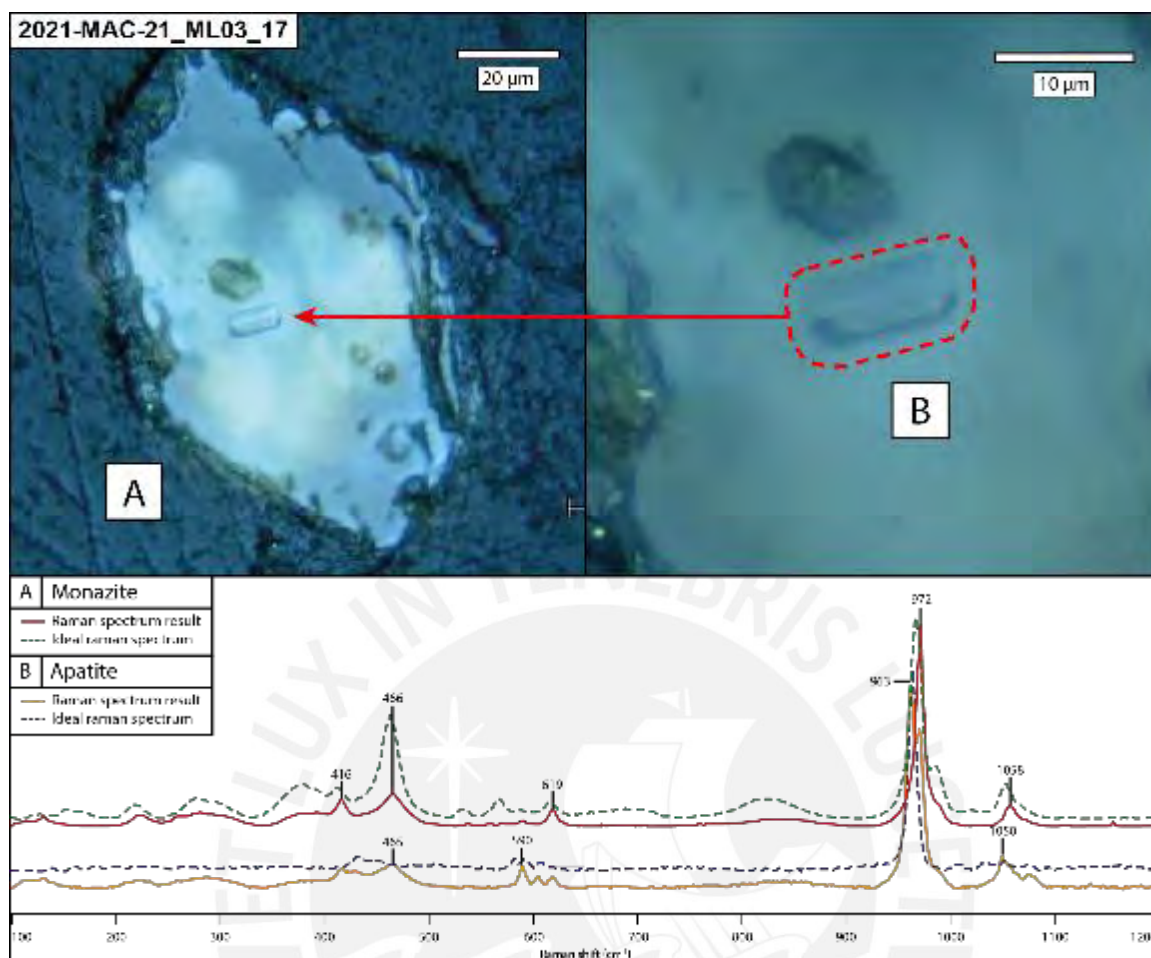


Figure 58. Apatite inclusion (dark) in a monazite-Ce crystal (bright).

### Xenotime-Y

Raman spectra of xenotime-Y were dominated by three intense bands located at 997, 1,116, and 1,162  $\text{cm}^{-1}$ , which matches the standard spectrum of xenotime-Y on the WiRE database (Fig. 59).

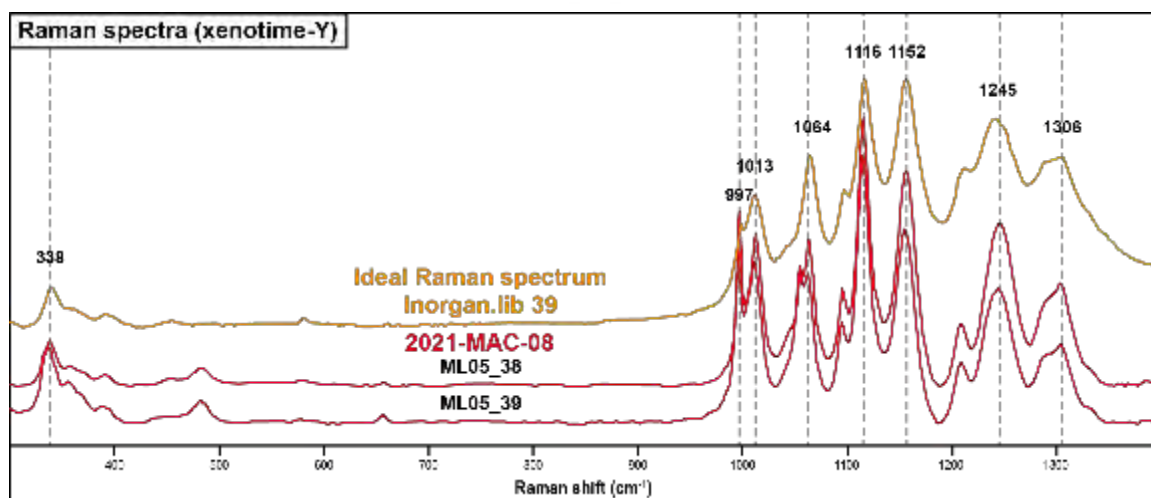


Figure 59. Raman results for xenotime-Y.

#### 4.3.7. Sulfides

##### Pyrite

Pyrite spectra matched the reference data from the WiRE database (Fig. 60). Three distinctive peaks could be resolved in the spectra, located at 347, 384, and 436  $\text{cm}^{-1}$ .

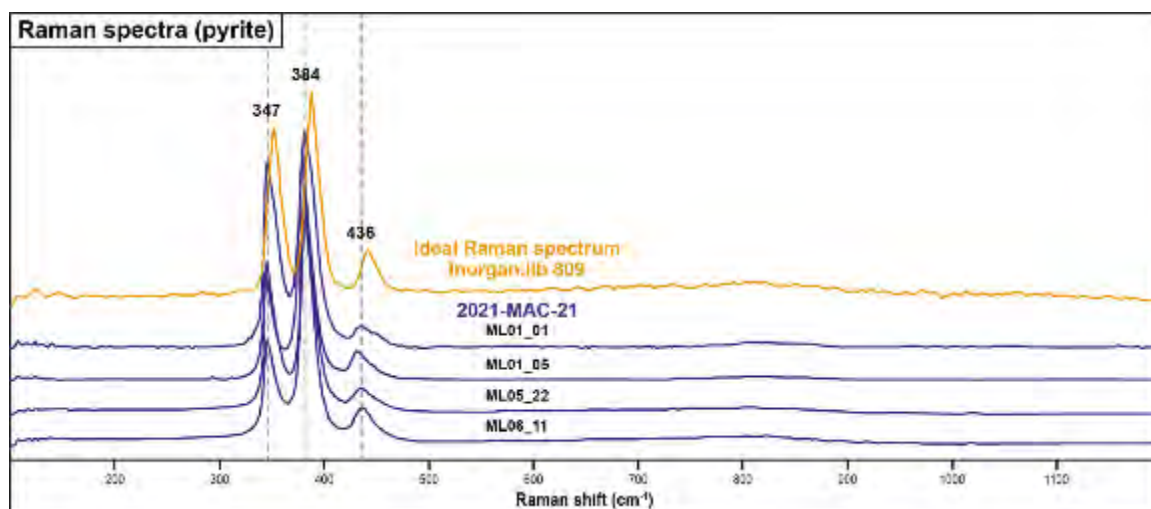
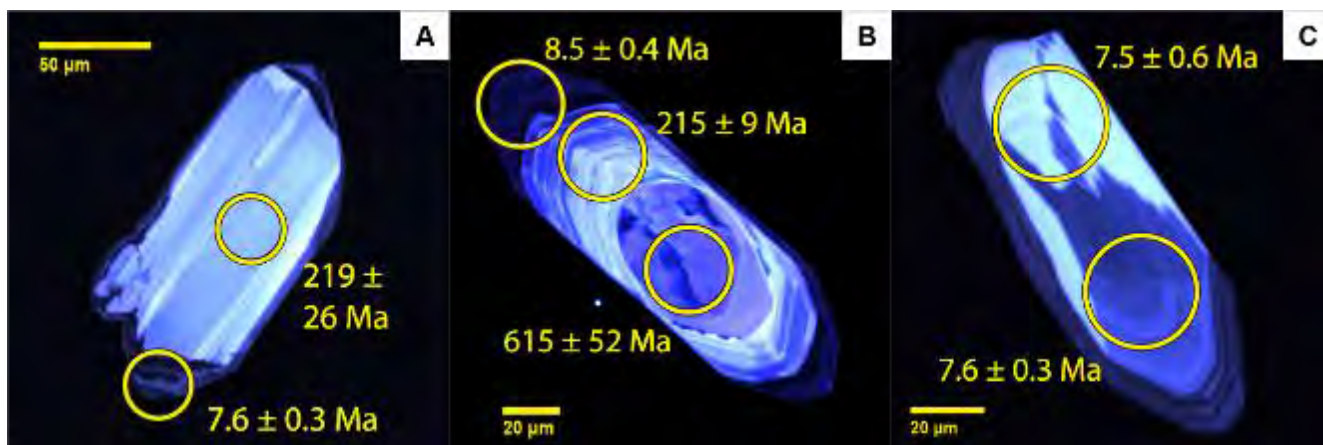


Figure 60. Raman results for pyrite.

#### 4.4. Geochronology

Zircons from sample 21-MAC-21 were subjected to cathodoluminescence analyses (Fig. 61). Figure 61A exhibits a subhedral zircon with a distinct high CL intensity core showing parallel zoning surrounded by a low-CL intensity rim. The core yielded a date of  $219 \pm 26$  Ma while the rim yielded a date of  $7.6 \pm 0.3$  Ma. The zircon grain shown in Figure 61B is euhedral and shows complex zoning including an ovoid resorbed core, which yielded a date of  $615 \pm 52$  Ma, overgrown by an oscillatory-zoned mantle with relatively high CL intensity yielding a date of  $215 \pm 9$  Ma. Finally, a low-CL intensity rim yielded a date of  $8.5 \pm 0.4$  Ma. Figure 61C illustrates a subhedral zircon with a resorbed core with poor CL intensity and subtle zoning yielding a date of  $7.6 \pm 0.6$  Ma, overgrown by an irregular polygonal, high-CL intensity mantle yielding a date of  $7.5 \pm 0.3$  Ma, and a thin and irregular, low-CL intensity rim.



**Figure 61.** Cathodoluminescence (CL) images of zircon grains from sample 21-MAC-21. A: Subhedral zircon with high-CL intensity core surrounded by a low-CL intensity rim. B: Euhedral zircon with a reabsorbed core, oscillatory-zoning mantle, and low-CL intensity rim. C: Zircon with euhedral habit with a resorbed and zoned core truncated by a high-CL convolute mantle and a low-CL intensity rim. Yellow circles show the location of the point analyses with the corresponding U-Pb dates.

**Figure 62** shows a Tera-Wasserburg U-Pb concordia diagram for analyzed zircon grains from sample 21-MAC-21 ( $n = 48$ ). A set of zircon datapoints are concordant and yield an average  $^{206}\text{Pb}/^{238}\text{U}$  date of  $7.36 \pm 0.1$  Ma. The rest of the analyses are discordant. A set of these discordant analyses yield a lower intercept discordia date of  $222 \pm 3$  Ma. The rest of the analyses define a mixing trend between ca. 222 Ma (i.e., cores) and ca. 7 Ma (i.e., rims; **Fig. 61**). Noteworthy, the zircon shown in **Figure 61B** has a core of apparent  $615 \pm 52$  Ma age surrounded by a mantle of  $215 \pm 9$  Ma and a rim of  $8.5 \pm 0.4$  Ma ages; however, the older date is discordant and is included in the discordia line yielding the lower intercept date at  $222 \pm 3$  Ma.

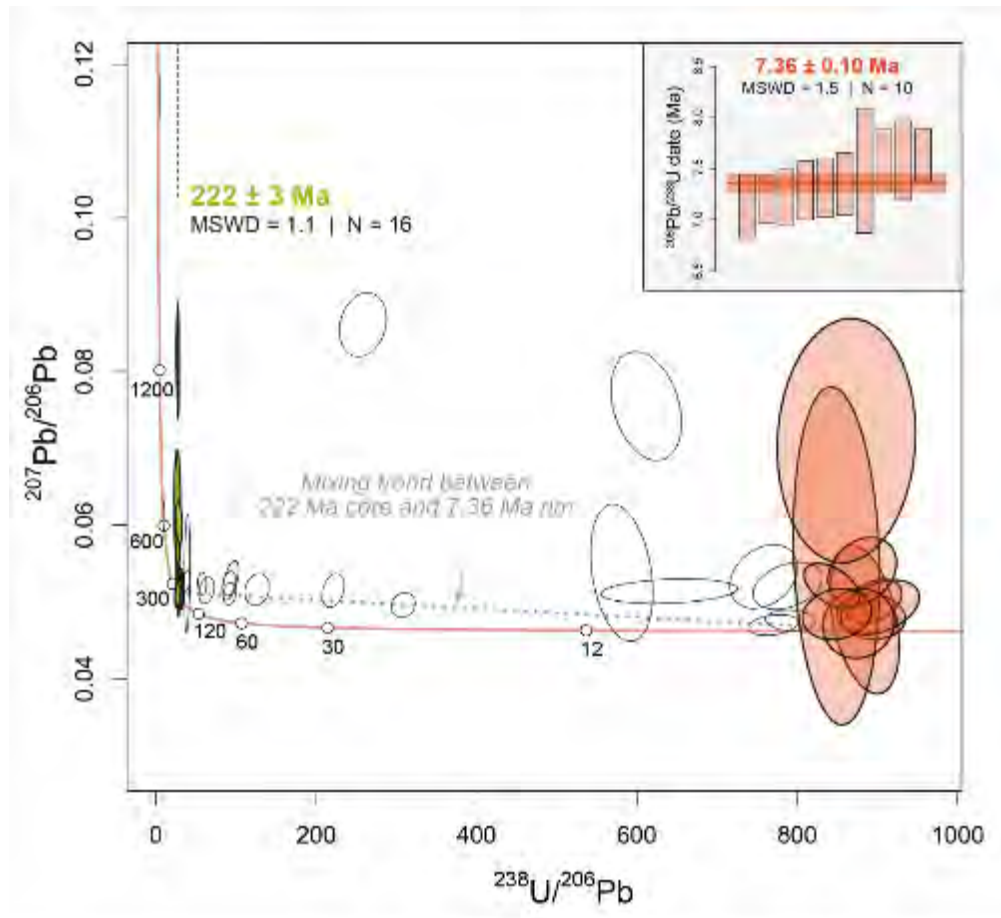


Figure 62. Results of in situ U-Pb isotope analyses of zircon grains from sample 21-MAC-21 in a Tera-Wasserburg concordia diagram. A weighted mean  $^{206}\text{Pb}/^{238}\text{U}$  date is provided for the youngest zircon population.

## 5. DISCUSSION

### 5.1. Heavy minerals in tuffaceous rocks of the Macusani Volcanic Field: Inventory and comparative abundances

In this chapter, heavy mineral populations are compared among the studied tuffaceous units from the Macusani Volcanic Field, i.e., the Lithium-rich Tuff sample (2021-MAC-08) and the white tuffaceous mudstone samples (2021-MAC-21 and 2021-MAC-67). In the sample of Lithium-rich Tuff (2021-MAC-08), a total of nineteen mineral species were identified, of which fourteen are considered heavy minerals, namely unidentified Ti-oxides ( $n = 145$  grains), rutile ( $n = 30$ ), jeremejevite ( $n = 26$ ), corundum ( $n = 22$ ), epidote ( $n = 8$ ), cassiterite ( $n = 5$ ), topaz ( $n = 5$ ), zircon ( $n = 5$ ), xenotime-Y ( $n = 4$ ), magnetite ( $n = 4$ ), pyrite ( $n = 3$ ), dumortierite ( $n = 2$ ), monazite-Ce ( $n = 2$ ), and titanite ( $n = 1$ ). The samples of white tuffaceous mudstones are characterized by a broadly equivalent variety of minerals. In sample 2021-MAC-21, a total of sixteen mineral species were identified, of which twelve are considered heavy minerals, namely zircon ( $n = 54$ ), apatite ( $n = 50$ ), monazite-Ce ( $n = 35$ ), magnetite ( $n = 21$ ), dumortierite ( $n = 19$ ), rutile ( $n = 18$ ), pyrite ( $n = 10$ ), unidentified Ti-oxides ( $n = 6$ ), tourmaline ( $n = 2$ ), titanite ( $n = 1$ ), hematite ( $n = 1$ ), and epidote ( $n = 1$ ). In sample 2021-MAC-67, a total of sixteen mineral species were identified, of which eleven are considered heavy minerals, namely tourmaline ( $n = 56$ ), apatite ( $n = 44$ ), rutile ( $n = 44$ ), anatase ( $n = 25$ ), unidentified Ti-oxides ( $n = 18$ ), goethite ( $n = 9$ ), zircon ( $n = 8$ ), wickmanite ( $n = 7$ ), monazite-Ce ( $n = 5$ ), ilmenite ( $n = 1$ ), andradite ( $n = 1$ ), and pyrite ( $n = 1$ ).

Titanium oxide minerals have been identified in heavy mineral concentrates from the three samples. The Lithium-rich Tuff (2021-MAC-08) is characterized by the occurrence of rutile-like minerals including rutile *s.s.* and unidentified Ti-oxide grains that could probably represent distorted rutile-like structures—according to some shared Raman spectra features. The unidentified Ti-oxide grains are significantly more abundant ( $n = 145$ ) and show enrichment in Ta ( $3 \pm 1$  wt.%) and Nb ( $6 \pm 2$  wt.%) in the Lithium-rich Tuff relative to samples of white tuffaceous mudstone, which contain only minor amounts of unidentified Ti-oxide grains ( $n = 24$  for both samples) without enrichment in Ta and Nb. As for rutile *s.s.*, it is less common in the sample of Lithium-rich Tuff ( $n = 30$ ) than in the samples of white tuffaceous mudstone ( $n = 62$  for both samples). Chemically, rutile in the Lithium-rich Tuff exhibit enrichment in Ta ( $2 \pm 2$  wt.%), Nb ( $4 \pm 3$  wt.%), and Fe ( $3 \pm 2$

wt.%), similar to rutile from the sample 2021-MAC-21 (white tuffaceous mudstone; Nb =  $1 \pm 1$  wt.%, Fe =  $1 \pm 2$  wt.%, Ta =  $3 \pm 4$  wt.%), whereas rutile from the sample 2021-MAC-67 (white tuffaceous mudstone) shows no evidence of enrichment in Ta, Nb, or Fe.

Anatase is limited to sample 2021-MAC-67 (white tuffaceous mudstone) and shows stoichiometric compositions with no enrichment in elements such as Nb and Ta according to EDS data. Likewise, titanite is very scarce and only one grain was recorded in the sample of Lithium-rich Tuff, and another grain in sample 2021-MAC-21 (white tuffaceous mudstone), both showing stoichiometric compositions (Fig. 63). Finally, only one grain of ilmenite was registered in sample 2021-MAC-67 (white tuffaceous mudstone) and yielded a stoichiometric composition.



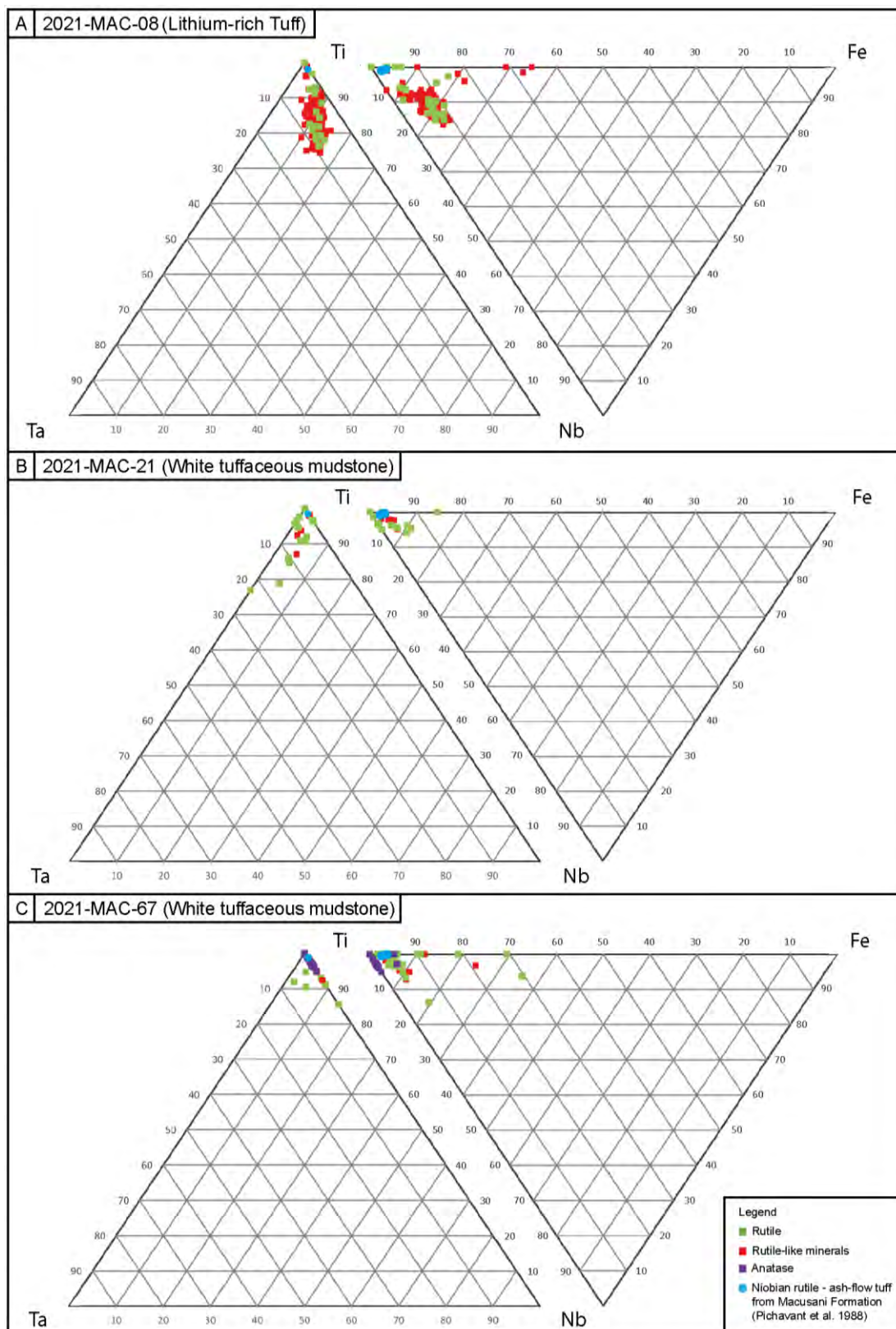


**Figure 63.** Ternary diagram for Ti-oxides (rutile, 'rutile-like' unidentified Ti-oxides, and anatase) found in the Lithium-rich Tuff (2021-MAC-08) and white tuffaceous mudstone (2021-MAC-21, 2021-MAC-67) samples. EDS data. In addition, EMPA data on rutile from ash-flow tuff of the Macusani Formation reported by [Pichavant et al. \(1988\)](#) is given for comparison purposes.

Zircon shows a remarkable contrast in abundance among the samples. Sample 2021-MAC-21 (white tuffaceous mudstone) yielded by far the largest number of zircon crystals ( $n = 54$ ), while samples 2021-MAC-08 (Lithium-rich Tuff) and 2021-MAC-67 (white tuffaceous mudstone) contained only 5 and 8 grains, respectively. Despite these differences in abundance, the most common zircon morphology across the three samples corresponds to elongated prismatic faces  $\{100\}$ ,  $\{110\}$  capped by dipyrramids  $\{101\}$ , which are common crystalline habits of zircon (Brites Martins et al. 2014).

Borosilicate minerals have been identified in the three samples. Tourmaline, which was absent in the Lithium-rich Tuff sample, is present in the white tuffaceous mudstone, particularly in sample 2021-MAC-67, with 54 euhedral crystals, while only two anhedral grains were found in sample 2021-MAC-21. As for dumortierite, only two grains were found in the Lithium-rich Tuff sample; in contrast, in sample 2021-MAC-21 (white tuffaceous mudstone), dumortierite was more abundant than tourmaline, with 19 grains identified. In both samples, dumortierite showed anhedral habits. Finally, jeremejevite, a rare borate, occurs exclusively in the sample of Lithium-rich Tuff ( $n = 26$ ), where it forms well-developed crystals with characteristic light blue color.

Tin-bearing minerals are present in low proportions in both lithologies. Cassiterite was recorded only in the sample of Lithium-rich Tuff ( $n = 5$ ), while wickmanite was detected exclusively in sample 2021-MAC-67 (white tuffaceous mudstone;  $n = 7$ ).

Phosphate minerals are present in each assemblage, with fluorapatite being the most abundant one. This mineral was registered only in two samples of white tuffaceous mudstone (2021-MAC-21 and 2021-MAC-67;  $n = 94$ ). In both cases, the apatite grains display similar morphologies and chemical composition. The second phosphate identified is monazite-Ce, which is significantly more abundant in the samples of white tuffaceous mudstone ( $n = 40$ ) than in the sample of Lithium-rich Tuff ( $n = 2$ ). Chemical analyses reveal no important variations between the samples in terms of REE such as Ce, La, and Nd. The third phosphate identified is xenotime-Y, which is restricted to the sample of Lithium-rich Tuff with only four crystals.

Magnetite was found in samples of Lithium-rich Tuff and white tuffaceous mudstone (2021-MAC-21). In sample 2021-MAC-08 the existence of magnetite grains is scarce, represented by only four grains, while in sample 2021-MAC-21 it is more abundant, with 21 grains registered, making it slightly more common than Ti-oxides in that sample. On

the other hand, pyrite occurs in all three samples but at varying proportions. The sample 2021-MAC-21 contains the highest abundance with 10 crystals, while samples 2021-MAC-08 and 2021-MAC-67 yielded only 3 and 1 crystals, respectively. In all cases, the grains show anhedral morphologies, with no well-defined habits. Regarding Al-rich phases, both corundum ( $n = 22$ ) and topaz ( $n = 5$ ) were recorded exclusively in the sample of Lithium-rich Tuff. A single crystal of garnet (andradite) was recorded in the sample of 2021-MAC-67 (white tuffaceous mudstone).

The presence of different dense minerals in the different studied samples of Lithium-rich Tuff and white tuffaceous mudstone, as well as their different proportions in dense mineral concentrates, indicate that these rocks could have experienced contrasting petrogenetic, pyroclastic/sedimentary, and/or hydrothermal processes. Notably, part of the dense mineral phases identified in the studied samples (i.e., rutile, zircon, and monazite) had been described by previous authors in ash-flow tuff from the Macusani Formation (Noble et al. 1984; Poupeau et al. 1993; Pichavant et al. 1997, 1988, 2024). In addition, rutile from the Macusani ash-flow tuff were identified as niobian rutile by Pichavant et al. (1988) and have compositions that partly overlap in terms of Ti, Nb, Ta, and Fe with those of rutile-like minerals in the studied samples. However, the contents of Nb (0.31 - 0.35 wt.%;  $n = 2$ ), Fe (1.09-1.53 wt.%), and Ta (no reported) in the niobian rutile from Macusani Formation ash-flow tuff are in general lower than those obtained in the samples of Lithium-rich Tuff and white tuffaceous mudstone (Fig. 63). In addition, other heavy minerals found in the white tuffaceous mudstone such as tourmaline and apatite had been described in ash-flow tuff from the Macusani Formation, which reflects a closer mineralogical composition between these two lithologies than with the Lithium-rich Tuff.

Dense mineral phases described in macusanite by London et al. (1988) include andalusite, apatite, zircon, and topaz, which evidence similarities with the heavy mineral assemblage of the Lithium-rich Tuff (zircon and topaz) and the white tuffaceous mudstone (zircon and apatite).

In contrast, several minerals identified in the Lithium-rich Tuff are documented hereby for the first time in volcanic material from the Macusani Volcanic Field, including the notable presence of Al- and B- associated minerals, represented by rare and uncommon species, such as jeremejevite and dumortierite. Other new Al-rich minerals reported include corundum. In addition, xenotime-(Y), magnetite, cassiterite, pyrite, and titanite were also

documented in this thesis for the first time for volcanic rocks of the Macusani Formation. In the case of the white tuffaceous mudstone, dense mineral phases not previously reported in the Macusani Volcanic Field include dumortierite, anatase, titanite, wickmanite, magnetite, and andradite.

## 5.2. Petrogenetic constraints from the identified heavy minerals

As discussed in the foregoing section, the heavy minerals assemblage found in the sample of Lithium-rich Tuff (2021-MAC-08) and the samples of white tuffaceous mudstone (2021-MAC-21 and 2021-MAC-67), exhibit a rich mineral variety. In this section, heavy mineral phases and compositions will be used to discuss some petrogenetic constraints.

Magmatism in the Macusani Volcanic Field, particularly in the Macusani Formation and macusanite, is strongly peraluminous (Noble et al. 1984; Pichavant et al. 1988). The strong peraluminous character of the Lithium-rich Tuff was also noted by Ramírez-Briones et al. (2025). Hence, the occurrence of Al-rich phases is expected. A clear contrast emerges when comparing the Lithium Rich Tuff and the white tuffaceous mudstone, by the fact that corundum and topaz were only found in the Lithium-rich Tuff. This suggests a stronger peraluminous signature of the magmas related to the former. Besides, rocks from the Macusani Volcanic Field record high contents of fluxing elements such as F and B (Barnes et al. 1970, Noble et al. 1984, London et al. 1988, Pichavant et al. 1988). For ash-flow tuff, Barnes et al. (1970) determined F contents of 2.1 wt.% and B contents of 0.03 wt.% while Noble et al. (1984) obtained F contents of  $0.21 \pm 0.05$  wt.% whereas they did not detect B. For macusanite, London et al. (1988) documented high contents of F (1.30 wt.%) and B (0.19 wt.%). For the Lithium-rich Tuff, Ramírez-Briones et al. (2025) reported F contents in the range between 1.54 and 1.98 wt.%, and B contents in the range between 0.02 and 0.18 wt.%. This high activity of F and B is consonant with the finding of borosilicates such as tourmaline and dumortierite, and borates, such as jeremejevite, in the concentrates. In the Lithium-rich tuff, B-bearing minerals are present as dumortierite and a very rare species such as jeremejevite, whereas in the white tuffaceous mudstone, B-bearing minerals correspond to more typical phases associated such as tourmaline, fluorapatite, and dumortierite.

Since boron is typically a mobile element in many geochemical environments, any introduction of B into the system will potentially enhance the crystallization of tourmaline and dumortierite (Choo and Kim 2001). Tourmaline is a common mineral found in granitic

rocks and associated with magmatic-hydrothermal deposits such as pegmatites and greisens (Harlaux et al. 2020). Notably, after tourmaline, dumortierite is the most stable and common borosilicate (Meshram and Ingle 2012). Dumortierite is typically found in granitic rocks as a product of hydrothermal or late stage pneumatolithic processes (Choo and Kim 2001; Khalegui and Karimzadeh 2019), often as a replacement of tourmaline (Galliski et al. 2012; Torró et al. 2024). Jeremejevite, one of the rarest minerals found, has been reported in a few deposits associated with volcanic slags and granitic pegmatites (e.g., Kutzschbach et al. 2017).

Regarding titanium oxides, rutile and “rutile-like” grains yielded variable contents of Fe, Ta, and Nb (Fig. 63), which in some of the analyses are very high according to EDS data (up to 19 wt % Fe, 9 wt % Nb, and 6 wt % Ta). Pichavant et al. (1988) reported EPMA data for two niobian rutile in ash-flow tuff of the Macusani Formation with Nb contents of 0.35 wt % and 0.31 wt %, Fe contents of 1.09 wt % and 1.53 wt%, and no detectable contents of Ta (Fig. 64). Pichavant et al. (1988) associated the niobian rutile to a late stage of biotite alteration during the emplacement of ignimbrite layers. The occurrence of variable amounts of Fe, Nb, and Ta is common in columbite-group minerals and Ti-bearing phases (including rutile), which are well recognized as dominant reservoirs of HFSE (Breiter et al. 2007; Wang et al. 2023). Usually, enrichment of Nb and Ta is associated with peraluminous granitoids, pegmatites of the Nb-Y-F (NYF) and Li-Cs-Ta (LCT) families, and carbonatites (e.g., Černý et al. 1999; Gammons et al. 2025; Wang et al. 2023) and/or hydrothermal alteration (Wang et al. 2023). Extremely low partition coefficients for Nb and Ta between fluid and melt pose that these elements preferentially concentrate in granitic and carbonatitic residual melts. Furthermore, the Nb and Ta enrichment is strongly influenced by the magma volatile contents, as volatile, fluxing elements such as F enhance the solubility of Nb and Ta in the residual melt and fluid (Wang et al. 2023). Nb<sup>+5</sup> and Ta<sup>+5</sup> are easily incorporated into rutile due to their ionic radii (Nb-0.64 Å, Ta-0.64 Å) being similar to that of Ti<sup>+4</sup> (0.61 Å) in the octahedral sites of the rutile structure (Chen et al. 2018). The high contents of Nb and Ta in rutile-like minerals in the Macusani Formation, particularly in the Lithium-rich Tuff, is compatible with the fluxing-element-rich, highly evolved character of the magmatic component of the lithium-ore unit, as constrained by Ramírez-Briones et al. (2025).

The occurrence of REE phosphates such as monazite-Ce and xenotime-Y is commonly reported as accessory phases in granitoids, from dioritic to evolved granites and pegmatites (Demartin et al. 1991, Wark and Miller 1993). It is documented to occur frequently in rocks derived from carbonatite-related magmatism as well (Williams et al. 2007). These phases frequently occur together and are typically associated with rutile and zircon, as observed in the obtained dense separates (Fig. 18), a mineralogical assemblage typical of predominantly granitic sources (Rosa et al. 2010).

Of the tin minerals, cassiterite is the main ore for this metal and may form through magmatic and hydrothermal processes (Bowles 2021). Magmatic cassiterite is found in pegmatites and highly evolved peraluminous granites, often incorporated into minerals crystallizing from Sn-rich melts, such as biotite, titanite, and ilmenite (Linnen et al. 1992; Liu et al. 2025; Zhang et al. 2025). Hydrothermal cassiterite forms in environments like hydrothermal-dominated greisen, skarn, and lode-vein systems (Lehmann 2021; Mathur et al. 2025). The rare wickmanite belongs to the schoenfliesite subgroup, a group of uncommon tin hydroxides, and has been described in pegmatites and skarns. Its occurrence has been associated with two main genetic mechanisms (Haase et al. 2021). The first is crystallization as primary minerals during the late stages of high-temperature hydrothermal activity or within a magmatic environment (Nefedov et al. 1977; Haase et al. 2021). The second is as secondary phases derived from the weathering of primary tin-bearing minerals (Moore and Smith 1966; Haase et al. 2021).

To sum up, the heavy mineral assemblages identified from the Lithium-rich Tuff and the white tuffaceous mudstone are consistent with the felsic and strongly peraluminous affinity of the Macusani volcanics. The presence of Al- and B- bearing phases, Nb- and Ta-enriched Ti-oxides, and other accessory phosphates reflect a mineralogical signature commonly shared with evolved peraluminous pegmatites and LCT pegmatites (Ballouard et al. 2016; Kaeter and Menuge 2025). In addition, some of the dense phases could be related to high-temperature (deuteric) hydrothermal processes. The similar geochemical signatures of the Lithium-rich Tuff with rare-metal peraluminous granites and LCT pegmatites had been noted by Ramírez-Briones et al. (2025) based on lithogeochemical analysis.

### 5.3. Zircon as a tracer of basement and magmatism in the Macusani Volcanic Field

Zircon U-Pb results from a sample of white tuffaceous mudstone (2021-MAC-21) reveal two geologically meaningful dates at  $222 \pm 3$  and  $7.36 \pm 0.10$  Ma (Fig. 62). The  $222 \pm 3$

Ma date aligns with Triassic peraluminous granitic plutonism that occurred at ~220 Ma in a transpressive setting within the southern Cordillera de Carabaya in Peru (Clark et al., 1983, 1990; Kontak et al., 1985, 1990; Mišković et al. 2009) and its extension in the Cordillera Real in Bolivia (Kontak et al. 1990, Iriarte et al. 2021). Noteworthy, Triassic ages are also registered in zircons from the San Rafael Miocene-Oligocene granitoids with a major peak at 225 Ma (Harlaux et al. 2021).

Finally, a second distinctive date of  $7.36 \pm 0.10$  Ma is interpreted as the emplacement age of the white tuffaceous mudstone in the Quelcaya zone (Fig. 2). The emplacement age is coeval with the deposition of the Macusani Formation, which is constrained between ca. 10 and 6.5 Ma (Sandeman et al. 1997). In particular, it would be coeval with a second volcanic episode documented at  $7 \pm 1$  Ma (Cheilletz et al. 1992; Sandeman et al. 1997). Furthermore, new  $^{40}\text{Ar}/^{39}\text{Ar}$  dates on Li-F mica crystals in the Lithium-rich Tuff of ca 8.9 – 8.7 Ma (Sanandres et al. 2024; Torró et al. 2025) are older than the  $7.36 \pm 0.10$  Ma emplacement age obtained in this study. This time span confirms the presence of distinct depositional levels within the volcanic sequence and reinforces the notion that the Lithium-rich Tuff represented a small-volume eruptive event (Torró et al. 2025). Moreover, it is consonant with compositional and mineralogical changes between general tuffaceous material within the Macusani Formation and the Lithium-rich Tuff as derived from temporally separated, punctuated magmatic events in the Macusani Volcanic Field (this thesis; Ramirez-Briones et al. 2025; Torró et al. 2025).

Out of five zircon grains separated from the Lithium Rich Tuff, three of them correspond to the G1 morphology type of Pupin (1980), which is associated with a high index A and magma temperatures of  $650 \pm 50$  °C (Figs. 1, 17). The high A index is in good agreement with the general highly peraluminous character of the magmas associated with the Lithium-rich Tuff. On the other hand, Ramírez-Briones et al. (2025) calculated monazite and zircon saturation temperatures of ~650-720 °C from the chemical composition of Lithium-rich Tuff samples. Besides, Pichavant et al. (1988) constrained the main crystallization stage in Macusani magmas (Macusani Formation ash-flow tuff) at ~650 °C. As for zircon grains separated from the white tuffaceous mudstone, the majority of grains fall within the G1 and S8 types, which indicates an intermediate to high index A, but there is a wide variety of morphologies including S10, S11, S12, S14, S17, S18, S19, and S20 suggesting very diverse origins (Figs. 1, 17).

#### 5.4. Economic potential of heavy minerals in the Macusani tuffs

Based on the inventory of heavy minerals found in the ore sample corresponding to the Lithium Rich Tuff, two main potential heavy mineral types stand as potential sources of valuable by-products. On one hand, titanium oxides, mostly rutile and similar mineral structures, host up to 9 wt.% Nb and 6 wt.% Ta according to EDS data. Both Nb and Ta are considered as critical raw materials ([European Commission 2023](#)), which highlights the importance of properly characterizing these elements in lithium deposits like Macusani to better assess the resource and recovery potential.

On the other hand, in this study, it was possible to identify the presence of monazite-Ce and xenotime-Y as principal rare earth minerals. In contrast to our study case, rare earth minerals reported in the Thacker Pass volcano-sedimentary lithium deposit in the McDermitt caldera, USA, include bastnäsite and synchsite in addition to monazite ([Crespo et al. 2025](#)). Although the proportion of these minerals are not significant, the authors concluded that a detailed analysis should be done to understand the mode of occurrence and distribution of REE to further assess their extractability.

Heavy minerals found in this study could be potential by-products as monazite and xenotime are considered viable ores for REE extraction ([Kumari et al. 2015](#)). However, it is important to consider that these REE phosphates present in the sample exhibit high thermal stability, making them difficult to decompose even at elevated temperatures ([Panda et al. 2014](#)). Moreover, during the metallurgical process, chemical reactions between REE and phosphorus may lead to the formation of phosphides, which will promote the pulverization of REE complexes ([Panda et al. 2014](#)). Therefore, it is essential to eliminate the phosphates in order to enhance the dissolution of these rare earth minerals. Although a wide range of methods have been developed for the extraction of REE from monazite, the most common industrial approach to extracting rare earths from xenotime is by leaching with sulfuric acid or by alkali leaching ([Alex et al. 1998](#); [Xu et al. 2012](#); [Panda et al. 2014](#); [Demol et al. 2018](#)). Given that in this study, REE are considered possible by-products rather than the main target of extraction, leaching represents a practical and widely applied method that could be developed as an option for recovery after separation of REE phosphates through gravimetric methods from the dominantly silicate host rock.

## 6. CONCLUSIONS

The heavy mineral assemblages separated from Lithium-rich Tuff and white tuffaceous mudstone of the Macusani Volcanic Field show a wide variety of phases. In the Lithium-rich Tuff, identified dense minerals include rutile-like minerals, zircon, monazite-Ce, pyrite, magnetite, corundum, jeremejevite, topaz, dumortierite, cassiterite, xenotime-Y, epidote, and titanite. In the white tuffaceous mudstone, identified dense minerals include rutile-like minerals, zircon, monazite-Ce, apatite, wickmanite, tourmaline, dumortierite, titanite, magnetite, pyrite, ilmenite, andradite, hematite, and goethite. Therefore, there are some shared minerals in both facies (e.g., rutile, zircon, monazite-Ce, titanite, dumortierite, epidote, magnetite, and pyrite), while there are some minerals (e.g., cassiterite, corundum, topaz, jeremejevite, and xenotime-Y) that are only found in the Lithium-rich Tuff and some others (e.g., anatase, apatite, wickmanite, andradite, goethite, and ilmenite) that are exclusively found in the white tuffaceous mudstone. Other observed differences include changes in the composition of given minerals. This is particularly notable for rutile-like minerals from the Lithium-rich Tuff, which are enriched in Ta and Nb regarding the white tuffaceous mudstone. These observations suggest that the volcanogenic material associated with both facies derived from magmatic pulses with contrasting petrogenetic processes.

Overall, in both studied facies, the heavy mineral assemblages agree with the peraluminous, volatile (e.g., F, B)-rich, and highly evolved character of Macusani volcanics. In the case of the Lithium-rich Tuff, the presence of REE phosphates (i.e. monazite-Ce and xenotime-Y), the predominance of B- and Al- bearing minerals, and the enrichment in Nb and Ta of Ti-oxides highlight the highly evolved character of the igneous material in this unit, which had been previously identified as close in composition to macusanite, rare metal peraluminous granites, and LCT pegmatites. It is also compatible with the general notion that the Lithium-rich Tuff derived from more evolved magmas relative to other tuffaceous units in the Macusani Formation.

The zircon U-Pb results from one sample of white tuffaceous mudstone reveal two age populations, one Triassic ( $222 \pm 3$  Ma), consistent with regional peraluminous granitic plutonism, and one Miocene age ( $7.36 \pm 0.10$  Ma) that aligns with volcanic activity in the Macusani Formation. The latter is older than  $^{40}\text{Ar}/^{39}\text{Ar}$  mica dates for the Lithium-rich Tuff (ca. 8.9 Ma), which reinforces the idea of derivation from different magmatic pulses in the volcanic field. The wide range of zircon morphologies probably reflects a variety of

populations related to different origins, being G1 and S8 morphologies of [Pupin 1980](#), which are often associated with peraluminous granitic rocks, the dominant morphologies. Heavy minerals, particularly in ore units such as the Lithium-rich Tuff, host potential to become valuable by-products. In particular, Ti-oxides were found to be enriched in Nb and Ta, and phosphates such as apatite, monazite-Ce, and xenotime-Y can become a source of REE. Further investigation on these potential subproducts is needed to further evaluate the occurrence, distribution, and extractability of by-products from heavy mineral concentrates in Falchani and other volcanogenic lithium deposits worldwide.



## 7. REFERENCES

- Alex P, Suri AK, Gupta CK (1998) Processing of xenotime concentrate. *Hydrometall* 50(3):331-338. [https://doi.org/10.1016/S0304-386X\(98\)00052-8](https://doi.org/10.1016/S0304-386X(98)00052-8)
- American Lithium (2024) Falchani Lithium Project, PERU. <https://americanlithiumcorp.com/falchani-lithium-project/>. Accessed 21 July 2024
- Azevedo M, dos Santos L, Stuaní L, Tello C, Rainho S, Figueroa P (2021) Physico-Chemical Characterization of Macusanite and Inclusions: A Volcanic Glass from Peruvian Andes. *Mater Res* 24. <https://doi.org/10.1590/1980-5373-MR-2021-0033>
- Badanina EV, Sitnikova MA, Gordienko VV, Melcher F, Gabler HE, Lodziak J, Sýritso LF (2015) Mineral chemistry of columbite–tantalite from spodumene pegmatites of Kolmozero, Kola Peninsula (Russia). *Ore Geology Rev* 64:720-735. <https://doi.org/10.1016/j.oregeorev.2014.05.009>
- Ballouard C, Poujol M, Boulvais P, Branquet Y, Tartèse R, Vignerresse JL (2016) Nb-Ta fractionation in peraluminous granites: A marker of magmatic-hydrothermal transition. *Geology* 44(3):231-234. <https://doi.org/10.1130/G37475.1>
- Barbarin B (1999) A review of the relationships between granitoid types, their origins and their geodynamic environments. *Lithos* 46(3):605-626. [https://doi.org/10.1016/S0024-4937\(98\)00085-1](https://doi.org/10.1016/S0024-4937(98)00085-1)
- Barnes VE, Edwards G, McLaughlin W, Friedman I, Joensuu O (1970) Macusanite Occurrence, Age, and Composition, Macusani, Peru. *Geol Soc Am Bull* 81:1539-1546. [https://doi.org/10.1130/0016-7606\(1970\)81\[1539:MOAACM\]2.0.CO;2](https://doi.org/10.1130/0016-7606(1970)81[1539:MOAACM]2.0.CO;2)
- Barnes C, Majka J, Schneider D, Walczak K, Bukala M, Kosminska K, Tokarski T, Karlsson A (2018) High-spatial resolution dating of monazite and zircon reveals the timing of subduction–exhumation of the Vaimok Lens in the Sve Nappe Complex (Scandinavian Caledonides). *Contrib Mineral Petrol* 174:5. <https://doi.org/10.1007/s00410-018-1539-1>
- Barnes C, Majka J, Jeanneret P, Ziemniak G, Kooijman E, Kosminska K, Kielman-Schmitt M, Schneider DA (2021) Using Th-U-Pb geochronology to extract crystallization ages of Paleozoic metamorphic monazite contaminated by initial Pb. *Chem Geol* 582:120450. <https://doi.org/10.1016/j.chemgeo.2021.120450>
- Baxter E, Caddick M, Ague J (2013) Garnet: Common Mineral, Uncommonly Useful. *Elements* 9(6):415-419. <https://doi.org/10.2113/gselements.9.6.415>
- Baxter E, Scherer E (2013) Garnet Geochronology: Timekeeper of Tectonometamorphic Processes. *Elements* 9(6):433-438. <https://doi.org/10.2113/gselements.9.6.433>
- Bea F, Montero P, Molina J (2018) Experimental evidence for the preservation of U-Pb isotope ratios in mantle-recycled crustal zircon grains. *Sci Rep* 8:12904. <https://doi.org/10.1038/s41598-018-30934-4>

- Belousova EA, Griffin WL, O'Reilly S (2006) Zircon Crystal Morphology, Trace Element Signatures and Hf Isotope Composition as a Tool for Petrogenetic Modelling: Examples From Eastern Australian Granitoids. *J Petrol* 47(2):329-353. <https://doi.org/10.1093/petrology/egi077>
- Benites D, Torró L, Vallance J, Laurent O, Quispe P, Rosas S, Uzieda MF, Holm-Denoma C, Pianowski L, Camprubi A, Colas V, Fernández-Baca A, Giraldo L, Chelle-Michou C, Sáez J, Kouzmanov K, Fontboté L (2022) Geology, mineralogy, and cassiterite geochronology of the Ayawilca Zn-Pb-Ag-In-Sn-Cu deposit, Pasco, Peru. *Miner Deposita* 57:481-507. <https://doi.org/10.1007/s00126-021-01066-z>.
- Bibienne T, Magnan JF, Rupp A, Laroche N (2020) From Mine to Mind and Mobiles: Society's Increasing Dependence on Lithium. *Elements* 16:265–270. <https://doi.org/10.2138/gselements.16.4.265>
- Bracciali L, Parrish RR, Horstwood MSA, Condon DJ, Najman Y (2013) U/Pb LA-(MC)-ICP-MS dating of rutile: New reference materials and applications to sedimentary provenance. *Chem Geol* 347:82-101. <https://doi.org/10.1016/j.chemgeo.2013.03.013>.
- Braun I, Appel P (2006) U-Th-total Pb dating of monazite from orthogneisses and their ultra-high temperature metapelitic enclaves: implications for the multistage tectonic evolution of the Madurai Block, southern India. *Eur J Mineral* 18(4):415-427. <https://doi.org/10.1127/0935-1221/2006/0018-0415>
- Breiter K, Škoda R, Usher P (2007) Nb-Ta-Ti-W-Sn-oxide minerals as indicators of a peraluminous P- and F-rich granitic system evolution: Podlesí, Czech Republic. *Min Petrol* 91:225-248. <https://doi.org/10.1007/s00710-007-0197-1>
- Brites Martins HC, Simoes PP, Abreu J (2014) Zircon crystal morphology and internal structures as a tool for constraining magma sources: Examples from northern Portugal Variscan biotite-rich granite plutons. *G R Geosci* 346:233-243. <https://doi.org/10.1016/j.crte.2014.07.004>
- BGS (2011) Tungsten. NERC Open Research Archive. <https://nora.nerc.ac.uk/id/eprint/17445>
- Bowell RJ, Lagos L, De Los Hoyos C, Declercq J (2020) Classification and Characteristics of Natural Lithium Resources. *Elements* 16:259-264. <https://doi.org/10.2138/gselements.16.4.259>
- Bowles JFW (2021) Oxides. In: Alderton D (ed) *Encyclopedia of Geology*, 2<sup>nd</sup> edn. Elsevier, pp 428-441
- Cabri L, Rudashevsky NS, Rudashevsky VN, Lastra R (2006) Hydroseparation: a new development in process mineralogy of platinum ores. *CIM Bull* 99:1-7
- Caddick M, Kohn M (2013) Garnet: Witness to the Evolution of Destructive Plate Boundaries. *Elements* 9:427-432. <https://doi.org/10.2113/gselements.9.6.427>

- Cambeses A, Chakraborty S, Jons N, Montero P, Bea F (2023) How does inherited zircon survive in partially molten mantle: Insights on modes of magma transport in the mantle from nanoscale melt-crystal interaction experiments. *Earth and Planetary Sci Letters* 601:117911. <https://doi.org/10.1016/j.epsl.2022.117911>
- Carlotto V, Quispe J, Acosta H, Rodríguez R, Romero D, Cerpa L, Mamani M, Diaz E, Navarro P, Jaimes F, Velarde T, Lu S, Cueva E (2009) Dominios geotectónicos y Metalogénesis del Perú. *Bol Soc Geo Perú* 103:1-90
- Carr P, Zink S, Bennett V, Norman M, Amelin Y, Blevin P (2021) A new method for U-Pb geochronology of cassiterite by ID-TIMS applied to the Mole Granite polymetallic system, eastern Australia. *Chem Geo J* 539(119359). <https://doi.org/10.1016/j.chemgeo.2020.119539>.
- Castroviejo R, Macharé J, Castro P, Pereira E, Rodriguez JF, Tassinari CG, Willner A, Acosta J (2010) Significado de las ofiolitas Neoproterozoicas de la Cordillera Oriental del Perú (9°30'-11°30'). *SGP, Pub Esp N°9, Cusco* 51-53. <https://hdl.handle.net/20.500.12544/2885>
- Černý P, Chapman R, Simmons WB, Chackowsky LE (1999) Niobian rutile from the McGuire granitic pegmatite, Park County, Colorado: Solid solution, exsolution, and oxidation. *Am Min* 84:754-763. <https://doi.org/10.2138/am-1999-5-607>
- Chakmouradian AR, Wall F (2012) Rare earth elements: Minerals, mines, magnets (and more). *Elements* 8(5):333-340. <https://doi.org/10.2113/gselements.8.5.333>
- Chávez VA, Salas AG, Gutiérrez SE, Cuadros PJ (1997) Geología de los cuadrángulos de Corani y Ayapata. Hojas: 28-u y 28-v: Lima, Instituto Geológico, Minero y Metalúrgico, Boletín A pp 90,-128. <https://hdl.handle.net/20.500.12544/197>
- Cheilletz A, Clark AH, Farrar E, Arroyo Pauca G, Pichavant M, Sandeman HA (1992) Volcano-stratigraphy and  $^{40}\text{Ar}/^{39}\text{Ar}$  geochronology of the Macusani ignimbrite field: monitor of the Miocene geodynamic evolution of the Andes of southeast Peru. *Tectonophysics* 205:307–327. [https://doi.org/10.1016/0040-1951\(92\)90433-7](https://doi.org/10.1016/0040-1951(92)90433-7)
- Chen W, Xiong X, Wang J, Xue S, Li L, Liu X, Ding X (2018)  $\text{TiO}_2$  Solubility and Nb and Ta Partitioning in Rutile-Silica-Rich Supercritical Fluid Systems: Implications for Subduction Zone Processes. *J Geophys Res Solid Earth* 123:4765-4782. <https://doi.org/10.1029/2018JB015808>
- Cheng Y, Spandler C, Kemp A, Mao J, Rusk B, Hu Y, Blake K (2019) Controls on cassiterite ( $\text{SnO}_2$ ) crystallization: evidence from cathodoluminescence, trace-element chemistry, and geochronology at the Gejiu Tin District. *Am Mineral* 104:118–129. <https://doi.org/10.2138/am-2019-6466>
- Cherniak DJ, Watson EB (2007) Ti Diffusion in zircon. *Chem Geol* 242(3-4):470-483. <https://doi.org/10.1016/j.chemgeo.2007.05.005>
- Chew DM, Schaltegger U, Miskovic A, Fontignie D, Frank M (2005) Deciphering the Tectonic Evolution of the Peruvian Segment of the Gondwana Margin. 6<sup>th</sup> International Symposium on Andean Geodynamic ISAG 166-169

- Chew DM, Schaltegger U, Košler J, Whitehouse M, Gutjahr M, Spikings R, Mišković A (2007) U-Pb geochronologic evidence for the evolution of the Gondwanan margin of the north-central Andes. *GSA Bulletin* 119(5-6):697-711. <https://doi.org/10.1130/B26080.1>
- Chew DM, Pedemonte G, Corbett E (2016) Proto-Andean evolution of the Eastern Cordillera of Peru. *Gondwana Res* 35:59-78. <https://doi.org/10.1016/j.gr.2016.03.016>
- Choo CO, Kim JJ Mineralogical studies of dumortierite from Miryang clay deposit, Korea (2001) *Geosci J* 5(4):273-279. <https://doi.org/10.1007/BF02912697>
- Clark AH, Farrar E, Kontak DJ, Langridge RJ, Arenas MJ, France LJ, McBride SL, Woodman PL, Wasteneys HD, Sandeman HA, Archibald DA (1990) Geologic and geochronologic constraints on the metallogenic evolution of the Andes of southeastern Peru. *Econ Geol* 85(7):1520-1583. <https://doi.org/10.2113/gsecongeo.85.7.1520>
- Clark AH, Palma VV, Archibald DA, Farrar E, Arenas MJ, Robertson RCR (1983) Occurrence and age of tin mineralization in the Cordillera Oriental, southern Peru. *Econ Geol* 78:514-520. <https://doi.org/10.2113/gsecongeo.78.3.514>
- Cordani UG, Sato K (2000) Crustal evolution of the South American platform based on Nd isotopic systematics on granitoid rocks. *Episodes* 22:167-173. <https://doi.org/10.18814/epiiugs/1999/v22i3/003>
- Crespo J, Muñoz-Saez C, Jowitt SM, Burns R (2025) Rare earth minerals in lithium clay deposits: Insights from the Thacker Pass Deposit, Northern Nevada, USA. *Econ Geol* 2025. <https://doi.org/10.5382/econgeo.5167>
- Damm K, Harmon R, Kelley S (1994) Some Isotopic and Geochemical Constraints on the Origin and Evolution of the Central Andean Basement (19°- 24°S). In: Reutter KJ, Scheuber E, Wigger PJ (eds) *Tectonic of the Southern Central Andes*. Springer, Berlin, Heidelberg pp 263-276
- Darby DA, Tsang YW (1987) Variation in ilmenite element composition within and among drainage basins; implications for provenance. *J of Sedimentary Research* 57: 831-838. <https://doi.org/10.1306/212F8C79-2B24-11D7-8648000102C1865D>
- Davis D (2015) Uranium-Lead, Igneous Rocks. In: Rink J, Thompson J (eds) *Ency of Scientific Dating Methods*, 1st edn. Springer, Netherlands pp 894-897
- Demartin F, Pilati T, Diella V, Donzelli S, Gentile P, Gramaccioli CM (1991) The chemical composition of xenotime from fissures and pegmatites in the Alps. *Can Mineral* 29:69-75. ISSN: 1499-1276
- Demol J, Ho E, Senanayake G (2018) Sulfuric acid baking and leaching of rare earth elements, thorium and phosphate from a monazite concentrate: Effect of bake temperature from 200 to 800 °C. *Hydrometall* 179:254-267. <https://doi.org/10.1016/j.hydromet.2018.06.002>

- Dorbath L, Dorbath C, Jimenes E, Rivera L (1991) Seismicity and tectonic deformation in the Eastern Cordillera and the sub-Andean zone of central Peru. *J South Am Earth Sci* 4:13-24. [https://doi.org/10.1016/0895-9811\(91\)90015-D](https://doi.org/10.1016/0895-9811(91)90015-D)
- Dushyantha N, Batapola N, Ilankoon IMSK, Rohitha S, Premasiri R, Abrysinghe B, Ratnayake N, Dissanayake K (2020) The story of rare earth elements (REEs): Occurrences, global distribution, genesis, geology, mineralogy and global production. *Ore Geology Reviews*. <https://doi.org/10.1016/j.oregeorev.2020.103521>.
- Elsner H (2010) Heavy Minerals of Economic Importance. Assessment Manual Bundesanstalt für Geowissenschaften und Rohstoffe (BGR) (Federal Institute for Geosciences and Natural Resources)
- European Commission (2020) Critical Raw Materials Resilience: Charting a Path towards greater Security and Sustainability. CELEX: 52020DC0474
- European Commission (2023) Study on the EU's list of Critical Raw Materials – Final Report. European Commission, Brussels, 158 p
- Farges F (1998) Titanium: Element and geochemistry. In: *Geochemistry. Encyclopedia of Earth Science*. Springer, Dordrecht. [https://doi.org/10.1007/1-4020-4496-8\\_327](https://doi.org/10.1007/1-4020-4496-8_327)
- Fiannacca P, Williams IS, Cirrincione R, Pezzino A (2008) Crustal contributions to late Hercynian peraluminous magmatism in the Southern Calabria – Peloritani Orogen, Southern Italy: Petrogenetic inferences and the Gondwana connection. *J Petrol* 48:1497-1514. <https://doi.org/10.1093/petrology/egn035>
- F3 Uranium Corp (2023) Macusani Project. <https://f3uranium.com/projects/peru/macusani-peru>. Accessed 19 June 2023
- Galliski MA, Márquez-Zavalía MF, Lira R, Cempírek J, Škoda R (2012) Mineralogy and Origin of the Dumortierite-Bearing Pegmatites of Viorco, San Luis, Argentina. *Can Mineral* 50 (4):873-894. <https://doi.org/10.3749/canmin.50.4.873>
- Gammons CH, Lowers HA, Thompson JM (2025) Niobium-rich Minerals from the Sheep Creek Carbonatite-Related Deposits, Montana USA. In: *Proceedings of the 18th SGA Biennial Meeting*, 3 – 7 August.
- Gansser (1973) Facts and theories on the Andes. *J Geol Soc* 129:93-131. <https://doi.org/10.1144/gsjgs.129.2.0093>
- Garzanti E, Andò S, Vezzoli G (2008) Settling equivalence of detrital minerals and grain-size dependence of sediment composition. *Earth Plane Sci Lett* 273:138-151. <https://doi.org/10.1016/j.epsl.2008.06.020>
- Gasik MI (2013) Technology of Niobium Ferroalloys. In: *Handbook of Ferroalloys*. Oxford, England, pp 411-419
- Gemmrich L, Torró L, Melgarejo JC, Laurent O, Vallance J, Chelle-Michou C, Sempere TPA (2021) Trace element composition and U-Pb ages of cassiterite from the

- Bolivian tin belt. *Miner Deposita* 56:1491-1520. <https://doi.org/10.1007/s00126-020-01030-3>.
- GEOCATMIN (2023). <https://geocatmin.ingemmet.gob.pe/geocatmin/>. Accessed 15 October 2023.
- Gérard B, Robert X, Audin L, Valla PG, Bernet M, Gautheron C (2021) Differential exhumation of the Eastern Cordillera in the Central Andes: Evidence for south-verging backthrusting (Abancay Deflection, Peru). *Tectonics* 40(4). <https://doi.org/10.1029/2020TC006314>
- Gheith A, Al-Balushi A, Hereher M, Sherief Y, Al-Awadhi T (2021) Petrography and heavy minerals analysis for recognition of the depositional history of the Wahiba Sand Sea, Sultanate of Oman. *Arabian J of Geosciences* 14:1444. <https://doi.org/10.1007/s12517-021-07790-0>
- Global Market Insights (2018) Tungsten Market Size By Application (Tungsten Carbide, Metal Alloys, Mill Products), By End-use (Automotive Parts, Aerospace Components, Drilling, Boring & Cutting Equipment, Logging Equipment, Electrical & Electronics Appliances), Industry Analysis Report, Regional Outlook, Application Growth Potential, Price Trends, Competitive Market Share & Forecast, 2018 – 2025. <https://www.gminsights.com/industry-analysis/tungsten-market>
- Global Market Insights (2020) Rare Earth Metals Market Size, Share and Industry Analysis Report by Metal (Cerium, Dysprosium, Erbium, Europium, Gadolinium, Holmium, Lanthanum, Lutetium, Neodymium, Praseodymium, Promethium, Samarium, Scandium, Terbium, Thulium, Ytterbium, Yttrium) and Applications (Magnets, Colorants, Alloys, Optical Instruments, Catalysts), Regional Outlook, Competitive Market Share & Forecast, 2020 – 2026. <https://www.gminsights.com/industry-analysis/rare-earth-metals-market>
- Godet A, Guilmette C, Labrousse L, Smit M, Cutts J, Davis D, Vanier MA (2021) Lu–Hf garnet dating and the timing of collisions: Palaeoproterozoic accretionary tectonics revealed in the Southeastern Churchill Province, Trans-Hudson Orogen, Canada. *J Metamorph Geol* 39:977-1007. <https://doi.org/10.1111/jmg.12599>
- Golroudbary SR, Makarava I, Kraslawski A, Repo E (2022) Global environmental cost of using rare earth elements in green energy technologies. *Science of The Total Environment* J 832. <https://doi.org/10.1016/j.scitotenv.2022.155022>
- Guo XY, Xu DP, Ding ZH, Su WH (2006) Preparation and Raman Spectrum of Rutile Single Crystals Using Floating Zone Method. *Chin Phys Lett* 23(6).1645. <https://iopscience.iop.org/article/10.1088/0256-307X/23/6/080>
- Haase P, Gorniak-Christensen H, Gro-Nielsen U, Bender-Koch C, Galazka Z, Majzlan M (2021) Stability and solubility of members of tin perovskites in the schoenfliesite subgroup,  $\square_2$  (B Sn<sup>4+</sup>)(OH,O)<sub>6</sub> (B = Ca, Fe<sup>3+</sup>, Mg, Mn<sup>2+</sup>, Zn, Cu). *Chem Thermodyn Therm Anal* 1-2:100005. <https://doi.org/10.1016/j.ctta.2021.100005>.
- Haldar SK (2020) Chapter 1 – Minerals and Rocks. In: Haldar SK (ed) *Introduction to Mineralogy and Petrology*, 2nd edn. Elsevier, West Bengal, pp 1-51

- Han Z, Golev A, Edraki M (2021) A Review of Tungsten Resources and Potential Extraction from Mine Waste. *Minerals J* 11(7):701. <https://doi.org/10.3390/min11070701>
- Hanawa T (2019) Titanium–Tissue Interface Reaction and Its Control with Surface Treatment. *Front Bioeng Biotechnol* 7:170. <https://doi.org/10.3389/fbioe.2019.00170>
- Hanchar J, van Westrenen W (2007) Rare Earth Element Behavior in Zircon-Melt Systems. *Elements J* 3(1):37-42. <https://doi.org/10.2113/gselements.3.1.37>
- Hanson BH (1986) Present and future uses of titanium in engineering. *Materials & Design J* 7(6):301-307. [https://doi.org/10.1016/0261-3069\(86\)90099-3](https://doi.org/10.1016/0261-3069(86)90099-3)
- Haque N, Hughes A, Lim S, Vernon C (2014) Rare Earth Elements: Overview of Mining, Mineralogy, Uses, Sustainability and Environmental Impact. *Resources J* 3(4):614-635. <https://doi.org/10.3390/resources3040614>
- Harlaux M, Kouzmanov K, Gialli S, Laurent O, Rielli A, Dini A, Chauvet A, Menzies A, Kalinaj M, Fontboté L (2020) Tourmaline as a Tracer of Late-Magmatic to Hydrothermal Fluid Evolution: The World-Class San Rafael Tin (-Copper) Deposit, Peru. *Econ Geol* 115(8):1665-1697. <https://doi.org/10.5382/econgeo.4762>
- Harlaux M, Kouzmanov K, Gialli S, Clark AH, Laurent O, Corthay G, Prado-Flores E, Dini A, Chauvet A, Ulianov A, Chiaradia M, Menzies A, Villón-Durand G, Kalinaj M, Fontboté L (2021) The upper Oligocene San Rafael intrusive complex (Eastern Cordillera, southeast Peru), host of the largest-known high-grade tin deposit. *Lithos* 400-401. <https://doi.org/10.1016/j.lithos.2021.106409>
- Harlaux M, Kontak DJ, Clark AH, Kouzmanov K, Holm-Denoma CS, Gialli S, Laurent O, Spikings R, Chauvet A, Dini A, Kalinaj M, Fontboté L (2023) Depositing >1.5 Mt of Tin Within <1 m.y. of Initial Granitic Intrusion in the San Rafael Tin (-Copper) Deposit, Southeastern Peru. *Econ Geol* 118(6):1371-1396. <https://doi.org/10.5382/econgeo.5021>
- Harley SL, Kelly NM (2007) Zircon Tiny But Timely. *Elements J* 3(1):13-18. <https://doi.org/10.2113/gselements.3.1.13>
- Hatch GP (2012) Dynamics in the Global Market for Rare Earths. *Elements J* 8(5):341-346. <https://doi.org/10.2113/gselements.8.5.341>
- Hawkesworth CJ, Kemp AIS (2006) Using hafnium and oxygen isotopes in zircons to unravel the record of crustal evolution. *Chem Geol* 226:144-162. <https://doi.org/10.1016/j.chemgeo.2005.09.018>
- Haynes WM (2014) Section 14: Geophysics, astronomy, and acoustics. In: *CRC Handbook of Chemistry and Physics*, 95<sup>th</sup> edn. CRC Press, Florida, pp 14-19
- Hellstrom JC, Paton C, Woodhead J, Hergt J (2008) Iolite: Software for spatially resolved LA-(quad and MC) ICP-MS analysis. In: Sylvester P (ed) *Laser ablation ICP-MS*

in the Earth sciences: Current practices and outstanding issues. Mineralogical Association of Canada: Vancouver, pp 343-348.

- Henriques VA (2009) Titanium production for aerospace applications. *J of Aerospace Technology and Management* 1(1):7-17. [10.5028/jatm.2009.01010717](https://doi.org/10.5028/jatm.2009.01010717)
- Horstwood MSA, Košler J, Gehrels G, Jackson SE, McLean NM, Paton C, Pearson NJ, Sircombe K, Sylvester P, Vermeesch P, Bowring JF, Condon DJ, Schoene B (2016) Community-Derived Standards for LA-ICP-MS U-(Th)-Pb Geochronology – Uncertainty Propagation, Age Interpretation and Data Reporting. *Geostand Geon Res* 40:311-332. <https://doi.org/10.1111/j.1751-908X.2016.00379.x>
- Horton B (2018) Sedimentary record of Andean Mountain building. *Earth Sci Rev* 178:279-309. <https://doi.org/10.1016/j.earscirev.2017.11.025>
- Iriarte AR, Cordani UG, Sato K (2021) Geochronology of the Cordillera Real granitoids, the inner magmatic arc of Bolivia. *Andean Geol* 48:403-441. <http://dx.doi.org/10.5027/andgeoV48n3-3326>
- Jones JV, Piatak NM, Bedinger GM (2017) Zirconium and Hafnium. Chapter V of *Critical Mineral Resources of the United States—Economic and environmental geology and prospects for future supply*. <https://doi.org/10.3133/pp1802V>
- Jones RV, Kirstein L, Kasemann S, Dhuime B, Elliott T, Litvak V, Alonso R, Hinton R (2015) Geodynamic controls on the contamination of Cenozoic arc magmas in the southern Central Andes: Insights from the O and Hf isotopic composition of zircon. *Geochim Cosmochim Acta* 164:386-402. <https://doi.org/10.1016/j.gca.2015.05.007>
- Jowitt SM, McNulty BA (2021) Battery and Energy Metals: Future Drivers of the Minerals Industry? *SEG Discovery* 127:11–18. <https://doi.org/10.5382/2021-127.fea-01>
- Kaeter D, Menuge JF (2025) Columbite-tantalite and cassiterite as indicator minerals for lithium pegmatites: implications from geospatial and mineralogical analyses of stream sediments in southeast Ireland. *Miner Deposita*. <https://doi.org/10.1007/s00126-025-01366-8>
- Kamilli RJ, Kimball BE, Carlin JF (2017) Tin. Chapter S of *Critical Mineral Resources of the United States—Economic and environmental geology and prospects for future supply*. <https://doi.org/10.3133/pp1802S>
- Kay S, Mpodozis C (2021) The Andes. In: Alderton D, Elias SA (eds) *Encyclopedia of Geology*, 2<sup>nd</sup> edn. Academic Press, Cambridge, pp 1-15. <https://doi.org/10.1016/b978-0-08-102908-4.00173-9>
- Kennedy AK, Wotzlav JF, Schaltegger U, Crowley JL, Schmitz M (2014) Eocene zircon reference material for microanalysis of U-Th-Pb isotopes and trace elements. *Can Mineral* 52(3):409-421. <https://doi.org/10.3749/canmin.52.3.409>
- Khalegui F, Karimzadeh Z (2019) Occurrence, mineral chemistry and origin of dumortierite in Ali Javad porphyry Cu-Au deposit, Sheivar Dagh alteration system, NW Iran. *Period Mineral* 88:131-145 <https://doi.org/10.2451/2019PM869>

- Kiernan C (2020) Titanium for Automotive Applications. AZO MATERIALS. <https://www.azom.com/article.aspx?ArticleID=553>. Accessed 5 April 2023.
- Kley J, Muller J, Tawackloli S, Jacobshagen V, Manutsoglu E (1997) Pre-Andean and Andean-age deformation in the Eastern Cordillera of southern Bolivia. *J S Am Earth Sci* 10:1-19. [https://doi.org/10.1016/S0895-9811\(97\)00001-1](https://doi.org/10.1016/S0895-9811(97)00001-1)
- Kontak DJ, Clark AH, Farrar E, Strong DF (1985) The rift associated Permo-Triassic magmatism of the Eastern Cordillera: a precursor to the Andean orogeny. In: Pitcher, WS, Atherton MP, Cobbing J, Beckinsale RD (eds) *Magmatism at a plate edge: The Peruvian Andes*. Blackie, Glasgow, and Halsted Press, New York: 36-44. [https://doi.org/10.1007/978-1-4899-5820-4\\_5](https://doi.org/10.1007/978-1-4899-5820-4_5)
- Kontak DJ, Clark AH, Farrar E, Archibald DA, Baadsgaard HA (1990) Late Paleozoic-early Mesozoic magmatism in the Cordillera de Carabaya, Puno, southeastern Peru: Geochronology and petrochemistry. *J S Am Earth Sci* 3:213-230. [https://doi.org/10.1016/0895-9811\(90\)90004-K](https://doi.org/10.1016/0895-9811(90)90004-K)
- Kumari A, Panda R, Kumar Jha M, Rajesh Kumar J (2015) Process development to recover rare earth metals from monazite mineral: A review. *Miner Eng* 79: 102-115. <https://doi.org/10.1016/j.mineng.2015.05.003>
- Kutzschbach M, Wunder B, Meixner A, Wirth R, Heinrich W, Franz G (2017) Jeremejevite as a precursor for olenitic tourmaline: consequences of non-classical crystallization pathways for composition, textures and B isotope patterns of tourmaline. *Eur J Mineral* 29:239-255. <https://doi.org/10.1127/ejm/2017/0029-2604>
- Kynicky J, Smith MP, Xu C (2012) Diversity of Rare Earth Deposits: The Key Example of China. *Elements* 8(5):361-367. <https://doi.org/10.2113/gselements.8.5.361>
- Laubacher G (1978) Estudio geológico de la región Norte del Lago Titicaca. Instituto Geológico, Minero y Metalúrgico, Boletín 5, 120 p. <https://hdl.handle.net/20.500.12544/197>
- Lehmann B (2021) Formation of tin ore deposits: A reassessment. *Lithos* J. <https://doi.org/10.1016/j.lithos.2020.105756>
- Li L, Shi Y, Lawford J, Ubide T, Nemchin A, Caulifield J, Wang X, Zhao J (2021) Dating mafic magmatism by integrating baddeleyite, zircon and apatite U-Pb geochronology: A case study of Proterozoic mafic dykes/sills in the North China Craton. *Lithos* J 380-391:105820. <https://doi.org/10.1016/j.lithos.2020.105820>
- Li J, Kusky TM, Huang X (2002) Archean Podiform Chromitites and Mantle Tectonites in Ophiolitic Mélange, North China Craton: A Record of Early Oceanic Mantle Processes. *GSA Today* J 12(7):4-11. [https://doi.org/10.1130/1052-5173\(2002\)012<0004:APCAMT>2.0.CO;2](https://doi.org/10.1130/1052-5173(2002)012<0004:APCAMT>2.0.CO;2)
- Linnen RT, Williams-Jones AE, Martin RF (1992) Evidence of Magmatic Cassiterite Mineralization at the Nong Sua Aplite-Pegmatite Complex, Thailand. *Can Mineral* 30:739-761

- Liu P, Lehmann B, Holtz F, Weyer S, Cook N, Scicchitano MR, Kirkland C, Li X, Bao Z, Wilker F, Yuan H, Mao J (2025) Timing of meteoric-water incursion controls the scale of tin mineralization. *Geochim Cosmochim Acta* 411:110-122. <https://doi.org/10.1016/j.gca.2025.10.032>.
- Liu T, Jiang SY, Zheng RH, Chen W (2022) Titanite U-Pb dating and geochemical constraints on the Paleozoic magmatic-metamorphic events and Nb-Ta mineralization in the Yushishan deposit, South Qilian, NW China. *Lithos* 412-413:106612. <https://doi.org/10.1016/j.lithos.2022.106612>
- Liu Z, Wu F, Guo C, Zhao Z, Yang J, Sun J (2011) In situ U-Pb dating of xenotime by laser ablation (LA)-ICP-MS. *Chin Sci Bull J* 56:2948-2956. <https://doi.org/10.1007/s11434-011-4657-y>
- Loewy S, Connelly J, Dalziel I (2004) An orphaned basement block: The Arequipa-Antofalla Basement of the central Andean margin of South America. *GSA Bulletin* 116(1-2):171-187. <https://doi.org/10.1130/B25226.1>
- London D, Hervig RL, Morgan GB (1988) Melt-vapor solubilities and elemental partitioning in peraluminous granite-pegmatite systems: experimental results with Macusani glass at 200 MPa. *Contr Mineral and Petrol* 99:360–373. <https://doi.org/10.1007/BF00375368>
- López JC (1996) Geología del cuadrángulo de Nuñoa. Hoja 29-u: Lima, Instituto Geológico, Minero y Metalúrgico, Boletín A, 171 p. <https://hdl.handle.net/20.500.12544/197>
- Loveday D, Kartick M (2023) Technical Report and Mineral Resource Estimate – Falchani Property. [https://americanlithiumcorp.com/wp-content/uploads/2025/05/Falchani-NI43-101\\_Technical\\_Report\\_Final\\_12-14-23.pdf](https://americanlithiumcorp.com/wp-content/uploads/2025/05/Falchani-NI43-101_Technical_Report_Final_12-14-23.pdf). Accessed 6 Jul. 2025
- MINDAT (2023) <https://www.mindat.org/>. Accessed 15 February 2023
- Maino M, Dallagiovanna G, Dobson KJ, Gaggero L, Persano C, Seno S, Stuart FM (2012) Testing models of orogen exhumation using zircon (U–Th)/He thermochronology: Insight from the Ligurian Alps, Northern Italy. *Tectonophysics* 560-561:84-93. <https://doi.org/10.1016/j.tecto.2012.06.045>
- Malusà M, Garzanti E (2019) The Sedimentology of Detrital Thermochronology. In: Malusà M, Fitzgerald P (eds) *Fission-Track Thermochronology and its Application to Geology*. Springer International Publishing, Cham, pp 123-143
- Mamani M, Wörner G, Hartmann G, Cassard D (2005) A GIS-based isotope map of the Central Andes (13°S–28°S) and implication for ore formation. In: *Extended Abstracts, 6th International Symposium on Andean Geodynamics*. IRD Editions (Institut de Recherche pour le Développement, Paris), pp 464–467
- Mange MA, Maurer HFW (1992) *Heavy Minerals in Colour*. Elsevier, London

- Mange MA, Morton AC (2007) Chapter 13 - Geochemistry of Heavy Minerals. In: Mange MA, Wriqth DT (eds) *Developments in Sedimentology*, Vol 58. Springer, pp 345-391
- Mao W, Zhong H, Yang J, Tang Y, Liu L, Fu Y, Zhang X, Sein K, Aung SM, Li J, Zhang L (2020) Combined zircon, molybdenite, and cassiterite geochronology and cassiterite geochemistry of the Kuntabin tin-tungsten deposit in Myanmar. *Econ Geol* 115:603–625. <https://doi.org/10.5382/econgeo.4713>
- Mariano AN, Mariano AJ (2012) Rare Earth Mining and Exploration in North America. *Elements J* 8(5):369-376. <https://doi.org/10.2113/gselements.8.5.369>
- MarketsandMarkets (2021) Titanium Market by Product Type (Titanium Dioxide, Titanium Metal), Titanium Dioxide By End-use Industry, Titanium Metal By End-use Industry and Region (North America, Europe, Asia-Pacific, MEA & South America) (2022-2026). <https://www.marketsandmarkets.com/Market-Reports/titanium-market-53889164.html>. Accessed 6 June 2023.
- Mathur R, Powell W, Yao J, Guimaraes F, Cheng Y, Godfrey L, Tornos F, Killick D, Stephens J, Mao Jingwen, Sun M, Lehmann B (2025) Global Sn Isotope Compositions of Cassiterite Identify the Magmatic–Hydrothermal Evolution of Tin Ore Systems. *Geosci J* 15(1):28. <https://doi.org/10.3390/geosciences15010028>
- Meshram RR, Ingle K (2012) Mineralogy and Origin of Dumortierite from Girola Area, Bhandara District, Eastern Maharashtra. *J Geol Soc India* 79:181-188. <https://doi.org/10.1007/s12594-012-0020-4>
- Mišković A, Spikings RA, Chew DM, Košler J, Ulianov A, Schaltegger U (2009) Tectonomagmatic evolution of Western Amazonia: Geochemical characterization and zircon U-Pb geochronologic constraints from the Peruvian Eastern Cordilleran granitoids. *GSA Bulletin* 121(9-10):1298-1324. <https://doi.org/10.1130/B26488.1>
- Montel JM, Foret S, Veschambre M, Nicollet C, Provost A (1996) Electron microprobe dating of monazite. *Chem Geol J* 131:37-53. [https://doi.org/10.1016/0009-2541\(96\)00024-1](https://doi.org/10.1016/0009-2541(96)00024-1)
- Moore PB, Smith JV (1966) Wickmanite,  $Mn^{+2}[Sn^{+4}(OH)_6]$ , a new mineral from Langhan. *Arkiv Mineral Geol* 4(16):395-399
- Mordor Intelligence (2022) Niobium market - Growth, trends, COVID-19 impact, and forecasts (2023 - 2028). <https://www.mordorintelligence.com/industry-reports/niobium-market>. Accessed 8 April 2023.
- Mordor Intelligence (2022) Tantalum market - Growth, trends, COVID-19 impact, and forecasts (2023 - 2028). <https://www.mordorintelligence.com/industry-reports/tantalum-market>. Accessed 8 April 2023.
- Mordor Intelligence (2022) Tin market - Growth, trends, COVID-19 impact, and forecasts (2023 - 2028). <https://www.mordorintelligence.com/industry-reports/tin-market>. Accessed 8 May 2023.

- Morton A (1978) Sedimentology. In: Heavy Minerals, Berlin, pp 574-578. [https://doi.org/10.1007/3-540-31079-7\\_109](https://doi.org/10.1007/3-540-31079-7_109)
- Morton A, Hallsworth C (1999) Processes controlling the composition of heavy mineral assemblages in sandstones. *Sediment Geol* 124(1-4):3-29. [https://doi.org/10.1016/S0037-0738\(98\)00118-3](https://doi.org/10.1016/S0037-0738(98)00118-3)
- Naeser CW, Izett GA, Obradovich JD (1980) Fission-track and K-Ar ages of natural glasses. *Bull US Geol Surv* 1489:1-31.
- Nefedov EI, Griffin WL, Kristiansen R (1977) Minerals of the schoenfliesite-wickmanite series from Pitkaranta, Karelia, U.S.S.R. *Can Mineral* 15(4):437-445.
- Neymark L, Holm-Denoma C, Moscati R (2018) In situ LA-ICPMS U–Pb dating of cassiterite without a known-age matrix-matched reference material: Examples from worldwide tin deposits spanning the Proterozoic to the Tertiary. *Chem Geo J* 483:410-425. <https://doi.org/10.1016/j.chemgeo.2018.03.008>
- Noble DC, Vogel TA, Peterson PS, Landis GP, Grant NK, Jezek PA, McKee, EH (1984) Rare-element-enriched, S-type ash-flow tuffs containing phenocrysts of muscovite, andalusite, and sillimanite, southeastern Peru. *Geol* 12(1):35-39. [https://doi.org/10.1130/0091-7613\(1984\)12%3C35:RSATCP%3E2.0.CO;2](https://doi.org/10.1130/0091-7613(1984)12%3C35:RSATCP%3E2.0.CO;2)
- Nwamba MN, Kelepile T, Ngatcha RB, Suh C, Ilouga CD, Shemang E, Tantoh B, Tata E, Agyingi C (2023) Compositional provenance study of alluvial cassiterite at Bambol and Mayo Seni localities of the Mayo Darlé massif, northern Cameroon. *J Sediment Environ.* <https://doi.org/10.1007/s43217-023-00136-8>
- Olierook HK, Kirkland C, Szilas K, Hollis J, Gardiner NJ, Steinfeldt A, Jiang Q, Yakymchuk C, Evans N, McDonald BJ (2020) Differentiating between Inherited and Autocrystic Zircon in Granitoids. *J Petrol* 61(8). <https://doi.org/10.1093/petrology/egaa081>
- Oncken O, Hindle D, Kley J, Elger K, Victor P, Schemmann S (2006) Deformation of the Central Andean Upper Plate System – Facts, Fiction, and Constraints for Plateau Models. In: Oncken O, et al. *The Andes. Frontiers in Earth Sciences.* Springer, Berlin, Heidelberg, pp 3-27
- Panda R, Kumari A, Kumar Jha M, Hait J, Kumar V, Kumar JR, Young Lee J (2014) Leaching of rare earth metals (REMs) from Korean monazite concentrate. *J Ind Eng Chem* 20(4):2035-2042. <https://doi.org/10.1016/j.jiec.2013.09.028>
- Parrish R (2015) Uranium-Lead Dating. In: Rink J, Thompson J (eds) *Ency of Scientific Dating Methods*, 1st edn. Springer, Netherlands pp 848-856
- Paton C, Woodhead JD, Hellstrom JC, Hergt JM, Greig A, Maas R (2010) Improved laser ablation U-Pb zircon geochronology through robust downhole fractionation correction. *Geochem Geophys Geosyst* 11:1-36. <https://doi.org/10.1029/2009GC002618>

- Pepper M, Gehrels G, Pullen A, Ibanez-Mejia M, Ward K, Kapp P (2016) Magmatic history and crustal genesis of western South America: Constraints from U-Pb ages and Hf isotopes of detrital zircons in modern rivers. *Geosphere* 12(5):1532-1555. <https://doi.org/10.1130/GES01315.1>
- Perez ND, Horton BK, Carlotto V (2016) Structural inheritance and selective reactivation in the Central Andes: Cenozoic deformation guided by pre-Andean structures in Southern Peru. *Tectonophysics* 671:264-280. <https://doi.org/10.1016/j.tecto.2015.12.031>
- Perez ND, Horton BK, McQuarries N, Stübner K, Ehlers TA (2016) Andean shortening, inversion and exhumation associated with thin- and thick-skinned deformation in southern Peru. *Geol Mag* 153:1013-1041. <https://doi.org/10.1017/S0016756816000121>
- Petrus JA, Kamber BS (2012) VizualAge: A Novel Approach to Laser Ablation ICP-MS U-Pb Geochronology Data Reduction. *Geostand Geoanal Res* 36(3):247-270. <https://doi.org/10.1111/j.1751-908X.2012.00158.x>
- Pichavant M, Erdmann S, Kontak D, Michaud J, Villaros A (2024) Trace element partitioning in strongly peraluminous rare-metal silicic magmas – Implications for fractionation processes and for the origin of the Macusani Volcanics (SE Peru). *Geoch Cosm Acta* 365:229-252. <https://doi.org/10.1016/j.gca.2023.11.021>
- Pichavant M, Kontak DJ, Valencia-Herrera J, Clark AH (1988) The Miocene-Pliocene Macusani Volcanic, SE Peru. *Contrib Mineral Petrol* 100:300-324. <https://doi.org/10.1007/BF00379742>
- Pichavant M, Valencia-Herrera J, Boulmier S, Briquet L, Joron JL, Juteau M, Marin L, Michard A, Sheppard AMF, Treuil M, Vernet M (1987) The Macusani glasses, SE Peru: evidence of chemical fractionation in peraluminous magmas. In: Mysen BO (ed) *Magmatic processes, physicochemical principles*. *Geochem Soc Special Publ* 1:359–373.
- Plimer IR, Lu J, Kleeman JD (1991) Trace and rare earth elements in cassiterite - sources of components for the tin deposits of the Mole Granite, Australia. *Mineral Deposita* 26:267–274. <https://doi.org/10.1007/BF00191072>
- Pohlner J, Schmitt A, Chamberlain K, Davies J, Hildenbrand A, Austermann G (2020) Multimethod U–Pb baddeleyite dating: insights from the Spread-Eagle Intrusive Complex and Cape St. Mary's sills, Newfoundland, Canada. *Geochronol J* 2:187-208. <https://doi.org/10.5194/gchron-2-187-2020>.
- Polliand M, Schaltegger U, Frank M, Fontboté L (2005) Formation of intra-arc volcanosedimentary basins in the western flank of the central Peruvian Andes during Late Cretaceous oblique subduction: field evidence and constraints from U–Pb ages and Hf isotopes. *Int J Earth Sci (Geol Rundsch)* 94:231-242. <https://doi.org/10.1007/s00531-005-0464-5>

- Pollington A, Baxter E (2010) High resolution Sm-Nd garnet geochronology reveals the uneven pace of tectonometamorphic processes. *Earth Planet Sci Letters* 293(1-2):63-71. <https://doi.org/10.1016/j.epsl.2010.02.019>
- Proenza JA, Gonzáles-Jiménez JM, Garcia-Gasco A, Belousova E, Griffin WL, Talavera C, Rojas-Agramonte Y, Aiglsperger T, Navarro-Ciurana D, Pujol-Solá N, Gervilla F, O'Reilly SY, Jacob DE (2018) Cold plumes trigger contamination of oceanic mantle wedges with continental crust-derived sediments: Evidence from chromitite zircon grains of eastern Cuban ophiolites. *Geosci Front* 9(6):1921-1936. <https://doi.org/10.1016/j.gsf.2017.12.005>
- Poupeau G, Labrin E, Sabil N, Bigazzi G, Arroyo G, Vatin-Pérignon N (1993) Fission-track dating of 15 macusanite glass pebbles from the Macusani volcanic field (SE Peru). *Nucl Tracks Radiat Meas* 21:499–506. [https://doi.org/10.1016/1359-0189\(93\)90189-G](https://doi.org/10.1016/1359-0189(93)90189-G)
- Pupin JP (1980) Zircon and granite petrology. *Contr Mineral and Petrol* 73:207-220. <https://doi.org/10.1007/BF00381441>
- Quinde B (2020) Macusani Yellowcake estima que Perú superará a Chile en su quinto año de explotación de litio. *American Mining, Rumbo Minero Internacional*. <https://www.rumbominero.com/peru/noticias/mineria/macusani-yellowcake-estima-que-peru-superara-a-chile-en-su-quinto-ano-de-explotacion-de-litio/>. Accessed 19 June 2023
- Quinde B (2023) Producción de proyecto de litio Falchani iniciaría entre 2026 y 2027. <https://www.rumbominero.com/peru/produccion-de-proyecto-de-litio-falchani/>. Accessed 18 October 2023
- Ramírez-Briones JS (2025) Elemental and isotope characterization of the Lithium-rich Tuff from the Macusani Volcanic Field, Puno, Peru. PUCP-tesis. <http://hdl.handle.net/20.500.12404/28552>
- Ramírez-Briones JS, Torró L, Chiaradia M, Laurent O, Mandrou S, Tavazzani L, Chelle-Michou C, Vallance J, Baby P (2025) Petrogenesis of Volcanogenic Sedimentary Lithium Ore in the Neogene Macusani Volcanic Field, Puno, Peru. *J Petrol* 66(5): egaf041. <https://doi.org/10.1093/petrology/egaf041>
- Ramos V (1999) Plate tectonic setting of the Andean Cordillera. *Int J Geosci* 22:183-190. <https://doi.org/10.18814/epiiugs/1999/v22i3/005>
- Ramos V (2008) The basement of the Central Andes: The Arequipa and related terranes. *Annu Rev Earth Planet Sci* 36(1):289-324. <https://doi.org/10.1146/annurev.earth.36.031207.124304>
- Ramos V (2009) Anatomy and global context of the Andes: Main geologic features and the Andean orogenic cycle. In: Kay SM, Ramos V, Dickinson W (eds) *Backbone of the Americas: Shallow Subduction, Plateau Uplift, and Ridge and Terrane Collision: Geological Society of America Memoir* 204, pp 31-65

- Ramos V (2018) Tectonic evolution of the Central Andes: From terrane accretion to crustal delamination. *Annu Rev Earth Pl Sc* 36:289-324. <https://doi.org/10.1146/annurev.earth.36.031207.124304>
- Redacción EC (2018) Fission, otra firma que explora potencial de litio en el Perú. El Comercio. <https://elcomercio.pe/economia/peru/fission-firma-explora-potencial-litio-peru-noticia-538835-noticia/>. Accessed 19 June 2023
- Reiners PW (2005) Zircon (U-Th)/He Thermochronometry. *Rev Mineral Geochem* 58:151-179. <https://doi.org/10.2138/rmg.2005.58.6>
- Reinhardt N, Proenza JA, Villanova-de-Benavent TA, Bover-Arnal T, Torró L, Salas R, Dziggel A (2018) Geochemistry and Mineralogy of Rare Earth Elements (REE) in Bauxitic Ores of the Catalan Coastal Range, NE Spain. *J Minerals* 8:562. <https://doi.org/10.3390/min8120562>
- Rojas-Agramonte Y, Garcia-Casco A, Kemp A, Kröner A, Proenza J, Lázaro C, Liu D (2016) Recycling and transport of continental material through the mantle wedge above subduction zones: A Caribbean example. *Earth Planet Sci Lett* 436:93-107. <https://doi.org/10.1016/j.epsl.2015.11.040>
- Romer R (2015) Uranium-Lead, Ore deposits. In: Rink J, Thompson J (eds) *Ency of Scientific Dating Methods*, 1st edn. Springer, Netherlands pp 903-906
- Romero D, Valencia K, Alarcón P, Peña D, Ramos V (2013) The offshore basement of Perú: Evidence for different igneous and metamorphic domains in the forearc. *J South Am Earth Sci* 42:47-60. <https://doi.org/10.1016/j.jsames.2012.11.003>
- Roperch P, Sempere T, Macedo O, Arriagada C, Formari M, Tapia C, Garcia M, Laj C (2006) Counterclockwise rotation of late Eocene–Oligocene fore-arc deposits in southern Peru and its significance for oroclinal bending in the central Andes. *Tectonics* 25(3) <https://doi.org/10.1029/2005TC001882>
- Rosa D, Salgueiro R, Inverno C, de Oliveira D, Guimarães F (2010) Occurrence and Origin of Alluvial Xenotime from Central Eastern Portugal (Central Iberian Zone/Ossa-Morena Zone). *Comun Geol* 97:63-70. <http://repositorio.ineg.pt/bitstream/10400.9/1241/1/34368.pdf>
- Rubatto D (2015) Uranium-Lead, Metamorphic rocks. In: Rink J, Thompson J (eds) *Ency of Scientific Dating Methods*, 1st edn. Springer, Netherlands pp 898-903
- Rudashevsky NS, Lupal SD, Rudashevsky VN (2001) The hydraulic classifier. Russia patent N 2165300, Patent Cooperation Treaty PCT/RU01/00123 (Moscow: 20 April 2001; 10 May 2001) (in Russian and English)
- Rudashevsky NS, Garuti G, Anderson JC, Kretser Yu L, Rudashevsky VN, Zaccarini F (2002) Separation of accessory minerals from rocks and ores by hydroseparation (HS) technology: Method and application to CHR-2 chromitite, Niquelândia intrusion, Brazil. *Trans Inst Mining Metall* 111(1):87-94. <https://dx.doi.org/10.1179/aes.2002.111.1.87>

- Rupich SM, Chabal YJ (2018) Wet Chemical Modification of H-Terminated Si Surfaces as a First Step in Atomic Layer Deposition. In: Encyclopedia of Interfacial Chemistry, Elsevier, pp 886-900. <https://doi.org/10.1016/B978-0-12-409547-2.13136-1>
- Sanandres-Flores M, Torró L (2024)  $^{40}\text{Ar}/^{39}\text{Ar}$  geochronology of the Lithium-rich Tuff in the Macusani Volcanic Field, Oriental Cordillera, Peru. PUCP-tesis. <http://hdl.handle.net/20.500.12404/28843>
- Sandeman HA, Clark AH, Farrar E, Arroyo-Pauca G (1997) Lithostratigraphy, petrology and  $^{40}\text{Ar}$ - $^{39}\text{Ar}$  geochronology of the Crucero Supergroup, Puno Department, SE Peru. *J South Am Earth Sci* 10:223–245. [https://doi.org/10.1016/S0895-9811\(97\)00023-0](https://doi.org/10.1016/S0895-9811(97)00023-0)
- Sangine E, Gambogi J (2018) Zirconium and Hafnium. Geological Survey, Mineral Yearbook. <https://pubs.usgs.gov/myb/vol1/2018/myb1-2018-zirconium-hafnium.pdf>. Accessed 24 April 2023.
- Schaltegger U (2007) Hydrothermal Zircon. *Elements J* 3(1):51-79. <https://doi.org/10.2113/gselements.3.1.51>
- Scherer E, Whitehouse M, Münker C (2007) Zircon as a Monitor of Crustal Growth. *Elements J* 3(1):19-24. <https://doi.org/10.2113/gselements.3.1.19>
- Schouten C (1962) Determination Tables for Ore Microscopy. Elsevier, Amsterdam
- Schulz KJ, Piatak NM, Papp JF (2017) Niobium and tantalum. Chapter M of Critical Mineral Resources of the United States—Economic and environmental geology and prospects for future supply. <https://doi.org/10.3133/pp1802M>
- Scibiorski E, Kirkland CL, Kemp AIS, Tohver E, Evans NJ (2019) Trace elements in titanite: A potential tool to constrain polygenetic growth processes and timing. *Chem Geo J* 509:1-19. <https://doi.org/10.1016/j.chemgeo.2019.01.006>
- Segovia-More MK, Torró L, Villanova-de-Benavent C, Ramírez-Briones J, Vallance J, Monnier L, Laurent O, Salvi S, Baby P, Proenza JA, Nieto F (2023) High-resolution mineralogy of ‘lithium-rich tuff’ from the Macusani Volcanic Field, Puno, Peru. In: Proceedings of the 17<sup>th</sup> SGA Biennial Meeting, 28 August – 1 September 2023, 2:280-283.
- Sempere T (1995) Phanerozoic evolution of Bolivia and adjacent regions. In: Tankard AJ, Suárez R, Welsink JH (eds) Petroleum Basins of South America. AAPG Mem 62:207-230. <https://doi.org/10.1306/M62593C9>
- Sempere T, Butler RF, Richard DR, Marshall LG, Sharp W, Swisher CC III (1997) Stratigraphy and chronology of Late Cretaceous – Early Paleogene strata in Bolivia and Northwest Argentina. *Geol Soc Am Bull* 109:709-727. [https://doi.org/10.1130/0016-7606\(1997\)109%3C0709:SACOUC%3E2.3.CO;2](https://doi.org/10.1130/0016-7606(1997)109%3C0709:SACOUC%3E2.3.CO;2)
- Sempere T, Carlier G, Soler P, Fornari M, Carlotto V, Jacay J, Arispa O, Néraudeau D, Cárdenas J, Rosas S, Néstor J (2002) Late Permian-Middle Jurassic lithospheric

- thinning in Peru and Bolivia, and its bearing on Andean-age tectonics. *Tectonophysics* 345:153-181. [https://doi.org/10.1016/S0040-1951\(01\)00211-6](https://doi.org/10.1016/S0040-1951(01)00211-6)
- Sempere T, Javier J (2008) Anatomy of Central Andes: Distinguishing between western, magmatic Andes and eastern, tectonic Andes. 7<sup>th</sup> International Symposium on Andean Geodynamics ISAG 504-507
- Serranti S, Ferrini V, Umberto M, Cabri LJ (2002) Trace-element distribution in cassiterite and sulfides from rubané and massive ores of the Corvo deposit, Portugal. *Can Mineral* 40(3):815–835. <https://doi.org/10.2113/gscanmin.40.3.815>
- Shanks WC, Kimball BE, Tolcin AC, Guberman DE (2017) Germanium and Indium. Chapter I of Critical Mineral Resources of the United States—Economic and environmental geology and prospects for future supply. <https://doi.org/10.3133/pp1802I>
- Shedd KB (2022) TUNGSTEN. U.S. Geological Survey, Mineral Commodity Summaries. <https://pubs.usgs.gov/periodicals/mcs2022/mcs2022-tungsten.pdf>. Accessed 7 April 2023
- Shimizu M, Sano N, Ueki T, Komatsu T, Yasue K, Niwa M (2019) Provenance identification based on EPMA analyses of heavy minerals: Case study of the Toki Sand and Gravel Formation, central Japan. *Island Arc* 28(2):12295. <https://doi.org/10.1111/iar.12295>
- Spikings R, Reitsma MJ, Boekhout F, Mišković A, Ulianov A, Chiaradia M, Gerdes A, Schaltegger U (2016) Characterisation of Triassic rifting in Peru and implications for the early disassembly of western Pangaea. *Gondwana Res* 35:124-143. <https://doi.org/10.1016/j.gr.2016.02.008>
- Stearns MA, Hacker BR, Ratschbacher L, Rutte D, Kylander-Clark ARC (2015) Titanite petrochronology of the Pamir gneiss domes: Implications for middle to deep crust exhumation and titanite closure to Pb and Zr diffusion. *Tectonics* 34(4):784-802. <https://doi.org/10.1002/2014TC003774>
- Stow M (1946) Dating sedimentation, vulcanism, and orogeny in Bear Tooth Mountain region, Montana, by heavy minerals. *GSA Bull* 57(7):675-686. [https://doi.org/10.1130/0016-7606\(1946\)57\[675:DSVAOI\]2.0.CO;2](https://doi.org/10.1130/0016-7606(1946)57[675:DSVAOI]2.0.CO;2)
- Strategic Metals Invest (2023) Hafnium Prices. <https://strategicmetalsinvest.com/hafnium-prices/#forecast>. Accessed 25 April 2023
- Subasinghe CS, Ratnayake AS, Roser B, Sudesh M, Wijewardhana DU, Attanayake N, Pitawala J (2022) Global distribution, genesis, exploitation, applications, production and demand of industrial heavy minerals. *Arabian J of Geosciences*. <https://doi.org/10.1007/s12517-022-10874-0>
- Sun J, Yang J, Wu F, Xie L, Yang Y, Liu Z, Li X (2012) In situ U-Pb dating of titanite by LA-ICPMS. *Chi Sci Bull* 57(20):2506-2516. <https://doi.org/10.1007/s11434-012-5177-0>.

- Sundell K, Saylor J, Pecha M (2019) Chapter 13 - Provenance and recycling of detrital zircons from Cenozoic Altiplano strata and the crustal evolution of western South America from combined U-Pb and Lu-Hf isotopic analysis. In: Horton B, Folguera A (eds) *Andean Tectonics*. Elsevier, Amsterdam, pp 363-397
- Tassinari CCG, Macambira, MJB (1999) Geochronological provinces of the Amazonian craton. *Episodes* 22:174–182. <https://doi.org/10.18814/epiiugs/1999/v22i3/004>
- Taylor RT, McLennan SM (1995) The geochemical evolution of the continental crust. *Rev of Geophysics* 33(2):241-265. <https://doi.org/10.1029/95RG00262>
- The Mineral Corporation (2019) Mineral Resource Estimates for the Falchani Lithium Project in the Puno District of Peru. Plateau Energy Metals Inc. [https://plateauenergymetals.com/wp-content/uploads/2019/04/43-101-Falchani-Project-20190418\\_final.pdf](https://plateauenergymetals.com/wp-content/uploads/2019/04/43-101-Falchani-Project-20190418_final.pdf). Accessed 19 June 2023
- Torró L, Harlaux M, Castro-Morante A, Vallance J, Tavazzani L, Bouvier AS, Bovay T, Chelle-Michou C, Sempere T, Melgarejo JC (2024) Tin Mineralization in the Triassic Chacaltaya District (Cordillera Real, Bolivia) Traced by In Situ Chemical and  $\delta^{18}\text{O}$ - $\delta^{11}\text{B}$  Compositions of Tourmaline. *Econ Geol* 119:471-500. <https://doi.org/10.5382/econgeo.5051>
- Torró L, Proenza JA, Rojas-Agramonte Y, Garcia-Casco A, Yang JH, Yang YH (2018) Recycling in the subduction factory: Archaean to Permian zircons in the oceanic Cretaceous Caribbean island-arc (Hispaniola). *Gondwana Res* 54:23-27. <https://doi.org/10.1016/j.gr.2017.09.010>
- Torró L, Ramirez-Briones J, Sanandres-Flores MK, Monnier L, Villanova-de-Benavent C, Zanetti KA, Konrad K, Vallance J, Laurent O, Salvi S, Baby P, Proenza JA, Bachmann O, Nieto F (2025) Lithium mica clasts document magmatic evolution prior to eruption in the Macusani Volcanic Field in Peru. *Sci Rep* 15:13023. <https://doi.org/10.1038/s41598-025-96173-6>
- Valdivia W, Chapilliquén P, Gonzales V, Ochoa J (2021) Geología del cuadrángulo de Jauja (hojas 24m1, 24 m2, 24m3, 24m4). Instituto Geológico, Minero y Metalúrgico, Boletín Serie L: Actualización Carta Geológica Nacional (Escala 1: 50 000) N° 22 90 pp. <https://hdl.handle.net/20.500.12544/3142>
- Villanova-de-Benavent C, Proenza JA, Torró L, Aisglsperger T, Domenech D, Domínguez-Carretero D, Llover X, Suñer P, Ramírez A, Rodríguez J (2023) REE ultra-rich karst bauxite deposits in the Pedernales Peninsula, Dominican Republic: Mineralogy of REE phosphates and carbonates. *Ore Geol Revs* 157:105422. <https://doi.org/10.1016/j.oregeorev.2023.105422>
- Wall C, Scoates J (2016) High-precision u-pb zircon-baddeleyite dating of the J-M reef platinum group element deposit in the Stillwater Complex, Montana (USA). *Econ Geol* 111(3):771–782. <https://doi.org/10.2113/econgeo.111.3.771>
- Wang A, Freeman JJ, Jolliff BL (2015) Understanding the Raman spectral features of phyllosilicates. *J Raman Spectrosc* 46:829–845. <https://doi.org/10.1002/jrs.4680>

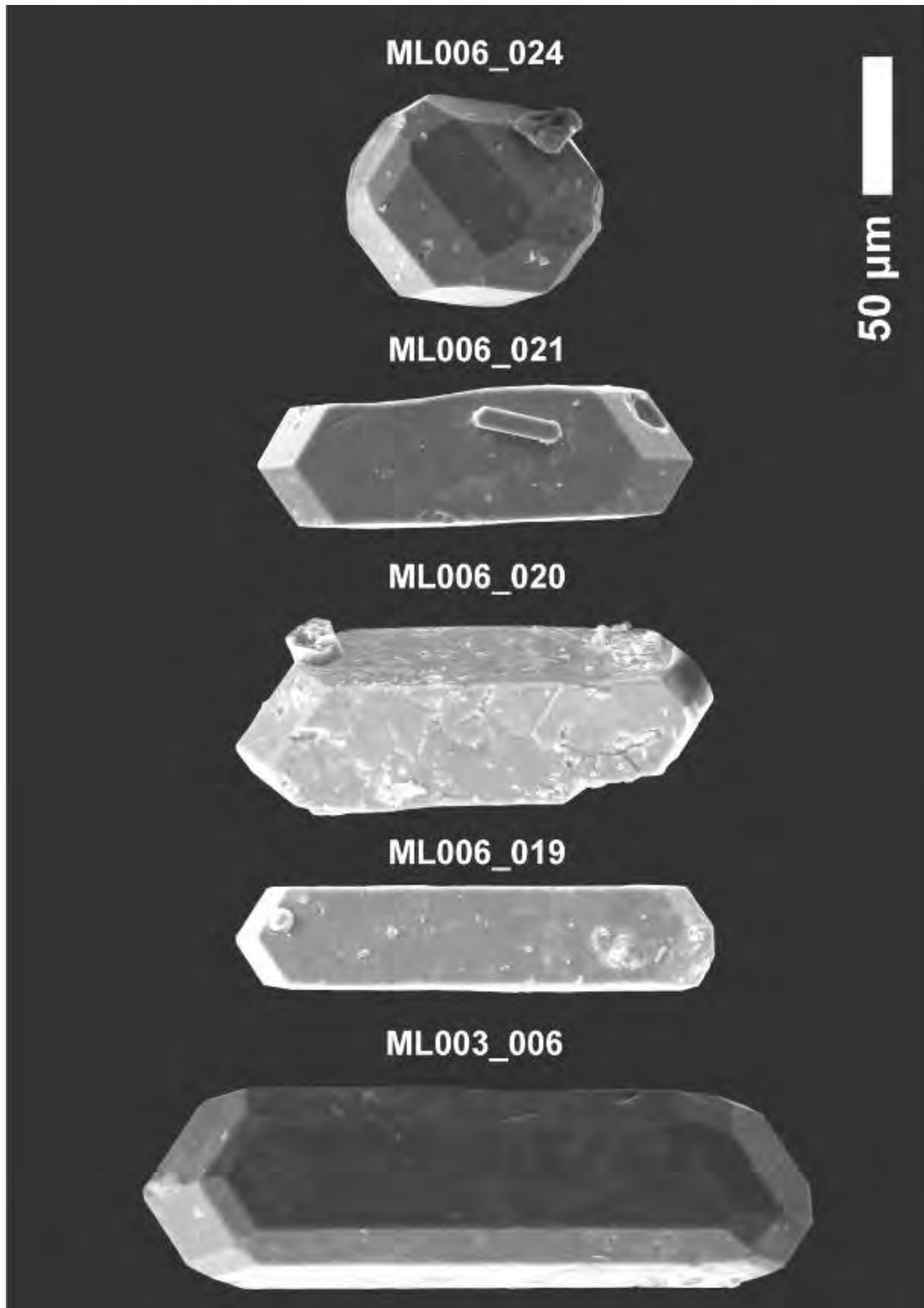
- Wang X, Chen X, Zou S, Jia Z, Li B, Wang H, Xu D (2023) Geochronology, geochemistry, and mineral chemistry of the Lingshan-Huangshan complex, South China: Insights into Nb and Ta enrichment. *Ore Geol Rev* 157:105433. <https://doi.org/10.1016/j.oregeorev.2023.105433>
- Wark DA, Miller CF (1993) Accessory mineral behavior during differentiation of a granite suite: monazite, xenotime and zircon in the Sweetwater Wash pluton, southeastern California, U.S.A. *Chem Geol* 110:49-67. [https://doi.org/10.1016/0009-2541\(93\)90247-G](https://doi.org/10.1016/0009-2541(93)90247-G)
- Watson EB, Wark DA, Thomas JB (2006) Crystallization thermometers for zircon and rutile. *Contrib Mineral Petrol* 151:413–433. <https://doi.org/10.1007/s00410-006-0068-5>
- Williams ML, Jercinovic MJ, Hetherington CJ (2007) Microprobe Monazite Geochronology: Understanding Geologic Processes by Integrating Composition and Chronology. *Annu Rev Earth Planet Sci* 35:75-137. <https://doi.org/10.1146/annurev.earth.35.031306.140228>
- Wood B, Kiseeva E, Matzen A (2013) Garnet in the Earth's Mantle. *Elements J* 9(6):421-426. <https://doi.org/10.2113/gselements.9.6.421>
- Woodruff LG, Bedinger M, Piatak NM (2017) Titanium. Chapter T of Critical mineral resources of the United States—Economic and environmental geology and prospects for future supply. <https://doi.org/10.3133/pp1802T>
- Wörner G, Mamani M, Blum-Oeste M (2018) Magmatism in the Central Andes. *Elements* 14:237-244. <https://doi.org/10.2138/gselements.14.4.237>
- Xu Y, Liu H, Meng Z, Cui J, Zhao J, Zhao W, Li L (2012) Decomposition of bastnasite and monazite mixed rare earth minerals calcined by alkali liquid. *J Rare Earth* 30(8):155-158. [https://doi.org/10.1016/S1002-0721\(12\)60014-3](https://doi.org/10.1016/S1002-0721(12)60014-3)
- Yim WW, Gleadow AJM, van Moort JC (1985) Fission track dating of alluvial zircons and heavy mineral provenance in Northeast Tasmania. *J Geol Soc London* 142(2):351-356. <https://doi.org/10.1144/gsjgs.142.2.0351>
- Zhang YB, Li QL, Lan ZW, Wu FY, Li XH, Yang JH (2015) Diagenetic xenotime dating to constrain the initial depositional time of the Yan-Liao Rift. *Precambrian Res J* 271:20-32. <https://doi.org/10.1016/j.precamres.2015.09.024>
- Zhang, D., Luan, Y., Li, Y., Zhang, R., Wei, J., Qiu, K (2025) Geochronology and geochemistry of cassiterite from the Yichun Ta-Nb-Li deposit, South China: New constraints on the mineralization age and implications for rare metal enrichment. *Ore Geol Rev* 186:106937. <https://doi.org/10.1016/j.oregeorev.2025.106937>
- Zhu YS, Yang JH, Sun JF, Wang H (2017) Zircon Hf-O isotope evidence for recycled oceanic and continental crust in the sources of alkaline rocks. *Geol* 45(5):407–410. <https://doi.org/10.1130/G38872.1>

Zi J, Rasmussen B, Muhling JR, Fletcher IR, Thorne AM, Johnson SP, Cutten HN, Dunkley DJ, Korhonen FJ (2015) In situ U–Pb geochronology of xenotime and monazite from the Abra polymetallic deposit in the Capricorn Orogen, Australia: Dating hydrothermal mineralization and fluid flow in a long-lived crustal structure. *Precambrian Res* 260:91-112. <https://doi.org/10.1016/j.precamres.2015.01.010>

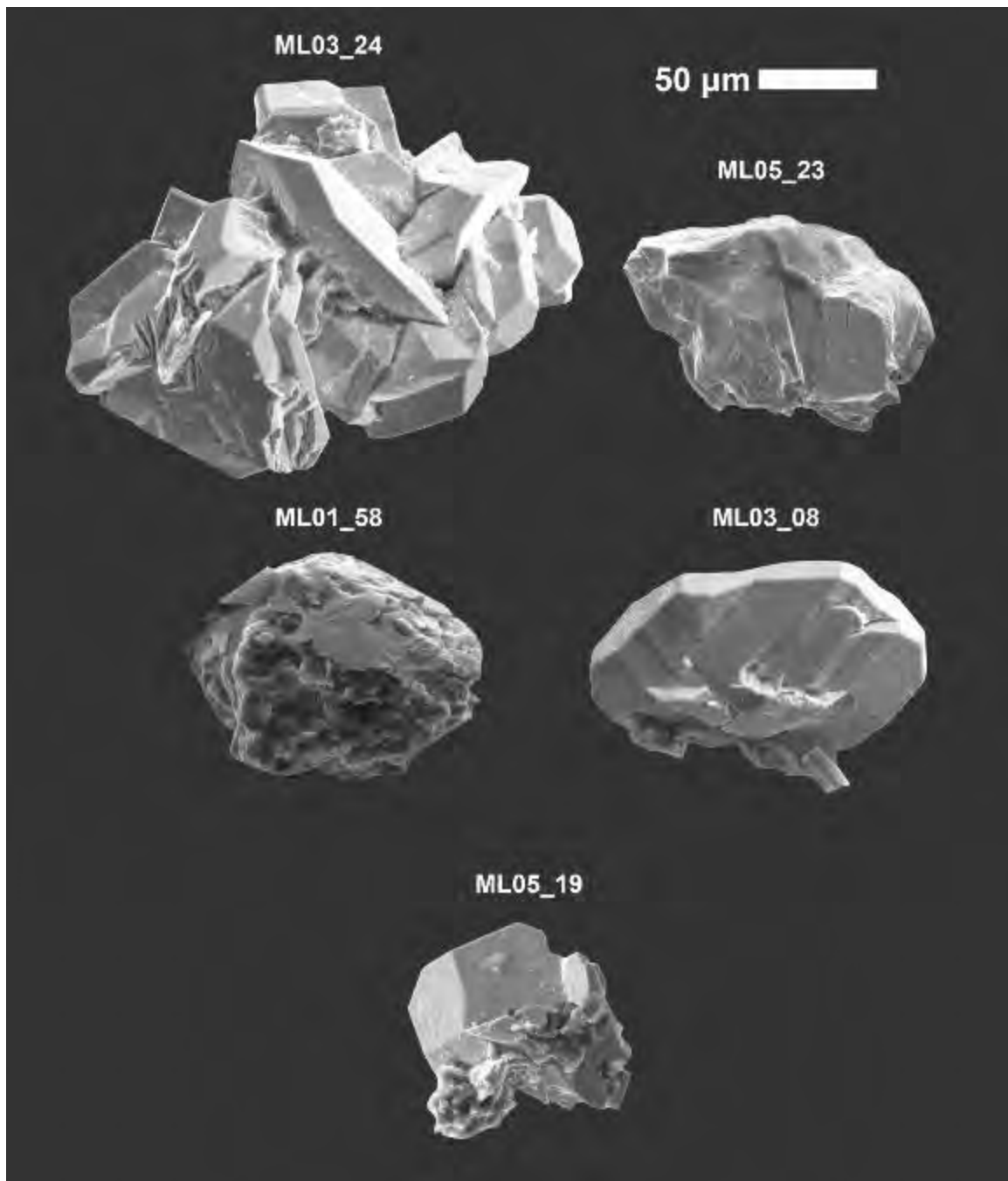


Appendix A

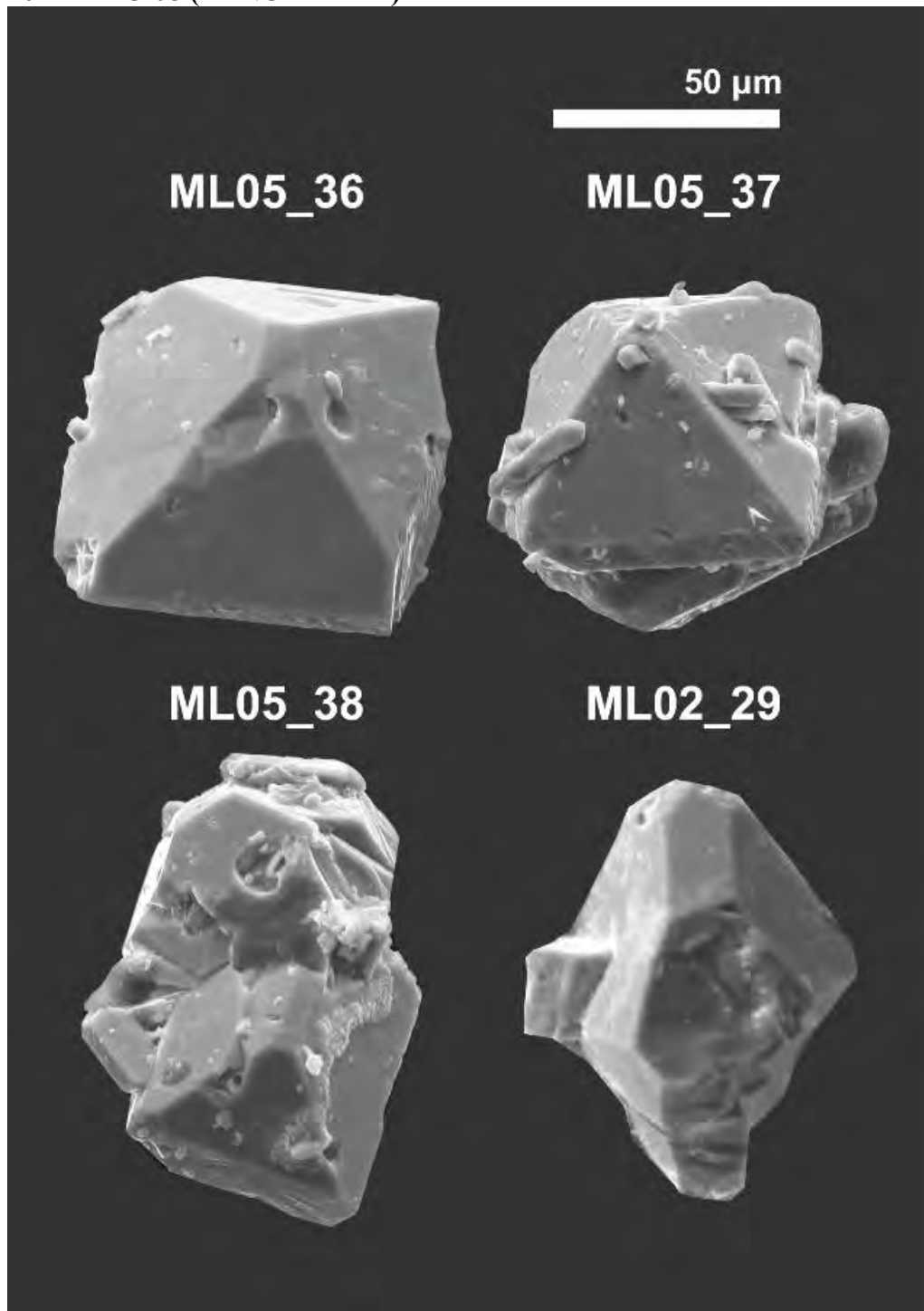
2021-MAC-08 (ZIRCON)



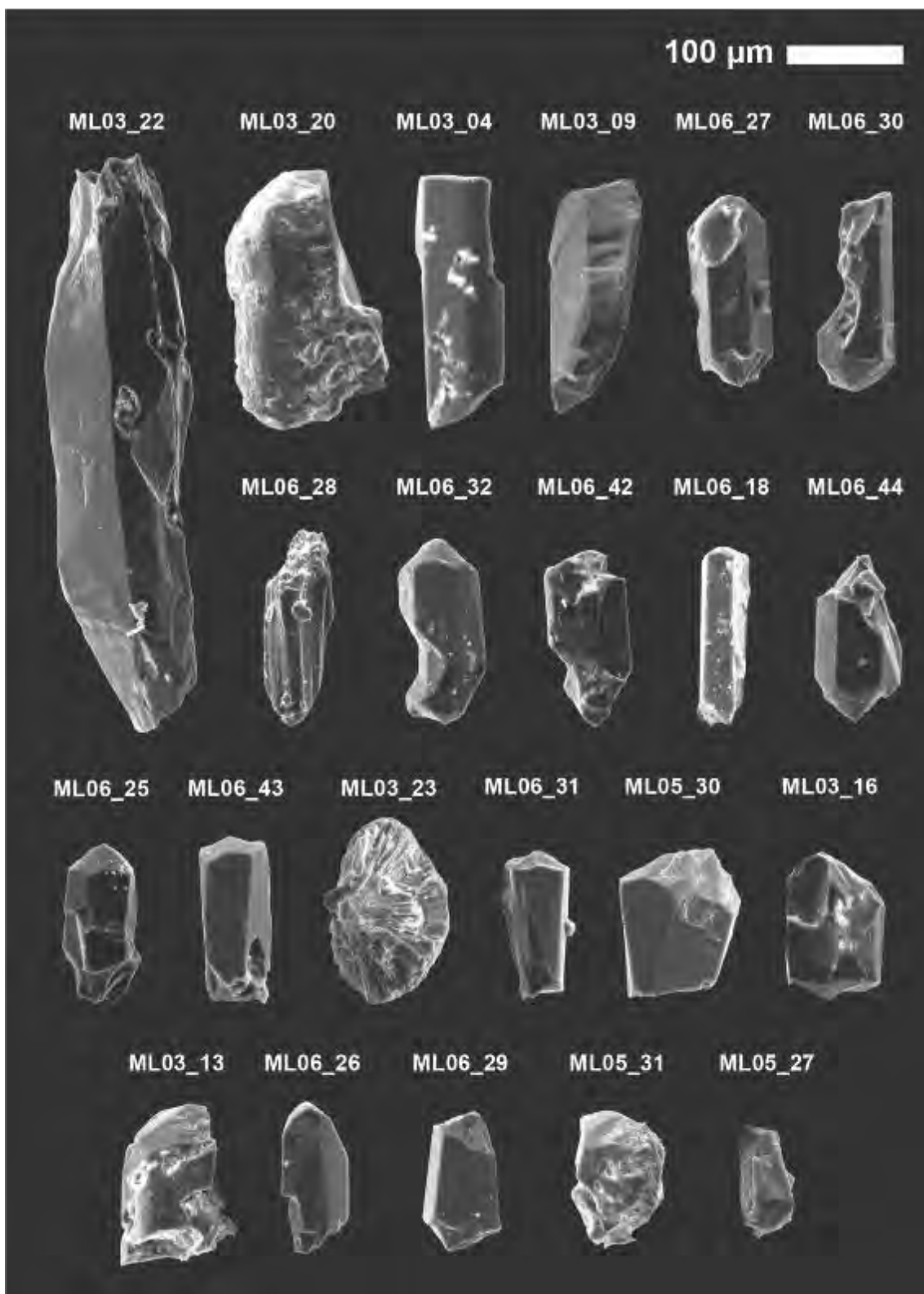
2021-MAC-08 (CASSITERITE)



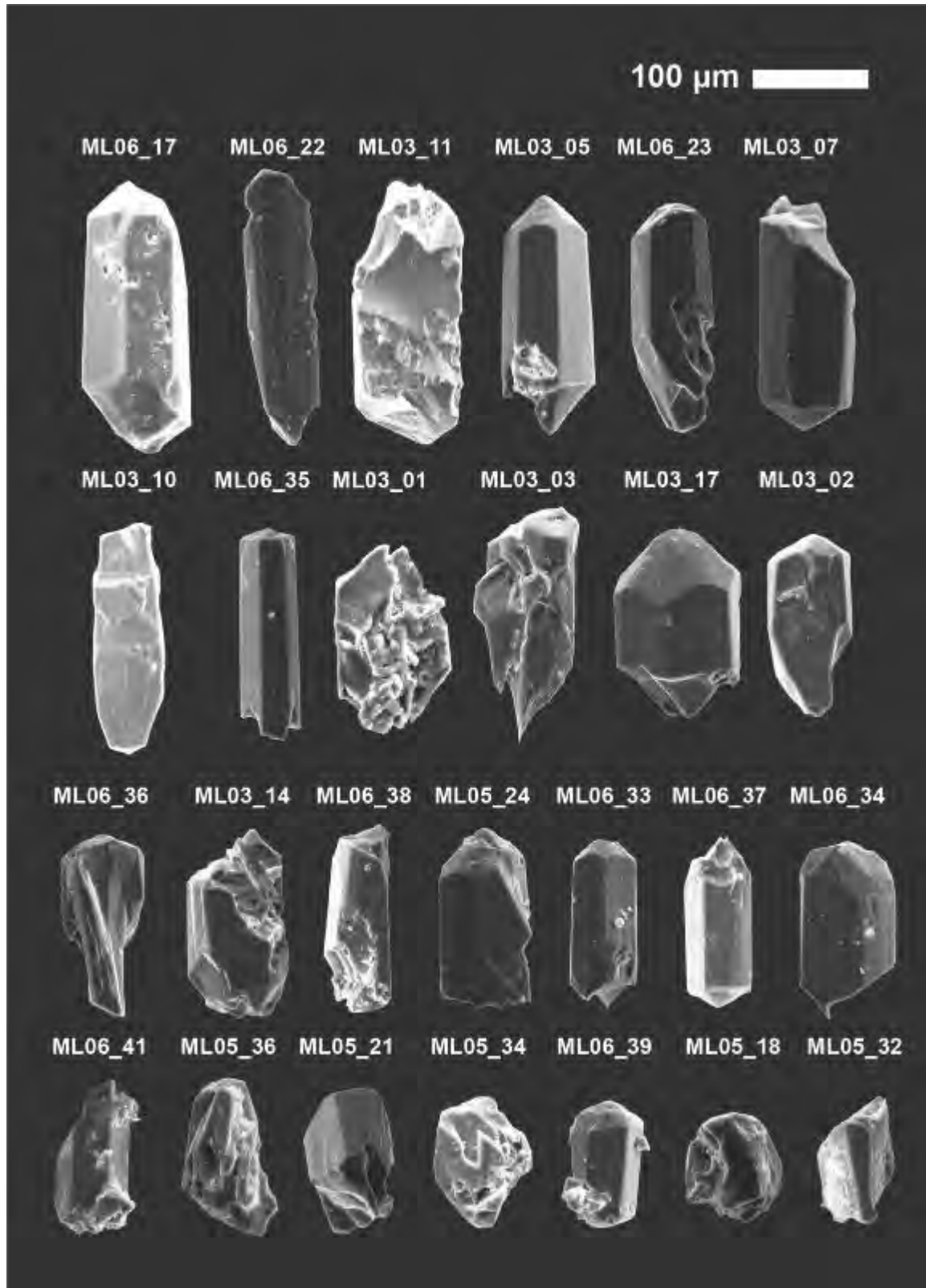
2021-MAC-08 (XENOTIME-Y)



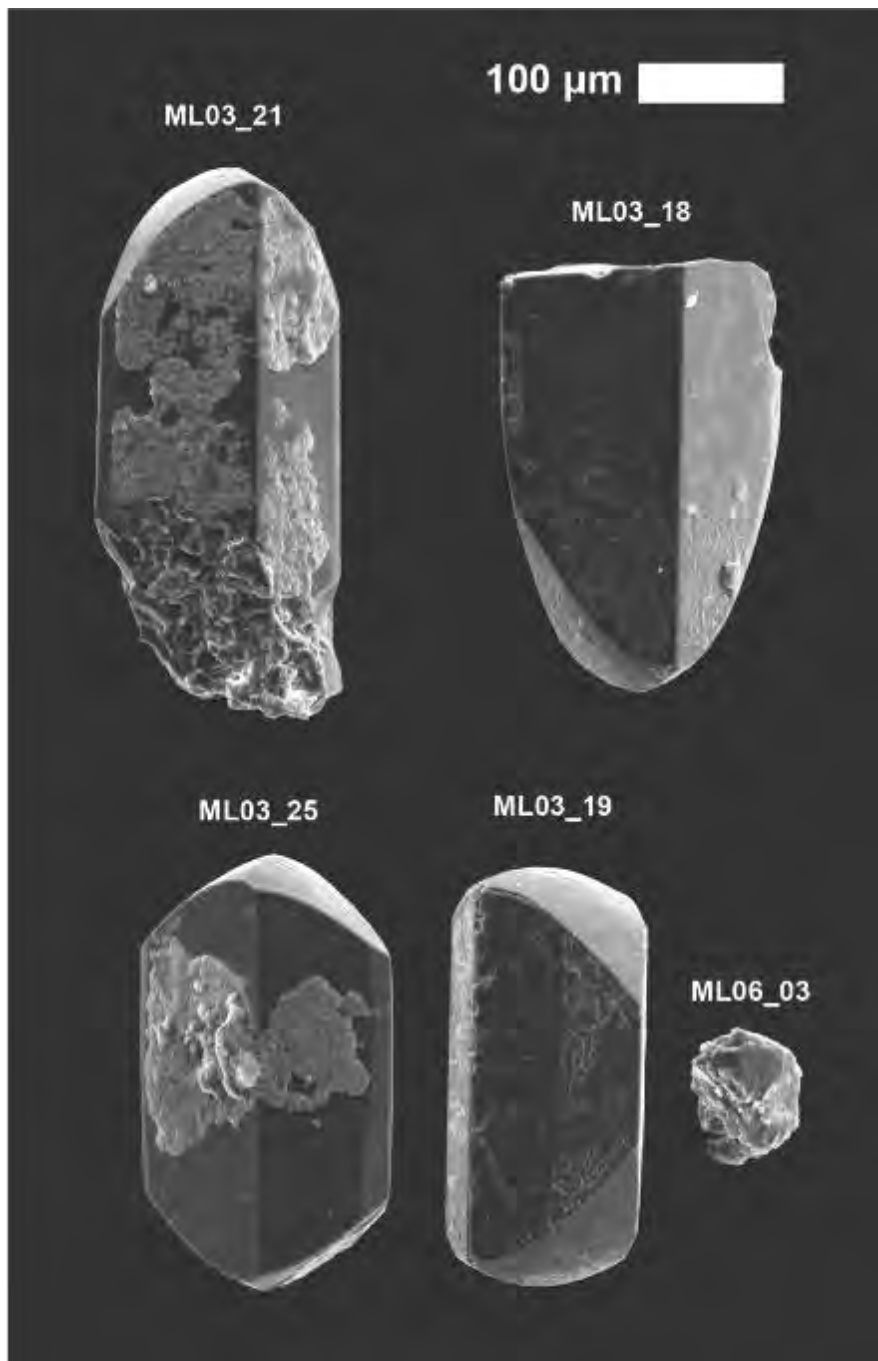
## 2021-MAC-08 (CORUNDUM)

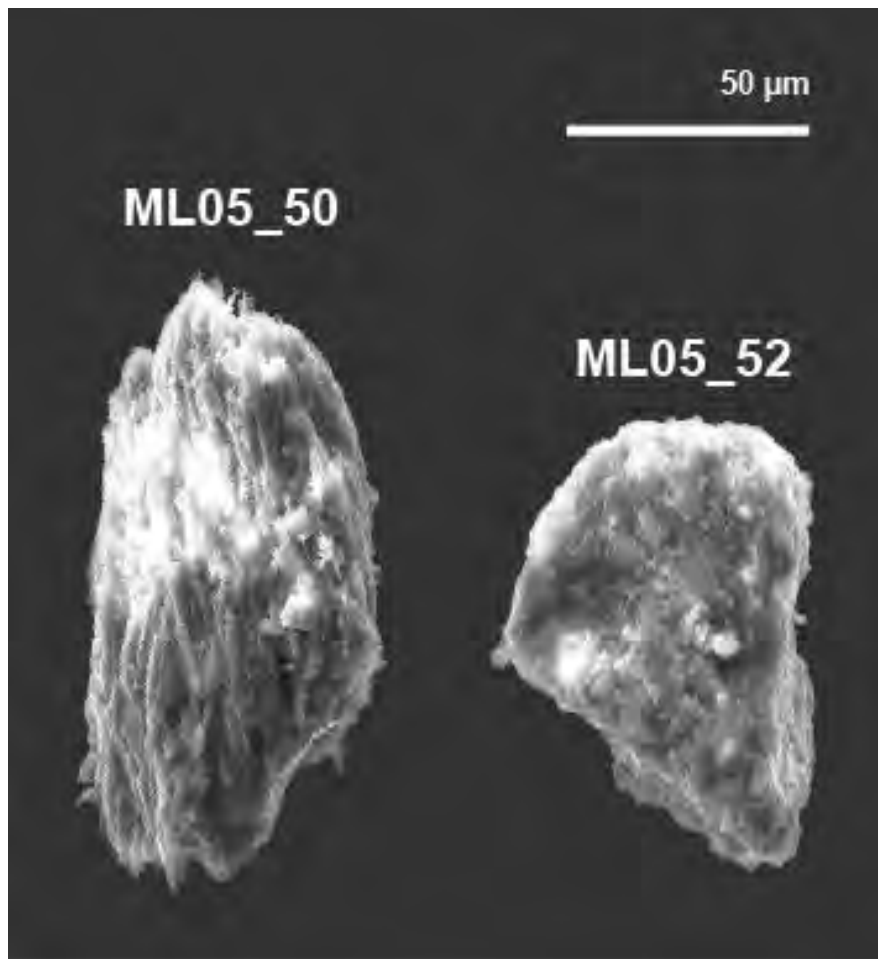


## 2021-MAC-08 (JEREMEJEVITE)



2021-MAC-08 (TOPAZ)

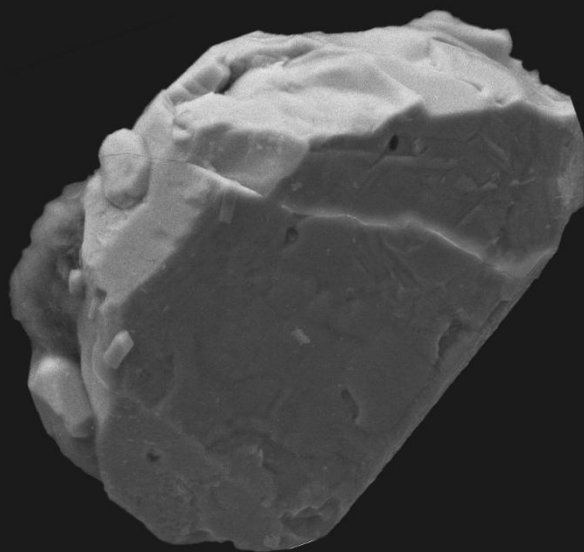


**2021-MAC-08 (DUMORTIERITE)**

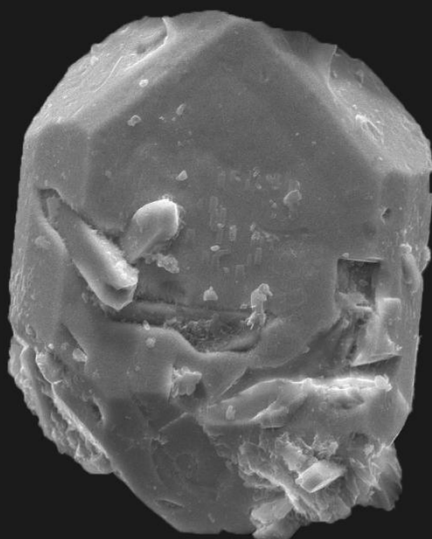
## 2021-MAC-08 (MONAZITE-Ce)

50  $\mu\text{m}$ 

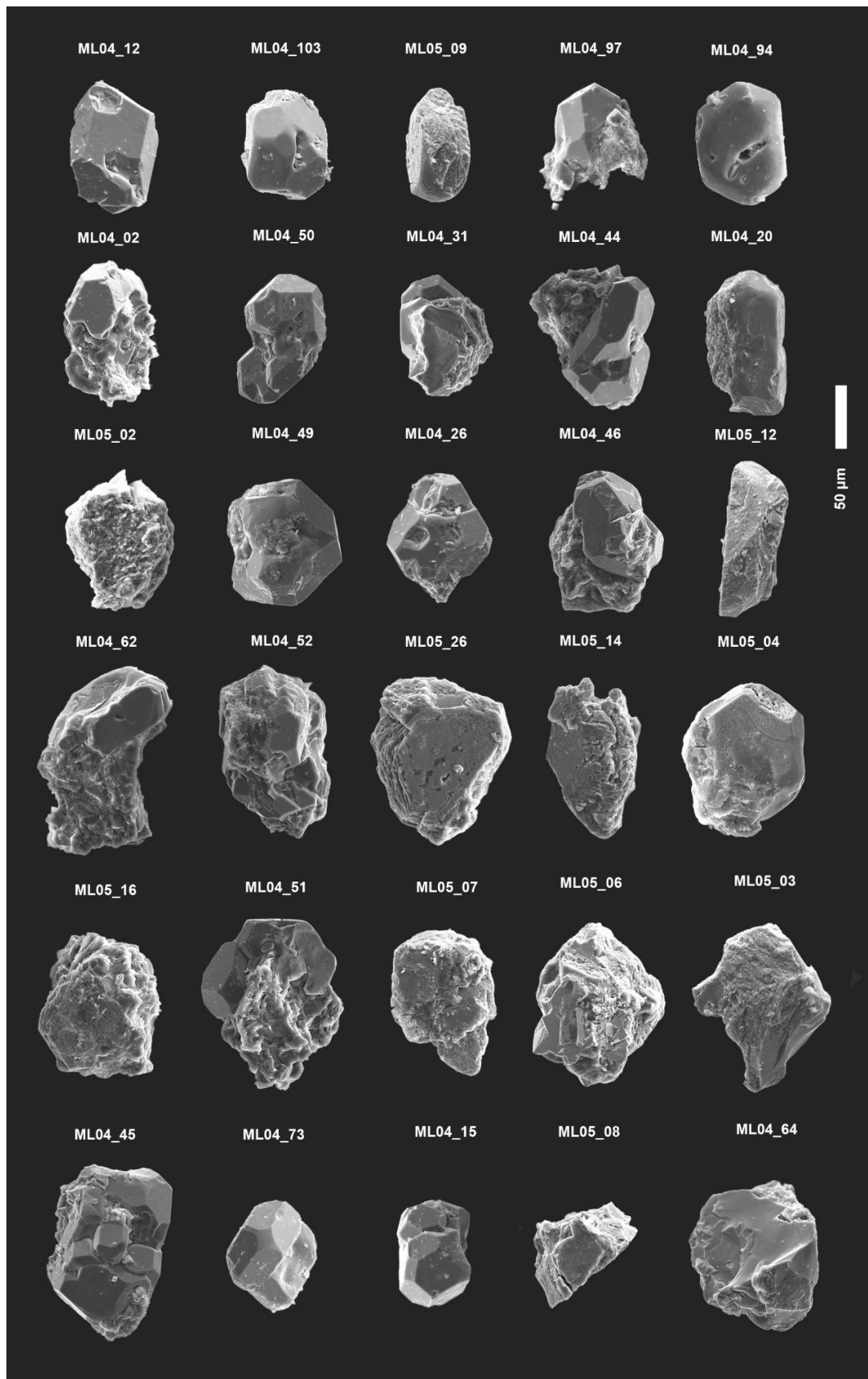
ML02\_25



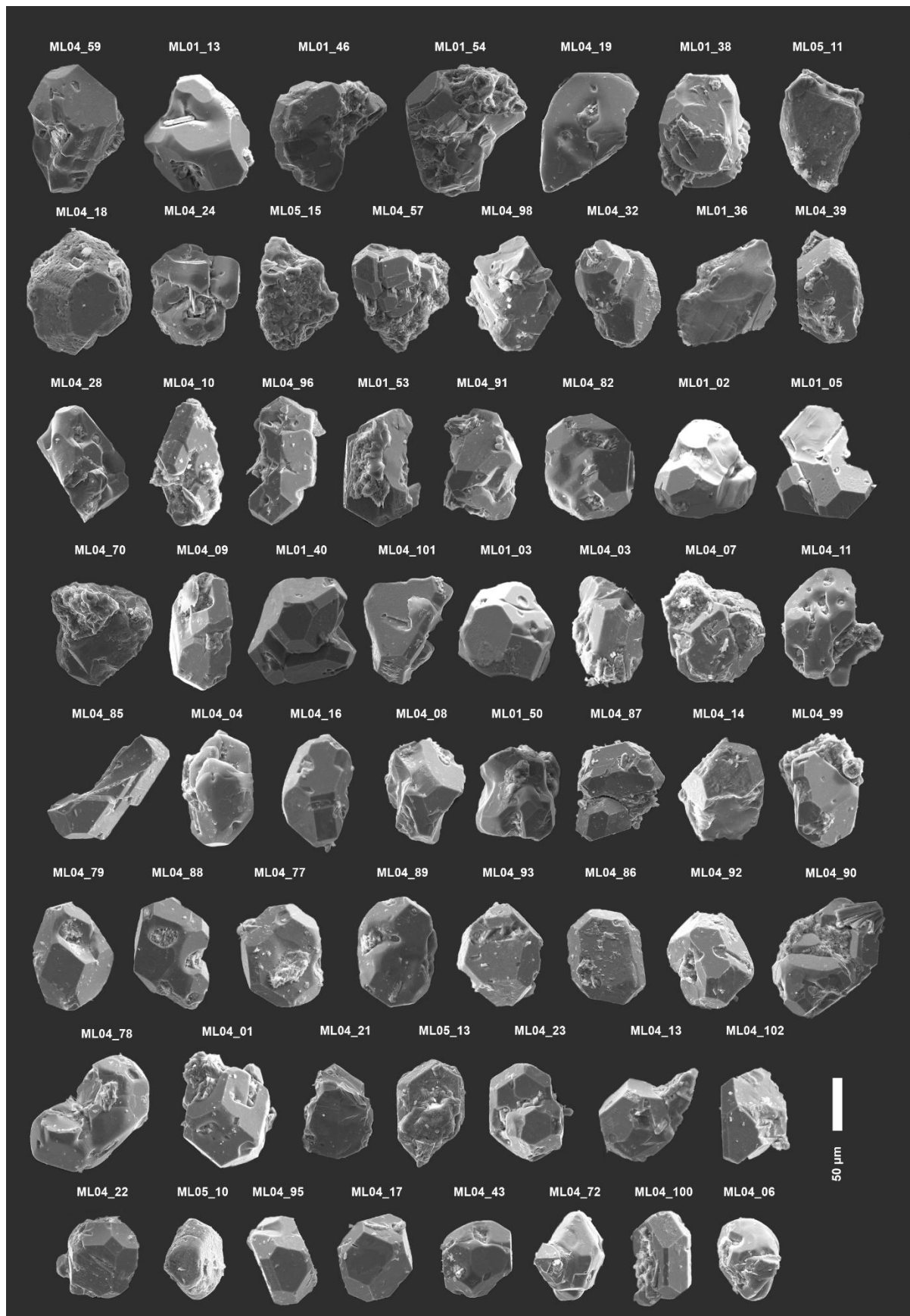
ML05\_40

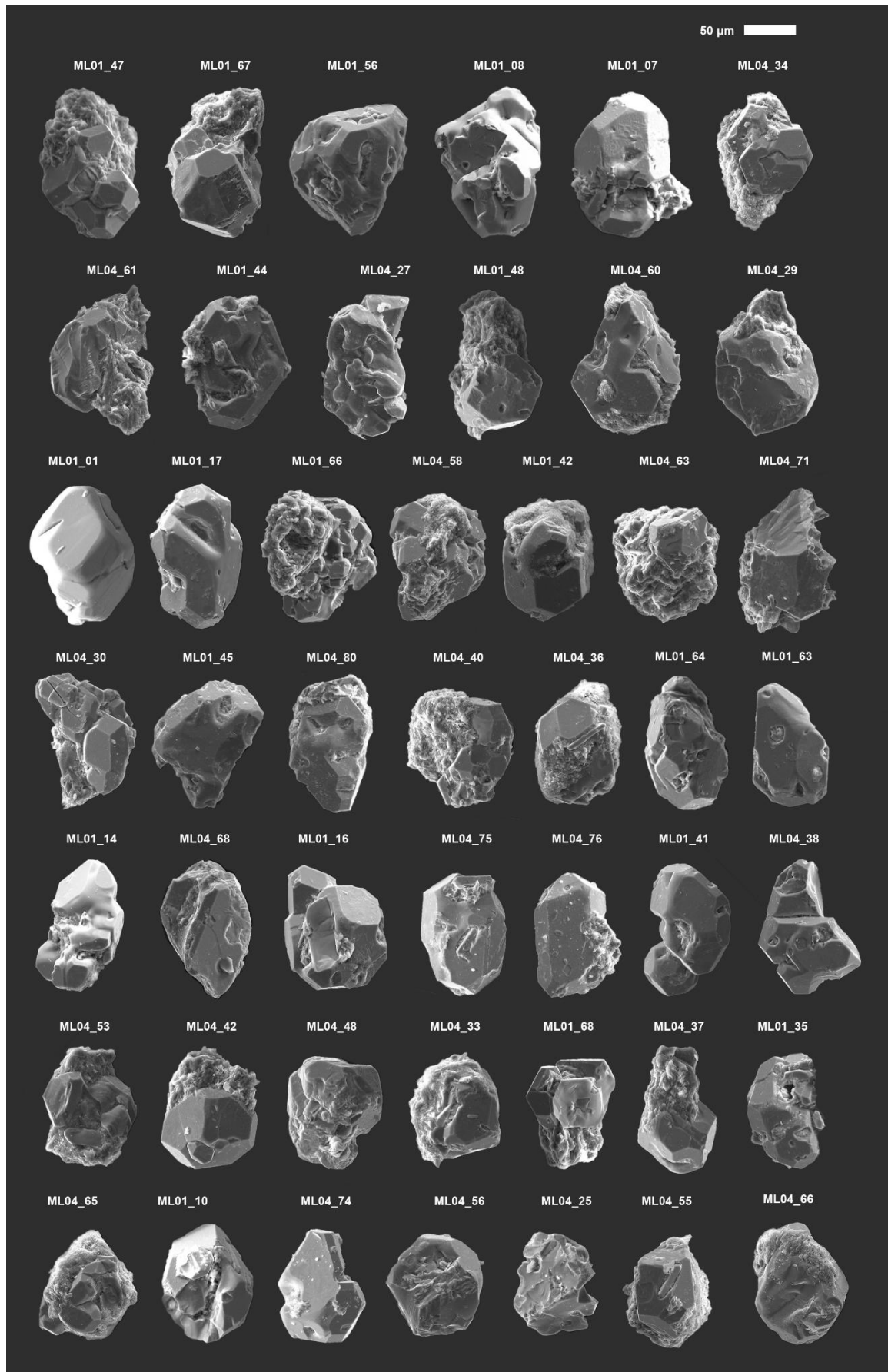


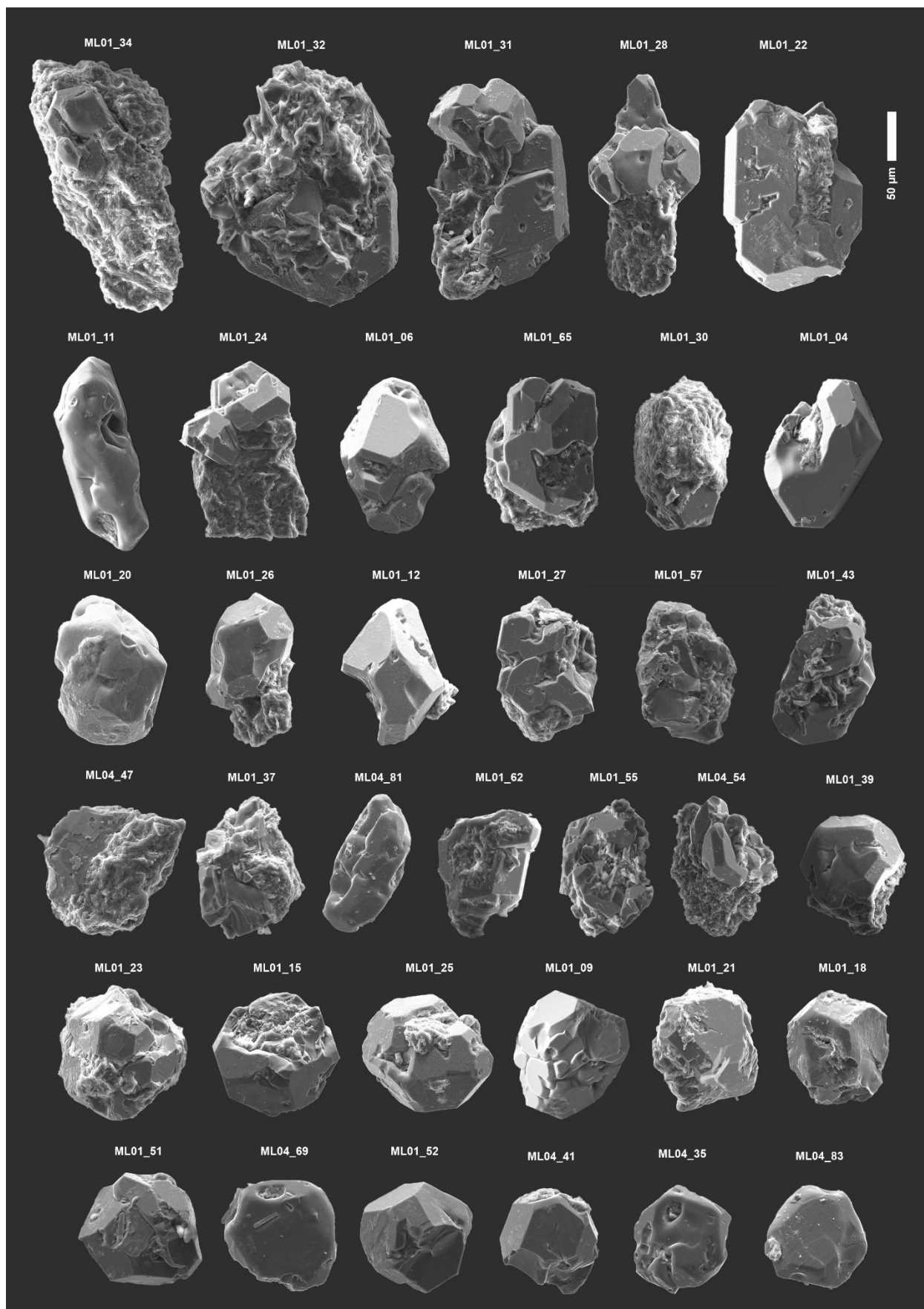
## 2021-MAC-08 (RUTILE)



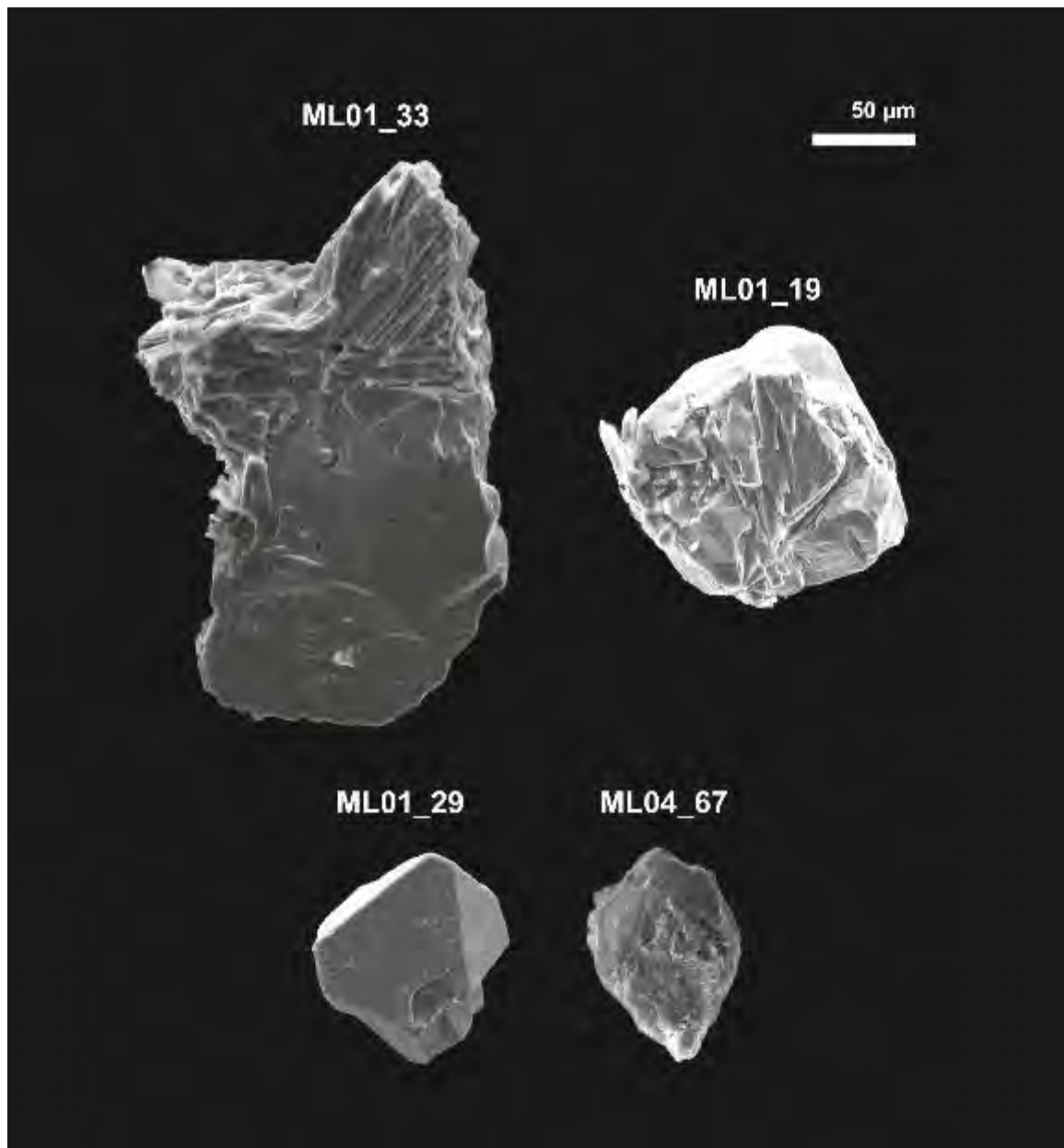
## 2021-MAC-08 (RUTILE-LIKE GRAINS)



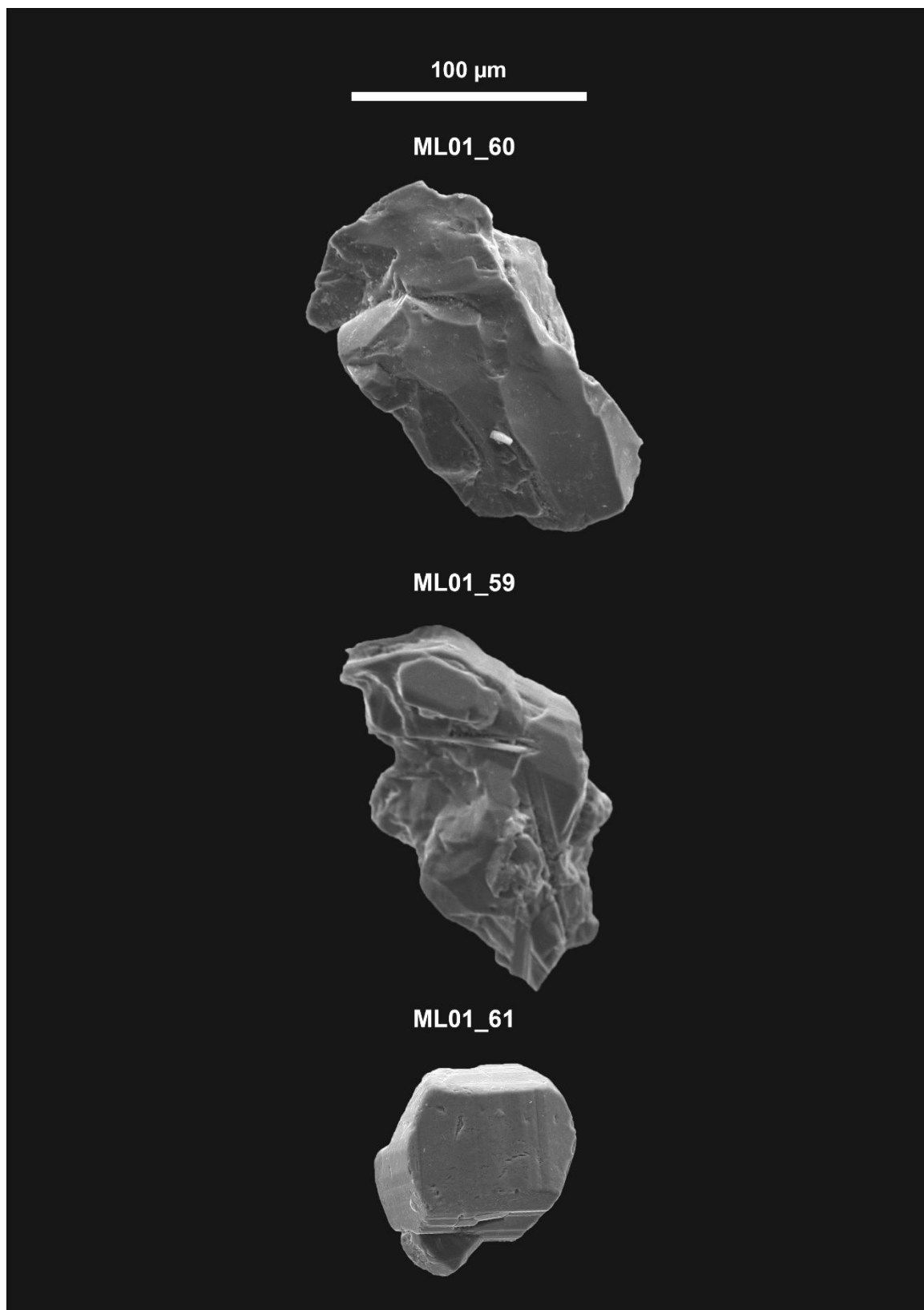




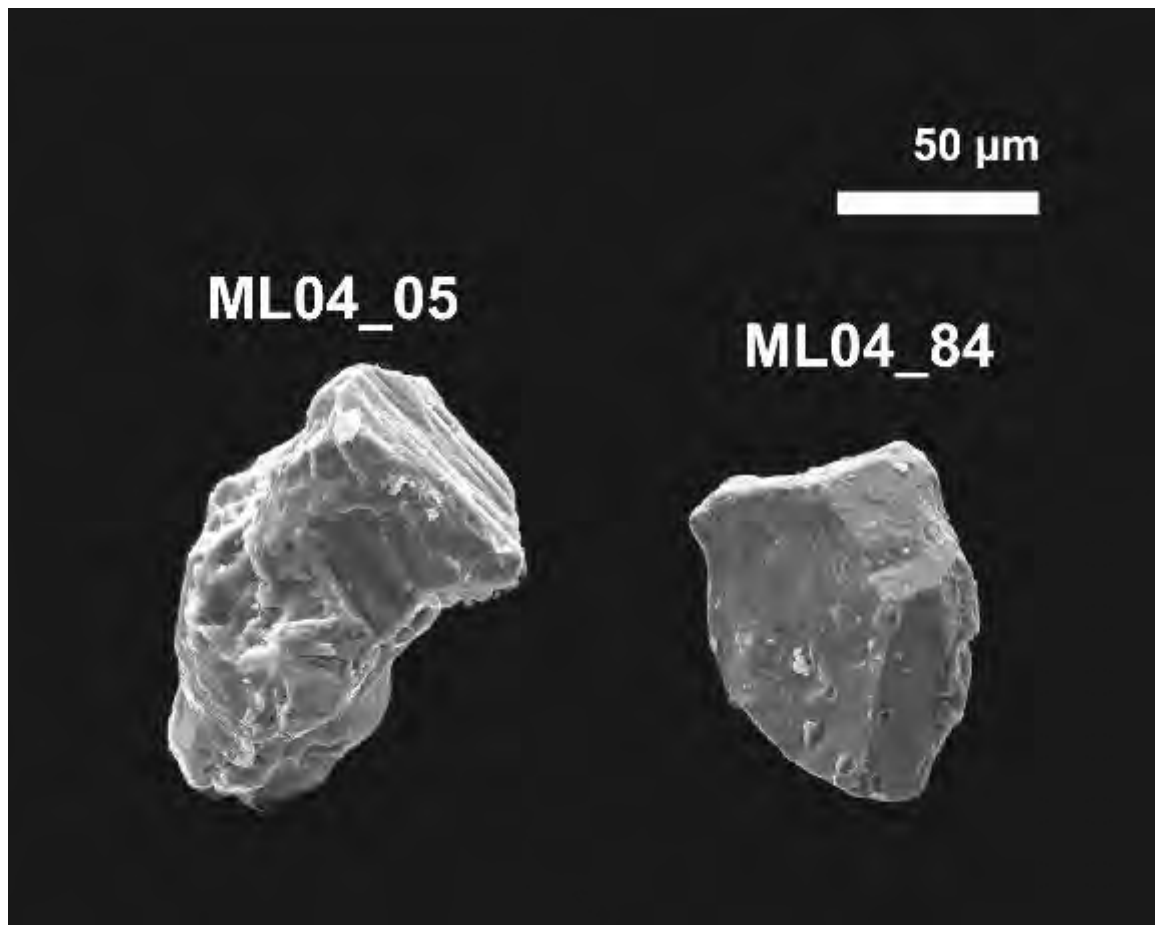
## 2021-MAC-08 (MAGNETITE)



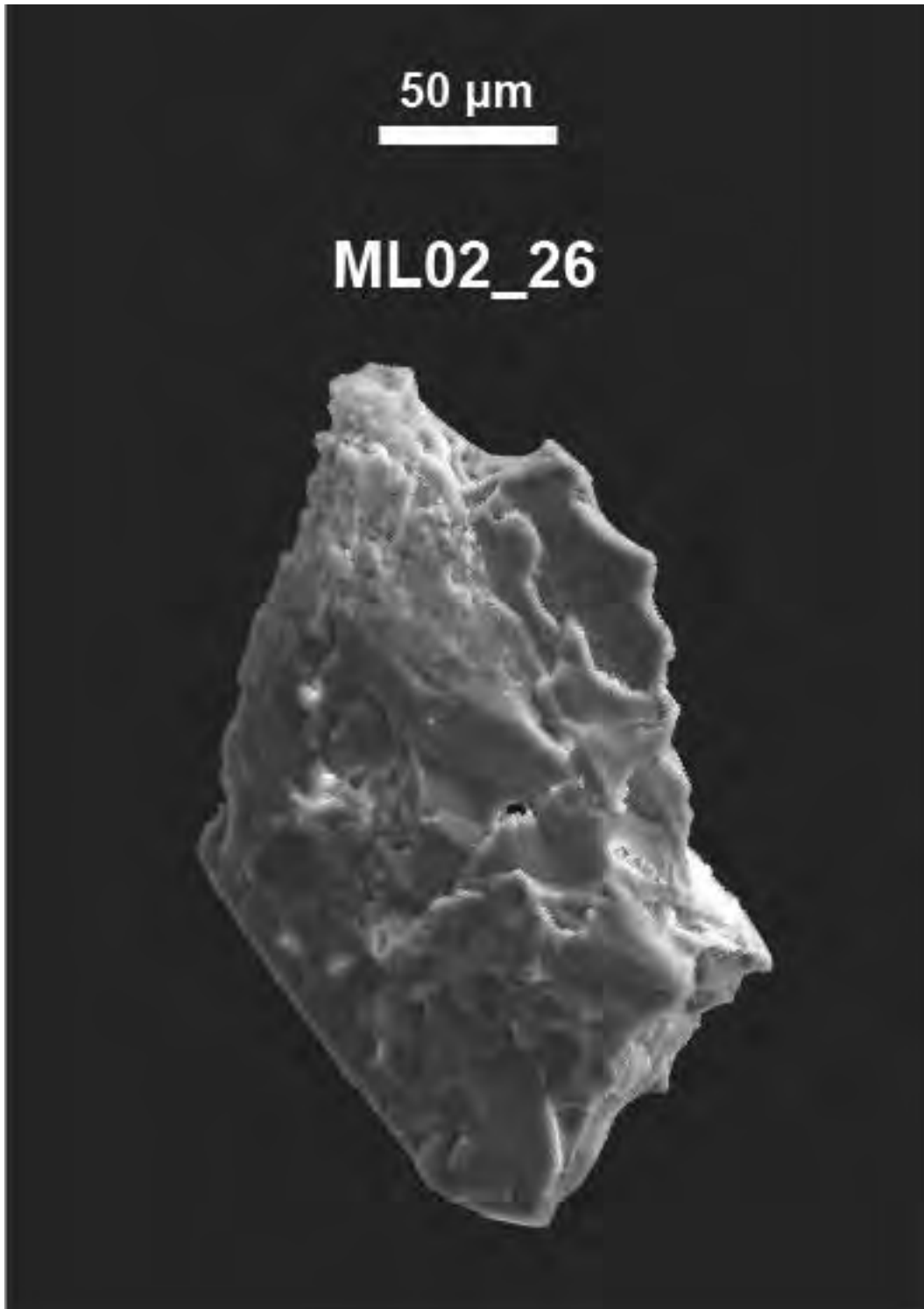
## 2021-MAC-08 (PYRITE)



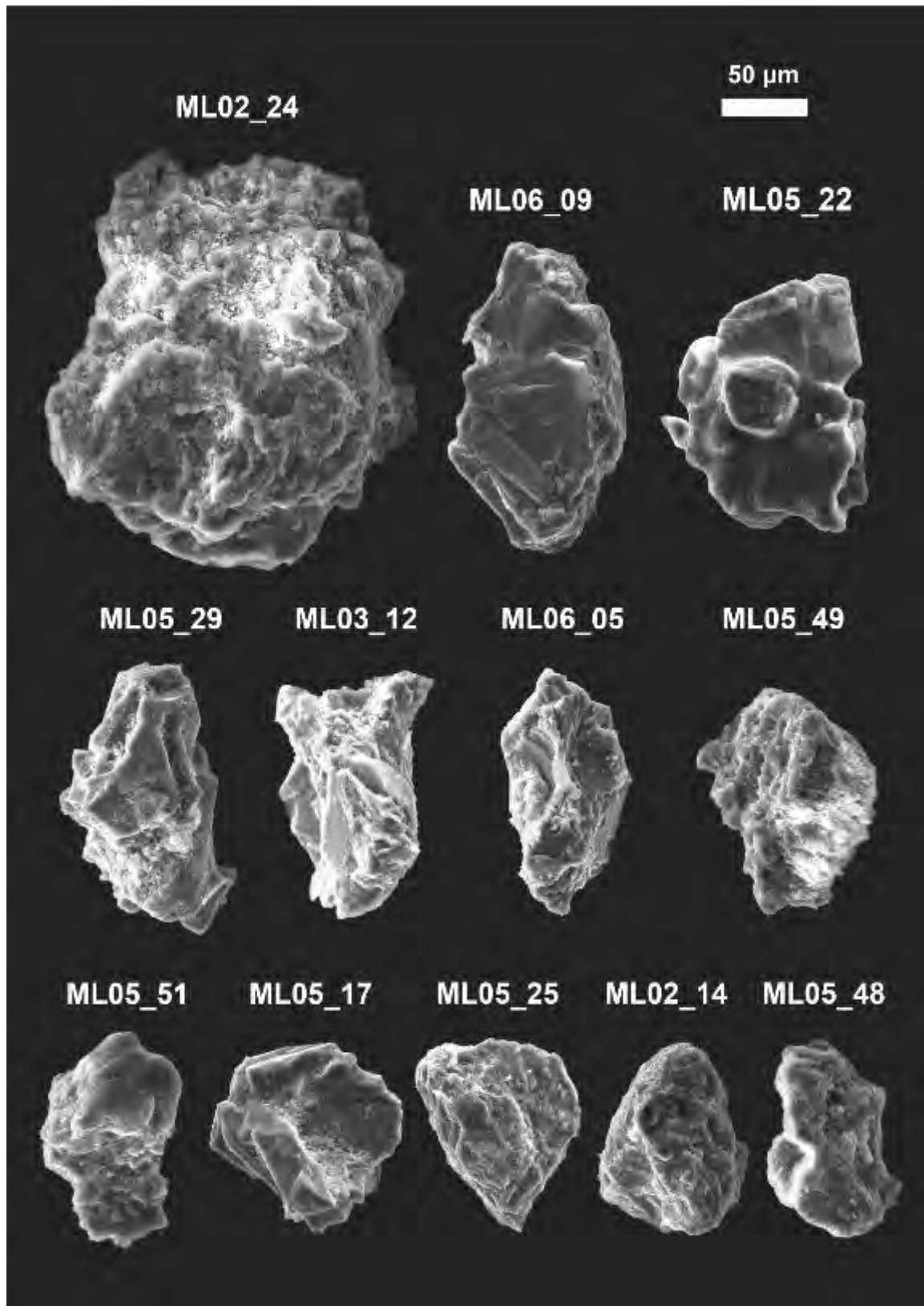
## 2021-MAC-08 (Fe-OXIDE)



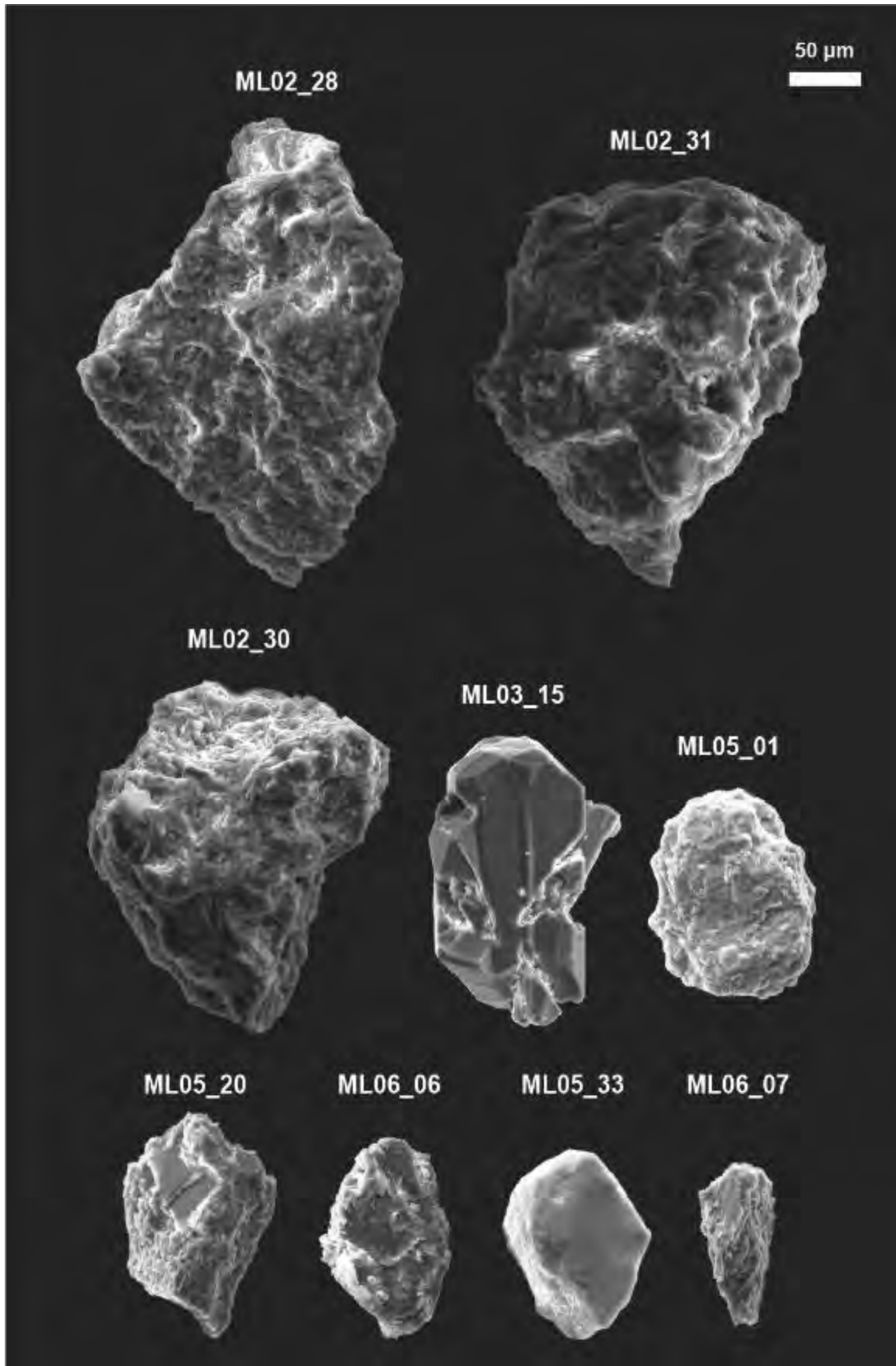
2021-MAC-08 (TITANITE)



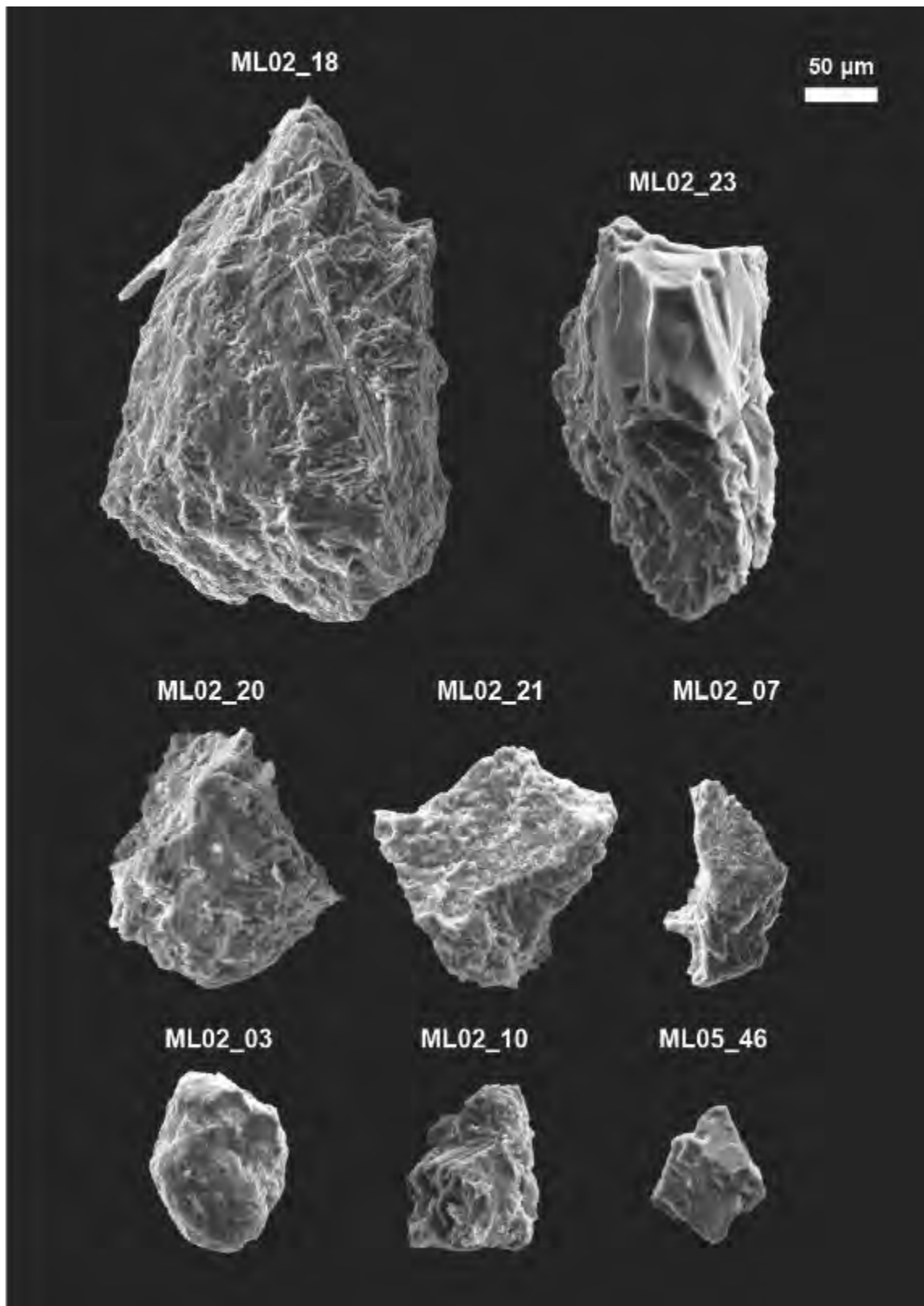
## 2021-MAC-08 (QUARTZ)



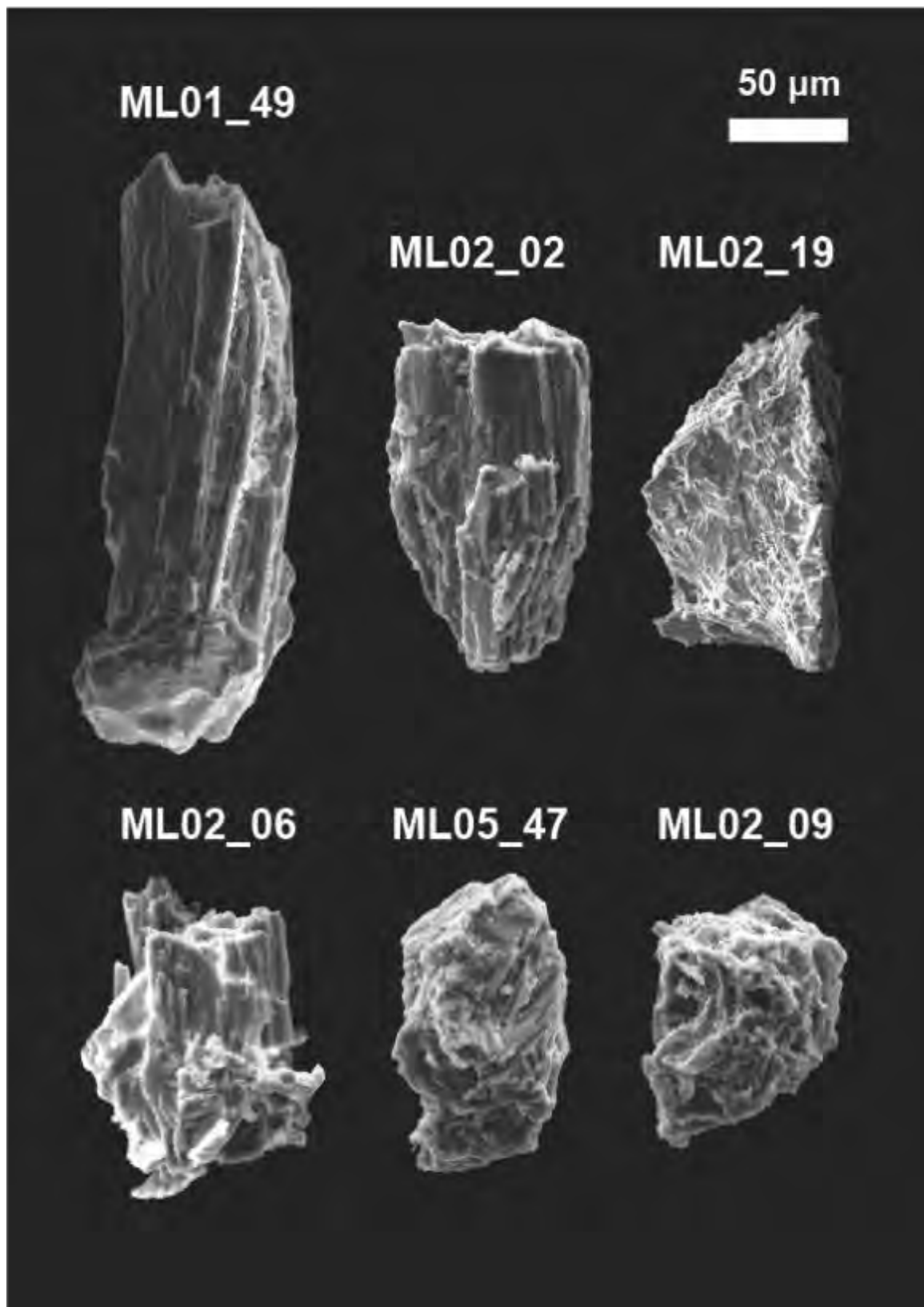
2021-MAC-08 (FELDESPAR)



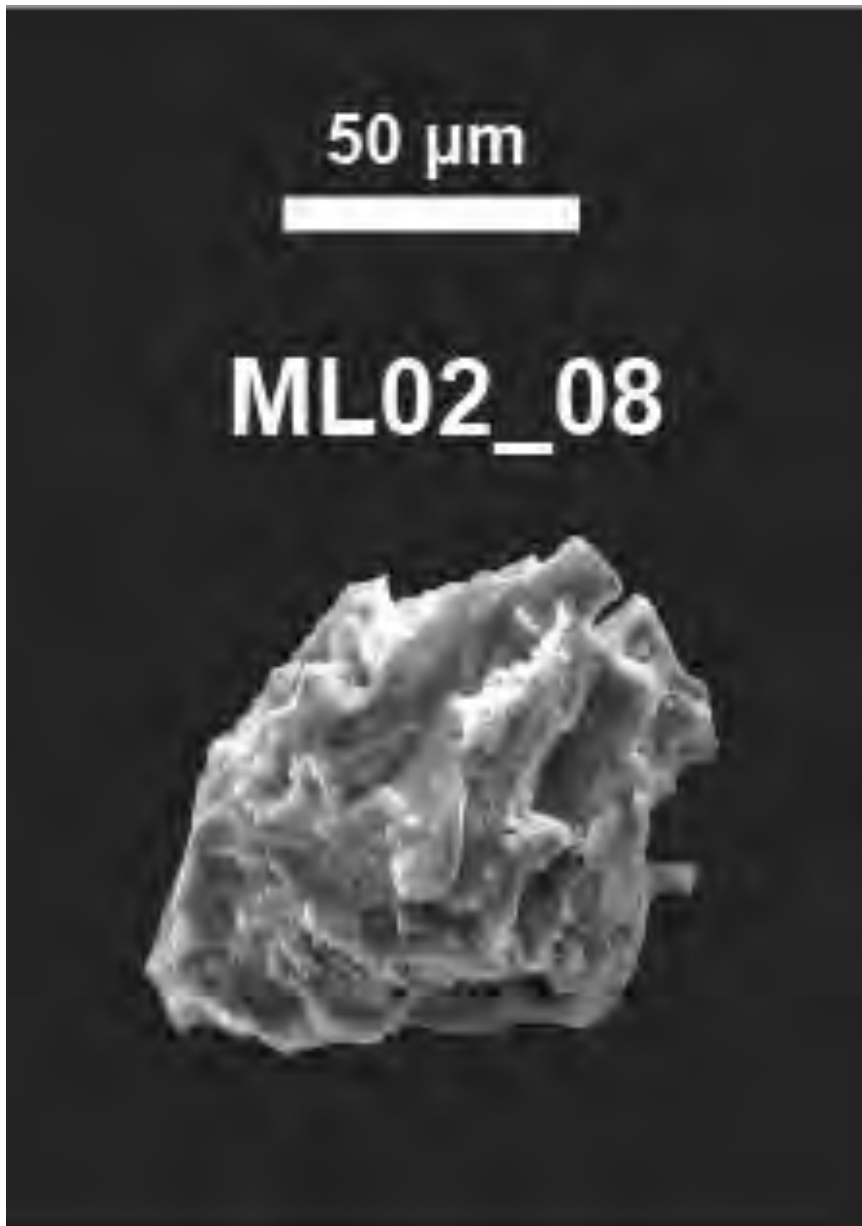
## 2021-MAC-08 (EPIDOTE)



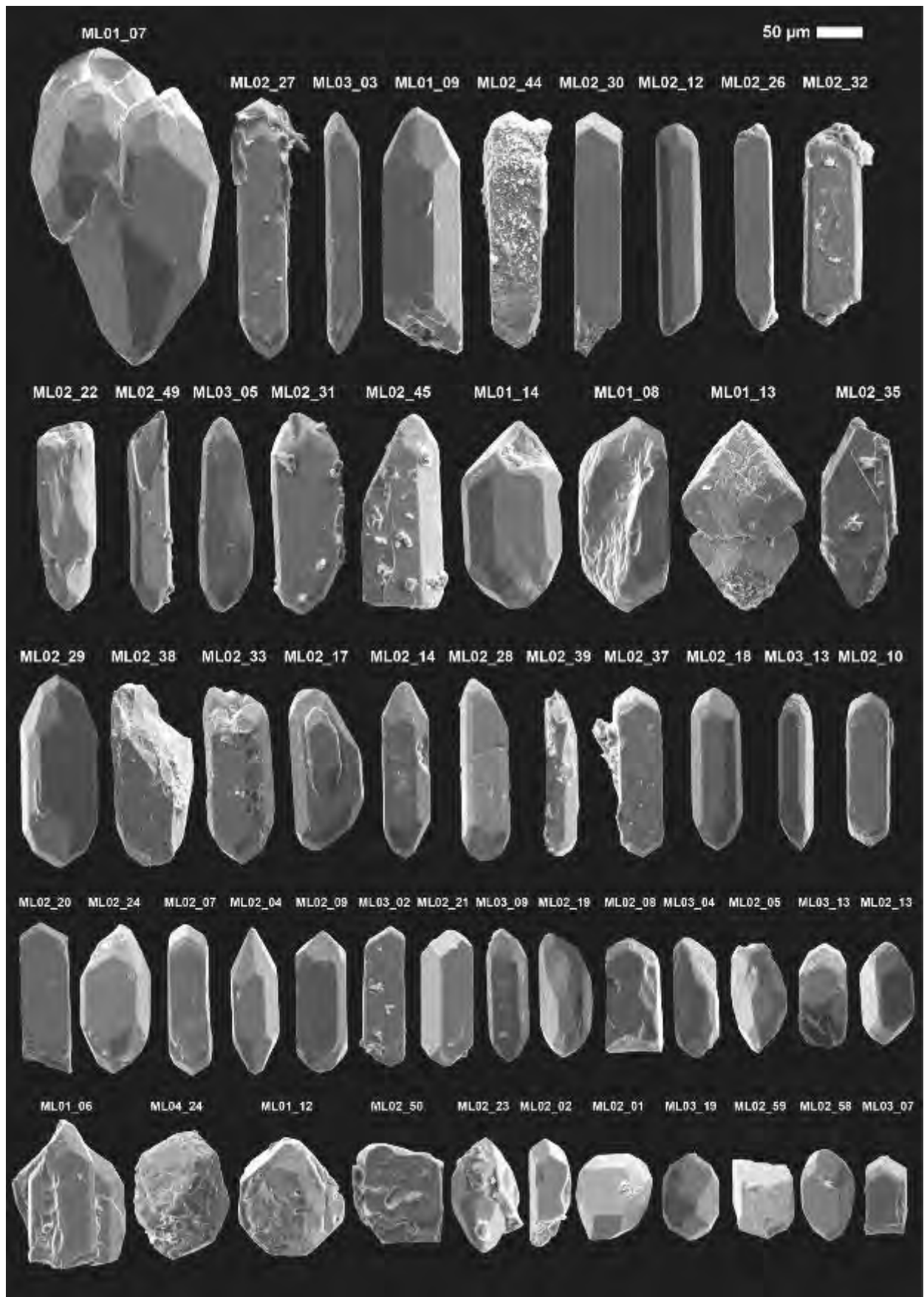
## 2021-MAC-08 (ACTINOLITE)



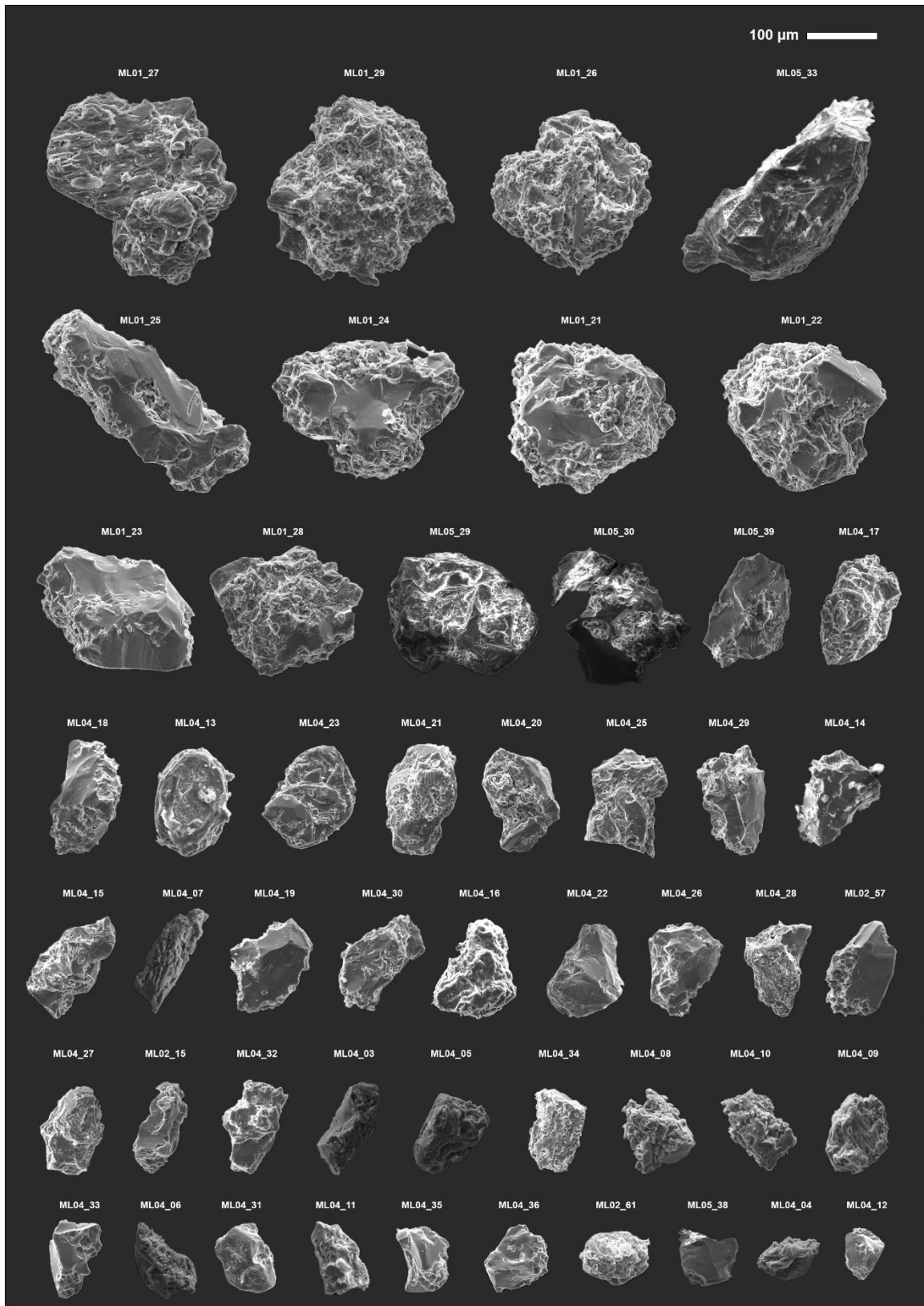
2021-MAC-08 (CHLORITE)



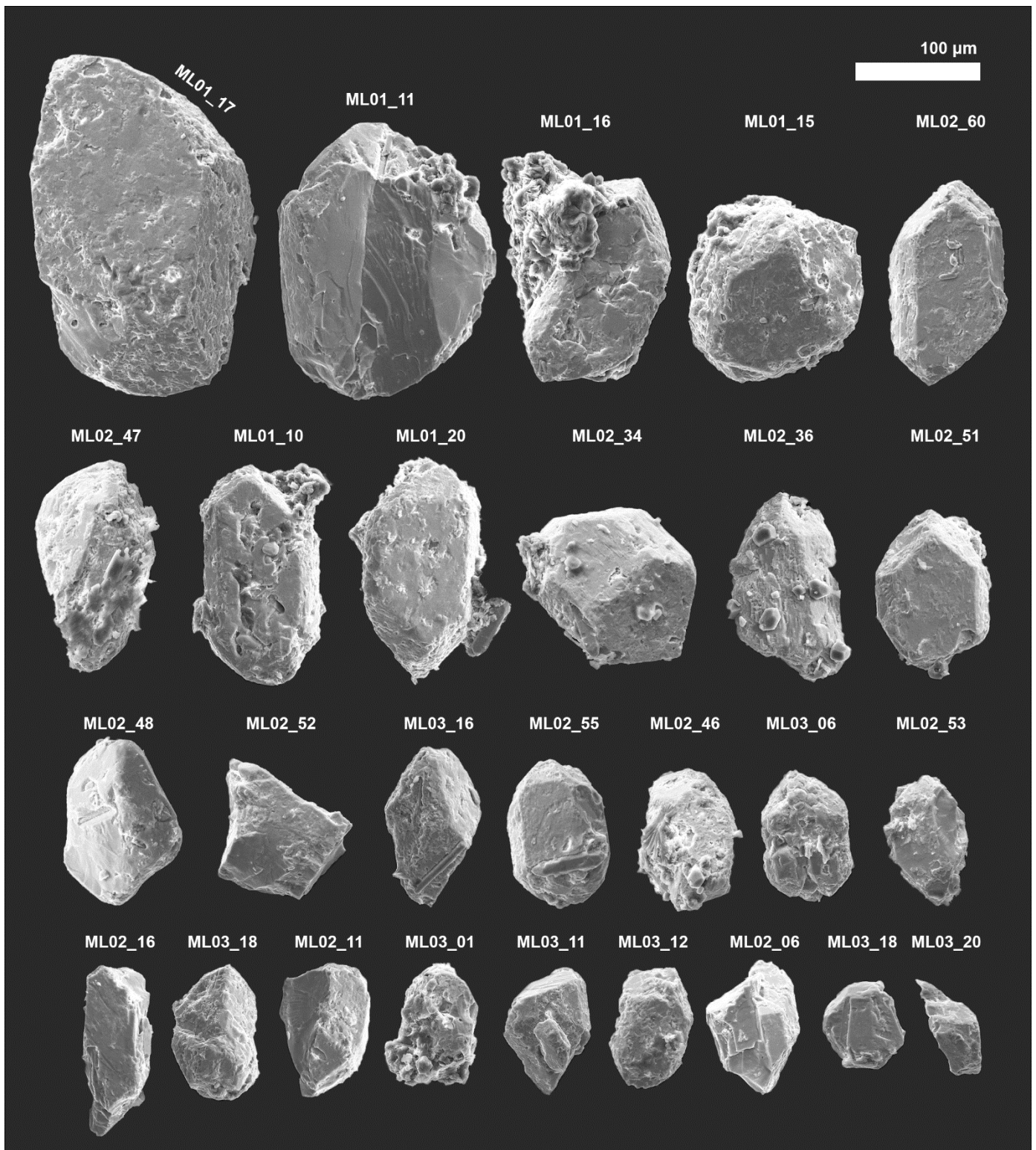
## 2021-MAC-21 (ZIRCON)



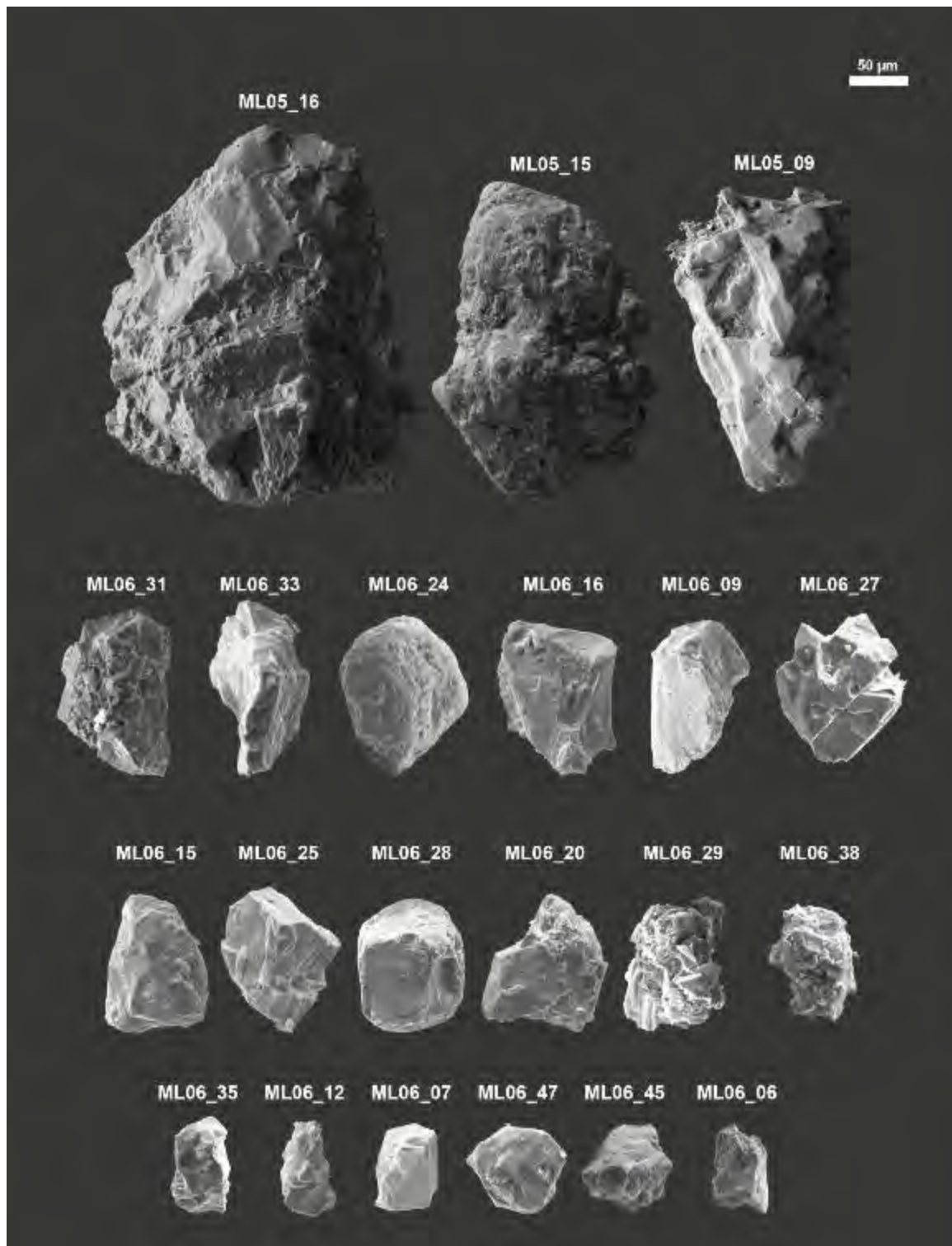
## 2021-MAC-21 (APATITE)



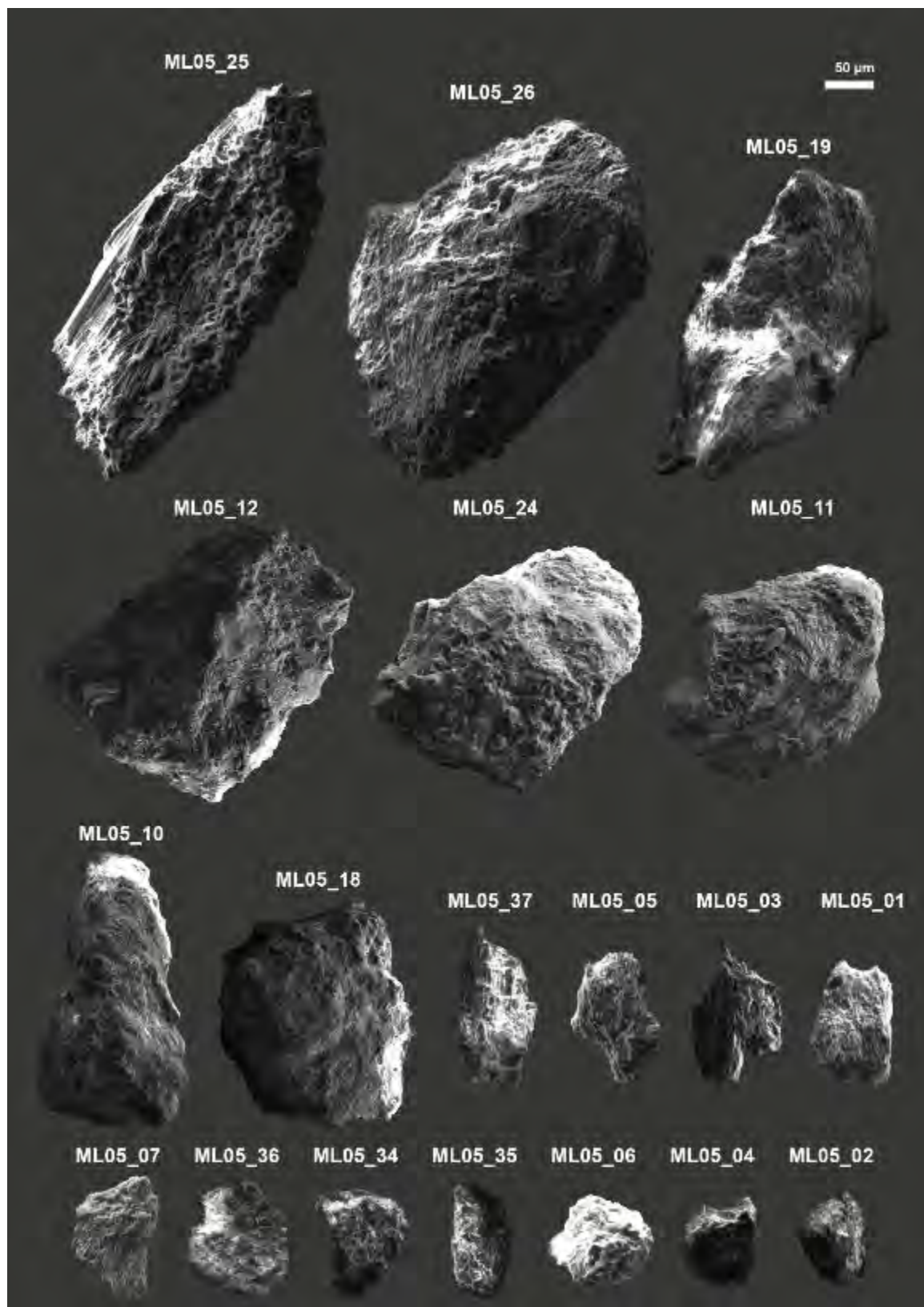
## 2021-MAC-21 (MONAZITE-Ce)



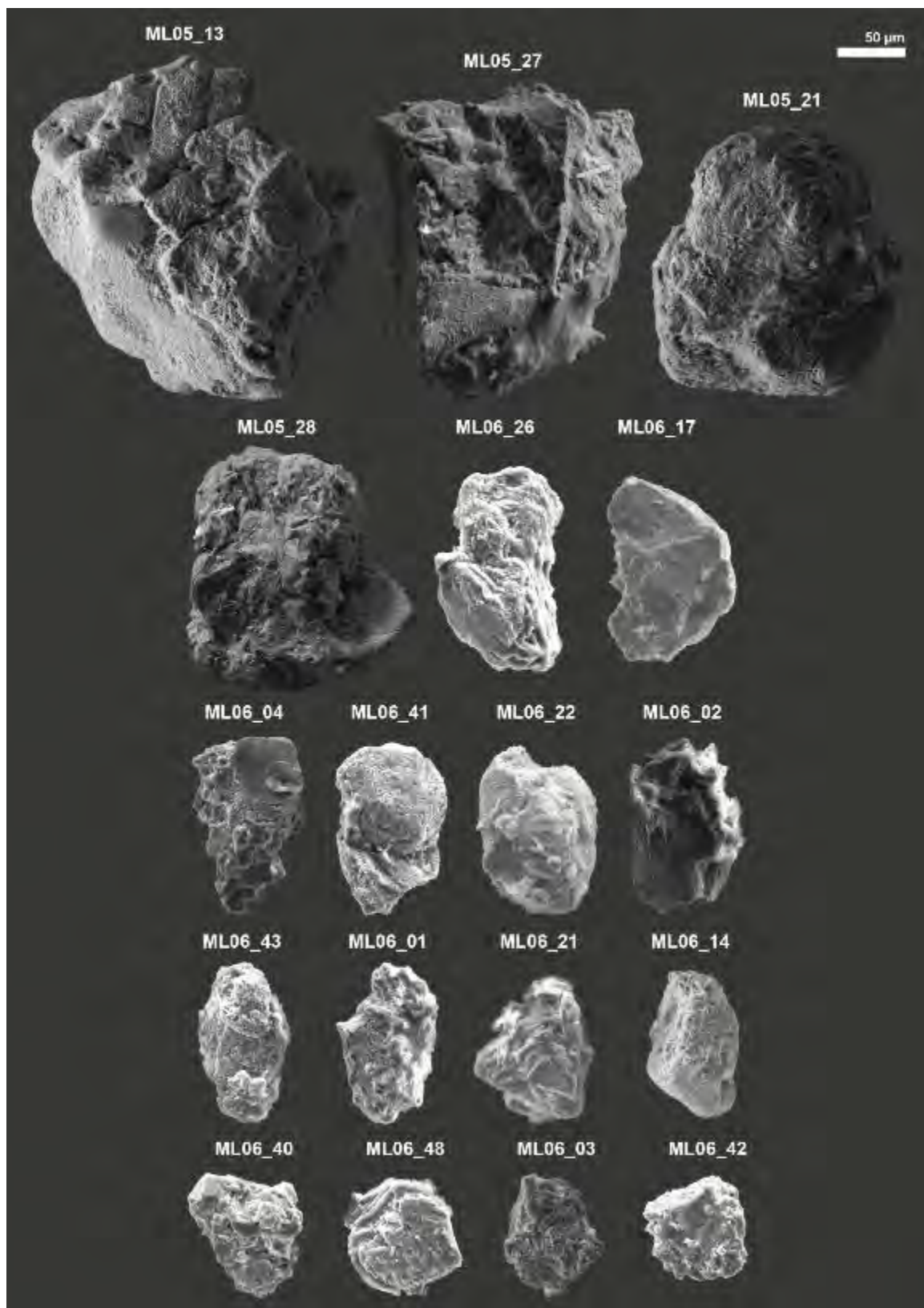
## 2021-MAC-21 (MAGNETITE)



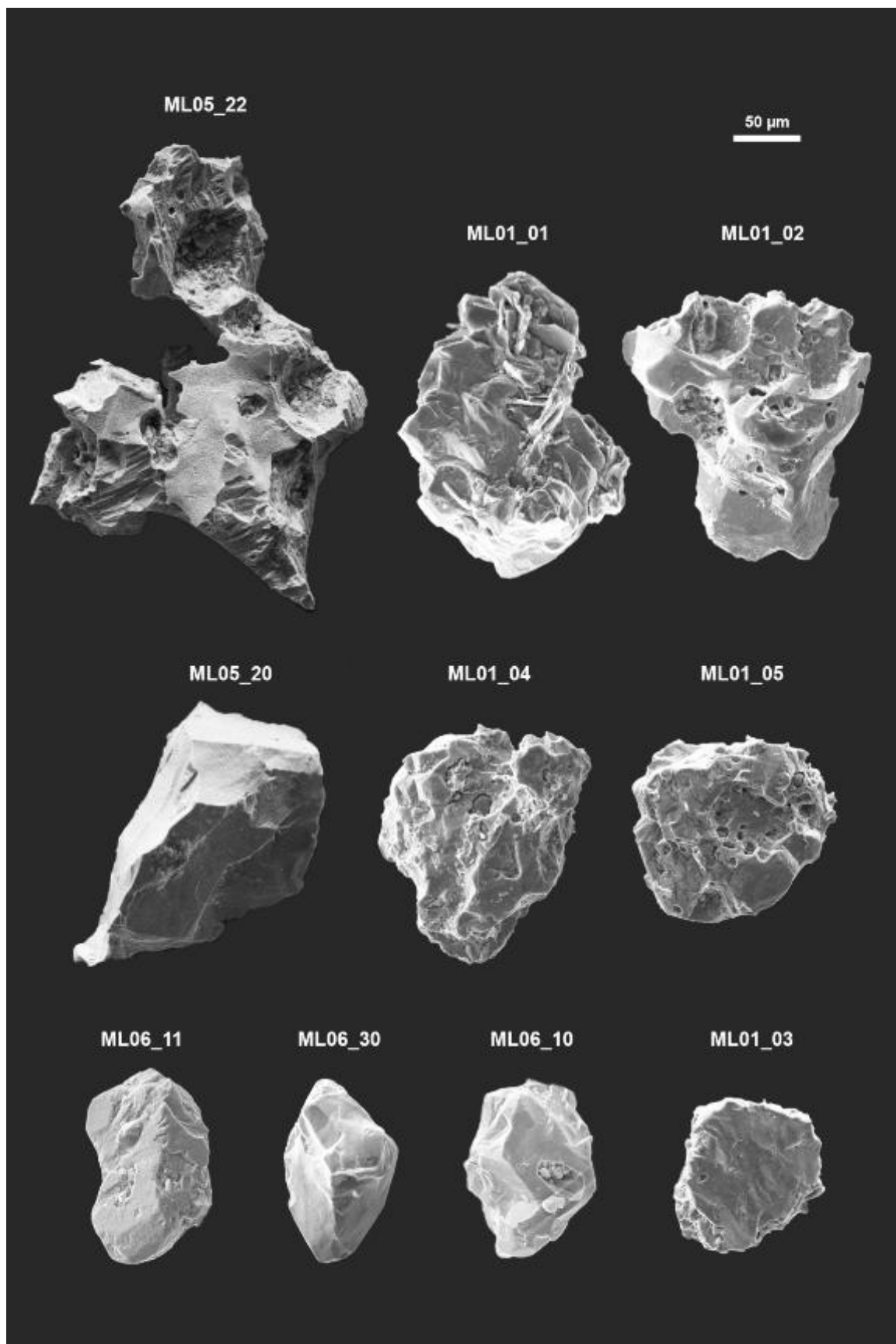
## 2021-MAC-21 (DUMORTIERITE)

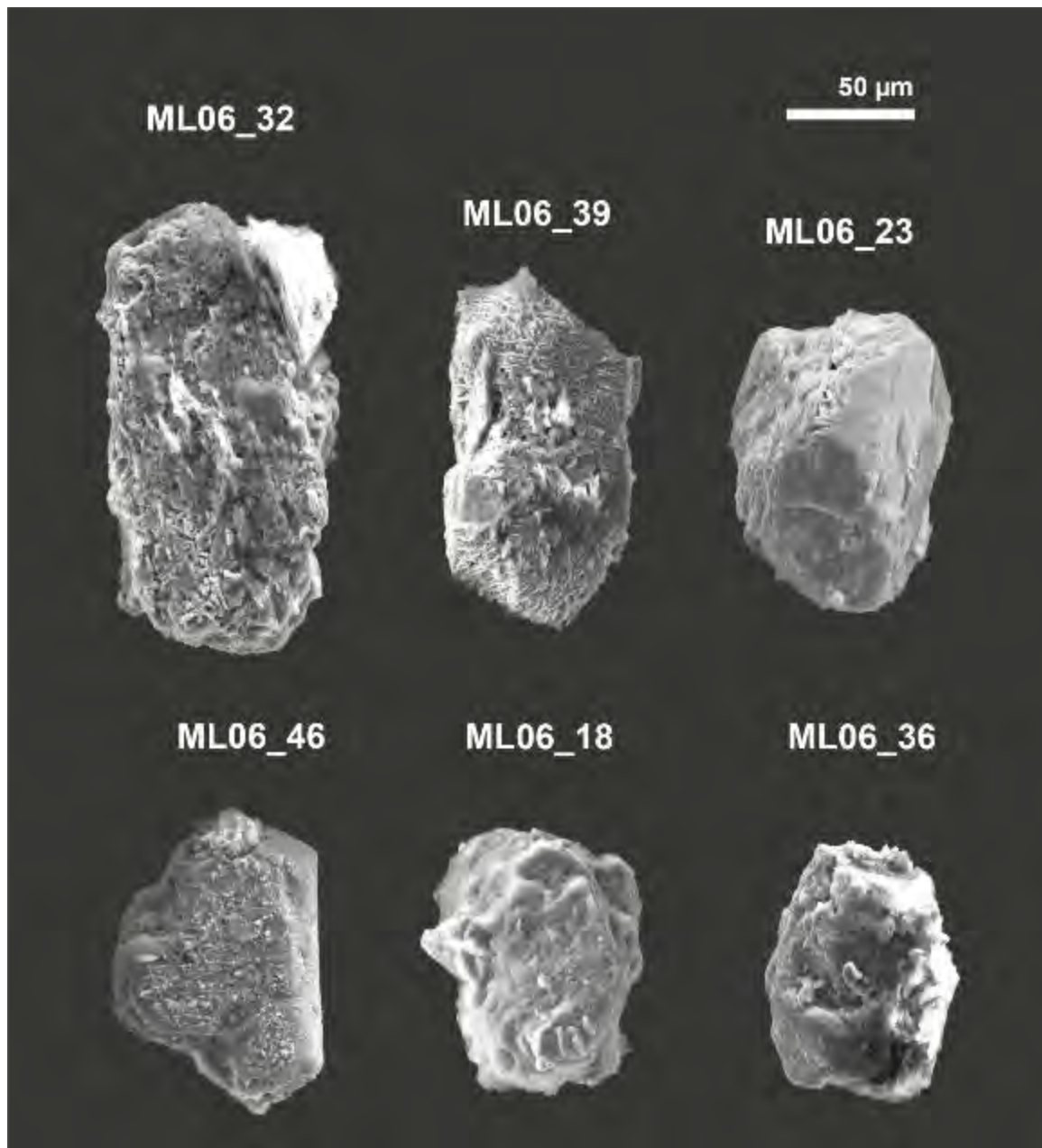


## 2021-MAC-21 (RUTILE)

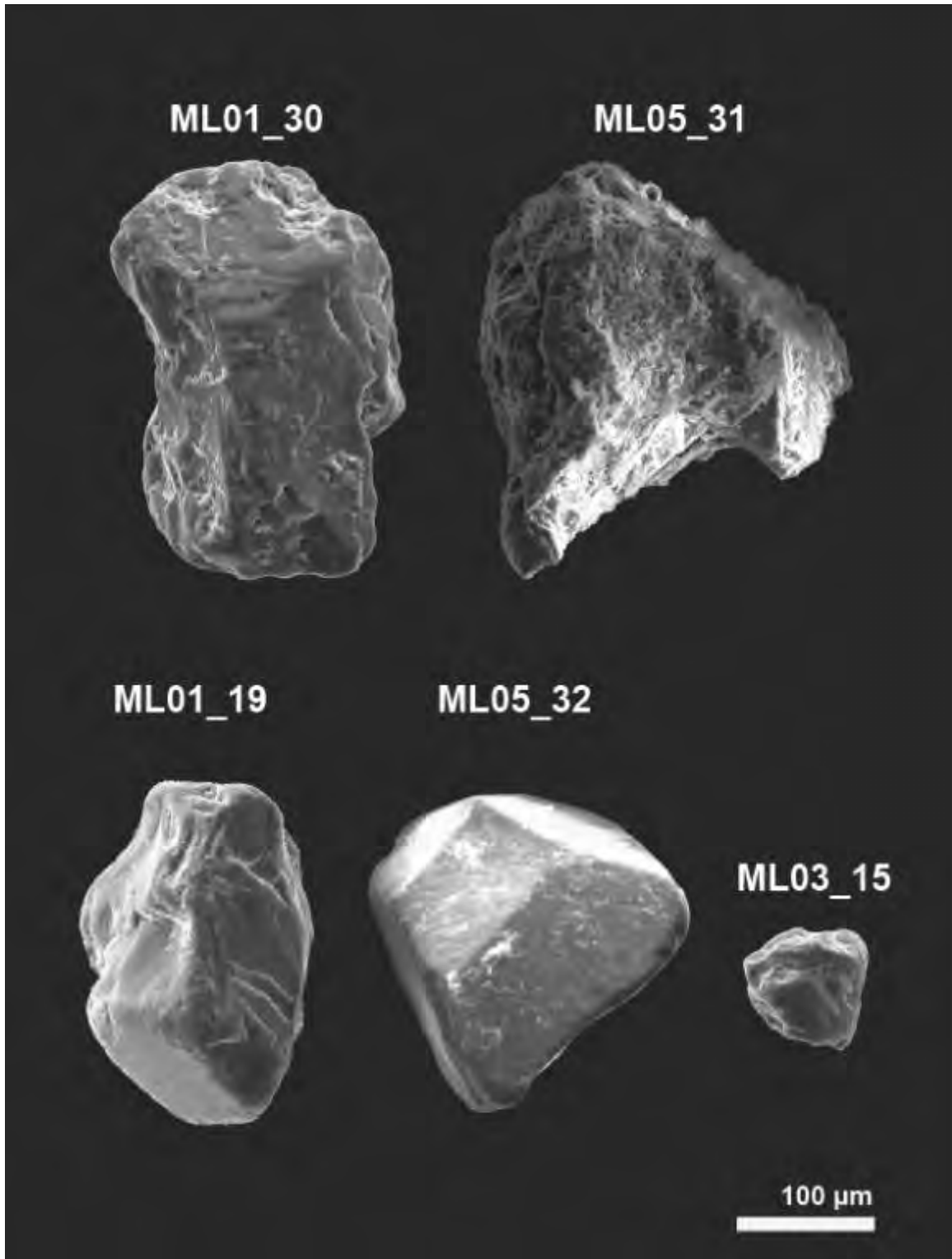


## 2021-MAC-21 (PYRITE)

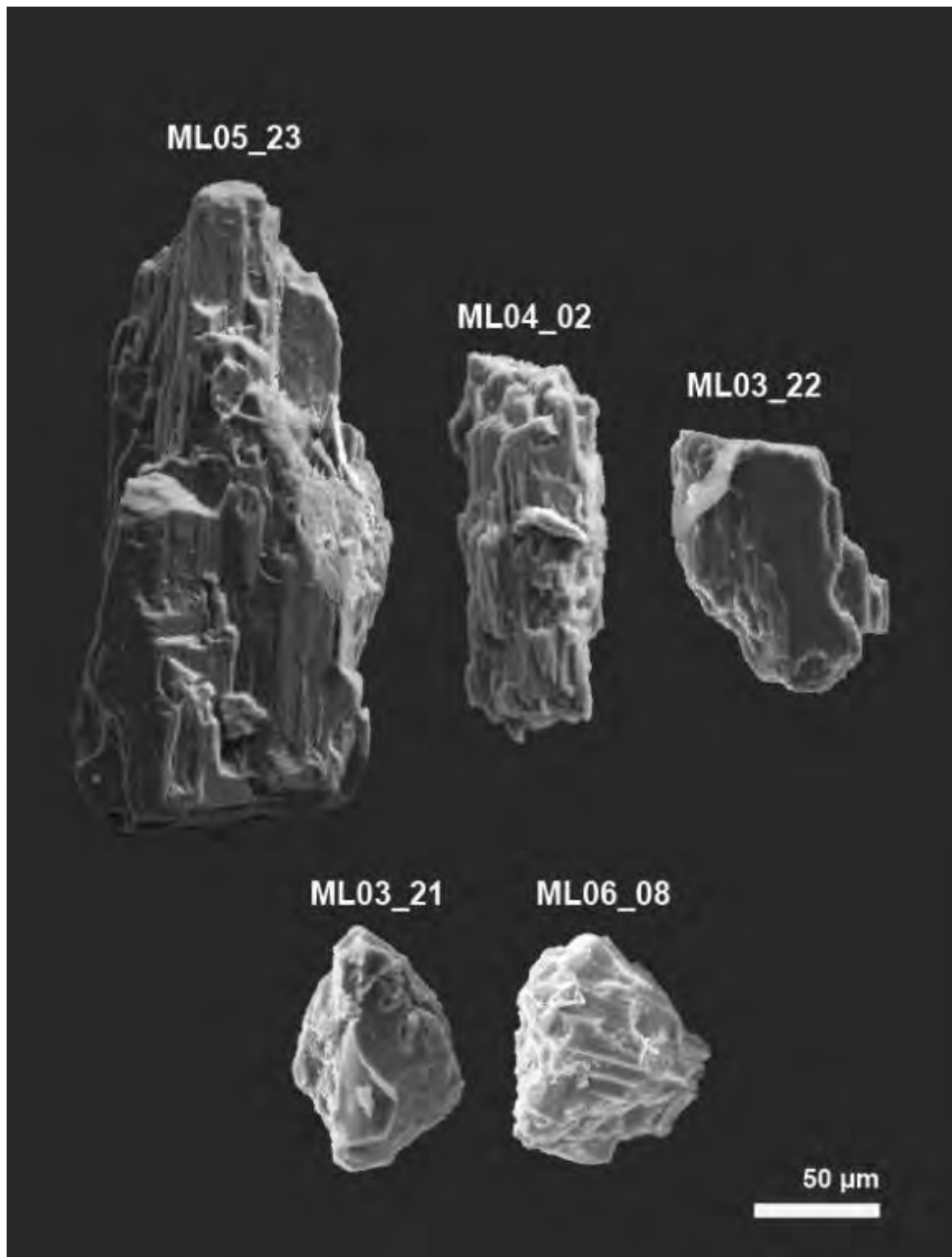


**2021-MAC-21 (RUTILE-LIKE GRAINS)**

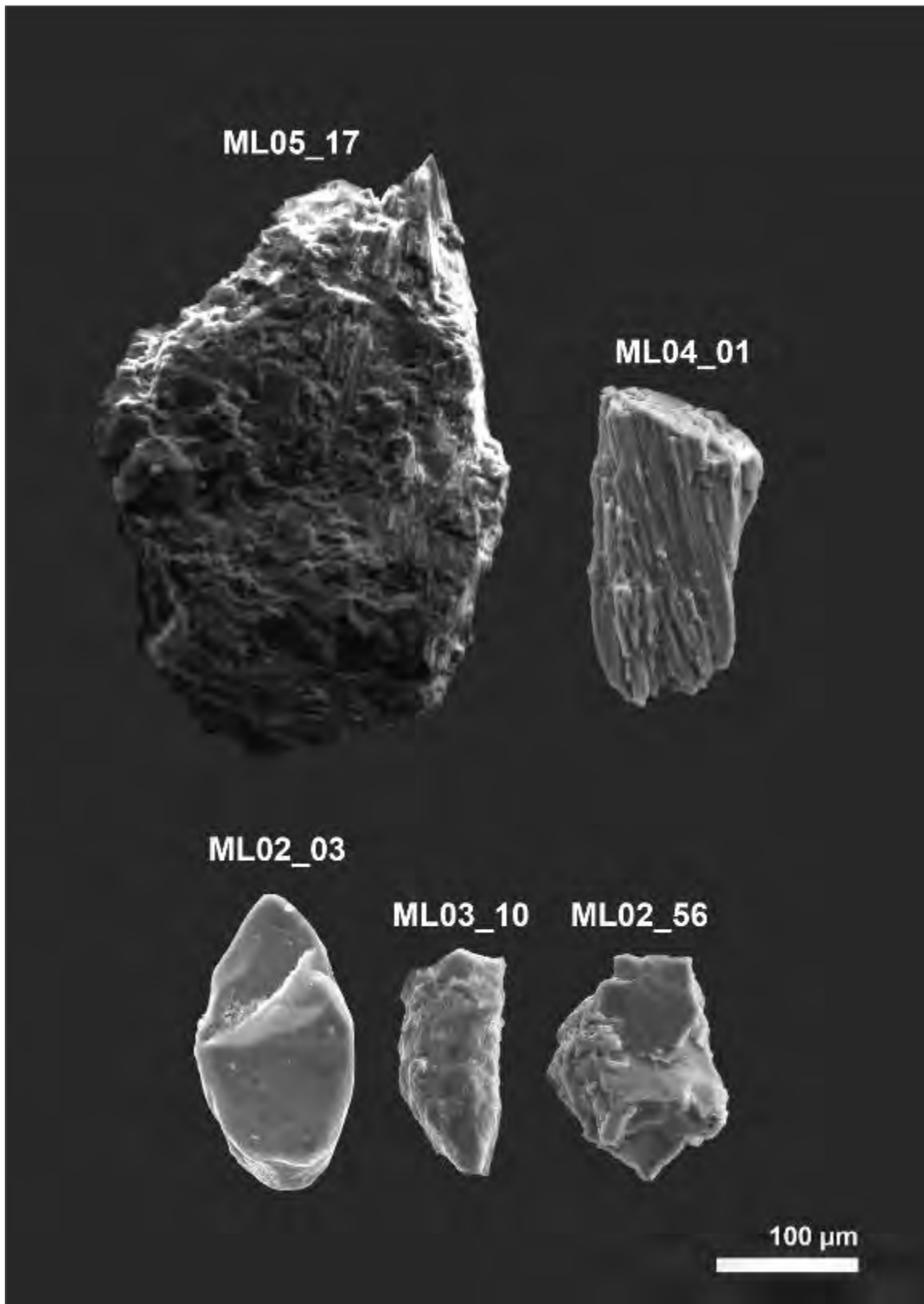
2021-MAC-21 (FELDSPAR)



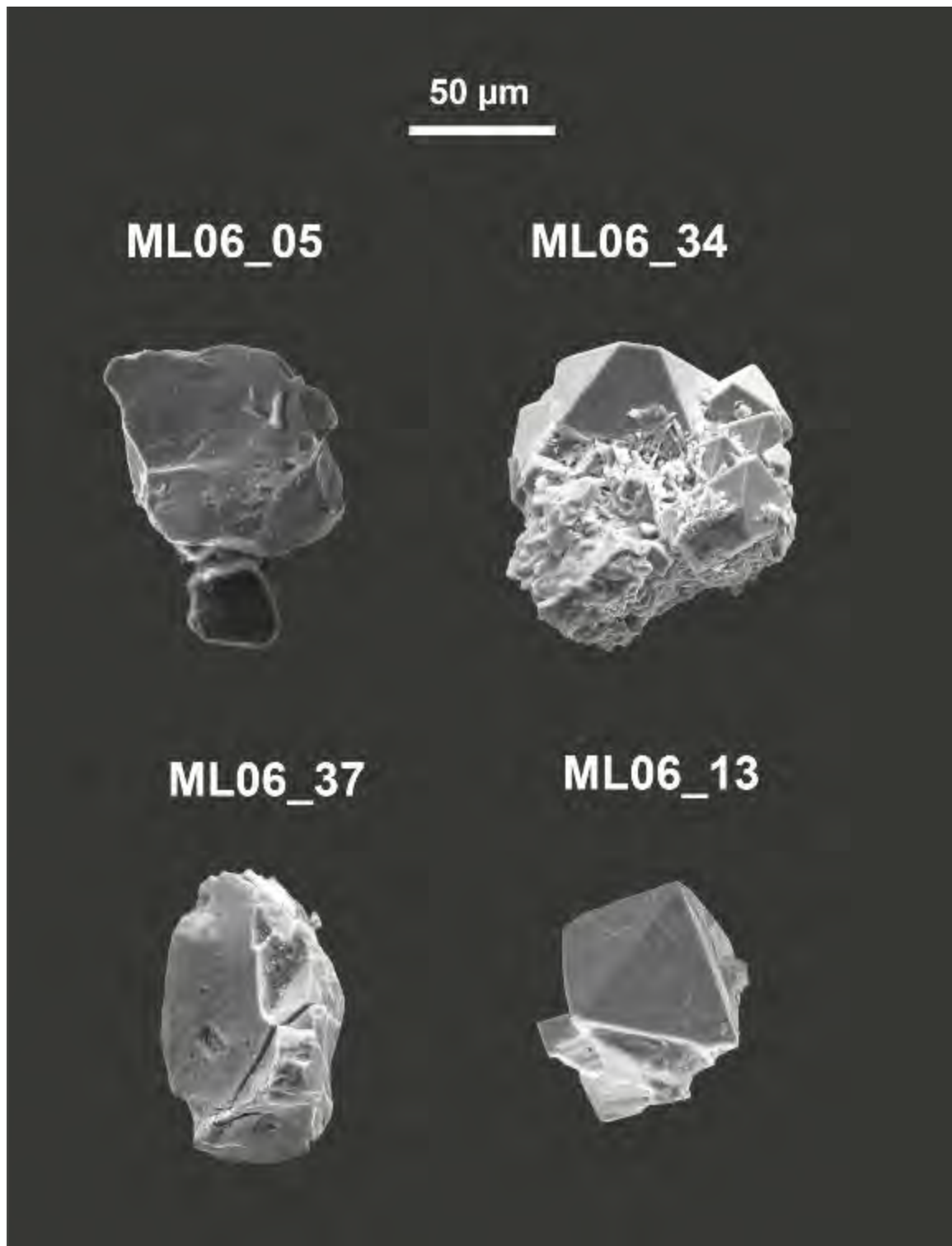
## 2021-MAC-21 (ACTINOLITE)



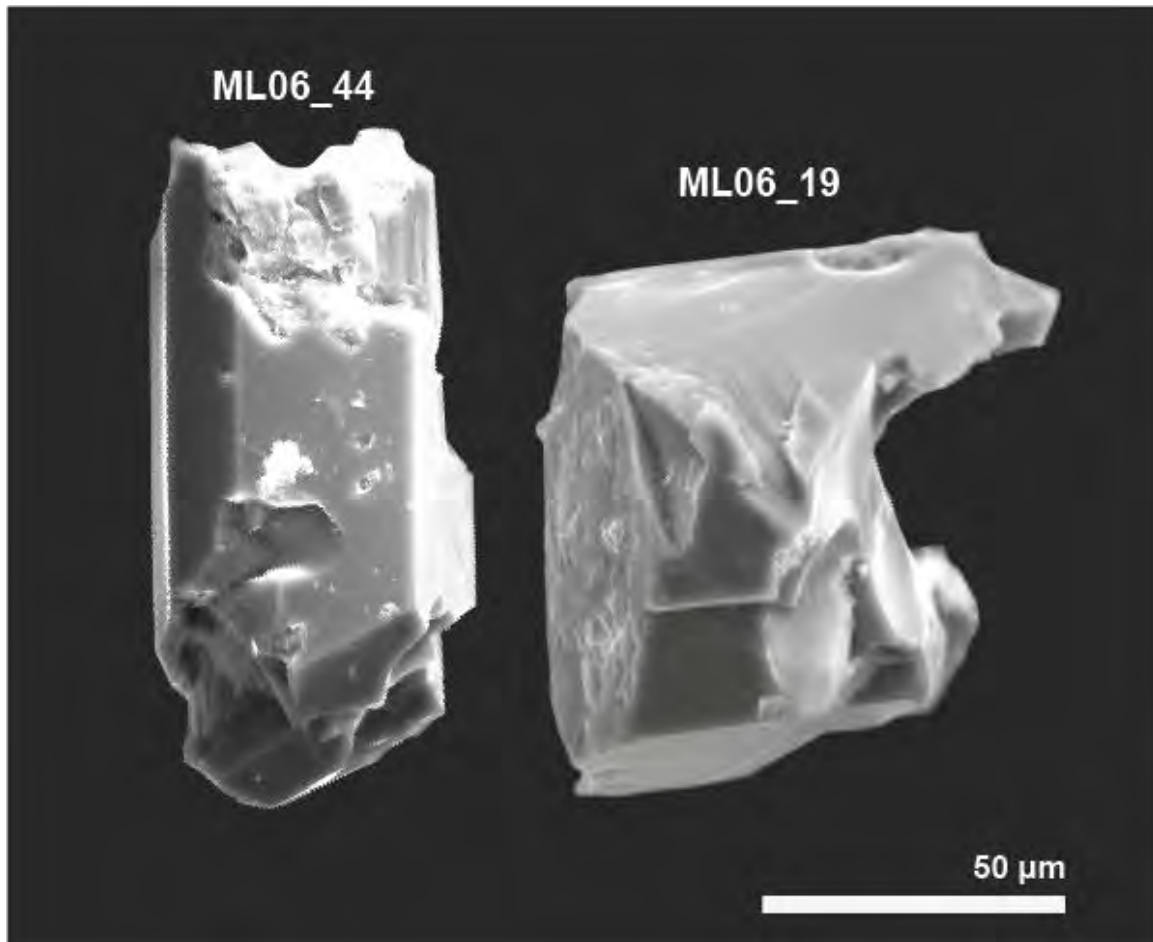
2021-MAC-21 (QUARTZ)

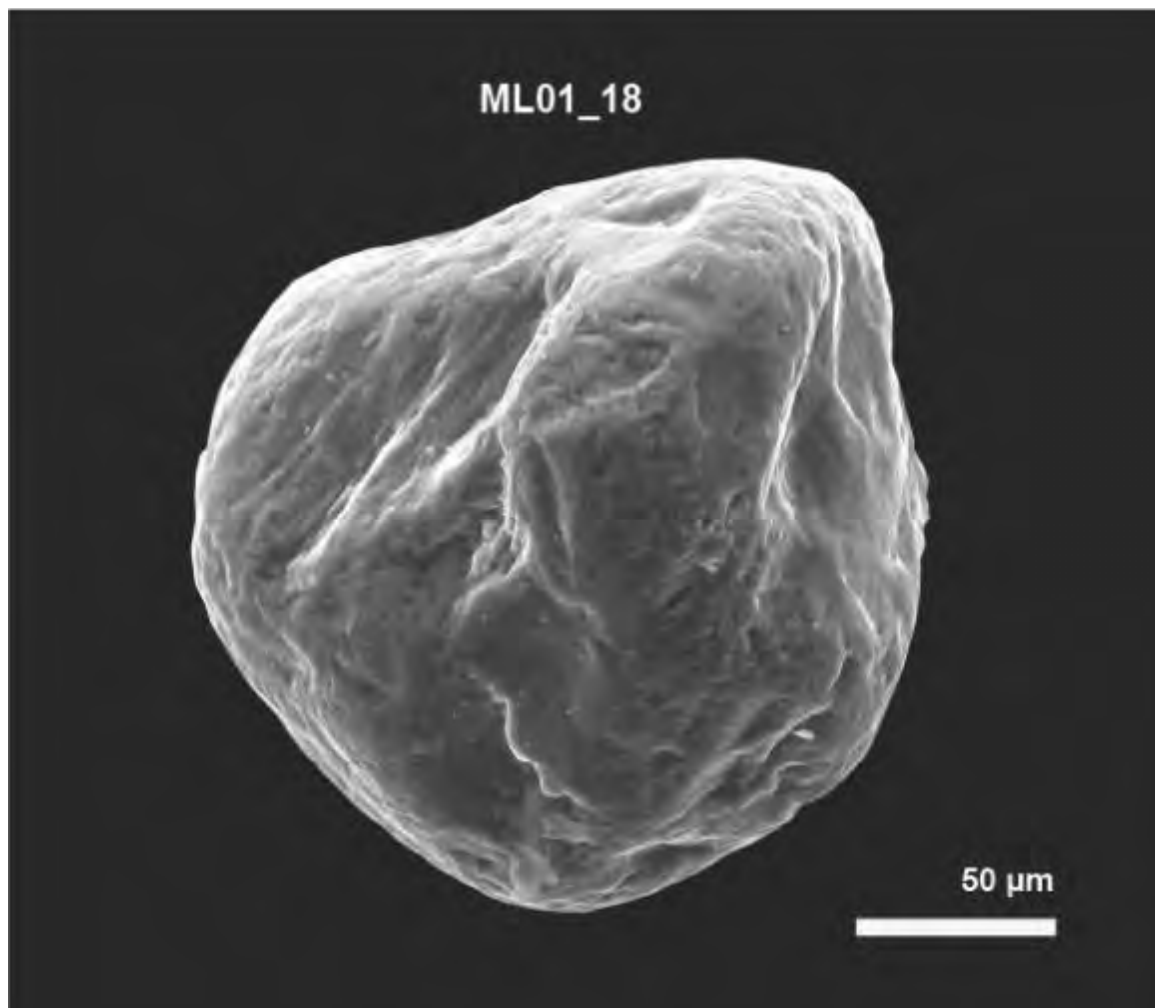


## 2021-MAC-21 (Fe-OXIDE)

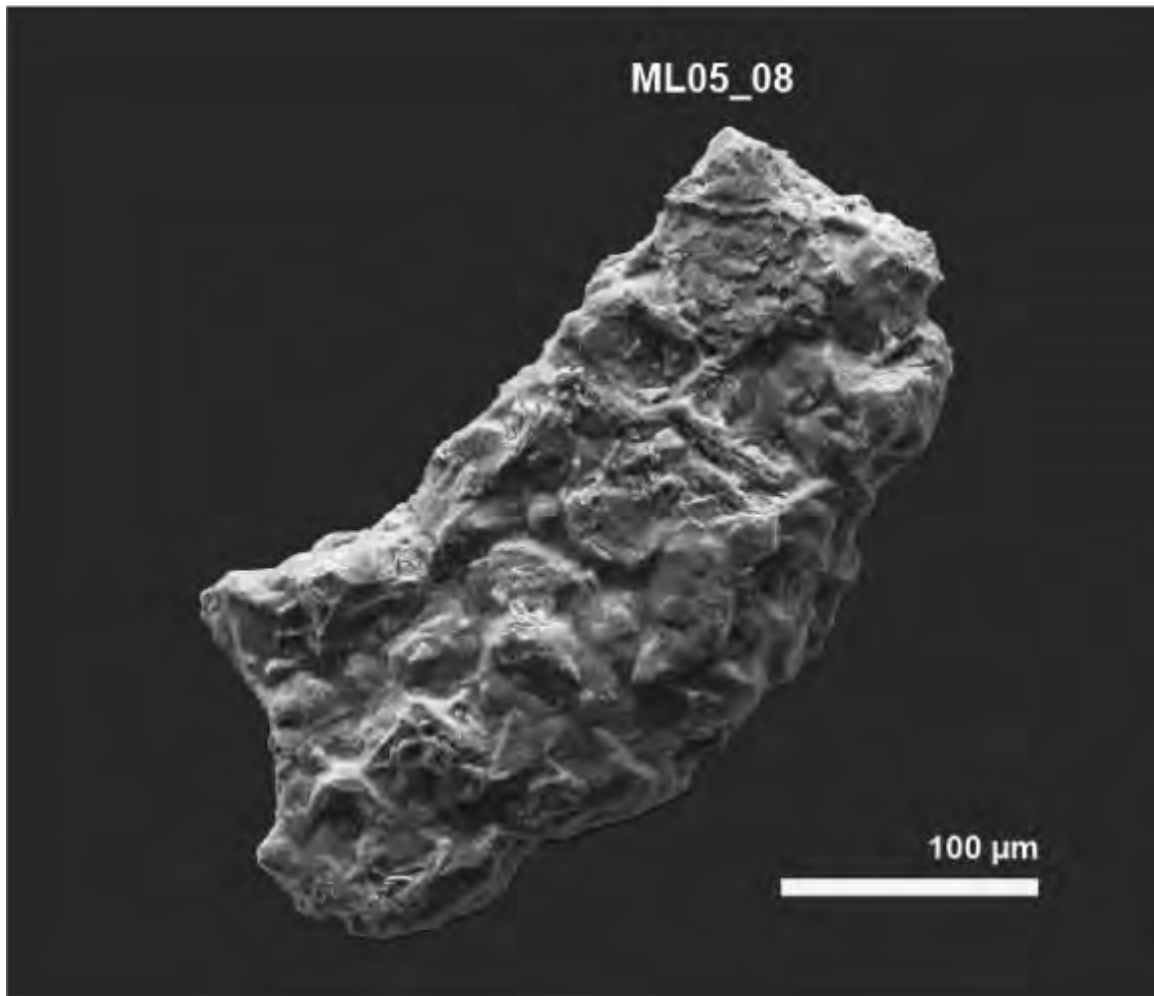


2021-MAC-21 (TOURMALINE)

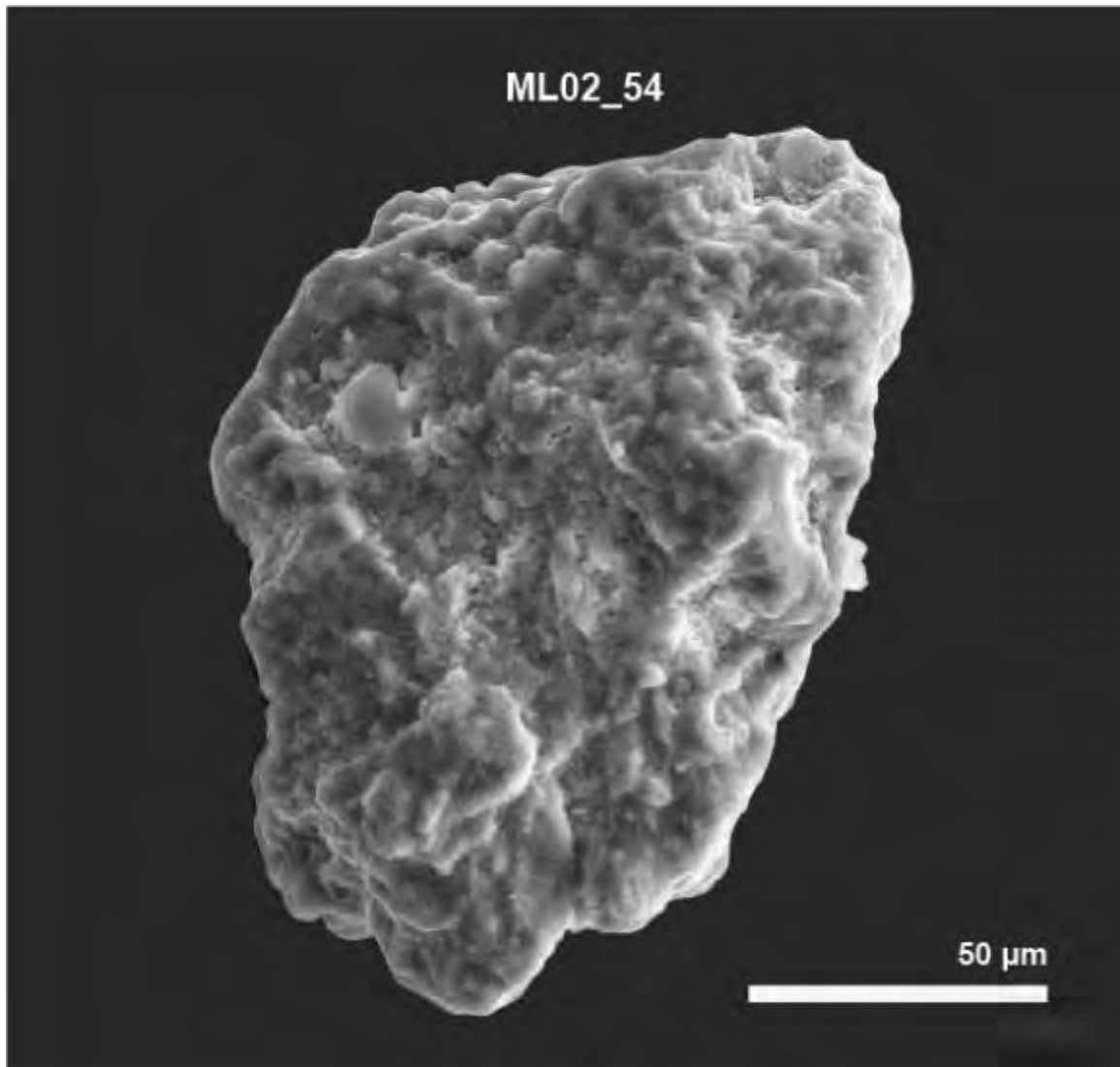


**2021-MAC-21 (TITANITE)**

2021-MAC-21 (HEMATITE)

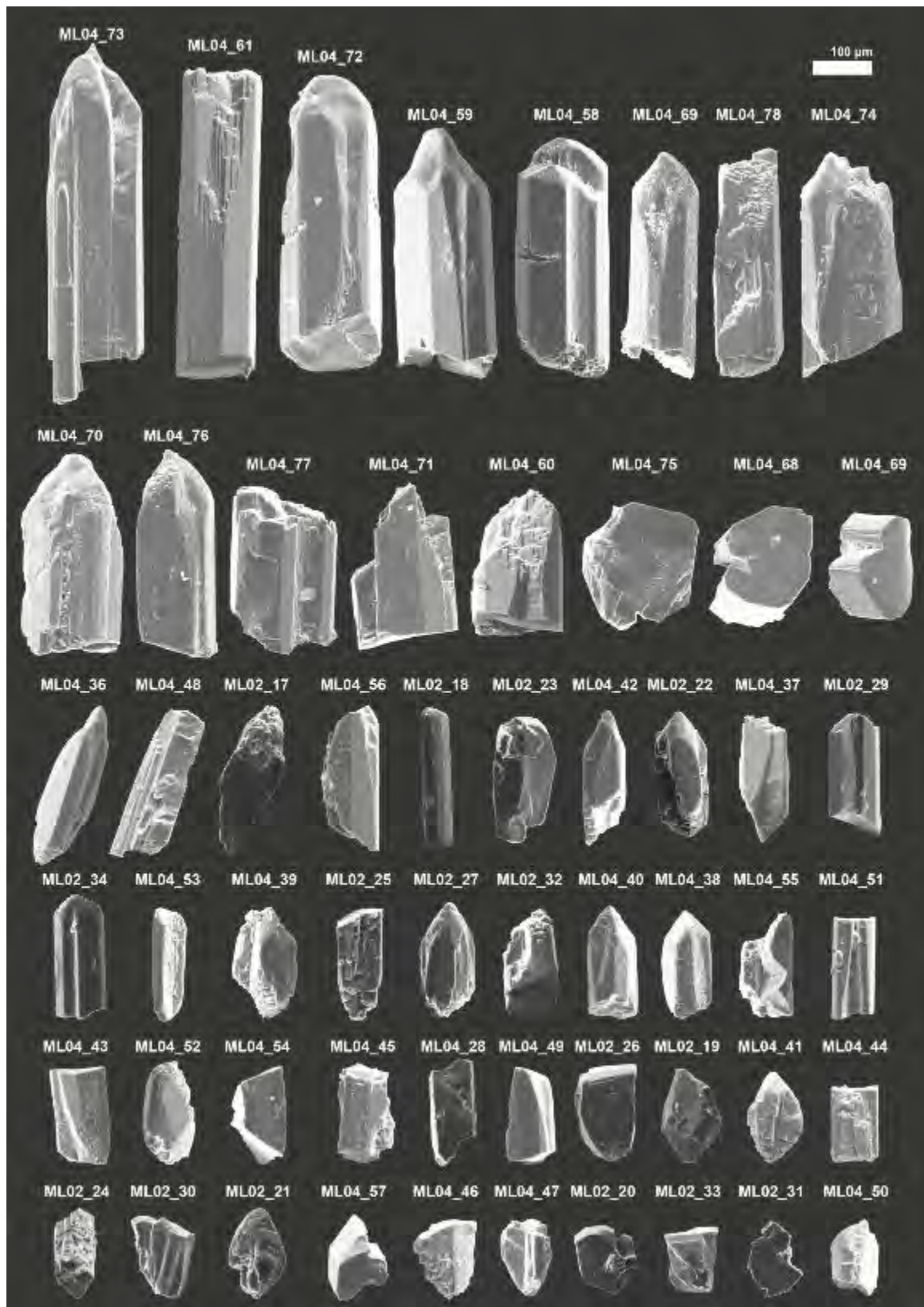


2021-MAC-21 (EPIDOTE)

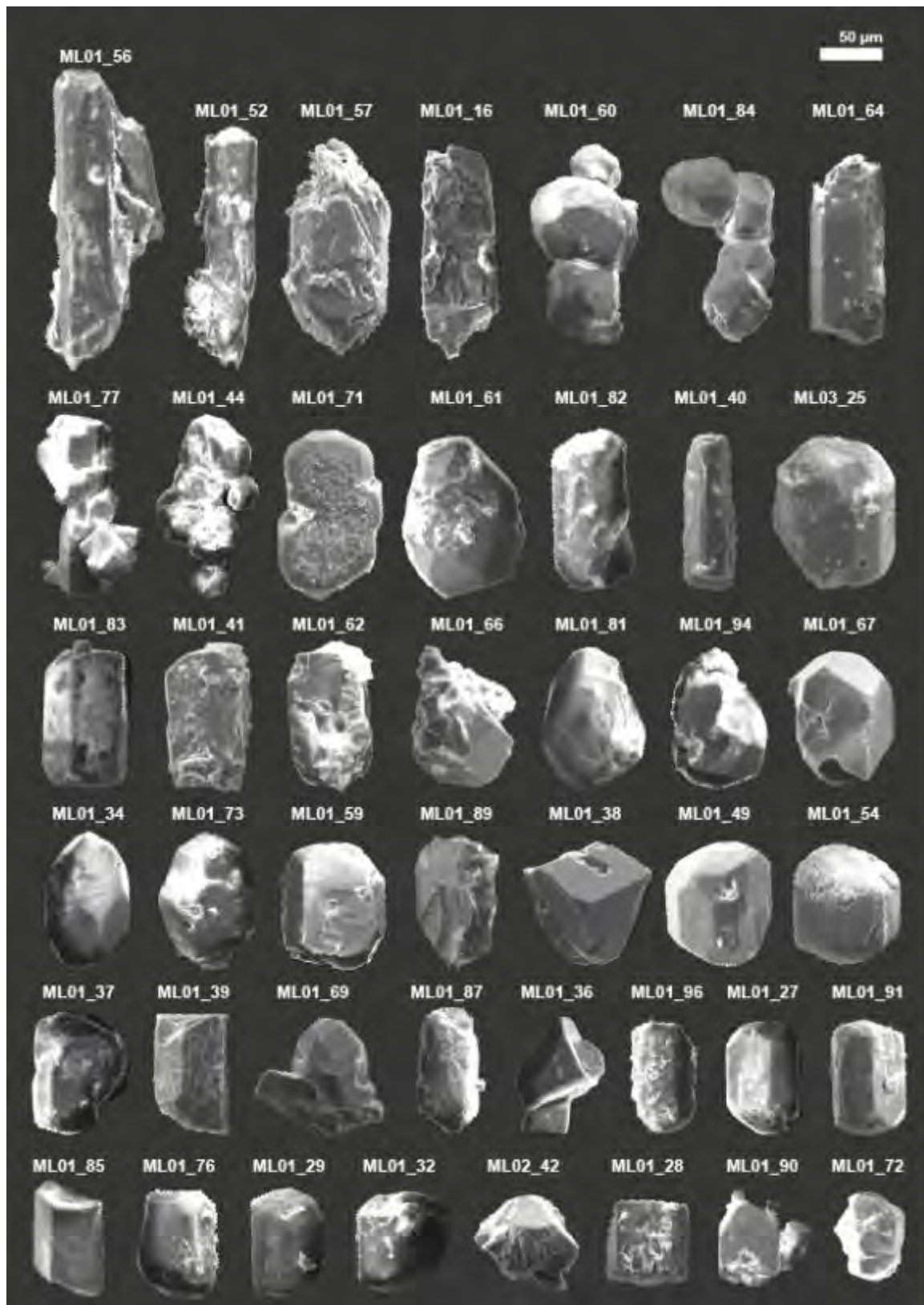


MCMXVII

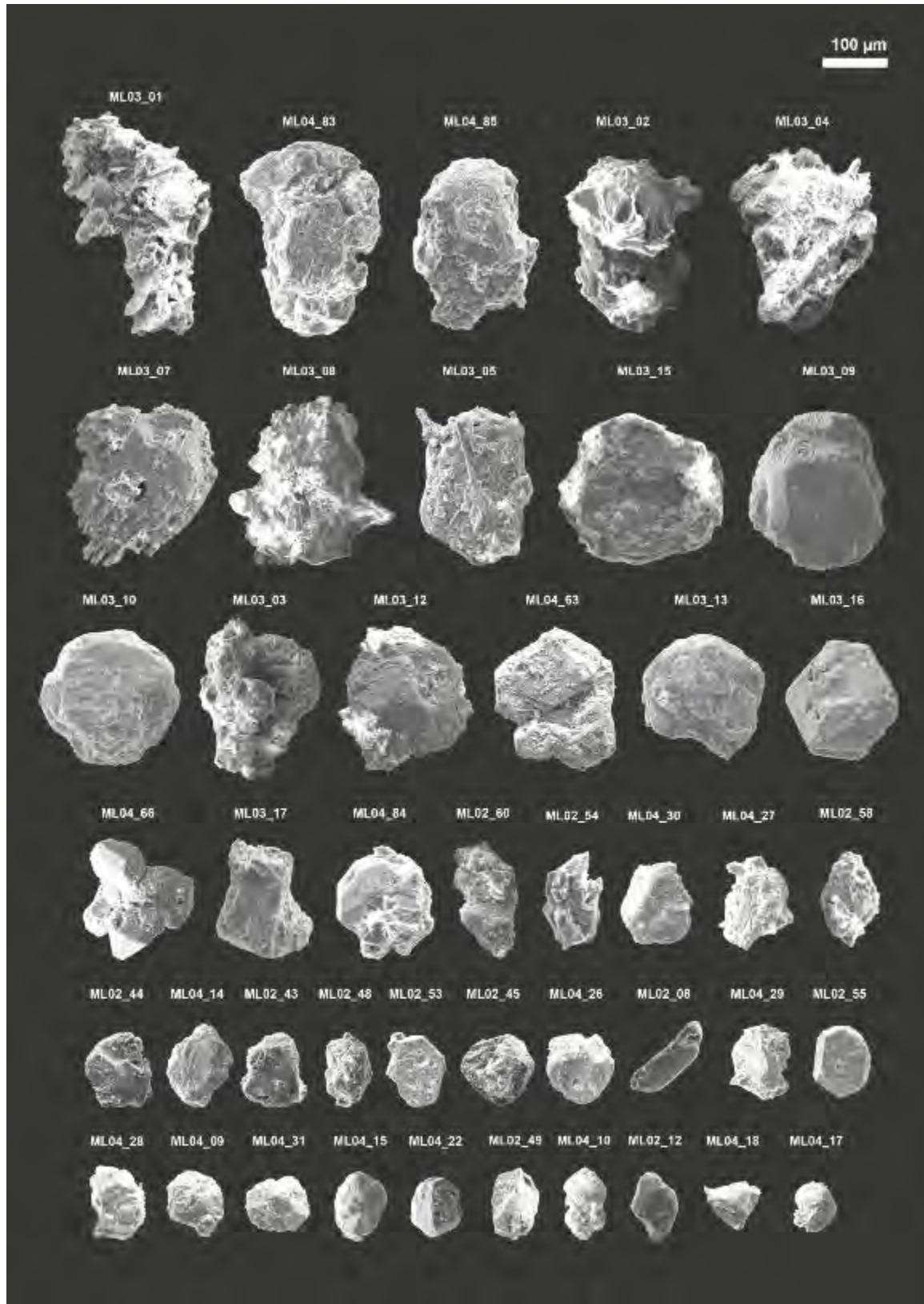
## 2021-MAC-67 (TOURMALINE)



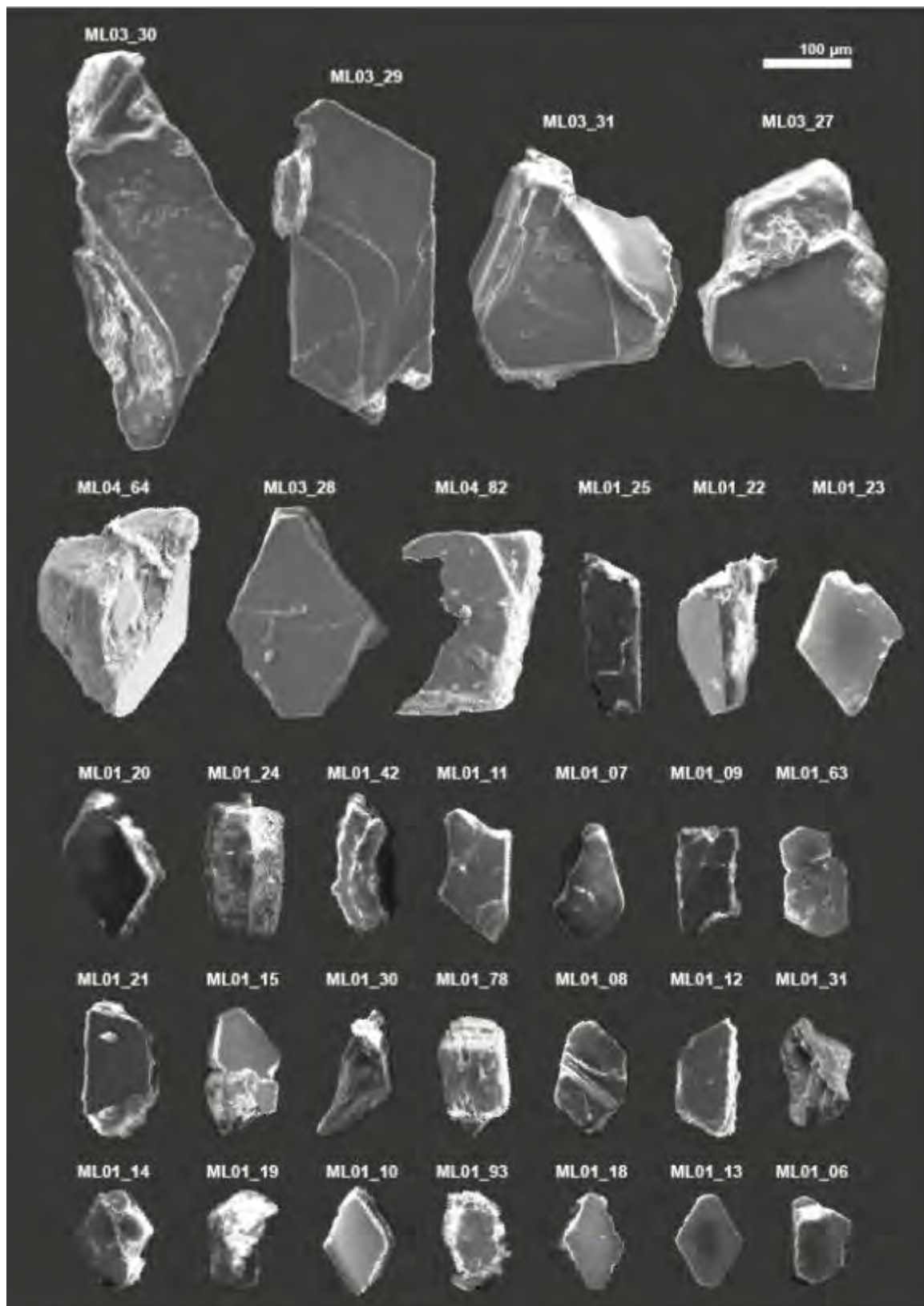
## 2021-MAC-67 (APATITE)



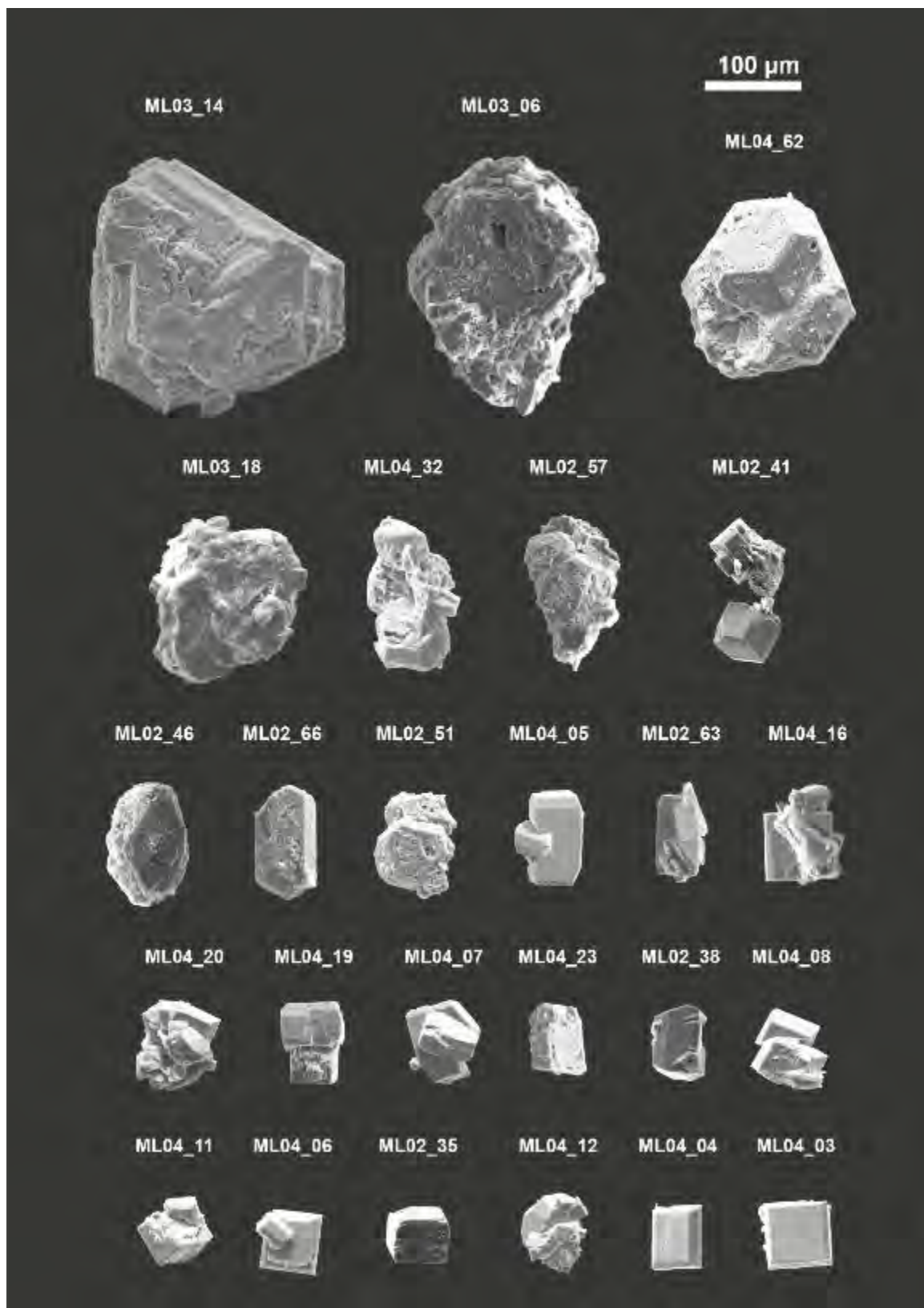
## 2021-MAC-67 (RUTILE)



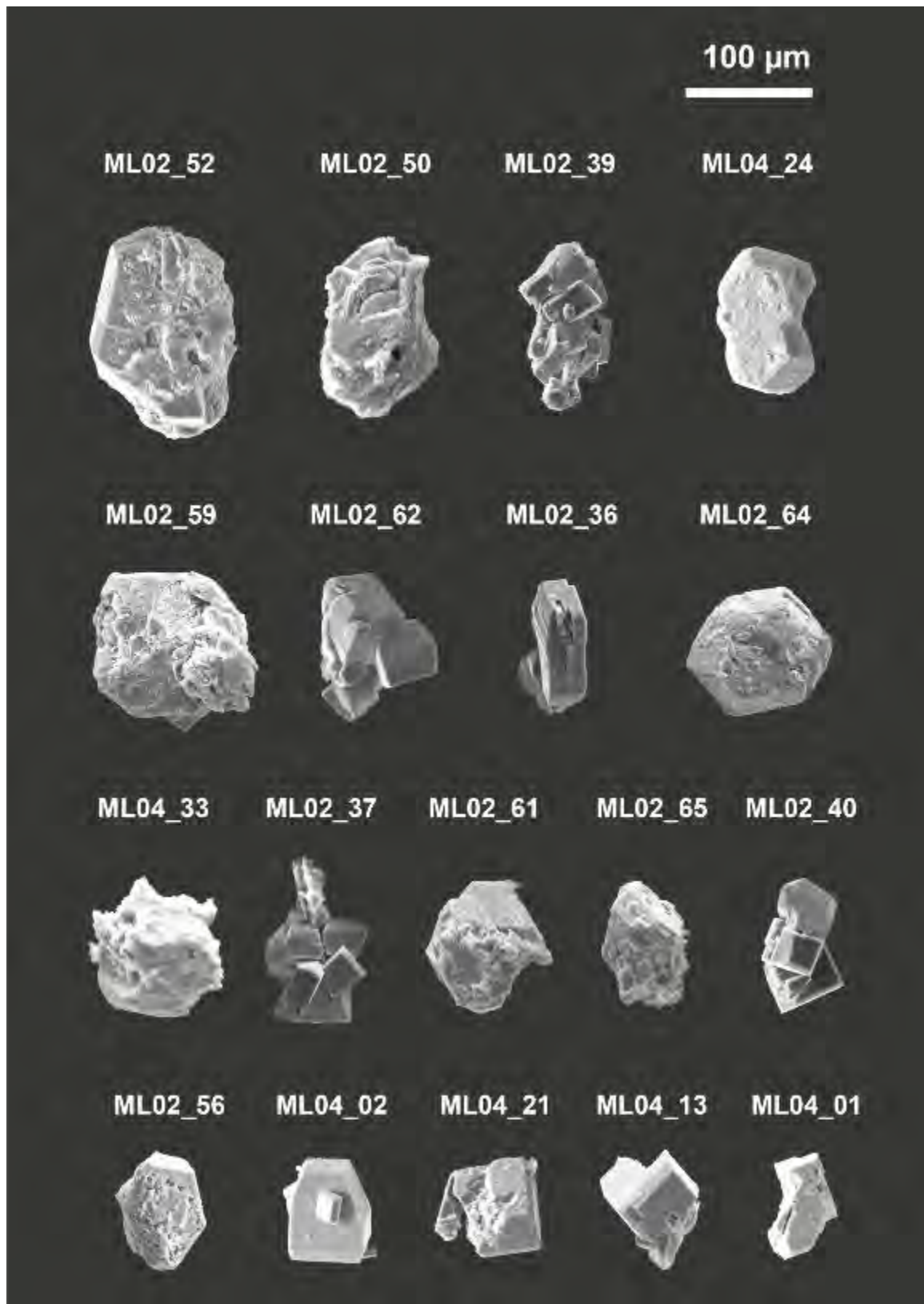
## 2021-MAC-67 (MUSCOVITE)



## 2021-MAC-67 (ANATASE)



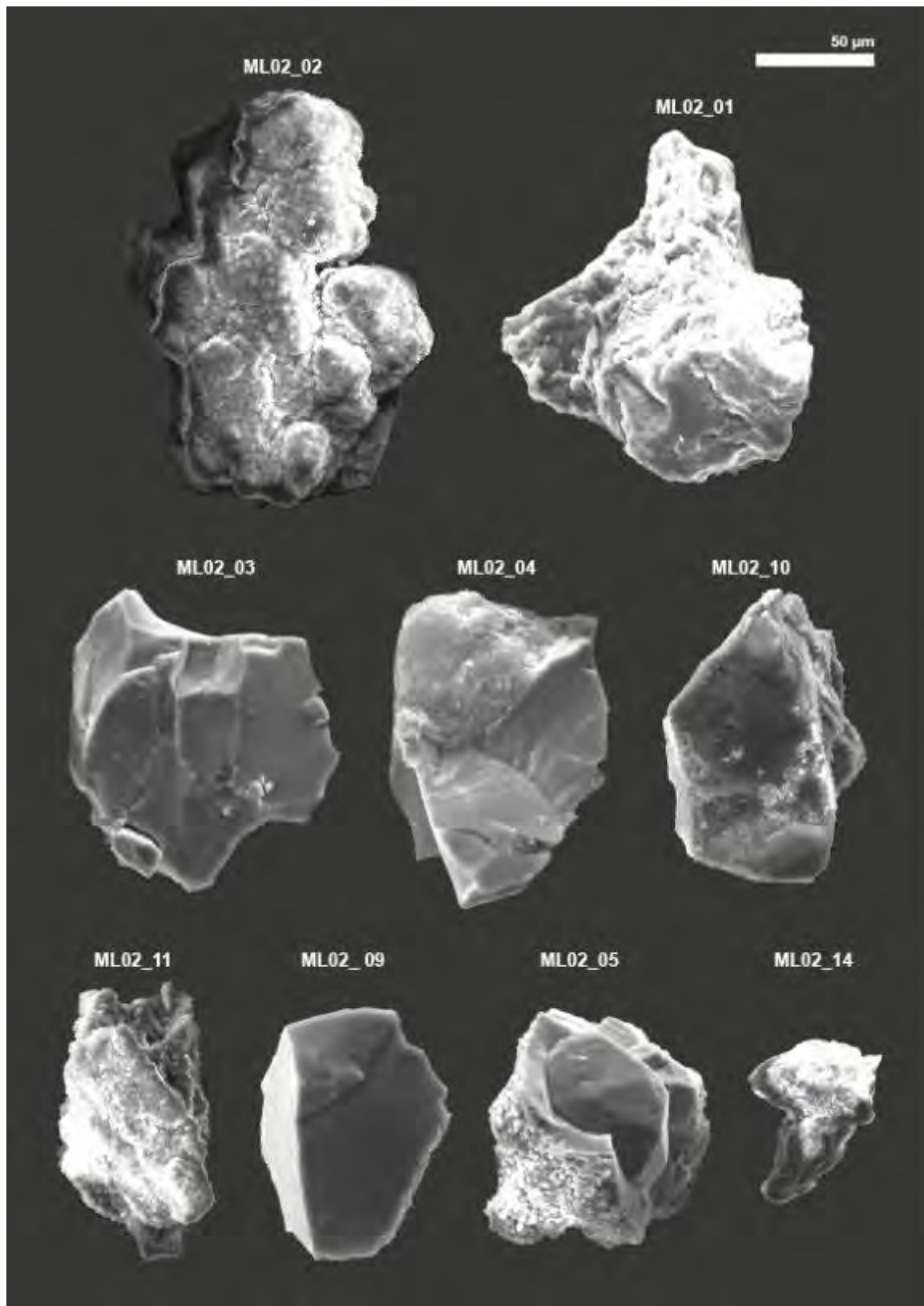
## 2021-MAC-67 (RUTILE-LIKE GRAINS)



2021-MAC-67 (QUARTZ)



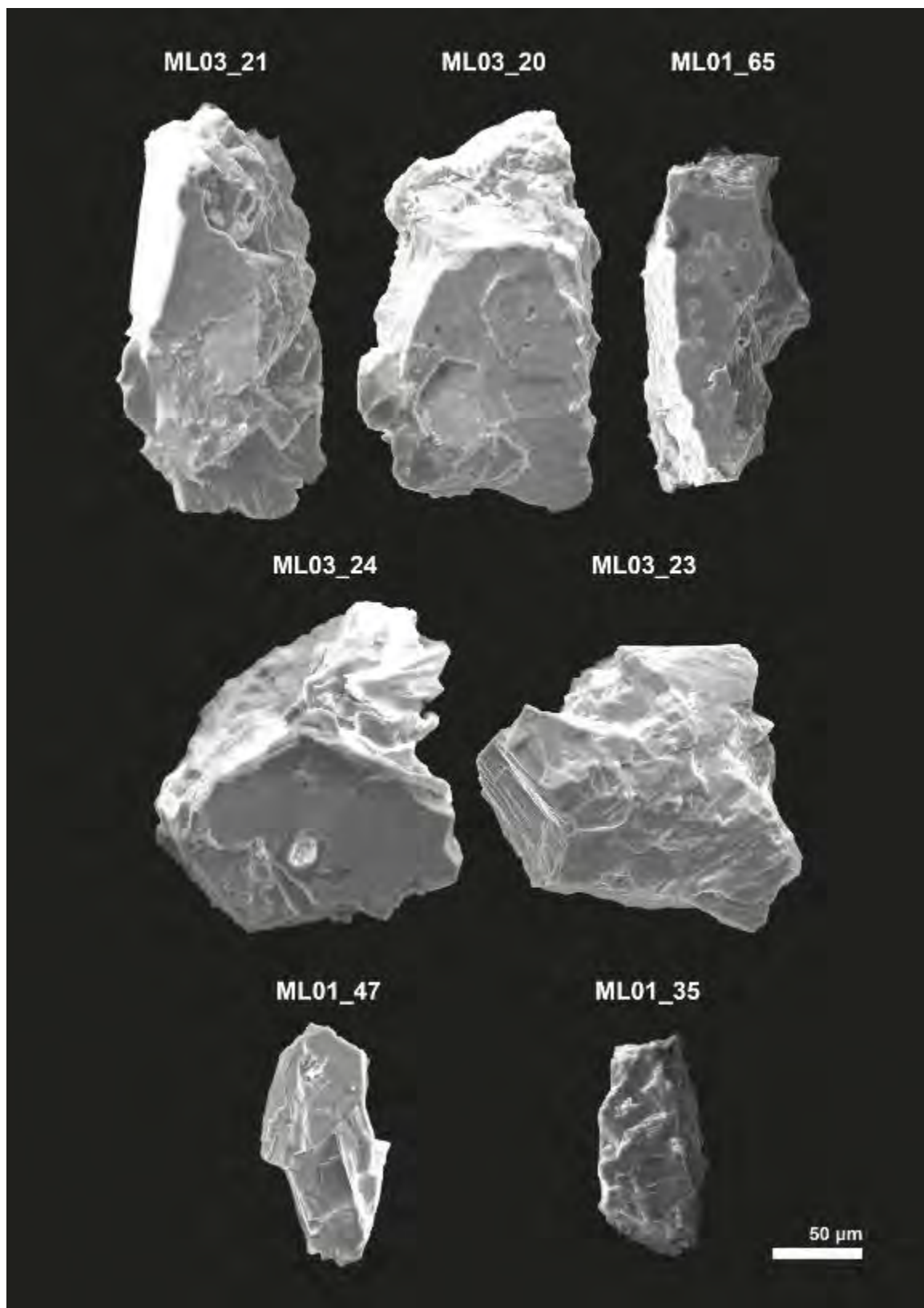
## 2021-MAC-67 (GOETHITE)



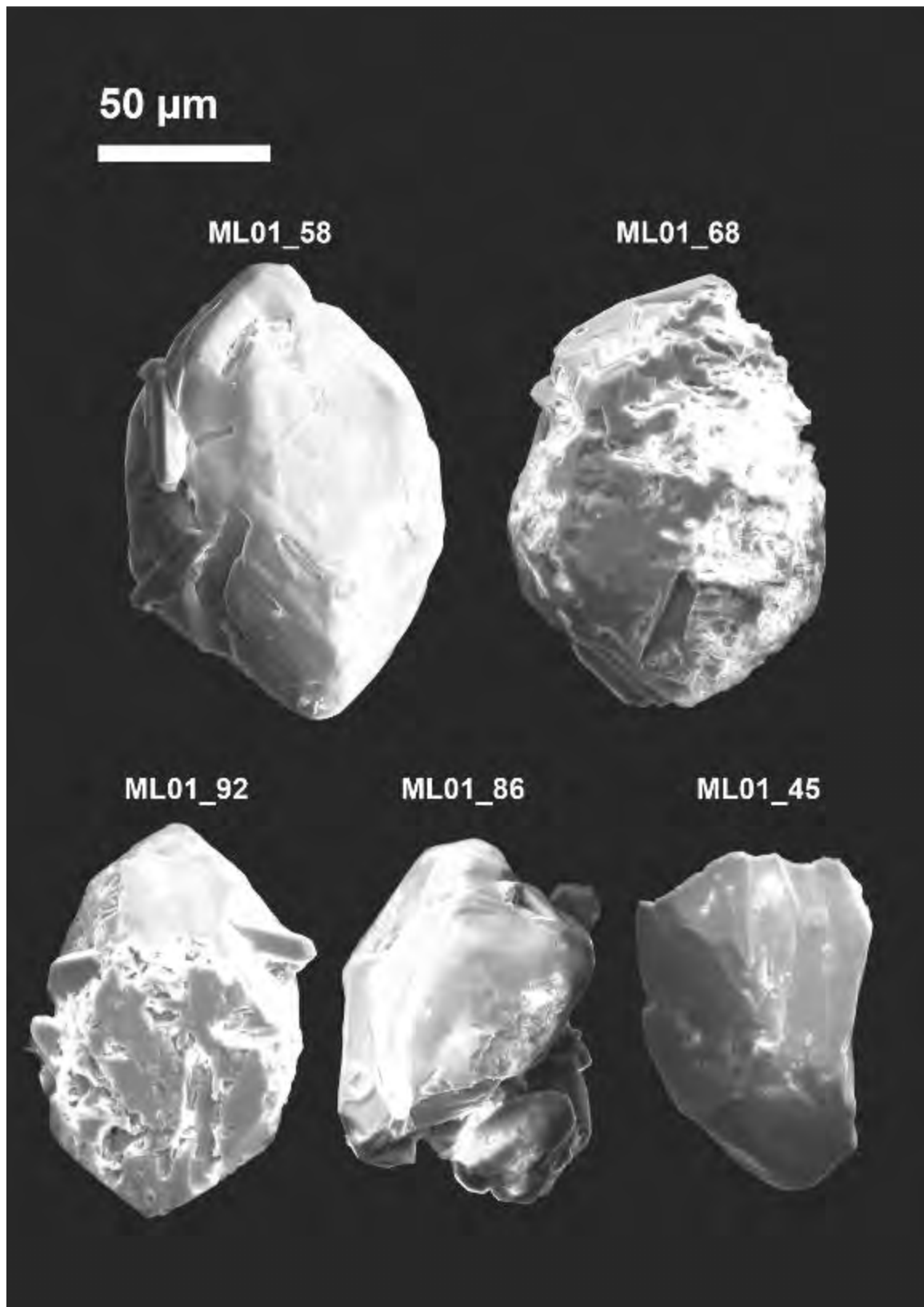
2021-MAC-67 (ZIRCON)



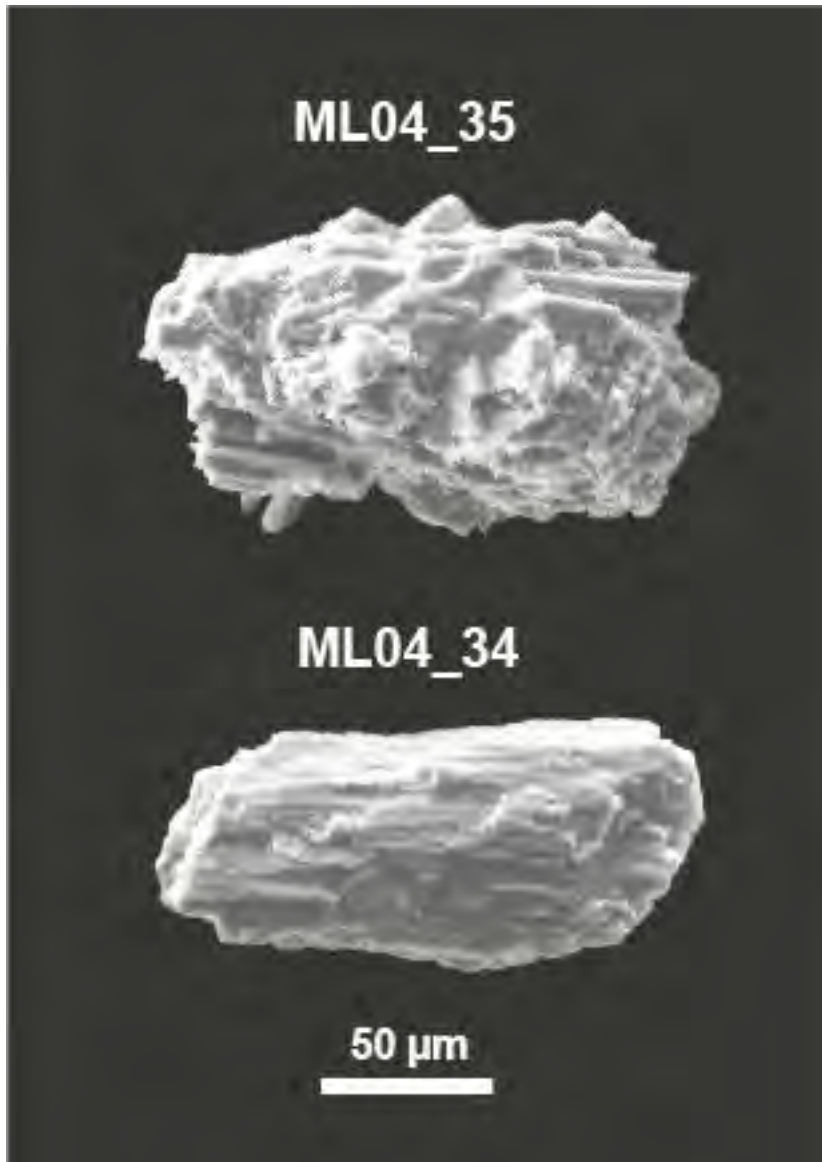
## 2021-MAC-67 (WICKMANITE)



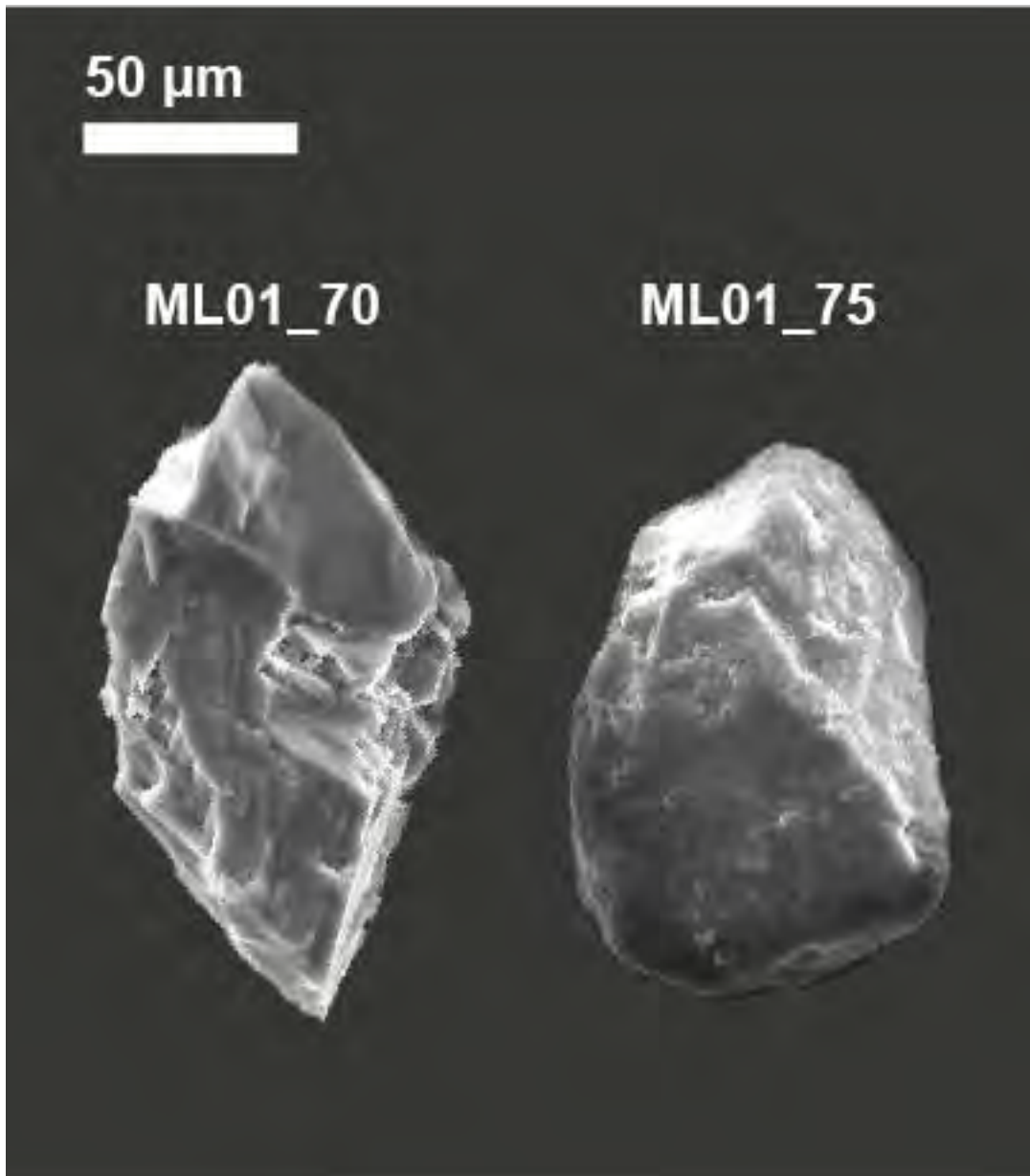
## 2021-MAC-67 (MONAZITE-Ce)



2021-MAC-67 (ACTINOLITE)



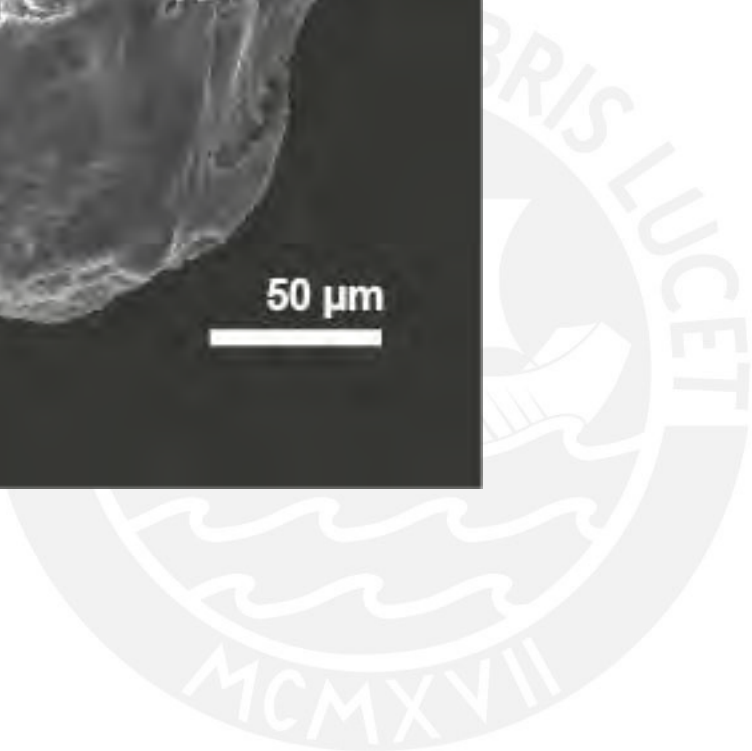
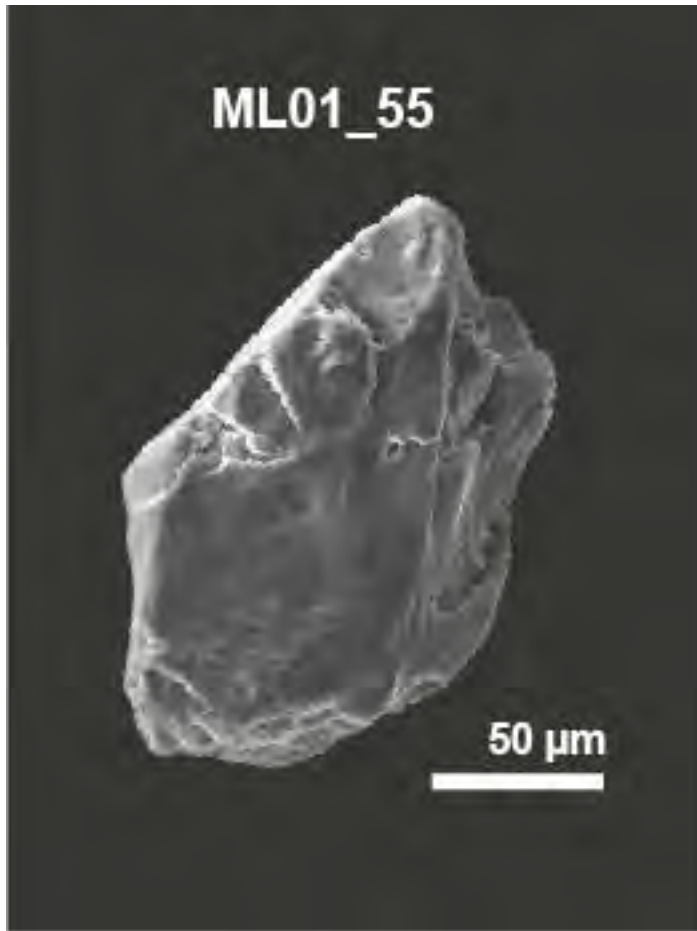
2021-MAC-67 (FELDSPAR)



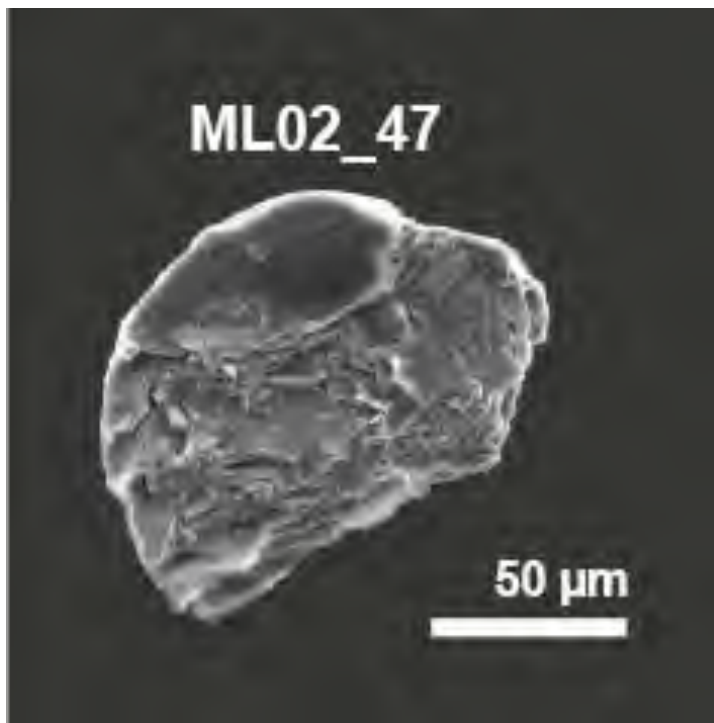
2021-MAC-67 (ILMENITE)



2021-MAC-67 (ANDRADITE)



2021-MAC-67 (PYRITE)





















CÓDIGO	MINERAL	O	Si	Na	Al	K	Ti	Fe	Ta	Nb	Sn	Mg	Ca	W	S	F	Y	P	Zr	Cl	Mn	As	Th	U	La	Ce	Nd	Sm	Mo
2021-MAC-21_ML002_010	Zircon	34.74	17.92	-	-	-	-	-	-	-	-	-	-	-	-	-	-	-	47.34	-	-	-	-	-	-	-	-	-	-
2021-MAC-21_ML002_011	Monazite	30.71	1.35	-	-	-	-	-	-	-	-	-	0.9	-	-	-	-	16.19	-	-	-	-	5.16	1.24	12.14	21.87	7.42	3.02	-
2021-MAC-21_ML002_012	Zircon	38.54	16.89	-	-	-	-	-	-	-	-	-	-	-	-	-	-	-	44.57	-	-	-	-	-	-	-	-	-	-
2021-MAC-21_ML002_013	Zircon	35.48	17.3	-	-	-	-	-	-	-	-	-	-	-	-	-	-	-	47.22	-	-	-	-	-	-	-	-	-	-
2021-MAC-21_ML002_014	Zircon	34.64	17.87	-	-	-	-	-	-	-	-	-	-	-	-	-	-	-	47.49	-	-	-	-	-	-	-	-	-	-
2021-MAC-21_ML002_015	Apatite	41	-	-	-	-	-	-	-	-	-	-	35.27	-	-	6.33	-	17.41	-	-	-	-	-	-	-	-	-	-	-
2021-MAC-21_ML002_016	Monazite	26.37	-	-	-	-	-	-	-	-	-	-	1.41	-	-	-	-	17.26	-	-	-	-	5.69	1.61	11.73	21.57	9.86	4.49	-
2021-MAC-21_ML002_017	Zircon	33.9	18.18	-	-	-	-	-	-	-	-	-	-	-	-	-	-	-	47.92	-	-	-	-	-	-	-	-	-	-
2021-MAC-21_ML002_018	Zircon	30.47	17.98	-	-	-	-	-	-	-	-	-	-	-	-	-	-	-	51.55	-	-	-	-	-	-	-	-	-	-
2021-MAC-21_ML002_019	Zircon	36.77	17.73	-	-	-	-	-	-	-	-	-	-	-	-	-	-	-	45.5	-	-	-	-	-	-	-	-	-	-
2021-MAC-21_ML002_020	Zircon	33.3	18.51	-	-	-	-	-	-	-	-	-	-	-	-	-	-	-	48.19	-	-	-	-	-	-	-	-	-	-
2021-MAC-21_ML002_021	Zircon	37.06	18.32	-	-	-	-	-	-	-	-	-	-	-	-	-	-	-	44.62	-	-	-	-	-	-	-	-	-	-
2021-MAC-21_ML002_022	Zircon	32.59	19.69	-	-	-	-	-	-	-	-	-	-	-	-	-	-	-	47.72	-	-	-	-	-	-	-	-	-	-
2021-MAC-21_ML002_023	Zircon	31.82	18.33	-	-	-	-	-	-	-	-	-	-	-	-	-	-	-	49.85	-	-	-	-	-	-	-	-	-	-
2021-MAC-21_ML002_024	Zircon	31.69	18.34	-	-	-	-	-	-	-	-	-	-	-	-	-	-	-	49.97	-	-	-	-	-	-	-	-	-	-
2021-MAC-21_ML002_025	Monazite	33.65	-	-	-	-	-	-	-	-	-	-	1.17	-	-	-	-	17.19	-	-	-	-	5.02	1.59	9.95	19.95	7.69	3.78	-
2021-MAC-21_ML002_026	Zircon	31.24	18.69	-	-	-	-	-	-	-	-	-	-	-	-	-	-	-	50.07	-	-	-	-	-	-	-	-	-	-
2021-MAC-21_ML002_027	Zircon	34.06	16.73	-	-	-	-	-	-	-	-	-	-	-	-	-	-	-	49.21	-	-	-	-	-	-	-	-	-	-
2021-MAC-21_ML002_028	Zircon	39.17	17.51	-	-	-	-	-	-	-	-	-	-	-	-	-	-	-	43.32	-	-	-	-	-	-	-	-	-	-
2021-MAC-21_ML002_029	Zircon	35.2	17.92	-	-	-	-	-	-	-	-	-	-	-	-	-	-	-	46.88	-	-	-	-	-	-	-	-	-	-
2021-MAC-21_ML002_030	Zircon	34.95	16.97	-	-	-	-	-	-	-	-	-	-	-	-	-	-	-	48.08	-	-	-	-	-	-	-	-	-	-
2021-MAC-21_ML002_031	Zircon	33.84	17.77	-	-	-	-	-	-	-	-	-	-	-	-	-	-	-	48.39	-	-	-	-	-	-	-	-	-	-
2021-MAC-21_ML002_032	Zircon	36.67	17.2	-	-	-	-	-	-	-	-	-	-	-	-	-	-	-	46.13	-	-	-	-	-	-	-	-	-	-
2021-MAC-21_ML002_033	Zircon	28.7	20.15	-	-	-	-	-	-	-	-	-	-	-	-	-	-	-	51.15	-	-	-	-	-	-	-	-	-	-
2021-MAC-21_ML002_034	Monazite	28.78	0.9	-	-	-	-	-	-	-	-	-	1.6	-	-	-	-	15.52	-	-	-	-	5.18	1.1	12.16	23.44	11.32	-	-
2021-MAC-21_ML002_035	Zircon	32.48	20.12	-	-	-	-	-	-	-	-	-	-	-	-	-	-	-	47.4	-	-	-	-	-	-	-	-	-	-
2021-MAC-21_ML002_036	Monazite	35.51	1.59	-	-	-	-	-	-	-	-	-	1.33	-	-	0.71	-	15.54	-	-	-	-	5.64	1.31	9.95	20.21	8.22	-	-
2021-MAC-21_ML002_037	Zircon	34.21	19.18	-	-	-	-	-	-	-	-	-	-	-	-	-	-	-	46.61	-	-	-	-	-	-	-	-	-	-
2021-MAC-21_ML002_038	Zircon	43.16	15.52	-	-	-	-	-	-	-	-	-	-	-	-	-	-	-	41.32	-	-	-	-	-	-	-	-	-	-
2021-MAC-21_ML002_039	Zircon	35.17	17.4	-	-	-	-	-	-	-	-	-	-	-	-	-	-	-	47.43	-	-	-	-	-	-	-	-	-	-
2021-MAC-21_ML002_040	Monazite	30.07	-	-	-	-	-	-	-	-	-	-	1.58	-	-	-	-	16.59	-	-	-	-	6.46	1.06	10.49	22.85	10.89	-	-
2021-MAC-21_ML002_041	Monazite	19.25	-	-	-	-	-	-	-	-	-	-	1.6	-	-	-	-	15.62	-	-	-	-	3.81	1.89	13.95	29.46	14.42	-	-
2021-MAC-21_ML002_042	Monazite	35.57	-	-	-	-	-	-	-	-	-	-	1.32	-	-	-	-	17.35	-	-	-	-	3.53	2.1	13.72	26.41	-	-	-
2021-MAC-21_ML002_043	Monazite	28.4	-	-	-	-	-	-	-	-	-	-	1.67	-	-	-	-	16.35	-	-	-	-	5.2	0.77	11.02	23.25	9.75	3.58	-
2021-MAC-21_ML002_044	Zircon	37.24	16.54	-	-	-	-	-	-	-	-	-	-	-	-	-	-	-	46.22	-	-	-	-	-	-	-	-	-	-
2021-MAC-21_ML002_045	Zircon	37.86	16.12	-	-	-	-	-	-	-	-	-	-	-	-	-	-	-	46.02	-	-	-	-	-	-	-	-	-	-
2021-MAC-21_ML002_046	Monazite	37.8	1.18	-	-	-	-	-	-	-	-	-	0.53	-	-	-	-	16.56	-	-	-	-	3.56	0.96	9.94	21.24	8.23	-	-
2021-MAC-21_ML002_047	Monazite	24.75	1.84	-	-	-	-	-	-	-	-	-	1.42	-	-	-	-	13.83	-	-	-	-	5.23	1.18	13.15	24.5	8.94	5.15	-
2021-MAC-21_ML002_048	Monazite	21.72	0.92	-	-	-	-	-	-	-	-	-	1.35	-	-	-	-	14.95	-	-	-	-	5.82	0.95	14.52	24.4	11.21	4.16	-
2021-MAC-21_ML002_049	Zircon	34.39	17.82	-	-	-	-	-	-	-	-	-	-	-	-	-	-	-	47.79	-	-	-	-	-	-	-	-	-	-
2021-MAC-21_ML002_050	Zircon	33.49	18.13	-	-	-	-	-	-	-	-	-	-	-	-	-	-	-	48.38	-	-	-	-	-	-	-	-	-	-
2021-MAC-21_ML002_051	Monazite	18.15	1.24	1.57	-	-	-	-	-	-	-	-	2.23	-	-	-	-	15.35	-	-	-	-	5.12	1.64	13.88	28.49	12.33	-	-









## SUMMARY OF EDS ANALYSES IN 2021-MAC-67

RAMAN ANALYSIS																												
CÓDIGO	MINERAL	O	Si	Na	Al	K	Ti	Fe	Ta	Nb	Sn	Mg	Ca	W	S	F	Y	P	Zr	Cl	Mn	As	Th	U	La	Ce	Nd	Sm
2021-MAC-67_ML001_001	Actinolite	50.12	22.86	-	15.67	7.36	-	2.85	-	-	-	1.14	-	-	-	-	-	-	-	-	-	-	-	-	-	-	-	-
2021-MAC-67_ML001_002	Actinolite	44.64	26.15	-	1.02	-	-	5.78	-	-	-	12.65	9.76	-	-	-	-	-	-	-	-	-	-	-	-	-	-	-
2021-MAC-67_ML001_003	Actinolite	49.75	23.31	-	2.45	-	-	4.24	-	-	-	13.32	6.94	-	-	-	-	-	-	-	-	-	-	-	-	-	-	-
2021-MAC-67_ML001_004	?	29.41	15.22	-	12.12	-	-	29.09	-	-	-	8.21	5.95	-	-	-	-	-	-	-	-	-	-	-	-	-	-	-
2021-MAC-67_ML001_005	Zircon	35.91	17.80	-	-	-	-	-	-	-	-	-	-	-	-	-	-	-	46.28	-	-	-	-	-	-	-	-	-
2021-MAC-67_ML001_006	Muscovite	45.71	22.85	-	19.66	8.98	-	2.8	-	-	-	-	-	-	-	-	-	-	-	-	-	-	-	-	-	-	-	-
2021-MAC-67_ML001_007	Muscovite	42.58	23.56	-	20.33	10.08	-	3.44	-	-	-	-	-	-	-	-	-	-	-	-	-	-	-	-	-	-	-	-
2021-MAC-67_ML001_008	Muscovite	42.95	22.58	-	19.44	10.04	-	3.84	-	-	-	1.15	-	-	-	-	-	-	-	-	-	-	-	-	-	-	-	-
2021-MAC-67_ML001_009	Muscovite	47.59	21.98	-	17.71	7.89	-	4.84	-	-	-	-	-	-	-	-	-	-	-	-	-	-	-	-	-	-	-	-
2021-MAC-67_ML001_010	Muscovite	44.68	22.18	-	19.03	9.93	-	4.18	-	-	-	-	-	-	-	-	-	-	-	-	-	-	-	-	-	-	-	-
2021-MAC-67_ML001_011	Muscovite	42.29	23.00	-	19.71	10.70	-	4.31	-	-	-	-	-	-	-	-	-	-	-	-	-	-	-	-	-	-	-	-
2021-MAC-67_ML001_012	Muscovite	42.98	23.29	-	19.63	10.44	-	3.66	-	-	-	-	-	-	-	-	-	-	-	-	-	-	-	-	-	-	-	-
2021-MAC-67_ML001_013	Muscovite	45.21	22.95	-	19.27	9.21	-	3.37	-	-	-	-	-	-	-	-	-	-	-	-	-	-	-	-	-	-	-	-
2021-MAC-67_ML001_014	Muscovite	44.19	22.55	-	19.71	9.90	-	3.65	-	-	-	-	-	-	-	-	-	-	-	-	-	-	-	-	-	-	-	-
2021-MAC-67_ML001_015	Muscovite	49.30	19.48	-	17.68	6.13	-	2.20	-	-	-	-	-	-	-	5.21	-	-	-	-	-	-	-	-	-	-	-	-
2021-MAC-67_ML001_016	Apatite	37.10	-	-	-	-	-	-	-	-	-	-	39.64	-	-	4.52	-	18.74	-	-	-	-	-	-	-	-	-	-
2021-MAC-67_ML001_017	Quartz	59.04	40.96	-	-	-	-	-	-	-	-	-	-	-	-	-	-	-	-	-	-	-	-	-	-	-	-	-
2021-MAC-67_ML001_018	Muscovite	48.80	22.02	-	18.37	7.81	-	2.99	-	-	-	-	-	-	-	-	-	-	-	-	-	-	-	-	-	-	-	-
2021-MAC-67_ML001_019	Muscovite	47.41	21.26	-	18.21	9.08	-	4.05	-	-	-	-	-	-	-	-	-	-	-	-	-	-	-	-	-	-	-	-
2021-MAC-67_ML001_020	Muscovite	36.60	23.47	-	19.25	13.44	-	7.25	-	-	-	-	-	-	-	-	-	-	-	-	-	-	-	-	-	-	-	-
2021-MAC-67_ML001_021	Muscovite	44.37	22.76	-	19.51	9.41	-	3.95	-	-	-	-	-	-	-	-	-	-	-	-	-	-	-	-	-	-	-	-
2021-MAC-67_ML001_022	Muscovite	48.37	21.30	-	18.88	8.37	-	3.09	-	-	-	-	-	-	-	-	-	-	-	-	-	-	-	-	-	-	-	-
2021-MAC-67_ML001_023	Muscovite	44.52	22.99	-	19.08	9.67	-	3.74	-	-	-	-	-	-	-	-	-	-	-	-	-	-	-	-	-	-	-	-
2021-MAC-67_ML001_024	Muscovite	47.12	23.32	-	19.01	7.73	-	2.82	-	-	-	-	-	-	-	-	-	-	-	-	-	-	-	-	-	-	-	-
2021-MAC-67_ML001_025	Muscovite	43.00	23.37	-	19.84	10.34	-	3.45	-	-	-	-	-	-	-	-	-	-	-	-	-	-	-	-	-	-	-	-
2021-MAC-67_ML001_026	Quartz	46.64	53.36	-	-	-	-	-	-	-	-	-	-	-	-	-	-	-	-	-	-	-	-	-	-	-	-	-
2021-MAC-67_ML001_027	Apatite	43.16	-	-	-	-	-	-	-	-	-	-	32.39	-	-	7.86	-	16.6	-	-	-	-	-	-	-	-	-	-
2021-MAC-67_ML001_028	Apatite	34.87	-	-	-	-	-	-	-	-	-	-	41.63	-	-	3.95	-	19.54	-	-	-	-	-	-	-	-	-	-
2021-MAC-67_ML001_029	Apatite	34.20	-	-	-	-	-	-	-	-	-	-	43.42	-	-	4.14	-	18.25	-	-	-	-	-	-	-	-	-	-
2021-MAC-67_ML001_030	Muscovite	45.57	22.88	-	19.48	9.35	-	2.71	-	-	-	-	-	-	-	-	-	-	-	-	-	-	-	-	-	-	-	-
2021-MAC-67_ML001_031	Muscovite	50.73	29.56	-	11.07	8.64	-	0.00	-	-	-	-	-	-	-	-	-	-	-	-	-	-	-	-	-	-	-	-
2021-MAC-67_ML001_032	Apatite	46.74	2.49	-	-	-	-	22.87	-	-	-	-	21.6	-	-	-	-	6.29	-	-	-	-	-	-	-	-	-	-
2021-MAC-67_ML001_033	Quartz	51.83	48.17	-	-	-	-	-	-	-	-	-	-	-	-	-	-	-	-	-	-	-	-	-	-	-	-	-
2021-MAC-67_ML001_034	Apatite	41.24	-	-	-	-	-	-	-	-	-	-	34	-	-	7.66	-	17.09	-	-	-	-	-	-	-	-	-	-
2021-MAC-67_ML001_035	Wickmanite	29.20	-	-	-	-	-	-	-	-	45.54	-	-	-	-	-	-	-	-	-	-	25.26	-	-	-	-	-	-
2021-MAC-67_ML001_036	Apatite	32.54	-	-	-	-	-	-	-	-	-	-	44.69	-	-	5.63	-	17.14	-	-	-	-	-	-	-	-	-	-
2021-MAC-67_ML001_037	Apatite	28.14	-	-	-	-	-	-	-	-	-	-	50.59	-	-	3.04	-	18.23	-	-	-	-	-	-	-	-	-	-
2021-MAC-67_ML001_038	Apatite	46.27	-	-	-	-	-	-	-	-	-	-	29.52	-	-	8.65	-	15.57	-	-	-	-	-	-	-	-	-	-
2021-MAC-67_ML001_039	Apatite	41.78	-	-	-	-	-	4.31	-	-	-	-	32.45	-	-	4.31	-	12.15	-	-	-	5.00	-	-	-	-	-	-











